ADVANCES IN LOCALIZED FLOOD HAZARD MODELLING IN URBANIZED AND DATA-SCARCE AREAS

Yakob Umer

ADVANCES IN LOCALIZED FLOOD HAZARD MODELLING IN URBANIZED AND DATA-SCARCE AREAS

DISSERTATION

to obtain
the degree of doctor at the University of Twente,
on the authority of the rector magnificus,
Prof.dr.ir. A. Veldkamp,
on account of the decision of the Doctorate Board,
to be publicly defended
on Wednesday, January 19, 2022, at 12:45

By

Yakob Umer

Born on 10th January 1985
in Bale, Ethiopia

This thesis has been approved by:

prof. dr. V.G. Jetten (Supervisor)
dr.ir. J. Ettema (Supervisor)

ITC dissertation number 410
ITC, P.O. Box 217, 7500 AE Enschede, The Netherlands

ISBN 978-90-365-5324-7
DOI 10.3990/1.9789036553247
Cover designed by J.Duim and Y.Umer
Printed by CTRL-P, Hengelo

UNIVERSITY OF TWENTE. | ITC

Graduation committee:

Chair

Prof.dr. F.D. van der Meer

Supervisor(s)

prof.dr. V.G. Jetten

dr. ir. J. Ettema

Members

Prof.dr. R.V. Sliuzas

Prof.dr. M.K. van Aalst

Prof.dr. S.M. de Jong

Prof.dr. C. Ritsema

dr. ing. G.J. Steeneveld

To Mama and Kikila

Acknowledgments

First of all, I would like to thank my benevolent God for giving me strength and patient throughout this Ph.D. time.

Next, I acknowledge a group of people who supported and helped me on this Ph.D. research and shared social life with me during these four years in Enschede.

Starting from the beginning, my deepest gratitude goes to my supervisor, Prof. dr. Victor Jetten and dr.ir. Janneke Ettema, for their support, insight, and expertise throughout all these years. Not only have they introduced me to the scientific world, but they also have contributed to educating me to be a better researcher over these years. Indeed, their patience and unlimited advice are what lead to unfolding this thesis.

My gratitude also goes to Dr.Gert-Jan Steeneveld from Wageningen University, Meteorology, and Air Quality Section. His expertise and support helped me to further my knowledge of the WRF model. I must also acknowledge Dr.Ronda Reinder from Wageningen Unversity for showing me the WRF software programming and diagnosis to adjust the urban fraction in the WRF model I have used throughout this Ph.D. I want to thank also Dr.Gemechu Fanta Garum from the University of Quebec, Canada, for his assistance in managing static data in the WRF model.

My acknowledgment also goes to Dr.Eduardo Perez Molina, a colleague from the PGM department, for developing the land cover fraction of Kampala that I have used throughout this dissertation. I must also thank my co-author Dr. Luigi Lumbardo, for his expertise, insightful comments, and recommendations. I must also thank Dr.Bastian van der Bout for his support and experience sharing on the openLISEM model. My thanks also go to Dr. Harald van der Werff and Dr. Islam Fadel for their technical support on computational facilities. I would like to describe my sincere gratitude to also Professor Cees for editing my thesis.

I would like to thank all members of the ESA department and colleagues for their help and support when needed. I always remember the warm discussions we had on social and other issues during tea break. A big thanks to all my wonderful friends and Ph.D. community at ITC, and it’s always lovely to be in such an environment. Oscar, thanks for your friendship and also for your help with the Dutch summary. Hakan, Kartika, Yan, and Tunde, it was great to share the office with you guys. Especial thanks to all my current and former Ph.D. friends Evelien, Saman, Vasily, Jonathan, Fardad, Matthew, Riswan, Saad, Biao, Sofia, Sobhan, Junior, Tingxuan, Chanitnart, Semi, and Kumah. Over these four years, so many friends whose friendship made this journey possible, and I apologize for the miss if not mentioned here.

In the end, I would like to thank all my family members, especially my father, mother, brothers, and sisters, for being my side when I needed both physically and spiritually. Especial thanks to my beloved wife Amina for your understanding and support: your inspiration always kept me going forward when otherwise I have stopped. To my son Amyar, I apologize for being away from you. Soon we will reunite again!

Table of Contents

List of figures

List of tables

(blank)

Chapter 1: Background

Flooding is a natural phenomenon, but with an increasing effect of urbanization and climate change in recent times, urban flooding is becoming more frequent and hazardous (Hirabayashi et al., 2013; Duan et al., 2016). While climate change has increased precipitation extremes (through thermodynamic forcing as reported by the Intergovernmental Panel on Climate Change (IPCC) Masson-Delmotte et al. (2021) that are causing flood hazards (e.g., Grum et al. (2006); (Arnbjerg-Nielsen et al., 2013)), urbanization has caused imperviousness, resulting in more and faster flooding (Huong and Pathirana, 2013). Moreover, urbanization also intensifies precipitation extremes by affecting local forcing, increasing localized flood hazards in the urban environment (Zhang et al., 2019). Future increases in climate change and urbanization enhance warming in the city, as reported by the Intergovernmental Panel on Climate Change (IPCC) 6th report Masson-Delmotte et al. (2021), which further enhances extreme rainfall; hence, expected to increase flood hazards in the urbanized environment. Although flooding is a natural hazard and becoming a global threat, it disproportionately affects more low-income countries, mainly located in Africa and Asia (CRED and UNISDR, 2015). Particularly, in recent years, recurring floods have been reported in many cities in Sub-Saharan Africa (Bhattacharya and Lamond, 2011; Amoako, 2012). Kampala is an example of a fast-growing city that has seen increased flood hazards and risks more often. For instance, Markandya et al. (2015) reported that the city had experienced 11 severe flood events from 1995 to 2014, resulting in 38 deaths, 67,713 people affected, 123 homes destroyed, and around 21,000 homes damaged. According to this report, expected damages are estimated between \$3.7 million and \$17.6 million by 2025 and between \$33.2 million and \$101.7 million by 2050.

More impoverished communities in developing countries cities like Kampala are disproportionately affected by urban floods due to several known reasons. Firstly, the lack of data leads to a poor understanding of urban flooding and the processes leading to urban flooding; consequently, it results in inadequate flood management measures (Schipper and Pelling, 2006; Rahmati et al., 2020). Notably, the detailed lack of knowledge on the sources of floods, flood pathways, and recipients makes the extent/consequence of floods more challenging to predict and hence, challenging to manage the flood hazards. Secondly, anthropogenic activities such as poor drainage systems management, encroachments of wetlands, and flood plains also increase potential flood hazards (Sliuzas et al., 2013). Thirdly, poor urban planning following land-use and land-cover (LULC) changes results in a lack of open space, the so-called Blue-Green areas for flood relief. Consequently, urban development occurs in improper locations such as slums, which increases flood vulnerability (Isunju and Kemp, 2016; Isunju et al., 2016). Lastly, but not least, is overpopulation and urbanization and its physical expansion. While urbanization increases surface runoff through the creation of impervious areas, overpopulation causes a higher vulnerability. For example, Abebe (2013) indicated a tremendous urban expansion of Kampala in the last decades, with a total of 25168 ha of non-built-up land converted into built-up land over the period of 1989 to 2010 (Figure 1.1). Mass migration in search of a better life caused the city to expand rapidly, resulting in the removal of natural vegetation and being replaced by unplanned and low-cost housing on hill slopes and wetlands (Douglas, 2017). This expansion certainly increases the impervious surface areas of the city, which reduces infiltration processes and increases surface runoff in uphill areas, and consequently increases flooding in the wetlands (Pérez-Molina et al., 2017). Moreover, as a result of urban expansion, former wetlands, which are used to be the natural drainage systems, are then occupied by slums mainly of the poor population (Vermeiren et al., 2012). As the population grows, many poor communities start to live in flood plains and reclaim wetlands; they are exposed to localized and frequent flooding during the rainy season, resulting in loss of lives and property (Sliuzas et al., 2013; Perez Molina, 2019). It is also vital to point out here that poverty makes the effect of flooding worse. The big influence of poverty is also more victims, more damage. People live in unsuitable areas, possibly the areas that are naturally prone to flooding, hence more vulnerability.

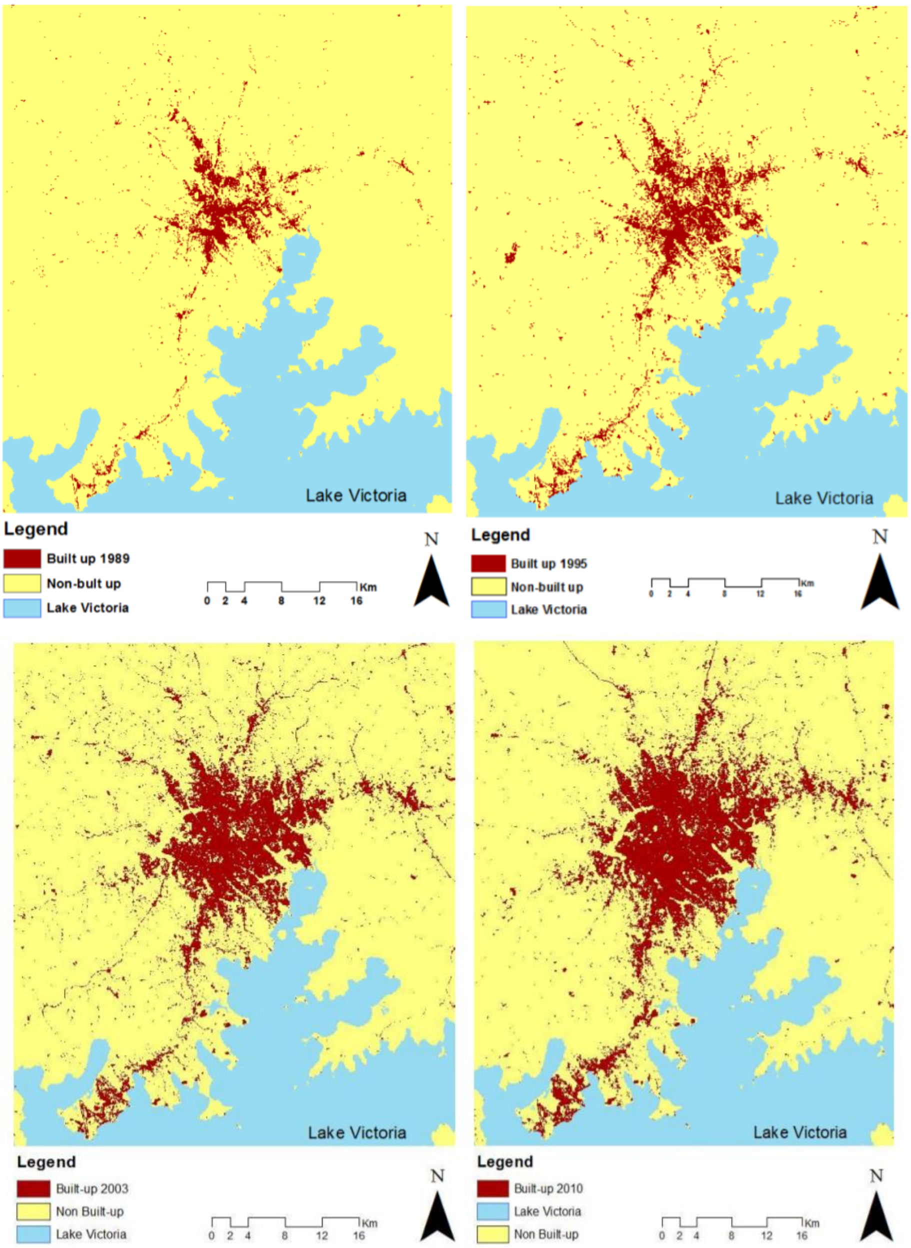

Figure 1.1 Urban growth of Kampala from 1989 to 2010 (source: Abebe 2013)

Flood management measures such as the Integrated Flood Management (IFM) are essential in reducing urban flood damage through proactive measures (Vojinovic, 2015; Debele et al., 2019; Sahani et al., 2019). The overall aim of IFM is to build a resilient city under changing conditions, which implies that the more residents adapt to flood hazards, the more opportunities for sustainable urban development (Jha, 2012; Liao, 2012). To achieve this aim, the proposed IFM measures are targeted to approach the flood impact from a holistic point of view (source-pathways-recipient–consequence) to develop robust but low-cost methodologies to reduce flood hazards (Management, 2009; Fratini et al., 2012; Juarez Lucas and Kibler, 2016). Such effective flood management requires proper flood hazard assessment.

Within the integrated flood management, the starting point is obtaining the information required for optimal flood hazard assessment. However, despite devastating flood-related fatalities and damages of livelihoods in developing country cities, there is often limited spatial and time-series data related to flooding, it's triggering, and hazard (Westerberg and McMillan, 2015; Kabenge et al., 2017). For instance, high-quality information on rainfall data, urban soil information, flood information, and up-to-date land cover changes due to city expansion to better understand and study the hydrological processes leading to the flood hazard is lacking; consequently, poor flood adaptation and mitigation strategies (Schipper and Pelling, 2006). Besides, these developing country cities are changing rapidly in infrastructure and population, making urbanized areas quickly outdated. Many developing nations are data-scarce mainly because of economic marginalization, which leads to a lack of infrastructure to periodically collect and document the required data for flood hazard modelling. Moreover, localized urban floods are often related to certain weather conditions that are highly variable in space. Hence, the available density of rain gauges is not high to capture the extreme precipitation related to these weather conditions, which restricts optimal flood hazard modlling in the data-scarce area. Among the lacking data for integrated flood management is also data on vulnerability, which is very important towards addressing the impacts of flooding (Nur and Shrestha, 2017; Hamidi et al., 2020). It is worth noting that flood risk and mitigation depend on hazards and vulnerability, and both are very difficult to assess without ground-based data. However, this thesis focuses on the flood hazard modelling part and does not study vulnerability.

1.1. Challenges in data-scarcity for flood hazard modelling in developing countries

The main challenge in urban flood management in developing countries is the lack of spatiotemporal data for optimal urban flood hazard modelling. Flood hazard assessment often relies on the flood modelling approaches, which theoretically involves developing algorithms designed to solve the numerical expressions of key hydrological processes and flow approximations leading to the flood hazard (O'brien, 2007; Delestre et al., 2014b; Bout and Jetten, 2018). Conventionally, such approaches require high-quality spatiotemporal input datasets for a detailed understanding of each potential flood trigger as well as to make realistic urban flood hazard assessments. However, urban flood hazard modelling is highly influenced by the lack of data availability and quality in the data-scarce area. In particular, data scarcity on rainfall, soil moisture information, and static datasets required for flood models is lacking, hindering effective flood hazard modeling studies in developing countries.

Regarding rainfall data, urban flood hazard assessment requires design storms of a given return period, which are derived from the intensity-duration-frequency (IDF) curves constructed from high quality and long-term observed rainfall data. In many developing country cities, the rain gauge network is not sufficient to capture a full picture of rainfall event development and movement. In addition, the length of the existing observed rainfall data is often insufficient for establishing reliable IDF curves. Besides, the existing rainfall data used to construct IDF curves is often only available on a daily time scale, which can result in an unrealistic derivation of the corresponding short-duration design storms (Di Baldassarre et al., 2006). Moreover, in the case of localized flood events, finely-gridded high-intensity rainfall events are required for detailed flood modelling (Liu et al., 2015), which is even more challenging to obtain in a developing country. In particular, the equatorial East African region has a high spatial-temporal variability of rainfall (Onyutha and Willems, 2015; Ongoma et al., 2018); thus, the problem with the lack of and quality of rainfall data severely affects the prediction of quantity and timing of flooding (Kabenge et al., 2017).

As proxies to the gauging rainfall observation, a Numerical Weather Prediction (NWP) model, such as the Weather Research and Forecasting (WRF) model (Powers et al., 2017), could be used as an alternative tool to produce the rainfall input for flood modelling in data scarce-areas. The WRF model can simulate a long-time series rainfall product from which IDF curves can be constructed. For instance, Liew et al. (2014) derive IDF curves derived from WRF rainfall driven by ERA40 reanalysis dataset daily and 30 km spatial resolution. This approach has been applied on an ungauged site (Java, Indonesia) and indicated a promising result compared to existing IDF curves. The WRF model can also be used to simulate the high-intensity rainfall events triggering the localized flood at high spatial-temporal resolutions in the catchment. For example, a study by Sikder et al. (2019) showed the usability of WRF rainfall simulations of moderate-intensity and high-intensity rainfall events for urban flood modelling in the urbanized area of Houston, the USA. When properly configured, the WRF model is found to be a promising alternative source to produce rainfall products used for flood hazard assessment in a data-scarce area.

Soil water characteristics are another factor that controls whether a given rainstorm produces a flood or not, due to the non-linear nature of runoff response to rainfall (Zehe and Blöschl, 2004; Grillakis et al., 2016). Hence, in the framework of IFM, in particular, for localized flood modelling, knowledge of soil is crucial (Van Steenbergen and Willems, 2013; Raynaud et al., 2015). Traditionally, hydrological modelling systems rely on the use of soil information available from in-situ measurements (Yang and Zhang, 2011; Wang et al., 2018a) or extracted from global soil databases, for example, by the Food and Agricultural Organization (FAO) (FAO, 1991). The global soil databases are soil maps based on classification systems that lack the information required for hydrology and flood modelling; the FAO maps are based on soil genesis, geomorphology, visual characteristics, and some basic chemistry. The information is, at best, a texture class, which is somewhat related to soil hydraulics. However, due to interference of the soil processes by urbanization, soil characteristics in the urban area are highly altered, and also, the natural soil has been replaced by human-made materials. As a detailed in-situ measurement of soil information becomes expensive and time-consuming, the extrapolation of a few measurements to a neighborhood and other parts of the urban area is impossible (Holanda and Soares, 2019). Moreover, detailed urban surfaces such as wetlands and built-up areas are hidden when using the global soil database alone. So, it is impossible to extract the optimum soil information required for flood modelling. When using the global FAO soil database, detailed soil information that determining the processes by which rain storms separated into surface runoff and soil infiltration, is lacking in many urban areas, which is a crucial issue that has affected the effective studies of flood hazard assessment.

Nevertheless, with recent improvements in the availability of high-resolution geospatial data such as LULC and soil information databases, there is an increasing effort to develop effective flood modelling approaches in data-scarce areas. For instance, taking advantage of global geospatial dataset availability, International Soil Reference and Information Center (ISRIC) developed a gridded spatial distribution of soil properties called SoilGrids (Hengl et al., 2017). The big advantage of SoilGrids is that it estimates directly detailed soil properties maps for six layers of depth in a reproducible way for flood modelling. Hence, from these maps of soil properties, we can produce essential soil water characteristics (e.g., porosity, saturated hydraulic conductivity, initial soil moisture, and soil depth) needed for hydrological modelling in a data-scarce area (Trinh et al., 2018). However, the soil database alone cannot provide detailed urban soil structure information, for example, compacted soil versus uncompacted soil. Hence, the LULC and soil database integration would be essential to prove the optimal soil information required for flood modelling. Toward this, high-quality LULC information, the main driving factor for urban flooding, can be obtained from satellite images (Pérez-Molina et al., 2017). The LULC data obtained from the satellite images include information on urban sealing, bare soil, and fragmented vegetation cover in the city that can explicitly be constructed. Thus, interferences of urbanization on soil physical structure can be overcome by incorporating the LULC information from satellite images into soil information.

In the context of optimum urban flood hazard modelling in the data-scarce environment, the existing methodology regarding the use of available geospatial datasets and the NWP model out for flood modelling is not sufficient and straightforward, particularly in the limited resource area. Therefore, advances in modelling systems that can elevate the uses of the open-source geospatial dataset and the NWP model output as well as their integration for flood modelling are vital. This thesis is designed to address this gap. In doing so, we better enable academics and decision-makers to understand the niceties of geospatial databases and integrated modelling systems to improve flood hazard assessment in the urbanized and data-scarce environment.

1.1.1. *Flood processes and triggers in Kampala*

A flood in Kampala is a typically localized flood triggered by high-intensity rainfall events. It is pluvial flooding generated as a surplus of rainfall from rainfall-runoff processes. Overall processes are conceptualized as the area of the landscape over which rain falls, and part of this rain infiltrates into the soil. The fraction of rainfall that infiltrates is larger for vegetated areas and zero for non-vegetated areas (built-up and compacted areas). Further, another fraction of the rainfall is intercepted by vegetation. The fraction of rainfall that remains becomes the runoff, and it moves downslope, eventually reaching the drainage channels. The capacity of these drainage channels may, in turn, be exceeded, which causes overflow into adjacent areas – in other words, flooding. The impact of land use land cover changes comes through urban construction, creating impervious areas and soil compaction. So, the flooding in Kampala is not about a large river overflowing; rather, it is localized flooding when runoff is based on a detailed model simulation of the infiltration processes. This means we need to have high-resolution rainfall in space and time to compare with the infiltration rate. As this high-resolution data is not available locally, we model rainfall data using the Numerical Weather Prediction(NWP), the WRF model.

Kampala's main flood triggering mechanisms are high-intensity rainfall events from tropical weather conditions and soil infiltration properties. The flood is also exacerbated by urban growth and physical expansion.

The primary triggering mechanism for flash floods in Kampala is precipitation extremes, characterized by high-intensity rainfall events. Flood regularly occur in the two main rainy seasons, which are controlled by the persistent synoptic-scale and mesoscale prevailing weather systems; hence, rainfall has a large scale monsoon characteristic with less spatial variability. The rainfall in the two main seasons is primarily controlled by the persistent seasonal migration of the Inter-Tropical Convergence Zone (ITCZ) and its interactions with the surrounding topography and Lake Victoria (Anyah, 2005). Floods in the city also occur at the end of the rainy season and the transition between the two main rainy seasons but not as regularly as in the main rainy seasons. The weather systems for floods in the non-main rainy season are mostly the mesoscale and local scale systems; they are mostly convection systems associated with lake circulation and the surrounding mountains (Anyah, 2005; Sun et al., 2015). The rainfall is often very localized and is characterized by high-intensity rainfall events as it is associated with highly variable weather systems; hence, available rain gauges are not sufficient to capture the spatial variability of these events.

Another triggering mechanism that determines the flooding in Kampala is urban growth and its physical expansion. Urban growth and its physical expansion is a big issue that alters the surface characteristics leading to flooding. Urbanization triggers flash floods in two ways: firstly, through direct effect, creating an impervious surface that hinders infiltration (Pérez-Molina et al., 2017). This effect is considered by including the satellite-derived urban elements into the flood modelling system; secondly, by changing urban rainfall patterns via microclimatic changes, as indicated (Paul et al., 2018). Local climate changes created by urbanization and the resulting impact on extreme rainfall triggering localized flooding are well studied (Dixon and Mote, 2003; Zhong et al., 2015). Hence, the satellite-driven urban fraction is coupled with the NWP model as a fraction of building and impervious surfaces and considered its impact on the simulated rainfall pattern. Satellite-derived urban fraction is the combined fraction of buildings and impermeable surfaces.

Moreover, embedded within the main causes of floods (i.e., extreme rainfall events and creation of impervious surfaces), soil infiltration properties also lead to flash flooding by creating large runoff volumes. Kampala has vast valley areas that are characterized by clay soil. According to Bhattacharya-Mis and Lamond (2011), low-lying areas with high clay content reduced soil infiltration. When combined with low elevation, it creates a natural drainage system for runoff from hills and impervious surfaces within the catchment, which leads to flooding. Therefore, in order to get the correct flood dynamics in the catchment, accurate soil information is crucial. Since detailed soil information is not locally available, in this thesis, we explored the existing soil databases and field observations and experiments and compared their advantages and disadvantages for flood hazard modelling.

1.2. Aim of the thesis

One of the main challenges in urban flood modelling for effective flood risk management is the lack of a high-quality dataset. This challenge is even larger in developing countries where there is sparse or infrequent ground observation. However, with the current advancement in remote sensing data and numerical weather prediction modelling, there is an increasing opportunity to do effective urban flood hazard modelling in the data-scarce areas. The thesis's main objective is *to assess the suitability of open-source geospatial datasets and their integration with hydro-meteorological modelling systems to overcome the data-scarcity challenges, more specifically to advance the modelling system and utilization of data on extreme rainfall events, soil, and land-cover information for flood hazard modelling in an urbanized and data-scarce area.* Different soil databases are evaluated and compared to derive soil water characteristics used for flood hazard modelling. Moreover, the WRF model, a mesoscale NWP model, is evaluated to generate precipitation input for flood event modelling. In order to answer the main research objective, the thesis persuaded to answer the following research questions:

I. How suitable is soil information derived from three different soil databases for modelling flood dynamics in an urbanized area?
II. How appropriate is the satellite-derived urban fraction in the WRF model for simulating high-intensity rainfall events in the urbanized area?
III. How to optimize the performance of the WRF model in simulating high-intensity rainfall events triggering localized floods?

IV. How suitable is the WRF rainfall product for urban flood hazard modelling in a data-scarce area?

The following section presents the methodological framework used in the thesis and then describes the study area and thesis outline in sections 1.4 and 1.5, respectively.

1.3. Modelling framework

Figure 1.2 illustrates the overall modelling framework followed in this thesis. The figure shows that open-source geospatial datasets are used to derive land cover and soil information required for flood event modelling. This land cover and soil information are also used as input to the WRF model. The WRF model is used to simulate high-intensity rainfall data used for flood modelling. A detailed description of each methodological framework component is discussed in the later chapters of this thesis.

1.3.1. Integrated flood modelling

Flood hazard modelling is developed by using flood models. Flood models are useful tools to study the flood characteristics and also explore solutions for practical flood management to support decision-makers in preventing and mitigating flood hazards. The flood modelling process refers to both the hydrologic and hydrodynamic phenomenon of the flood. Hydrological modelling is concerned with the simulation of flood hydrology and hydrological processes in a catchment, which requires less computational time at the price of representing less detailed physical processes (Hapuarachchi et al., 2011; Pappenberger et al., 2011). Hydrodynamic modelling is concerned with water systems simulation and predictions relating to water levels, flows, and velocities (Teng et al., 2017). The array of hydrodynamic models goes from 1D profile line models (Brunner, 1995a) to 2D shallow-water models (Horritt and Bates, 2002; Neal et al., 2011) and fully dynamic wave models (Dottori and Todini, 2013). Both hydrologic and hydrodynamic models often operate as stand-alone for practical application. Integration of these two model types has recently gained attention for urban flood application, particularly when dealing with flash floods on a catchment scale (Zischg et al., 2018; Liu et al., 2019). Therefore, a single model, which can efficiently consider fully integrated flood modelling to obtain a detailed understanding of flood hazards in urban areas, is used in this thesis.

Under the framework of integrated flood modelling in the urbanized and data-scarce environment, the flood model's suitability and selection depend on several other factors (Nkwunonwo et al., 2020). First, whether the selected model can fulfill the aim of the study, the adequacy of datasets, the availability of the model itself - a freely available model is usually recommendable. The second is whether the model is physically sound and practically viable. The second factor includes a proper formulation of shallow water equations (SWEs) and numerical equations to solve flood propagation and associated flood driving factors such as hydrology, climate, LULC, and soil surface characteristics (e.g., soil compaction). In particular, urban sealing and soil compaction in urbanized Sub-Saharan Africa cities are essential to be considered. As urban sealing and soil compaction are the key flood driving factors, they require proper formulation in the flood model. In the context of flood hazard modelling in an urbanized catchment, the choice of model also depends on the adequacy and availability of databases where a high-resolution representation of complicated topographic features is necessary (Hunter et al., 2007; Tayefi et al., 2007).

In this thesis, we will focus on the application of the spatially distributed integrated flood model, open-source Limburg Soil Erosion Model (OpenLISEM)(Bout and Jetten, 2018), to simulate flood hazards in Kampala catchment, Uganda (see chapters 2 & 5)). What makes openLISEM an integrated flood model instead of not just a flood model is that it considers catchment hydrological processes leading to flooding, particularly the rainfall-infiltration dynamics. As an integrated model, openLISEM simulates the effect of high-intensity rainfall events (HIRE) in terms of surface runoff and flooding. Firstly, for hydrological processes, catchment water balance processes such as interception, infiltration, and surface storage are calculated at the gridcell level (1 D). Surface runoff is considered as the spatial process, which is accumulated towards river channels (downhill) and determined using a kinematic wave approach over a predefined network. Secondly, for the hydrodynamic model, the spatial process of the channel flow is routed through the channels with a 1 D Kinematic wave. Channel overflow resulting in flooding is modelled as overflow from the river channels towards the higher elevations of the floodplain, using a 2D dynamic wave of the shallow water equations (Delestre et al., 2014a). Details on the model`s data used and simulated physical processes are given under each chapter (Chapters 2 & 5). The kinematic wave uses the flow velocity based on the manning formula for overland and channel flow, where Manning`s N values for resistance were estimated based on the land use data. The N for the main channel is set to a constant, according to the channel type. This model has been used for both river and urban flood modelling (Van Westen et al., 2015; watershed St Lucia, 2016; Pérez-Molina et al., 2017; Bout and Jetten, 2018; Bout et al., 2018) and for many more flood applications world-wide. As a spatially distributed model, the openLISEM model uses a topography-following grid based on the digital elevation model (DEM) to solve both cell-specific processes and differential equations governing the flows. The model is also freely available and open-source, allowing researchers to access the source code for further development.

1.3.2. Geospatial data

An integrated flood modelling system requires soil water characteristics, which include: initial soil moisture, saturated hydraulic conductivity, porosity, suction parameter, and soil depth. These soil water characteristics are derived from existing soil databases and field observations, and experiments. The detailed information does not exist locally, but open sources geospatial datasets are possibly detailed enough for this purpose. Hence, in this thesis, we explored open source geospatial databases for soil information used for flood hazard modelling in Kampala. As the urban environment changes, the existing data on urban elements are outdated quickly; hence we included the effect of urbanization from the latest databases and satellite imagery.

The main geospatial datasets used for urban flood modelling in this thesis are land cover and soil information. In the case of land cover data, the required data is derived from satellite remote sensing and data fusion as a combination of remote sensing data with ground observation, in the case of soil information. The urban land cover data (hereafter urban land use fraction) is derived based on Landsat image 2016 and classified using a supervised classification by sorting the satellite image into three categories: Built-up, which included buildings and pavements, non-built, and bare soil following Perez Molina (2019). The derived urban fractions are used directly as input to the flood model and integrated with soil databases to produce essential soil information required for the flood model. Besides, following the procedure given by (Wang et al., 2007); Brousse et al. (2019), the built-up fraction of the urban land use is used to update the urban fraction in the WRF model, as discussed in chapter 3 of the thesis. In the case of soil, three different soil databases are used to derive soil water information required for flood hazard modelling. These are in-situ soil information extrapolated to the whole Kampala catchment using soil-landscape relationship (Sliuzas et al., 2013; Rossiter, 2014) (acronyms as SMLS), the global SoilGrids database (Hengl et al., 2017) (acronyms as SGSM), and the FAO soil database (FAO, 1991) (acronyms as SMFAO). The applicability of the derived soil information for flood hazard modelling is discussed in chapter 2. As shown in

Figure 1.1, soil information is used directly as input to the flood model as well as to update the soil water information in the WRF model, as described by Santanello Jr et al. (2011); (Lin and Cheng, 2016). It is worth noting that the level and details of soil information and built-up fraction for the flood model and WRF are not of the same order, and hence, both models could be sensitive to this information.

Moreover, Integrated flood modelling requires spatial data of detailed urban elements (buildings, infrastructure, drainage systems) for the infiltration rate. These datasets, including a digital elevation model and other spatial datasets, are extracted from the pre-established research database of Kampala. Here, urban elements used in this thesis are derived from the satellite image (Perez Molina, 2019). The digital elevation model (DEM) is derived from the city's contour map and has a resolution of 5 m, resampled to 10 m for flood hazard assessment. Kampala city's channel dimensions and manning coefficient (N) are taken from the Kampala city authority master plan 2010 (KCCA, 2010). A field experiment on channel depth, width, and other information was also carried out in 2013, and the suitability of these field data is evaluated and analyzed through previous project work and MSc thesis research (Chogyal, 2013; Mhonda, 2013b; Sliuzas et al., 2013; Habonimana, 2014; Pérez-Molina et al., 2017).

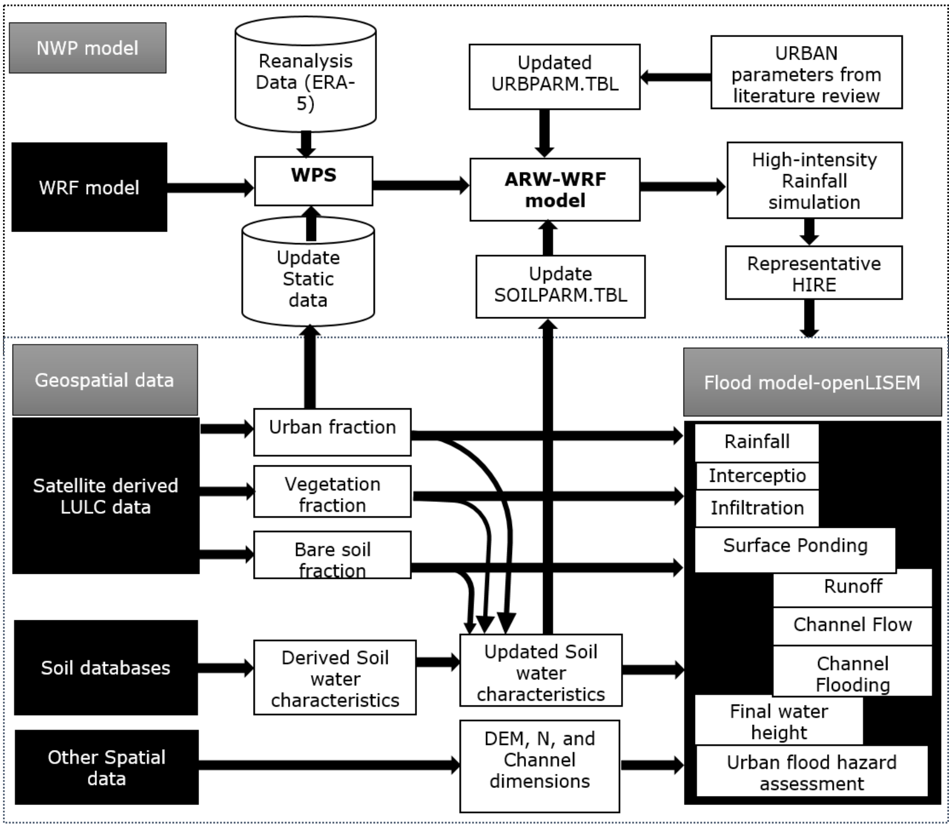

Figure 1.2 Modelling framework to study urban flood hazard in a data-scarce area

1.3.3. *Numerical Weather Prediction model*

An integrated flood modelling system requires high-resolution rainfall in space and time to compare with the infiltration rate. Recording the high-resolution rainfall requires a dense gauging network, as indicated in Jeworrek et al. (2019). Notwithstanding the need for denser and more frequent measurements in the gauge network in the area, various studies have pointed out the problem of scarcity and lack of quality of meteorological data in Kampala for effective flood modelling (Sliuzas et al., 2013; Habonimana, 2014; Mugume and Butler, 2017). The availability of observed rainfall data is limited due to the few weather stations in the area. Additionally, Standard World Meteorological Organization (WMO) meteorological stations are reporting only rainfall amounts once a 24-hour, which lacks information on a sub-hourly rainfall intensity required for localized urban flood modelling. Rainfall from satellites does not work because although the temporal resolution is better (i.e., 30 minutes), the intensities are not good yet. However, while the time series derived from Global Precipitation Measurement (GPM-IMERG) is already 20+ years with aggregated values (3-day and weekly totals) show good agreement with ground measurements Fang et al. (2019); Chen et al. (2020), the ground data is too scarce in Kampala for that. Hence, in this thesis, we explored a numerical weather prediction modelling system to get detailed rainfall information used for flood hazard modelling in Kampala. In order to do this, we built a high-resolution NWP model, WRF, to produce the rainfall data required for flood hazard modelling in the city.

Numerical weather prediction (NWP) is a weather forecasting method that employs a set of equations describing the flow of fluids, translated into computer code (Skamarock, 2004; Wikle, 2005; Knievel, 2006). This set of equations is combined with parameterizations of other processes, then integrated with initial and boundary conditions of a specific domain to produce data for climate application. NWP data are the most familiar form of weather model data, which depends on current weather observations to forecast future weather at various spatial and temporal scales, which can be considered as the added value over the observations (Hopson and Webster, 2010; Frank et al., 2020). WRF is among the first cloud-scale NWP model designed for both research and operational applications (Powers et al., 2017). It is the most widely used numerical weather prediction model with a wide range of applications (Dudhia, 2014). Besides, WRF is attractive because of its flexible configuration at high-resolution domains, variety of possible input data, and computational flexibility (particularly in limited-resource settings), along with the ability to leverage model advancements from a global research community.

This study applied WRF to simulate high-intensity rainfall events (HIRE) used for flood hazard modelling, as discussed in chapters 3, 4 & 5 (Paper II & III). The flood modelling approach considered here is that the WRF model rainfall output is used as input to OpenLISEM using an offline model coupling system. WRF has been recognized as a powerful tool to simulate physically reliable HIREs used for localized flood modelling (Sikder et al., 2019). The WRF model software framework (WSF) supports two dynamical solvers or cores: the Advanced Research WRF (WRF-ARW), which used in this research, developed and maintained by the Mesoscale and Microscale Meteorology Division of NCAR, and the nonhydrostatic Mesoscale Model (NMM) developed by the National Centers for Environmental Prediction with user support provided by the Developmental Testbed Center (www.wrf-model.org). Both dynamic solvers had an Eulerian height-based and mass-based vertical coordinate. The prognostic equations for the model variable (wind, potential temperature, moisture, and hydrometeor fields) are formulated in flux form using a terrain-following mass-vertical coordinate. The equations are summarized in the Advanced Research WRF Description Version 3 Manual (Skamarock, 2008). For atmospheric simulations (e.g., rainfall simulation), WRF has two components: the first is WRF pre-processing system (WPS), which is used for data preparation, and the forecast model part (i.e., WRF-ARW), used for model simulation.

Two gauging station rainfall data were used for WRF model verification work in chapters 4 & 5. The first one is with daily rainfall data available from WMO through a global summary of the day, and the second is an automatic weather station (AWS) recording rainfall every 10-minute. The AWS from Vantage Pro (http://www.davisnet.com) was installed at Makerere University to record rainfall data. This station may not fulfill all requirements by WMO and is also not linked to the meteorological authorities. This AWS data has been used for WRF model verification and flood hazard modelling. In addition, CHIRPS satellite rainfall data with a daily time step is used to evaluate the spatial distribution of WRF simulated rainfall events.

1.4. Study area description

The study area is Kampala city, both the capital and political city of Uganda and among the largest city in East Sub-Saharan Africa (UN, 2015). The Kampala metropolitan area is about 340 km^2 with the administrative division of five districts: Kampala Central Division, Kawempe, Makidye, Nakawa, and Rubaga, although a significant amount of new development beyond the city boundaries (Pérez-Molina et al., 2018). Kampala is an exemplary sub-Saharan African city that exhibits rapid growth and physical expansion in complicated contexts while frequently affected by flooding. The city is located near the equator, north of Lake Victoria, in a hilly terrain containing large wetlands. Its tropical weather and soil infiltration properties already lead to large runoff volumes, a leading cause of recurrent flash flooding exacerbated by urban growth. At the same time, the lack of high-quality rainfall data hinders the proper flood hazard modelling for managing this recurrent flooding. Therefore, the city is an ideal location to explore the objectives of the research.

The city's urban structure has been shaped by wetlands and the waters that flow into the Bay areas and Lake Victoria. The city depends on the wetlands throughout the settlement, which provides floodwater attenuation, sewage treatment, water purification, food, and building materials. However, due to physical development, the wetlands are forced to decrease and become degraded. Around 60% of wetlands changed into a settlement, agricultural cultivation, and construction of drainage channels (KCCA, 2010). These factors highly affect the function and system of hydrology, hence flood dynamics. Natural and human-made factors cause pluvial flooding in the city. Natural factors include soil infiltration properties in the area, high-intensity rainfall intensity, low lying, and flat terrain. Particularly, high-intensity rainfall events (HIREs) frequently cause storm runoff, which surpasses poorly managed city infrastructure's capacity and triggers localized flood events. Human-made causes of flooding include, but are not restricted to, increasing impervious surface area, and the surface is highly compacted, with poor quality of drainage systems, weak solid and liquid waste management (Perez Molina, 2019). Particularly drainages in Kampala are poorly maintained, sometimes filled with garbages, which can block flow in the channel with initial downpours and then cause the overflow of floodwater.

According to the Kampala master plan report KCCA (2010), the city has eight major wetland systems (i.e., Nakivubo, Lubigi, Nalukolongo, Kansanga, Mayanja, Kinawataka, Nalubaga, and Walufumbe), and these wetlands are also functioning as the primary drainage systems of the city. The primary drains' (*i.e.*, the widest channels draining the main valleys) and the former wetlands are canalized and widened. At the same time, narrow culverts are replaced by a series of large box culverts to drain a peak discharge of about 67 m^3/s, representing the 24-hour duration design storms of a 10-year return period (Sliuzas et al., 2013). In the master plan, it is also reported that the secondary and tertiary drainage systems were designed to accommodate the flood peak of a 2-year event. For the drainage system design, rainfall with a known probability is needed; this is constructed using the intensity-duration-frequency (IDF) curve of the daily rainfall amount. However, the currently functioning drainage systems are not fully preventing flooding. Recent studies and reports, for example, (Mhonda, 2013a; Perez Molina, 2019), indicate that high-intensity rainfall events frequently cause storm runoff, which surpasses the city infrastructure's capacity and triggers localized flood events. Consequently, causing estimated annual damage between the U.S. \$1.3 million and the U.S. \$7.3 million and is expected to increase under changing climate conditions (Taylor et al., 2015).

This study focused on urban flood hazard modelling both at a catchment scale and for the whole of Kampala city. Flood modelling was conducted using the openLISEM integrated hydrological model (see section 1.3.1). OpenLISEM is chosen for this study because it addresses the factors determining the hydrology processes leading to flooding in Kampala reasonably, particularly the processes related to rainfall-infiltration dynamics. Accordingly, two chapters in this thesis explicitly focused on flood hazard modelling in the Kampala catchment. In chapter 2, for the city's flood hazard modelling, we consider the model boundary from a hydrological modelling perspective following the draining area, particularly following the major wetland systems in the city with a total area of 350 km² (see Figure 1.3, Kampala catchment). In chapters 3 & 4, this thesis develops high-intensity rainfall events for 900 km² (the innermost domain of WRF, Figure 1.3), which cover sub-urban areas around the city. For the flood hazard modelling of chapter 5, the study considered the upper Lubigi catchment in Kampala city. The detailed flood impact and hazard analysis are evaluated for the upper Lubigi catchment, an area that roughly coincides with the Kawempe administrative division with a total of 130 km² (see Figure 1.3, Upper Lubigi catchment). This catchment has been the focus of several studies on flooding and urban growth because of the frequent flooding that happens in the former wetlands, where dense informal settlements (slums) exist.

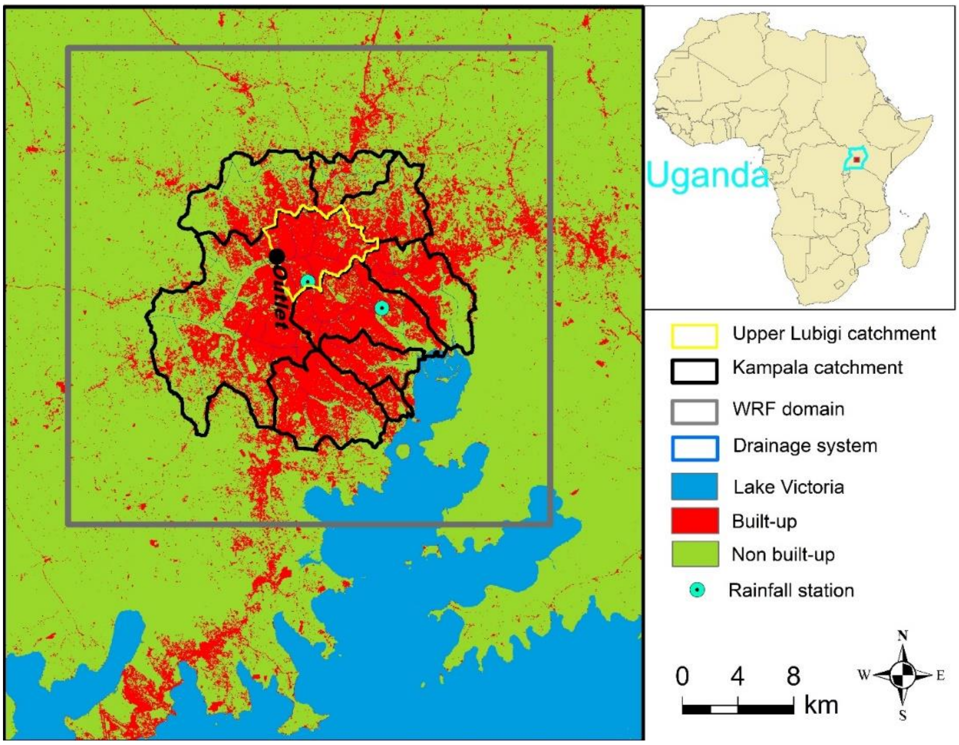

Figure 1.3 Study area: Map of Kampala city with land use fraction derived from Landsat image, source (Abebe, 2013); Upper Lubigi catchment used for flood modelling in Paper-III; Kampala catchment used for Paper-I & II; WRF domain is the innermost domain with 1 km spatial resolution that used for rainfall analysis.

1.5. Thesis outline

This thesis contains six main chapters, in which chapters 2-5 address the research questions presented above. All chapters are outlined as follow:

Chapter 1 presents the introduction part of the thesis. It introduces the background, the framework on flood hazard modelling in an urbanized and data-scarce area. In this chapter, the methodological framework to study flash flood modelling in Kampala’s urbanized and data-scarce city, the objectives, data sources, and the study area's description is introduced.

Chapter 2 addresses research question I. It presents research done on the suitability of three different soil information sources for flash flood modelling in Kampala's urbanized catchment. This chapter includes deriving soil water characteristics needed for flood event modelling based on three different soil databases (SMLS, SMSG, and SMFAO databases) by applying pedotransfer functions and comparing their results. None of the datasets have sufficient essential urban information in their databases, such as sealing, compaction, and vegetation cover fractions. Therefore, we developed a new methodology to incorporate land cover information into derived soil water characteristics. Finally, the derived soil water characteristics are used in the flood model OpenLISEM and compare their results.

Chapter 3 is designed to address research question II. It presents the WRF model configuration, static data setting, and model`s suitability to simulate high-intensity rainfall events triggering localized floods in the catchment. Attention is paid to building a strategy to insert the city's correct urban fraction into the WRF model for proper representation of urban extent and position for rainfall simulation. The new urban fraction is derived using the Landsat image of 2016. The appropriateness of the satellite-derived urban fraction in the WRF model for simulating HIRE is evaluated through sensitivity analysis and comparison with results when using the default WRF urban fraction.

Chapter 4 addresses research question III. It presents the evaluation and sensitivity analysis of WRF parametrization schemes and their combinations for proper simulation of HIRE over Kampala city. Specifically, we evaluated 24 different WRF parametrization combinations for sensitivity analysis. Finally, we selected the optimum parametrization combinations to simulate the case of 25 June 2012 HIRE over the city. Model validation is handled by comparing catchment rainfall with CHIRPS and rain gauge observations. The best physics options of the model can be determined in terms of cumulus parameterization, microphysics, and planetary boundary layer for the innermost domain of WRF.

Flood hazard assessment cannot be done using actual rainfall events as simulated by WRF because simulated events are highly spatiotemporally variable. In some cases, they are off the place. Hence, each sub-catchment of the city received different rainfall amounts, which would make a comparison between events of varying magnitude challenging. Therefore, **Chapter 5** presents an innovative construction of simple design storms based on WRF precipitation output for a proper flood hazard modelling in the city to address research question IV. Mainly, three design storms at different times of the year are constructed, and their feasibility for flood hazard modelling is compared with the historic design storm.

Chapter 6 presents the thesis's synthesis, including the main findings with respect to the main objective, contribution to flash flood modelling in urbanized and data-scarce areas. Moreover, this chapter indicates some ideas on the future direction of the study and flood management strategies in cities in developing countries.

Chapter 2: The sensitivity of flood dynamics to different soil information sources in urbanized areas

This chapter is published as a peer-reviewed paper:
Y.Umer, V.G.Jetten, J.Ettema. The sensitivity of flood dynamics to different soil information sources in urbanized areas. Journal of Hydrology, Volume 577, October 2019, 123945

Abstract

This study focused on the sensitivity of flood dynamics to soil hydraulic properties derived from three different soil databases: (1) upscaled locally observed soil texture data based on the soil-landscape relationships (SMLS); (2) the SoilGrids250m open data source (SMSG); and (3) the FAO soil map (SMFAO). The flash flood modelling was done using the integrated flood modelling system using openLISEM (Bout and Jetten, 2018) for the whole of Kampala (Uganda) using the 25th of June 2012 flood event. Infiltration dynamics were derived from the predicted soil hydraulic properties for these soil information sources and compared their relative performance with flood inundation using flooded areas from the earlier calibrated simulation as a benchmark. However, Kampala urban areas have two major conditions related to land cover and soil physical structure for which the information is not available in soil databases: the effect of fragmented vegetation cover and the effect of compaction of bare soil. Non-built-up areas can be covered by fragmented vegetation (grass and shrubs), which generally has high infiltration rates. In contrast, bare areas such as dirt roads and footpaths can be heavily compacted and have typically low infiltration rates. We used Pedotransfer functions (PTFs) with satellite-derived vegetation cover and bare soil to predict soil hydraulic properties related to the uncompacted and compacted scenarios. In the distributed openLISEM hydrological model, these two urban soil conditions have been treated separately. We have evaluated the sensitivity of flood dynamics to three different soil databases under both uncompacted and compacted urban soil conditions by using different flood indicators such as catchment water balance, infiltration rate, flood depth and duration, flooded area, and flood volume, and the average number of structures affected. The study results indicate that soil hydraulic properties needed for the distributed hydrological model are better predicted when using the SMSG and SMLS, which resulted in better infiltration simulation.

Compared to an earlier simulation that was verified with stakeholders and accepted for drainage system design, the simulated flood extent map's accuracy was better when using SMSG and SMLS. Moreover, soil compaction significantly reduces infiltration and consequently increases the flood depth and duration, and therefore must be included in the urban flash flood modelling study.

Keywords: *Flash floods, openLISEM, PTFs, Soil compaction, Soil hydraulic properties, vegetation cover fraction*

2.1. Introduction

Population growth and migration are the leading causes of urban expansion, particularly in developing countries. Sub-Saharan African cities are predicted to increase in total urban extent by nearly 20 fold in 2030 compared to the urban extent in 2000, which would intensify pressure on the natural environment (Güneralp et al., 2017). From a hydrological point of view, urbanization is a process by which natural vegetation and agriculture are replaced by compacted and constructed surfaces such as buildings and tarred roads (Chen et al., 2014). Also, the surface and subsurface drainage systems are usually altered, and topsoil may be replaced by building materials. Such changes in urban morphology can have a significant impact on hydrological processes, such as changing infiltration rates and consequently increasing storm runoff (Redfern et al., 2016). Urban expansion is not always through planned high-rise buildings but often a process of releasing building permits for small-scale private contractors that lead to vast sprawling areas with single-story houses built on the natural surface. These areas have many footpaths and dirt roads that appear semi-naturally (unplanned). Many studies have investigated the role of urban soil hydrology in urban storm runoff (Berthier et al., 2004; Ossola et al., 2015; Miller and Hess, 2017), highlighting the importance of urban soil heterogeneity in several cities, with alternative sealed and infiltrating surfaces that significantly affected soil water storage and therefore runoff.

One such example is the city of Kampala (Uganda), which has experienced tremendous expansion over the last two decades. A previous study by (Abebe, 2013) analyzed the development of the city from 1989 to 2010 and showed that the city expanded the urban footprint from 72.9 km^2 in 1989 to 325 km^2 in 2010, where the majority of the expansions were to the northern part of the city. Topographically, the city is characterized by rounded hills and wetlands, with residential density increasing on the hillslopes and the wetlands gradually being filled with informal settlements, in spite of laws protecting the wetlands. These areas have experienced intermittent flooding, but urbanization of the hillslopes combined with heavy rainfall events have increased their frequency (KCCA, 2012). The risk of flash flooding in Kampala has generally been associated with heavy rainfall occurring during the rainy season (Douglas et al., 2008). A similar study by (Sliuzas et al., 2013) concluded that the city's flooding had been greatly influenced by the formation of informal settlements in the flood-prone areas and the city's lack of workforce enforce spatial planning.

With increasing population growth, urban expansion, and intensified rainfall events resulting from climate change, Kampala city faces a significant risk of flash flooding. In 2002, a master plan was designed to upgrade and enlarge the drainage systems currently being implemented. In this plan, 10-year return period floods were simulated and were then verified with stakeholders. These simulated floods were used as a baseline for this study in the absence of measured water level values for calibration. The 'primary drains' (*i.e.*, the widest channels draining the main valleys) and former wetlands are canalized and widened, while narrow culverts are replaced by a series of large box culverts. Occasional local cleaning efforts remove waste and garbage to improve flow. However, there is visible evidence of erosion and siltation on new channels and storm basin structures, significantly decreasing their effectiveness. In a later stage, the concrete secondary drains leading from the hills to the main drain will be upgraded. It is not certain these drainage improvements will entirely remove the flood hazard. As housing density on slopes continues to increase in place of natural vegetation, flood problems continue to persist. Therefore, it is important to implement an integrated flood model that analyses the hydrological processes for the entire catchment, which is needed to mitigate flood risks and help in urban planning.

Flood models can be classified into two groups. The first one is models where the upstream generation of runoff is separated from downstream flooding (for so-called large river floods) by overflowing of channels (*e.g.*, HEC-RAS (Brunner, 1995b). The second type is integrated flood models, which simulate the catchment hydrological processes for the entire domain and consider a seamless conversion from runoff to flood water, treating all surface water as 2D flow. In this modelling type, flooding is not only due to overflowing channels but also from the overland flow and direct rainfall. Examples include the commercially available software for two-dimensional flood, FLO-2D (O'brien, 2007), and the open-source Limburg Soil Erosion Model (openLISEM) (Bout and Jetten, 2018). For this study, we used the openLISEM model to simulate the above ground and soil hydrology in detail and used a high-resolution representation of topography with a 2D-dynamic wave for all surface flow. The model does not consider subsurface storm drains, but in Kampala, sub-surface storms drains are of very limited use.

Soil texture and soil structure are very important in integrated flood modelling of urban watersheds (Salvadore et al., 2015), as they determine the rate of infiltration in the urbanized catchment. Urban soil properties are exposed to three different systems: (1) the surface is sealed with impervious structures (tarred roads, houses, concrete channels); and (2) non-sealed surfaces such as dirt roads and footpaths can be heavily compacted, and (3) surfaces that are vegetated, such as grassed parklands, have a positive effect on infiltration. On the sealed surfaces, urban soil covers have no infiltration rate, and hence high surface runoff (Konrad, 2003; Yang and Zhang, 2011). It is important to note that in Kampala, most of the houses are built directly on the natural soil surface (maybe removing the organic topsoil), and thus, the original soil information available is valid for most of the Kampala area. On locations where larger buildings are constructed, sand and gravel are used as a foundation. Unfortunately, there was no detailed information available as to their exact location, which prompted the need to assume that all buildings had been constructed using the original soil material for this study.

Soil texture information can be obtained from various sources (explained below), but the changes in soil physical structure are not usually included in soil information. The only way to incorporate this effect in the hydrological models is by including compaction in the input soil properties. This, therefore, means the exclusion of models that do not simulate infiltration (*e.g.*, based on the SCS Curve Number Method). In Kampala, there is limited direct information on soil hydrology, mainly on soil texture and texture classes (NRCS, 1993). These can be translated to soil hydraulic properties using either tabulated guide values per texture class (see (Cosby et al., 1984)) or Pedotransfer functions (see (Saxton and Rawls, 2006) and (Rawls and Brakensiek, 1989)). (Saxton and Rawls, 2006) investigated the effect of changing bulk density on hydrological properties, which makes the functions useful to simulate the effect of compaction on infiltration and soil water storage. In this study, we used "soil physical properties" (SP) to refer to texture, organic matter, and bulk density and "soil hydraulic properties" (SHP) to refer to saturated hydraulic conductivity (Ksat), porosity, wilting point, and field capacity.

A freely available high-resolution global soil database was recently made available: SoilGrids250m, developed by ISRIC (Hengl et al., 2017). This global database directly provides soil physical properties in seven soil layers and is based on geostatistical interpolation of soil data, using machine learning algorithms that include correlated terrain and land-use variables. The interpolation and correlation are done on a continental basis to have a large enough dataset. (Hengl et al., 2017) warn against the unconditional use in large-scale applications, but as a source of information, it is well worth investigating this. Another soil data for Kampala is a database from the Food and Agriculture Organization of the United Nations – United Nations Educational, Scientific, and Cultural Organization (FAO-UNESCO soil map of the world (FAO, 1974; FAO, 1991) which is available at 1:5, 000,000 scale. Its information is limited mainly to texture classes and falls short in providing landscape details (*e.g.*, the presence of wetlands). In addition to these databases, SHPs can also be developed using soil-landscape relationships based on observed soil texture classes (Rossiter, 2014). The geological history of Kampala has resulted in hard lateritic soils capping the hills, reddish sandy clay loams on the hills of weathered sandstone and slate, and heavy clays in the wetlands where sediment accumulated. This clear relation between soil type, soil material, and landscape (so-called soil catena) was used in the UN-HABITAT project (Sliuzas et al., 2013) to derive a texture class map based on geomorphology from field observation. The UN-HABITAT project has been conducted in the upper Lubigi catchment in Kampala, one of the northern watersheds. They deduced the soil-landscape relationship from a landscape analysis using the DEM. To prepare a concept map of soil-landscape units from DEM, first, the probable landscape segments (number and positions) were obtained mainly from the literature. Second, landscape segmentation was carried out by numerical landform analysis, using numerical programming: (1) Valley floor; (2) Bottom slope; (3) Mid-slope; and (4) Hilltop. The segmentation was carried out by fuzzy means clustering from elevation, slope, and profile curvature, and finally, the soil texture classes from the field experiment assigned to each landscape unit. In this study, we followed the same procedure to deduce different landscape units to the whole of Kampala and assigned the field experiment soil texture classes to the created landscape units.

In this study, since the pattern of the landscape of Kampala is consistent, which is ironstone-capped hills and swampy inter-hill valleys, we followed the same procedure and deduced four different landscape units for the whole of Kampala. Finally, we assigned the field experiment soil texture classes to the created landscape units.

As previously explained, soil hydrological information is vital in flood modelling and can influence a city's flood hazard modelling. The main objective of this research is to determine how sensitive the flood dynamics are to hydraulic properties derived from soil information based on the three different soil databases (SoilGrids250m, FAO, and upscaling of local soil information based on the soil-landscape relationships) and develop the best strategy for integrated flood modelling. All datasets were translated to SHP using Saxton's pedo-transfer functions. Since sealing and compaction play an essential role, all three data sources were used with and without compaction to see if the effect of sealing and compaction overrides the differences caused by the soil information sources. Finally, if there are clear effects, we aim to advise on the best strategy in case there is very little local soil data available.

2.2. *Methodology*

2.2.1. Conceptual framework of the study

This research's underlying hypothesis is that the freely available global soil database does not explicitly consider the effects of vegetation cover and compaction on soil hydraulic properties, which are crucial in modelling the hydrological processes. Although hydrologic models took into account vegetation cover for their land surface modelling, considering the explicit effect of vegetation cover on soil hydraulic properties before the hydrologic model simulation is essential to have the reliable values of SHPs used for the hydrologic model. Actual soil databases derived directly from global soil maps (e.g., ISRIC and FAO) are assumed to have a normal soil density, as shown in **Table 2.1**. In the PTFs (Saxton and Rawls, 2006), this is indicated with a relative density factor of 1.0. However, areas covered by vegetation have a density factor of less than one, while the compacted areas have a density factor greater than one. Thus, the effects of vegetation cover and compaction on estimated soil hydraulic properties can be accounted for by incorporating vegetation cover and compaction effects into PTFs to produce soil hydraulic properties under uncompacted and compacted conditions. Therefore, density adjustment factor can be analyzed based on the following scenarios: ***Scenario-1***: for density factor less than one; it is called uncompacted urban soil condition (the consideration of density adjustment factor due to vegetation cover fraction in the relative non-built-up fraction areas which is varying between 0.90 (loose soil) to 0.98. ***Scenario-2***: for density factor greater than one, it is called compacted urban soil condition (the consideration of compaction factor due to bare soil fraction, which is spatially varying between 1.0 and 1.2).

Figure 2.1 shows the methodological setup used in this study: (1) local soil texture classes scaled up through soil-landscape relationships, hereafter referred to as Soil Map Landscape-(SMLS); (2) soil texture data derived from the Global SoilGrids250m database, hereafter referred to as Soil Map SoilGrids-(SMSG); and (3) the soil texture class-map derived from the FAO 1:5,000,000 soil map, hereafter referred to as Soil Map FAO-(SMFAO). Soil hydraulic properties were derived from the above soil databases based on Saxton and Rawls, 2006 PTFs. All scenarios were modeled with openLISEM (version 5, 2018) using a 66.2 mm 1-in-2-year rainfall event that caused flooding in Kampala.

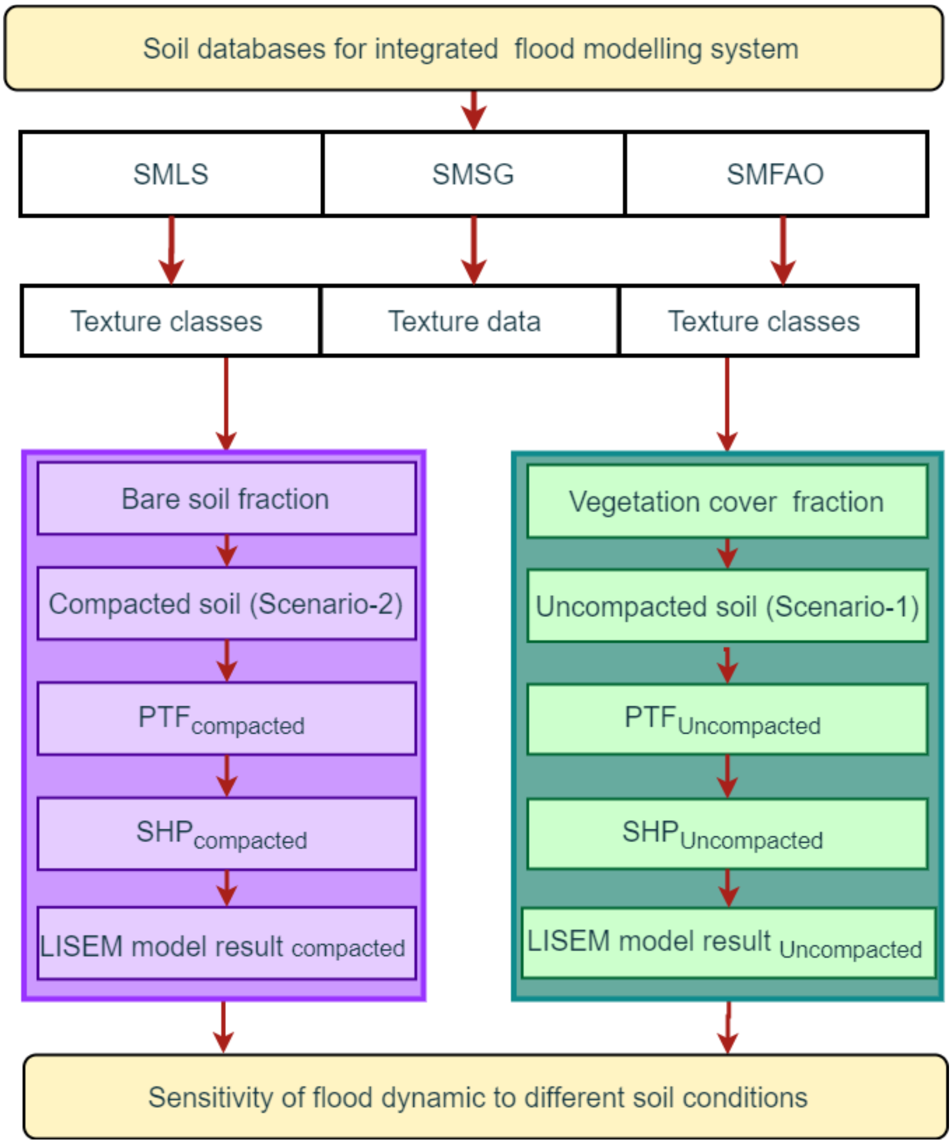

Figure 2.1 Conceptual framework: Soil hydraulic properties derived from different soil information sources for flash flood modelling (compaction refers to a density factor above 1.0, and uncompacted refers to a density factor <= 1.0, see Table 2.1)

2.2.2. *Pedo-transfer Functions (PTFs)*

Pedo-transfer functions (PTFs) are non-linear multiple regression of the combinations of soil physical properties (SP) to reproduce the soil hydraulic properties (SHP) (Cosby et al., 1984). The main SP used in PTFs is Sand and Clay content, organic matter content (OM), gravel, and bulk density. Numerous examples of PTFs are available in the literature. For example, (Cosby et al., 1984), (Rawls and Brakensiek, 1989), and (Saxton and Rawls, 2006) provide PTFs built from a collection of USA soil samples, and (Wösten et al., 1999) provide PTFs built based on European soil samples. These PTFs differ from each other in their required input parameters and underlying equations (Abdelbaki et al., 2009); (Harrison et al., 2012). PTFs can either take the form of lookup tables based on soil texture classes, for which soil maps are available, or the form of continuous functions with soil properties as inputs. A study by (Gijsman et al., 2002) has indicated that the (Saxton and Rawls, 2006) method was the most accurate based on RMSE (Root Mean Square Error) of 0.009 compared with a 0.25 average for all methods. In this regard, a previous study, e.g., (Abdelbaki et al., 2009), has suggested that Saxton and Rawls's approach is suitable for deriving soil hydraulic properties needed for hydrological modelling.

The predictive equations reported by Saxton and Rawls (1986) are mainly based on mean texture class data in the USDA texture class triangle, which is the dominant effect for the soil hydraulic properties. In addition to texture classes, variables such as OM and density can play a crucial role in the estimation methods. OM affects the values and distribution of the predicted soil hydraulic properties. For example, OM increases produce soil with increased saturated hydraulic conductivity, mainly because it influences soil aggregation and associated pore distribution. The value of OM is introduced in the predictive equations as percentage volume weight (%wt), and in this study, we used the constant value of 2.5 %w for all cases. In the PTFs, OM is directly multiplied by the texture classes to get moisture characteristics.

2.2.3. The effect of soil compaction

Soil bulk density varies across the space based on the underlying surfaces. Loose organic soils and uncompacted urban soil have bulk density ranges between 1.0-1.5g/cm^{3,} while compacted soils have a bulk density varying between 1.5-1.8 g/cm^3 (depending on the texture, as shown in **Table 2.1**). Increases in soil compaction, in general, increase bulk density and consequently decreases porosity and saturated hydraulic conductivity (**Figure 2.2**). Saxton and Rawls (2006) introduced a relative compaction factor to PTFs to provide a compacted density, which is higher than normal density condition. The compaction factors are categorized as 0.9 – 'loose,' 1.0 - 'normal,' 1.1- 'dense,' 1.20- 'hard,' and 1.3 'severe.'

Table 2.1 Bulk density (g/cm^3) for different density factor (loose soil, normal and compacted conditions) under different soil texture classes. For consistency, the terminology for compaction is based on Saxton & Rawls (2006)

Texture classe	Loose (0.9)	normal (1.0)	hard (1.1)	dense (1.2)	severe (1.3)
Sand (S)	1.28	1.42	1.57	1.70	1.85
Sandy Loam (SaL)	1.34	1.48	1.62	1.77	1.90
Sandy Clay Loam (SaCL)	1.35	1.50	1.65	1.80	1.96
Sandy Clay (SaC)	1.32	1.47	1.62	1.75	1.74
Clay (C)	1.25	1.39	1.53	1.65	1.57

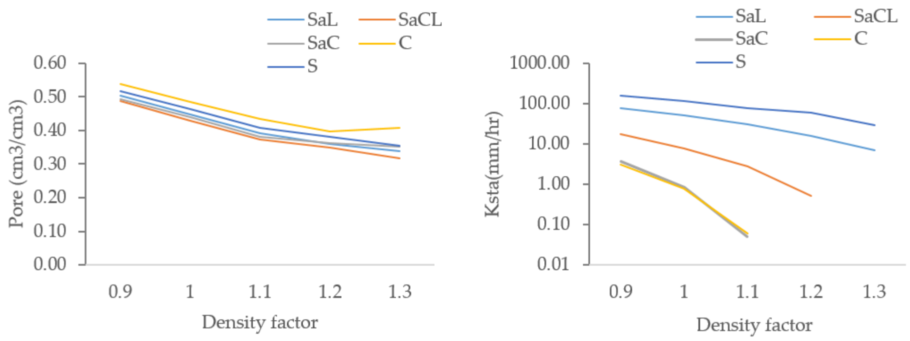

Figure 2.2 The effect of a modified density factor on porosity and Ksat within the equation of Saxton (2006). The values for SaC and C are almost the same. Ksat is shown here on a logarithmic scale to emphasize the differences

Saxton and Rawls (2006) predicted moisture content at the wilting point, field capacity, and porosity (among other properties) from a series of multilinear regression equations from Sand, Clay, and Organic Matter contents, using different combinations of these variables. They used selections of approximately three thousand samples from the soils in the US. The baseline porosity is then adjusted in case of compaction and the presence of gravel. Porosity and bulk density are simply related according to:

$$\phi = 1\frac{CF*\rho_{bulk}}{2.65} \quad 2.1$$

where ϕ is porosity (cm³/cm³), ρ_{bulk} is normal bulk density (g/cm³), CF is the relative compaction factor (**scenarios**), and 2.65 (g/cm³) is the particle density.
Saturated hydraulic conductivity is derived using the equation by (Brooks and Corey, 1964) as:

$$Ksat = a(\phi - \theta_{fc})^{(3-\lambda)r} \quad 2.2$$

$$\lambda = \frac{(ln\,(\theta_{fc}) - ln\,(\theta_{wp}))}{ln(1500) - ln(33)} \quad 2.3$$

$$r = \frac{1 - gravel}{1 - gravel * (1 - 1.5 * (\frac{\rho_{bulk}}{2.65}))} \quad 2.4$$

where r is a reduction factor, a is a regression constant set to 1930, and lambda (λ) is the pore size distribution index (Brooks and Corey, 1964), and θ_{fc} & θ_{wp} are moisture content at field capacity and wilting point. The reduction factor is estimated based on the applied gravel content which is assumed to be zero in this study in the absence of information. A gravel content of zero results in an r of 1 so that it does not affect the pore size distribution in equation 2 in this case.
The matric suction (suction head) at the wetting front is calculated assuming the initial soil moisture content (θ) to be 0.80 of the porosity (ϕ), which is approximately at field capacity (θ_{fc}) or slightly wetter. The following equation is used to calculate Psi:

$$Psi = \alpha\theta^{-b} \quad 2.5$$

Where b = (ln(1500)-ln(33))/(ln(θ_{fc})-ln(θ_{wp}));
a = exp(ln(33)+b ln(θ_{fc})); and, 1500 and 33 are matric suction in (kPa) for the wilting point and the field capacity, respectively.

In this study, the compaction factor (CF) is constructed from the bare soil fraction map (**Figure 2.3d**), which was derived from the Landsat image of 2010 (Fura, 2013), as follows. It is assumed that soil that has a higher fraction of bare surface is also more severely compacted. Therefore, the compaction factor CF for a grid cell is linearly scaled to the bare soil surface fraction, ranging from 1.0 to 1.20 for normal to fully bare grid cells. However, if there is vegetation cover in the grid cell, this is assumed to decrease the surface's compaction from 1.0 (no vegetation) to 0.9 (fully vegetated). Severe compaction with a factor of 1.30 was not used, as field tests on the compacted area still exhibited some infiltration (several mm/h) while a factor 1.30 would result in no infiltration (see also **Figure 2.2**). Therefore, the maximum compaction was set to 1.20. For example, a grid cell that has a cover fraction of 1/3 for a building, grass, and bare soil will have a Ksat and porosity, which is a weighted combination of 1/3 building is sealed (Ksat=0, porosity = 0), 1/3 is compacted with a CF of 1.07 related to the bare surface, and 1/3 has a CF of 0.96 related to the vegetation fraction.

2.2.4. OpenLISEM flood model

The open-access Limburg Soil Erosion Model (LISEM) (De Roo et al., 1996) has evolved from a catchment-based erosion model to an integrated erosion and flood model. It usually operates on a spatial resolution of 50m or less and time-steps between 0.1 and 30 sec and simulates flash floods for single rainfall events. The model combines a surface and soil water balance, including interception (by vegetation and buildings), surface storage, and infiltration, to calculate the surface runoff. Infiltration is done with the Green and Ampt equation for two soil layers, using a solution (Green and Ampt, 1911), and revised by (Kutílek and Nielsen, 1994). Flow routing is done with a 2D dynamic wave using a finite volume solution (Bout and Jetten, 2018). As such, the model does not distinguish between surface runoff and flood from a hydraulic perspective; a flood is assumed to be all water that is deeper than a user-defined value (such as 10 cm).

The infiltration process is very important in urban environments: the model uses input maps directly for saturated hydraulic conductivity (Ksat), porosity, suction head, and initial moisture content to calculate infiltration, which can be based on soil texture and land cover types. For each grid cell, the fractions of the building, tarred roads, and other sealed surfaces are used to calculate the impermeable fraction and a fraction of compacted area that uses compacted values for Ksat and porosity themselves. Different types of cover result in different flow resistance values (Manning’s n), and also buildings are assumed to increase the flow resistance. Water is routed by the dynamic wave to a channel system that can overflow if the water volume is larger than the channel dimensions, thus adding to the flooding process. Channel flow is done with a kinematic wave in the channel network. Stationary base flow can be assumed for the channel system where necessary. The direct use of detailed spatially variable soil and land cover information makes this model suitable for this study. Note that in this study, the 2-layer infiltration process assumes topsoil of 30 cm in thickness, which is affected by land cover and compaction, while the subsoil uses the PTFs directly based on the texture information, without any land cover information and influence of compaction.

The model has been used for flash flood modelling in the upper Lubigi urban sub-catchment in Kampala, Uganda (e.g., (Sliuzas et al., 2013; Habonimana, 2014; Mahmood et al., 2016; Pérez-Molina et al., 2017) and four Caribbean islands (Van Westen et al., 2015).

2.3. Data

2.3.1. Drainage systems

Kampala, the capital city of Uganda, is located in the equatorial East African region between 0.1 to 0.4 N and 32.32 to 32.42 E on the shore of Lake Victoria. The city is characterized by sprawling built-up areas with mostly one-story buildings on a series of hills separated by the lower slope valleys and wetlands. The city's drainage system is divided into nine central drainage systems following the natural catchments **(Figure 2.3).** The major drainage systems are further divided into semi-natural primary drains (partly canalized) in the central valley (with up to 20 m^2 cross-section), with secondary concrete drains (1-2 m^2 cross-section) concentrating water from the side valleys and numerous tertiary drains along the roads that are often in disrepair. The tertiary drains are not mapped and were ignored in this study. The main drainage systems are being upgraded to make them suitable to accommodate a storm with a ten-year return period but are currently still in disrepair. Storm runoff in the main channels drains into wetlands where runoff is stored, and flood peaks are attenuated. Due to urbanization and informal settlements, impermeable surfaces are increasing in the wetlands, resulting in increased storm runoff and flooding. Consequently, properties close to wetlands are exposed to flood risk with a higher frequency of rainfall events.

There has been very limited hydro-meteorological data monitoring in the city to carry out in-depth flood modelling. Fieldwork and *in-situ* data collection were conducted in 2012 as part of a joint UN-HABITAT`s cities and climate change (CCC) and Kampala Capital City Authority (KCCA) initiative. An automatic weather station was installed to collect rainfall data **(Figure 2.3)** and other meteorological data such as temperature and wind. Several studies have used these field datasets to assess flood modelling in the city by only focusing on the upper Lubigi sub-catchment (Mhonda, 2013b; Habonimana, 2014; Pérez-Molina et al., 2017).

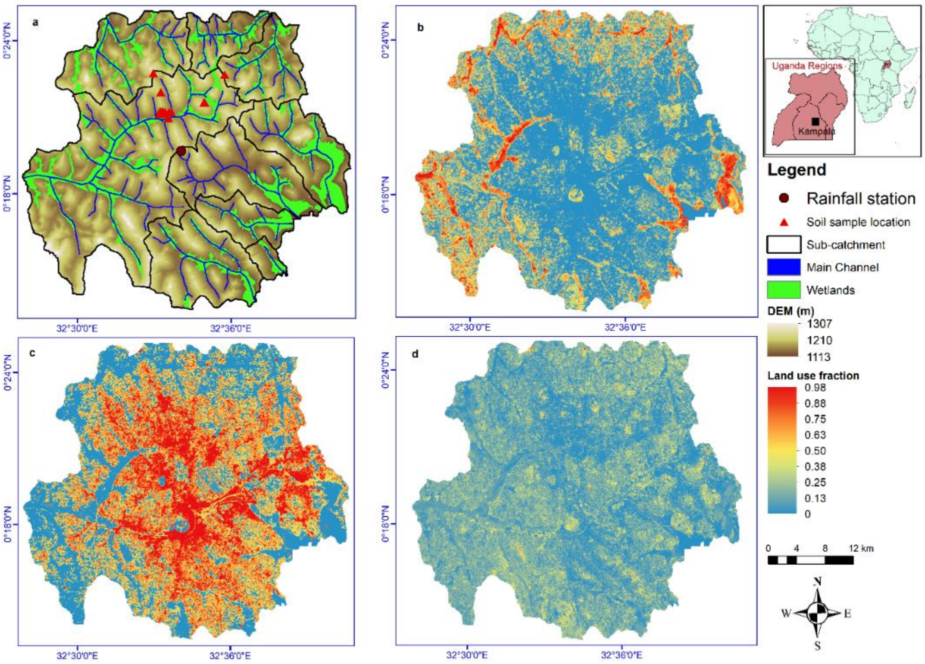

Figure 2.3 Study area and data used: (a) DEM, channel dimensions and sub-catchments; (b) vegetation cover fraction; (c) built-up fraction; and (d) bare soil fraction

2.3.2. Rainfall data

Figure 2.4 shows the rainfall intensity used for flash flood modelling in this study. Since only one rainfall station is available in the study area, situated in the upper Lubigi sub-catchment, the study assumed a spatially homogeneous rainfall distribution applied to the entire catchment. The rainfall event of 66.2 mm is measured by an automatic weather station equal to a 2-year return period event. The return periods are based on the Kampala Drainage Master Plan (KDMP) (2002).

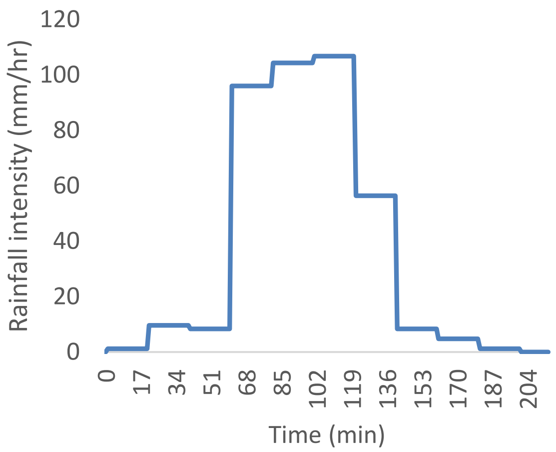

Figure 2.4 Rainfall intensity used for flash flood modelling. Flash flood produced event occurred on 25th June 2012

2.3.3. *Land use and infrastructure maps*

Figure 2.3 presents vegetation cover, built-up, and bare soil cover fractions of Kampala, which were derived from the Landsat image of 2010 (Fura, 2013). The vegetation cover map was used in the PTFs for the prediction of SHPs (**Scenario-1**) as well as directly used in the openLISEM software as a fraction of surface cover by vegetation for interception calculation.

A bare soil fraction map was created and used as a compaction factor in the PTFs equations. Bare soil is distributed everywhere in the city (*e.g.*, dirt roads, roadsides, playgrounds and fields, and footpaths) and is assumed to be compacted by traffic. The sum of these surfaces is converted into a fraction of bare soil per grid cell, which calculates the degree of compaction based on the PTFs. The larger the fraction of bare surface, the more the topsoil is assumed to be compacted.

2.3.4. *Soil map upscaled based on the soil-landscape relationship*

An UN-HABITAT project (Sliuzas et al., 2013) established a preliminary soil map of the upper Lubigi catchment based on the gathered preliminary soil data from 30 ring samples. Soil samples were collected from the representative landscape units, and the critical aspect was soil texture classes belonging to four landscape units (*i.e.,* Valley floor, bottom slope, Mid-slope, and hilltop). The dominant soil texture classes in the catchment were clay (C) for Valley floor; Sand Clay Loam (SaCL) and Sandy Clay (SaC) for the bottom slope; Sandy Clay Loam (SaCL) for Mid-slope; and SaCL and Sandy Loam (SaL) for hilltop areas as reported by (Rossiter, 2014). The catchment landscape was highly consistent regarding the pattern of Laterite-capped hills and swampy inter-hill valleys. Thus, a strong relationship between the texture classes and the landscape morphology appeared to be present. Therefore, the upscaling of Lubigi catchment observed soil texture classes to the whole Kampala city through the soil-landscape relationship is reasonably possible. Thus, for SMLS, this study used the upscaled soil texture classes to predict the necessary SHPs by applying PTFs, as shown in **Table 2.2**.

Table 2.2 Soil texture classes belong to the different landscape units according to SMLS, soil texture classes according to SMFAO, and Soil texture data ranges according to SMSG

Soil database	Landscape unit	Texture classes	C	S
SMLS	Valley floor	C	0.50	0.30
	Bottom slope	SaCL-SaC	0.35	0.55
	Mid-slope	SaCL	0.28	0.60
	Hilltop	SaCL-SaL	0.20	0.65
SMFAO		SaCL	0.28	0.60
		SaL	0.20	0.65
SMSG		Texture data ranges	0.20-0.50	0.33-0.64

S: Sand; C: Clay; SaCL: Sandy Clay Loam; SaL: Sandy Loam; SaC: Sandy Clay

2.3.5. Soil map based on FAO soil database

According to the 1:500000 scale FAO soil data source 1991, except for a few areas in the eastern part of Lake Victoria, which is covered by SaL, the soil texture class of Kampala city is represented by SaCL. The soil texture classes from the FAO database used for PTFs are shown in **Table 2.2**.

2.3.6. Soil map based on SoilGrids250m

According to the SMSG database, the soil texture data of sand and clay contents were used as the predictors for PTFs. Unlike SMFAO and SMLS, in SMSG, the soil texture data was obtained as the percentage of clay and sand, as shown in **Table 2.2**. Other inputs for PTFs are the same as those of SMFAO and SMLS. Soil texture data from the SMSG map shows that non-built-up and green areas (wetlands) are characterized by clay soil texture data, whereas built-up areas are dominated by sand content (as big as 64% in the city center). In this regard, the prediction of soil texture data by using the SMSG framework was able to consider the presence of urban areas, as indicated by (Hengl et al., 2017).

2.4. Results and Discussion

2.4.1. Bulk Density

Bulk density is one of the preceding soil physical properties used in the PTFs to predict the necessary SHPs. **Figure 2.5** presents the results of bulk density for uncompacted and compacted scenarios for the three soil databases. When the uncompacted scenario is considered, the soil becomes 'loose' with a lower bulk density, which was predicted in the wetlands and at the city's edge. For the SMLS, the lowest value of bulk density was predicted in the lower slope and valley floor landscape units characterized by C and SaC. In contrast, the higher bulk density was predicted in the middle slope and hilltop landscape units represented by SaL and SaCL **Figure 2.5 (a)**. In the case of SMFAO **Figure 2.5 (c)**, since the majority of the catchment area is represented by SaCL texture class, the predicted bulk density was only different according to the incorporated vegetation cover fraction. The result when using SMSG indicates that the predicted bulk density is higher in the built-up areas where the soil texture data is sandy soil. In non-built-up regions where the soil texture data is clay, the predicted bulk density is lower **Figure 2.5 (b)**. The predicted bulk density is higher when using SMSG than the other two soil databases, particularly in the built-up area, which is primarily due to its recent inclusion of land use (urbanization) in the ISRIC soil database prediction system (Hengl et al., 2017). The predicted bulk density distribution follows soil texture classes' distribution with the higher bulk density predicted in the sand content and SaCL areas. In contrast, the lower bulk density was predicted in the clay content areas.

When the compaction scenario is introduced in the predictive equations, the predicted bulk density increases significantly for all soil databases (**Figure 2.5)**. However, the increment is lower when using SMSG because, as shown in **Table 2.1**, both sand and clay soil texture data are less affected by compaction compared to the other soil texture classes used in the case of SMLS and SMFAO. As shown in the figure, the increment in the predicted bulk density varies between 9 - 22 according to the type of soil texture classes and the degree of compaction used in the prediction system. In general, bulk density increases with the increase in the degree of compaction, which runs from hard to dense, as shown in Table (1). Overall, the built-up areas are least affected by compaction mainly because the compacted areas are usually distributed outside the built-up areas (e.g., playing ground, murrum road, and tarred roadsides).

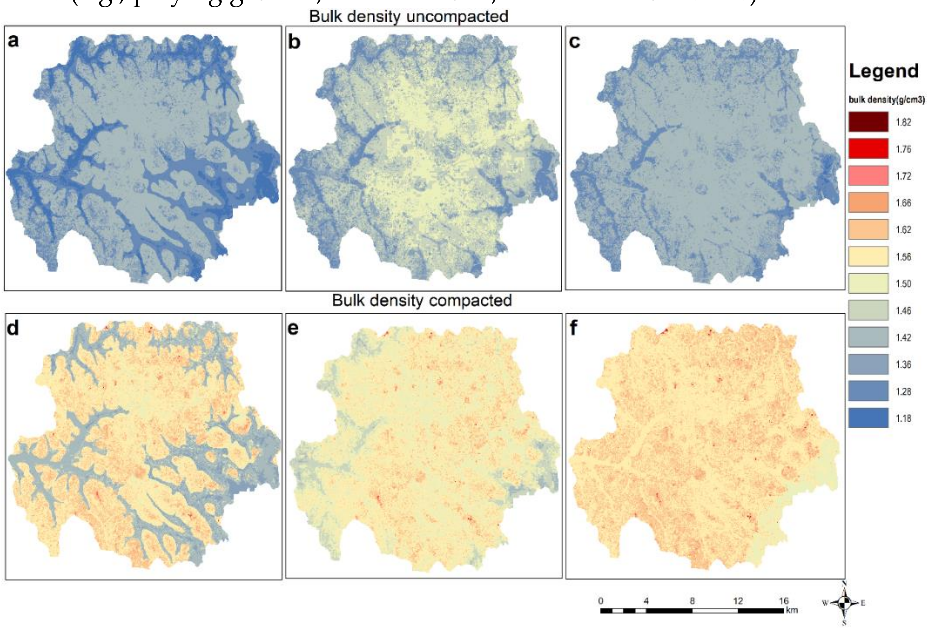

Figure 2.5 Predicted bulk density: (a) and (d) SMLS (increment due to compaction is 15-20%); (b) and (e) SMSG (increment due to compaction is 9-17%); (c) and (f) SMFAO (increment due to compaction is 14-22%)

2.4.2. Predicted soil hydraulic properties needed for flood model

Table 2.3 shows the ranges of the predicted soil hydraulic properties (SHPs) needed for openLISEM flood modelling for compacted and uncompacted scenarios. The SHPs needed for the openLISEM model are Ksat, porosity, initial soil moisture content, and matric suction (PSI), as predicted based on the three soil databases. The values and the spatial variability of the predicted SHPs mainly follow the results of bulk density distribution, which is predicted based on soil texture classes and soil organic matter. Initial soil moisture content (*thetai*) was predicted as 80% of the porosity; hence, the result follows porosity distribution (section 4.3.1), with higher values predicted in the wetlands (non-built-up). In contrast, the lower *thetai* is predicted in the built-up areas. Although the compaction scenario's effect is tested for all SHPs, for openLISEM hydrological modelling, we used only the compacted Ksat and compacted porosity. Ksat and porosity are the main SHPs that affect the infiltration characteristics of the openLISEM model. Therefore, we exclusively discussed their values and distribution under both compacted and uncompacted scenarios in the next section.

Table 2.3 Ranges of the predicted soil hydraulic properties (SHPs) used for openLISEM flood modelling for both compacted and uncompacted scenarios

Scenario	SHPs	SMLS	SMSG	SMFAO
Uncompacted	Ksat	17-144	9-84	44-220
	Porosity	0.46-0.59	0.44-0.56	0.47-0.56
	Initial soil moisture	0.37-0.47	0.35-0.44	0.37-0.45
	PSI	0-36	0-33	0-95
Compacted	Ksat	0-20	0-24	0-47
	Porosity	0.31-0.49	0.32-0.48	0.31-0.45
	Initial soil moisture	0.17-0.34	0.18-0.34	0.13-0.23
	PSI	33-71	17-33	0-69

i) Predicted porosity

The predicted porosity for the uncompacted scenario and the percentage changes due to soil compaction are presented in **Figure 2.6**. For the uncompacted scenario, the predicted porosity when using SMLS was varied across the landscape units, with the highest porosity predicted at the valley floor and bottom slope landscape units while the lowest porosity was predicted in the middle slope and hilltop landscape units **Figure 2.6a**. In SMSG, the predicted porosity was varying across the built-up (lowest porosity) and non-built-up (highest porosity) following the predicted bulk density distribution (**Figure 2.6b)**. Similarly, in SMFAO, the simulated porosity was higher at areas well covered by vegetation, while the lower value was predicted in the built-up (no vegetation cover) areas **Figure 2.6c**. Since in the SMFAO, the soil information other than the texture classes has no information on the existing features such as wetlands and urban areas, the predicted porosity followed the distribution of the introduced vegetation cover fraction. The result of the predicted porosity under the uncompacted scenario indicates higher and lower values in the non-built-up (valley floor) and built-up, respectively, which are well associated with the predicted bulk density distribution.

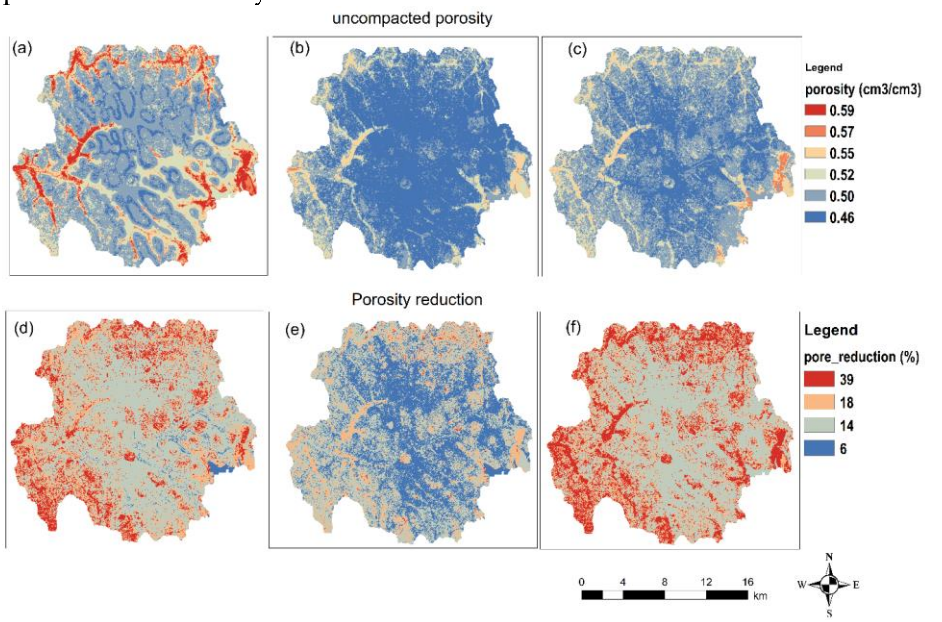

Figure 2.6 Predicted porosity: (a) and (d) SMLS; (b) and (e) SMSG; (c) and (f) SMFAO. Porosity differences represent the difference between the uncompacted and compacted scenarios, which are calculated based on the raster grid values.

ii) Predicted saturated hydraulic conductivity

The result of the predicted saturated hydraulic conductivity (Ksat) for the uncompacted scenario and the percentage changes due to soil compaction is presented in **Figure 2.7**. As shown in the figure, the predicted Ksat when using SMLS was varying across different landscape units (Valley floor and bottom slope versus mid-slope and hilltop) with the highest and lowest Ksat predicted at hilltop/middle slope and valley floor/lower slope landscape units, respectively (**Figure 2.7a)**. At both valley floor and lower slope landscape units, the predicted Ksat is about five times smaller than the values predicted at the hilltop landscape unit, mainly because of the higher porosity predicted at the valley floor and lower slope landscape units. When using SMSG, the predicted Ksat was varying across the built-up and non-built-up, with the highest Ksat predicted at the lowest porosity areas. In contrast, the lowest Ksat was predicted at the highest porosity areas (**Figure.7b**). In the case of SMFAO, the highest Ksat was predicted in the smallest area located in the vicinity of Lake Victoria, mainly because this area is characterized by SaL soil texture class, which creates lower bulk density. In contrast, the lowest Ksat was predicted in the built-up area following the bulk density and porosity distribution.

Since Ksat is primarily influenced by bulk density and porosity, the predicted Ksat was negatively correlated with bulk density and positively correlated with porosity. Wang et al. (2018a) also reported that an increase in bulk density decreases Ksat, while the increase in porosity increases the value. However, in the extremely higher porosity in the swampy areas characterized by clay soil texture, the predicted Ksat was lower. Furthermore, incorporating the uncompacted scenario into the predictive equation of PTFs decreases bulk density by creating a ‘loose’ soil, which consequently enhances the values and the spatial variability of the predicted Ksat based on the degree of vegetation cover fraction.

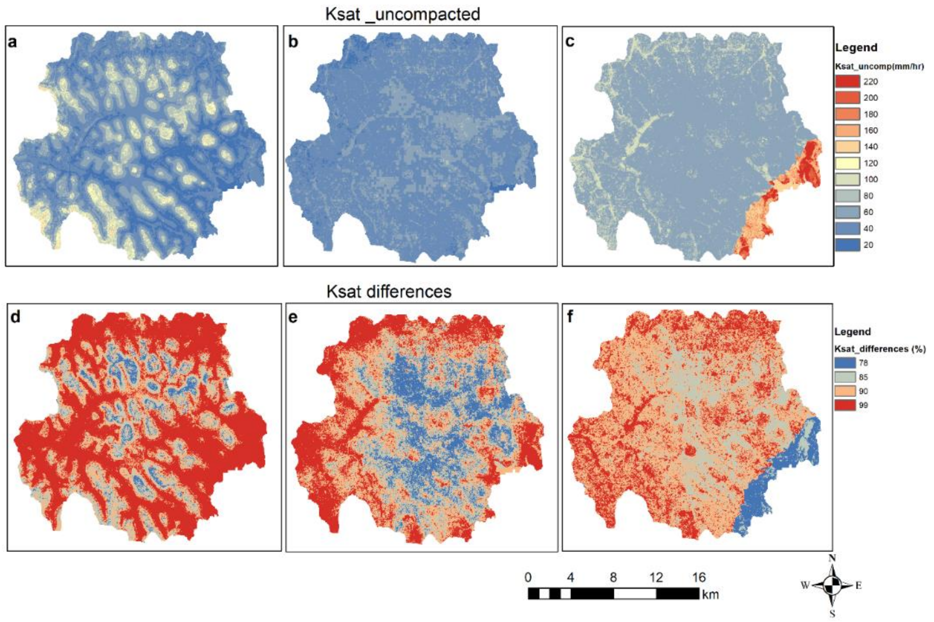

Figure 2.7 Predicted Ksat: (a) and (d) SMLS; (b) and (e) SMSG; (c) and (f) SMFAO. Kat differences represent the difference between the uncompacted and compacted scenarios, which are calculated based on the raster grid values.

2.4.3. *The effect of compaction on porosity and Ksat*

Figure 2.6 shows the percentage changes in the predicted porosity when using the three soil databases due to the compaction scenario. As shown in the figure, compaction affects both values and the spatial distribution of the porosity, which is well associated with the predicted bulk density under the compacted scenario. Under all soil databases, wetlands and non-built-up areas are profoundly affected by compaction, reducing the porosity by 18-39%. However, the built-up areas are least affected by compaction with porosity varying between 6-14%, which is entirely related to the lower compacted bulk density predicted in the built-up areas. Similarly, the incorporation compaction scenario into the predictive equation affects the values and the spatial distribution of Ksat (**Figure 2.7)**. As shown in the figure, the predicted Ksat was reduced significantly, with the percentage changes reaching up to 99% in the wetland areas.

The incorporation of the compaction scenarios into the predictive equation increased bulk density, consequently decreasing both Ksat and porosity values with the degree of compaction (Richard et al., 2001); (Saxton and Rawls, 2006). The result of the compacted scenario indicated that the predicted porosity when using SMSG was the least affected compared to SMLS and SMFAO. One possible reason is due to the inclusion of urbanized areas in the SoilGrids system, which causes a relatively homogeneous sandy soil texture data in the city center area. Since Ksat was predicted as a function of compacted porosity, a decrease in porosity caused a significant reduction in the predicted Ksat. Similar studies found that the increase in urban soil compaction has decreased saturated hydraulic conductivity. For instance, (Gregory et al., 2006) found that an increase in soil compaction caused a reduction in saturated hydraulic conductivity by 75%. Similarly, (Ossola et al., 2015) found a decrease in porosity in the compacted parks, consequently reducing saturated hydraulic conductivity.

2.4.4. Comparison of predicted SMLS with observations

The predicted Ksat and porosity under the uncompacted scenario using SMLS were compared with the field data collected from the upper Lubigi catchment, as shown in **Table 2.4**. Field data have shown that the valley floor landscape unit with heavy clay in the swampy/shrubs areas has lower Ksat varying between 1 to 20 mm/hr. The predicted Ksat at the same landscape unit when using SMLS shows higher values varying between 16 to 35 mm/hr. The observed values in the hilltop with sandy clay loam in the grass/shrubs areas have high Ksat values ranging between 90 to 150 mm/hr, while the predicted Ksat at the same landscape unit shows comparable values ranging between 78 to 140 mm/hr.

However, the predicted porosity at the valley floor was underestimated compared to the field data, as shown in **Table 2.4**, possibly because of a strong effect of organic matter in the samples that do not appear in the PTFs. Both observed and predicted porosity at the hilltop landscape unit have a relatively low value varying between 0.51-0.61 and 0.46-0.52 (cm^3/cm^3). The variation in values from the PTFs is smaller than the reality, but more samples would have to be taken to investigate this better.

Table 2.4 Observed versus predicted Ksat and porosity values for the dominant texture classes according to the classified landscape units in the study catchment (Ksat_O: observed Ksat; Ksat_P: simulated Ksat; Pore_O: observed porosity; Pore_P: simulated porosity)

Soil condition	Landscape unit	Texture classes	Ksat_O (mm/hr)	Ksat_P (mm/hr)	Pore_O (cm^3/cm^3)	Pore_P (cm^3/cm^3)	Number of samples
Uncompacted	Valley floor	C	1.0-20	16-35	0.58-0.70	0.52-0.59	5
	Bottom slope	SaCL-SaC	15-75	27-50	0.47-0.58	0.47-0.52	9
	Mid-slope	SaCL	20-90	40-75	0.53-0.65	0.46-0.51	2
	Hilltop	SaCL-SaL	90-150	78-144	0.51-0.61	0.46-0.52	5
Compacted	Valley floor	C	0.0-0.5	0.0-1.0	0.56-0.58	0.43-0.48	8
	Bottom slope	SaCL-SaC	1.0-6.5	0.5-3.0	0.48-0.50	0.33-0.43	5
	Mid-slope	SaCL	1.5-3.3	3.5-8.0	0.53-0.54	0.40-0.42	2
	Hilltop	SaCL-SaL	0.8-2.9	6.0-20	0.51-0.54	0.32-0.42	4

A comparison of the observed and predicted Ksat under the compacted scenario when using SMLS at the valley floor shows similar results, as shown in **Table 2.4**, mainly due to the high effect of compaction at the clay content area. As shown in the Table, the predicted Ksatcomp in the hilltop landscape unit was moderately overestimated compared to the observed Ksatcomp. In the other landscape units, the predicted Ksatcomp was within the range of the observed values. In the case of porosity, the predicted values at all landscape units were underpredicted compared to the observed values at the respective landscape units.

2.5. *The sensitivity of flood dynamics to different soil databases*

This section presents the effects of the derived soil information on the flood dynamics, which are presented as catchment hydrological characteristics, infiltration characteristics, flood behavior, and flooding on the number of building derived from the satellite image.

2.5.1. Flood simulations and catchment hydrological behaviour

Table 2.5 presents the catchment surface water balance results for six different model simulations and the percentage differences between compacted and uncompacted scenarios. The use of SMLS and SMSG appears in higher flood volumes than the SMFAO: 14.7x10^6 and 16.0x10^6 m^3 versus 6.2 x10^6 m^3, and flooded areas of 49.1 and 53.0 km^2 versus 26.1 km^2. This is caused by the infiltration dynamics, as illustrated by the infiltration amounts and overall runoff percentages (calculated as total discharge/total rainfall). When the compaction scenario is considered, the flooded area has grown by 6% for both SMLS and SMSG and 12% for SMFAO. The simulated peak discharges were also increased by 7%, 6%, and 13% for SMLS, SMSG, and SMFAO, respectively. The use of soil compaction increased the runoff percentage for all soil maps, but the increment is higher when using SMFAO than the other two soil maps.

Table 2.5 Total water balance for six model simulations by using uncompacted and compacted soil scenarios (C-N) represents compacted minus non-compacted

Catchment parameters	smls_n	smsg_n	smfao_n	smls_c	smsg_c	smfao_c	smls(c-n)	smsg(c-n)	smfao(c-n)
Catchment area (km^2)	358	358	358	358	358	358			
Total infiltration (mm)	44.7	43.6	56.6	42.3	41.3	55.2	-6%	-5%	-3%
Water in flood (mm)	10.9	11.5	4.4	12.3	12.7	5.2	11%	10%	15%
Total outflow (all flows) (mm)	7.9	8.5	3.5	8.9	9.4	3.9	11%	10%	10%
Total discharge/total rainfall (%)	12.0	12.9	5.3	13.4	14.2	6.0	10%	9%	12%
Flood volume (in million (m^3))	14.7	16.0	6.2	16.4	17.5	7.2	10%	9%	14%
Flood area (in million (m^2)	49.1	53.0	26.1	52.4	56.3	29.5	6%	6%	12%

n-uncompacted, c-compacted

2.5.2. Infiltration dynamics behaviour

Figure 2.8 shows infiltration maps simulated by using the three soil databases under the uncompacted scenario. When using SMLS (**Figure 2.8a**), the higher infiltration was simulated at the landscape units where the predicted Ksat and porosity were higher. However, due to the sealing characteristics of hilltop, middle slope, and lower slope landscape units, the simulated infiltration was relatively lower except at the grid cells where it is not sealed. Similarly, when using SMSG, the higher infiltration was simulated, where the higher Ksat and porosity were predicted (**Figure 2.8b**). Since the predicted porosity and Ksat followed the distribution of built-up and non-built-up areas, the dynamics of the simulated infiltration was certainly followed the same pattern with higher infiltration simulated in the non-built-up areas while the lower infiltration simulated in the built-up areas. When using the SMFAO database, the simulated infiltration shows a widespread distribution of high values of infiltration in the catchment (**Figure 2.8c**). As shown in the figure, the wide area of the catchment has infiltration values greater than 75 mm, particularly in the low-density urban areas and wetlands, significantly associated with the higher Ksat predicted in the catchment.

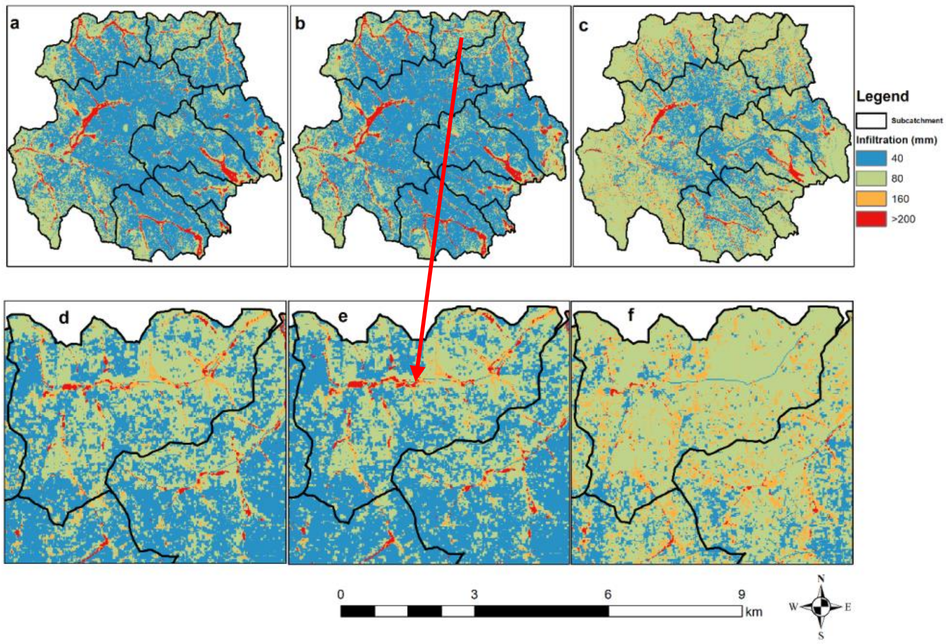

Figure 2.8 Simulated infiltration for uncompacted scenario: (a) and (d) SMLS; (b) and (e) SMSG; and (c) and (f) SMFAO. The red arrow indicates a sub-catchment zoomed in to see the differences among the soil databases

The result of this study indicates that the variability of the simulated infiltration was well associated with the values and the spatial variability of the SHPs, in particular, predicted Ksat and porosity. The higher infiltration was predicted in the well-vegetated and non-built-up areas (20.5% of the total catchment area), which is well connected with higher porosity and Ksat, while lower infiltration was associated with lower porosity and Ksat. However, the extreme higher value of infiltration simulated at swampy areas was due to floodwater overpressure during the event. The extreme lower infiltration simulated in the build-up was due to urban sealing, which accounted for 48% of the total catchment area (358 km^2).

2.5.3. Flood dynamics behaviour

The uncompacted flood depth scenario shows widespread flooding along the main channels (primary and secondary channels) as simulated by using the three soil databases **Figure 2.9**. The result indicated that the spatial distribution of flood dynamics (flood depth, flooded area, flood volume, and duration) follows the catchment's flat terrain and infiltration dynamics. To mention, the simulated flood depth along the primary channels when using SMLS and SMSG (0.5-2 m) was deeper than that of SMFAO (0.5-1 m), which is associated with the lower infiltration simulated when using SMLS and SMSG. Since the runoff coefficient depends on infiltration for the given rainfall intensity, the lower infiltration simulated when using SMLS and SMSG contributed to more overland flow, which resulted in more flooding. However, the deeper and low-velocity floodwater at the valley floor (flat terrain) was caused by water accumulation from the secondary channels and steep terrains.

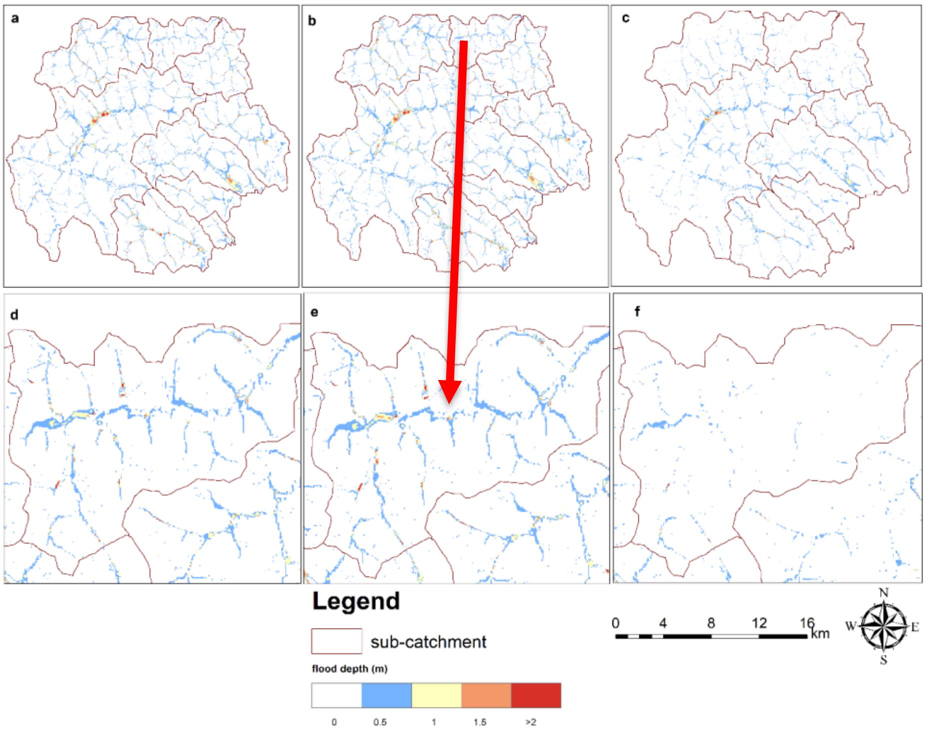

Figure 2.9 Simulated flood depth for uncompacted scenario: (a) and (d) SMLS; (b) and (e) SMSG; and (c) and (f) SMFAO. The red arrow indicates a sub-catchment zoomed in to see the differences among the soil databases

Similarly, the simulated flood duration when using SMLS and SMSG shows a longer duration along both primary and secondary channels than the SMFAO (**Figure 2.10**). Also, the calculated flooded areas and flood volume (e.g., at 0.5 m) were 23 km^2 and 11281 million m^3 when using SMLS and SMSG, almost double the result found when using SMFAO at the same time water depth (**Figure 2.11**). Since the simulated infiltration was higher in the case of SMFAO, there is little water left for direct runoff, which leads to shallow flood depth, consequently less flooded area, flood volume, and duration.

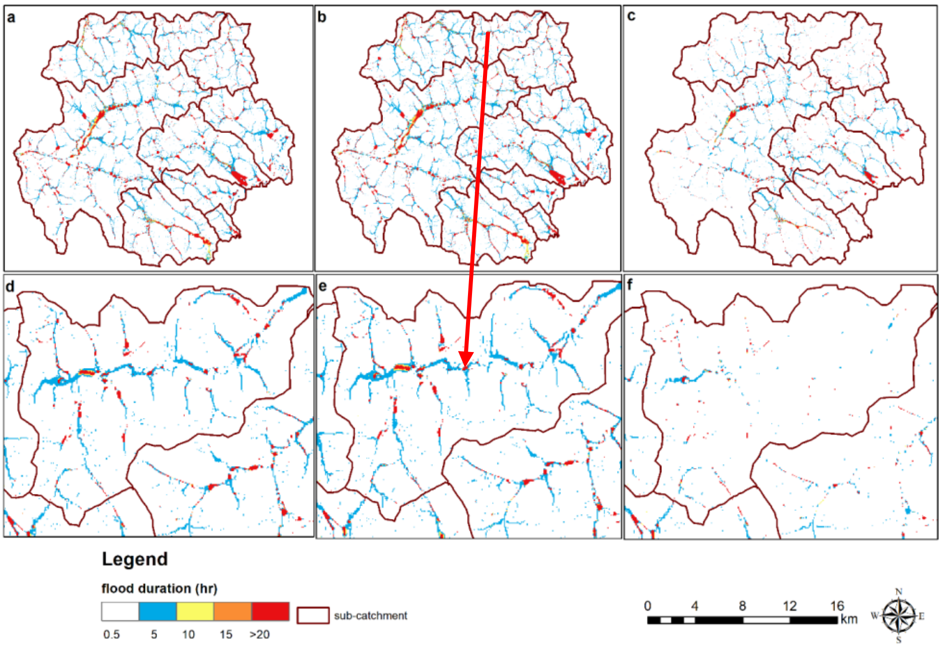

Figure 2.10 Simulated flood duration for uncompacted scenario: (a) and (d) SMLS; (b) and (e) SMSG; and (c) and (f) SMFAO. The red arrow indicates a sub-catchment zoomed in to see the differences among the soil databases

2.5.4. The effect of soil compaction on infiltration and flood dynamics

Table 2.6 shows the percentage reduction in total infiltration and the increments in the simulated flood depth due to soil compaction. As shown in the table, the simulated total infiltration was reduced by 16.2 %, 19.4 %, and 17.5 % for SMLS, SMSG, and SMFAO, respectively. The reduction is relatively higher for all soil databases in the infiltrated areas (40-80 mm). However, in the high infiltrated areas (160-200 mm), mainly in the swamps, the simulated total infiltration was increased instead of decreasing, likely due to an overpressure of greater than 1.5 m of floodwater produced due to compaction. As a result of reduced infiltration, flood depth at different levels was increased, as shown in **Table 2.6,** consistent with the infiltration reduction. However, the flood depth increment was high in the swampy areas, mainly due to floodwater concentration from high elevation areas. Similarly, the simulated flood duration (not shown here) and both the calculated flooded areas and flood volume (**Figure 2.11**) were all increased following the infiltration reduction and nearly overweight the difference caused as a result of using different soil databases.

The compaction effect on infiltration was high because there is a double effect on Green and Ampt infiltration as both porosity and Ksat are affected. Since the Ksat was predicted as a function of porosity, and the Green and Ampt infiltration equation used both variables, the combined effect reduced the predicted infiltration significantly. Consequently, more water is converted into the overland flow and increased water depth, flood areas, flood volume.

Table 2.6 Percentage reduction in infiltration and increments in flood depth due to compaction regarding infiltrated and flooded areas

Parameters	Variable range	SMLS (%)	SMSG (%)	SMFO (%)
Infiltration (mm) (reduction)	40-80	13.40	17.90	14.20
	80-160	2.80	1.50	3.30
	160-200	-0.01	0.00	-0.01
Total	**40-200**	**16.2**	**19.4**	**17.5**
Flood depth (m) (increament)	0.1	6	5	11
	0.5	4	3	10
	1	10	9	19
	1.5	18	16	19
	2	22	20	0
Total	**0.1-2**	**60**	**53**	**59**

2.5.5. The effects of flood depth and duration on built-up areas

The total number of buildings affected by flood depth and flood duration was calculated by using flood depth greater than 10 cm and flood duration greater than 30 minutes **(Figure 2.11)**. Since the individual structures and their functions are not available, only a built-up surface per grid cell in m^2 was used. The number of buildings is calculated using the structure density of 90 m^2, the average house density obtained from the field observation. As shown in the figure, the total number of buildings affected by flood depth was maximum at a lower water depth between 10 and 50 cm, which is the highest when using SMLS and SMSG under both uncompacted and compacted conditions. Under the uncompacted scenario, the number of buildings affected by flood depth at lower flood depths of 10 and 50 cm was 91113, 87686, and 67307 for SMSG, SMLS, and SMFAO, respectively. These numbers are increased to 93585 for SMSG, 90403 for SMLS, and 71333 for SMFAO under the compacted scenario. The number of structures is least affected by deep flood depth compared to low flood depth.

As shown in **Figure 2.11**, the duration the buildings stayed underwater was also high at a lower flood duration between 0.5-1 hour. The effect is high when using SMSG and SMLS compared to SMFAO under both uncompacted and compacted conditions. The number of buildings that stayed under flood water at a lower duration was mainly at the location of the secondary channels. Between 15-20 hours, the number of structures affected by flood duration was 34628, 34221, and 25350 under the compacted condition and 33022, 32737, and 23986 under an uncompacted condition for SMLS, SMSG, and SMFAO, respectively. The effect at 15-20 hr duration was mainly from the main channels in the wetlands. The effects of floodwater at those locations are mainly due to flat terrains (wetlands) naturally used for flood attenuation purposes but now are filled with informal settlements.

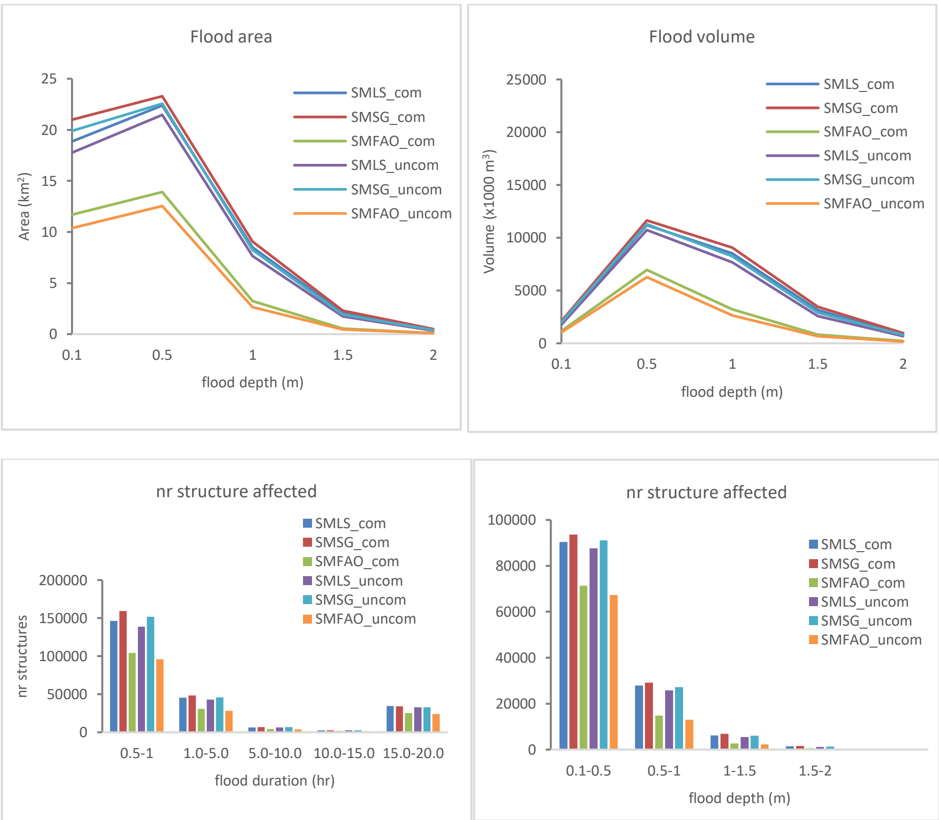

Figure 2.11 Calculated flood statistics: Comparison of uncompacted and compacted scenarios for SMLS, SMSG, and SMFAO. The number (nr) of structures was calculated based on the average structure size of $90m^2$.

2.5.6. Model verification with earlier calibrated simulations

Due to the lack of observed actual discharge data at the main outlets, the openLISEM model verification has only been handled by comparing the model flood inundation map with an earlier calibrated flood line developed by (KDMP) (KCCA, 2010). The earlier flood lines in Kampala were generated by using HEC-GeoRAS (River Analysis System of the Hydrologic Engineering Center of the US Army Corps of Engineers) for return periods of 2, 10, and 100 years. The generated flood lines are simply the strip or areas along the sides of drainage channels that will be prone to flood inundation for the different return periods. **(Figure 2.12a)** Shows the effect of a 2, 10, and 100-year return period on flood extent, and it`s reported that the flood extent for different return periods is all similar around the major wetlands, mainly due to the flat cross-section used in the simulation. When the capacity of the natural channel is exceeded (in most cases during floods with return periods of two years or less), floodwaters spread over the full extent of the floodplain, up to the steeper regions that define the floodplain, with the flood depth increases slightly for more extended return periods. The UN-HABITAT project (Sliuzas et al., 2013) have also found that the width of flooding along the primary and secondary channels of all drainage systems does not differ much for the different return periods, which is primarily caused by the relatively small cross-sectional areas of the natural channels along the floodplains.

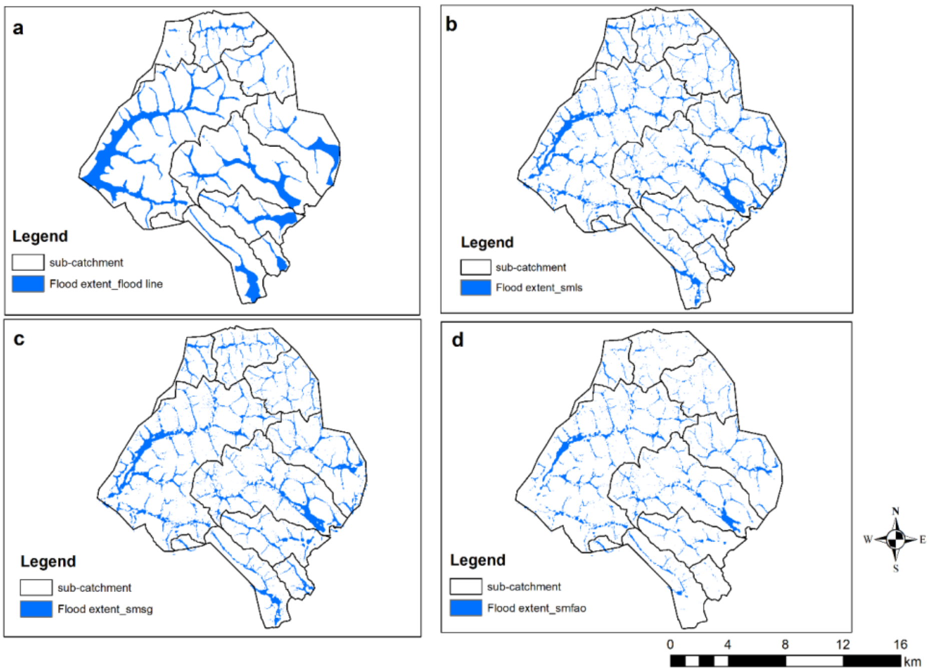

Figure 2. 12 Verification of flood simulation: Comparison of flood extent map constructed from flood lines (a) with flood extent map simulated by using SMLS (b), SMSG (c), and SMFAO (d)

The openLISEM model simulated with compacted scenarios by using the storm event of 66.2 mm, which is equivalent to an event of the 2-year return period, was used to compare the simulated flood extent with an earlier flood extent. As shown in **Figure 2.12**, the model result indicates that floodwater spread over the full extent of the plain around the main drainage channels but with different water depth distribution. The f-statistics goodness of fit was calculated by using (eq.2.6), and the result is shown in **Table 2.7**. The high value of f-statistics indicates a high goodness fit between areas of flood line and model simulation.

$$\boldsymbol{f} = \left(\frac{Aos}{Ao+As-Aos}\right) * \mathbf{100} \qquad 2.6$$

'Ao' refers to the flooded area observed under flood lines; 'As' indicates the flooded area simulated by the openLISEM model, and 'Aos' represents the intersected flooded area between Ao and As. The flood extent maps indicated that flood extent accuracy was lower when using lower-resolution SMFAO for hydrological modelling. The main reason for this is that the predicted soil hydraulic properties, in particular, Ksat was overestimated when using SMFAO, which resulted in overestimated infiltration, consequently, lower flood extent maps.

Table 2.7 Summary of the performance of soil maps for flood modelling against historical flood line

Flood map	Total flooded area (m^2)	Intersected areas (m^2)	f
SMLS	55821	34526	35
SMSG	57531	35149	36
SMFAO	33958	21113	24
Flood line	76127		

In general, the discrepancies between the historical flood lines and flood model arise from the following two reasons: first, due to the lower design storm used under the current study, although it's assumed that the valley floor can quickly be filled with a flood of a frequent high event (e.g., 2-year event) with different flood depth. Second, since the openLISEM model applied a 2D dynamic wave for flood simulation following the DEM, the flood model results have some flooded areas outside the earlier flood line where there are relatively flat terrains.

2.6. *Conclusion*

This study applied three different soil databases to predict soil hydraulic properties used in an integrated flood model to determine how sensitive the flood dynamics are to the predicted SHPs, and if possible, to select the best data source for integrated flash flood modelling in an urbanized area where there is a scarcity on local soil physical data. Three soil data sources were used: coupling soil texture to landscape form, using the SOILGRIDS250m database, and deriving texture information from the small-scale FAO soil map. In making flood predictions, one may choose to include compaction as an additional factor apart from surface sealing by roads and buildings. We assumed that bare areas would have a certain degree of compaction and investigated its impact on each of the three soil data sources.

The results indicate that the choice of the data source has a strong influence on both the quantity and spatial variability of infiltration, which naturally directly affects runoff and flooding. On top of that, the effect of sealing and compaction is equally essential and nearly outweighs the differences caused by the use of different soil databases. This indicates that sufficient effort should be attributed to getting actual compaction information in an area for which a flood simulation is done to establish how far this affects reality. The use of the Saxton and Rawls (2006) Pedotransfer functions have the added advantage of incorporating the effects of compaction and organic matter into their equations so that the urban fabric can be represented in detail, for instance, high-resolution earth observation.

The study found that soil databases with high variability of soil physical properties (e.g., when using SMLS and SMSG) can better predict SHPs used for flood modelling. The comparison of flood inundation areas using the three different soil maps with earlier calibrated simulations indicates that SMSG and SMLS are better strategies, although still different from the accepted flood extent in the Kampala Master Drainage Plan case of Kampala city. Given the fact that the SoilGrids database is available globally, while soil-landscape relations may not be available everywhere, it seems to be an acceptable source to derive infiltration properties. Because SOILGRIDS comes with a warning and an extensive error analysis and is not meant for detailed studies as is done here, it is, of course, advisable to check the results against local measurements of texture and, in combination with PTFs, against resulting hydrological properties. Nevertheless, the results seem promising for integrated flood modelling in those urbanized areas where most buildings are constructed directly on the original soil.

Chapter 3: Impact of improved urban fraction configuration on rainfall simulation using the WRF model over Kampala, Uganda

Abstract

Urbanization affects the initiation and intensification of convective activities by changing local meteorological variables, which alters the atmosphere's convective processes. Therefore, proper urban surface information is required to model the energy partitioning pattern and its contrast with neighboring grid cells. In this chapter, the mesoscale weather research and forecasting (WRF) model is configured with satellite-derived urban fraction for optimal rainfall simulation and to evaluate its impact on the simulated rainfall over Kampala, Uganda. The WRF urban parameter values associated with the considered urban fraction are adjusted based on literature reviews. The satellite-derived urban fraction represents the more realistic extent and intensity of the urban class with a more representative urban fraction. Three simulations are performed to distill the impact of changing urban fraction as well as of adjusting urban parameters: (1) DUF_DUP that used default urban fraction and default urban parameter values, (2) DUF_AUP that used the default urban fraction with adjusted urban parameter values, and (3) SUF_AUP that used the satellite-derived urban fraction and adjusted urban parameter values. For all three simulations, a single extreme rainfall event, which has caused a flood hazard in Kampala on 25th June 2012, is used. The simulated peak rainfall and its spatial distribution over the Kampala catchment were evaluated using observed rainfall data from gauging stations and CHIRPS satellite-based precipitation. Compared with the default urban fraction, the satellite-derived urban fraction represents the more realistic urban extent and intensity. As a result, SUF_AUP results in a more realistic rainfall simulation compared to when using the default urban fraction. For all three simulations, the modelled rainfall is overestimated compared to CHIRPS and underestimated when comparing gridcell values with gauging station records. The SUF_AUP simulation shows relatively better results with a lower absolute relative error score compared to the other two simulations.

Keywords: rainfall, Default urban fraction, Kampala, urban parameter, Updated urban fraction, and WRF model

3.1. Introduction

The effect of urbanization on mesoscale convection and intensive rainfall has received considerable attention over recent times (Alexander et al., 2006; Ashley et al., 2012). With an urban expansion, land-cover changes from natural vegetation/surface to artificial urban surface, which leads to changes in urban parameters such as roughness parameter, heat capacity, and thermal conductivity. Changes in these urban parameters can alter the near-surface radiation and energy budgets and the atmospheric thermodynamic characteristics, which affect the initiation and intensification of convective processes over a city (Paul et al., 2018). Moreover, with an urban expansion, a larger thermal contrast between the urban areas and the water body can result in stronger low-level circulation, which could be instrumental in forming convective rainstorms over cities (Ryu et al., 2016). Consequently, the meteorological conditions are altering that determine the mesoscale convection and intensive rainfall distribution over urban areas (Stewart and Oke, 2012; Wouters et al., 2016; Dai et al., 2019). In numerical weather prediction (NWP) models, the impact of such urban surface change can be handled through land surface modelling implemented in parameterization schemes.

With the mesoscale weather and research and forecasting (WRF) model currently operating at fine spatial resolution (e.g., 1 km) for high-intensity rainfall simulation, the impact of local climate processes induced by urban fraction needs to be incorporated (Paul et al., 2018). For instance, the impact of urban surfaces (e.g., street canyon morphology and built-up density) on energy partitioning patterns and their contrast from neighboring grid cells must be considered. In the WRF model, these processes are addressed using urban parameterization schemes and static surface parameters. A compressive dataset of urban surface information such as urban fraction and urban canopy is needed considering the inter-urban heterogeneity for energy partitioning patterns.

The default configuration of the WRF model uses urban surface information provided by the land surface models (LSM), which is based on various datasets. Notably, the current urban surface information is represented by the land use category 'urban and built-up category,' where the spatial extent of the land use categories are derived from Moderate-resolution Imaging Spectroradiometer (MODIS) observational data. The Noah LSM in WRF has three default sets of urban classes inside the urban category based on the US NCLCD 1992 (Chen et al., 2011): (1) Low-Intensity residential, (2) High-Intensity residential, and (3) Commercial/Industrial. Urban cells are assigned to one of these three categories, and the corresponding parameter values are linked through a table. However, these urban parameter values are site-specific and incorrectly represent a city's extent and position; hence it needs to be updated as suggested by (Alexander et al., 2016; Brousse et al., 2016); Wouters et al. (2016).

Several other urban fractions have been developed for different atmospheric modelling purposes. For example, local climate zoning (LCZ) is designed to study the thermal characteristics of the urban area (Stewart and Oke, 2012; Brousse et al., 2019), and in-homogeneous urban canopy parameters (UCP) are developed for air quality modelling (Dai et al., 2019). Therefore, the main objective of this chapter is to configure the WRF model optimally with urban fraction specifically developed for the city of Kampala, Uganda, and to evaluate the impact of adjusting urban fraction and parameters on the simulated rainfall event. The use of WRF to study the deep convection over Kampala requires a configuration that needs proper position and extent of the city for better consideration of the spatial contrast between the city and Lake Victoria. We are one of the first who perform such model evaluation in terms of explicit satellite-derived urban fraction for the application of deep convection triggering the localized flood.

This chapter provides a detailed analysis of (1) the WRF model's configuration with the adjusted urban fraction compared to the default urban fraction and (2) the impact of adjusted urban fraction, including adjusted urban parameters on the simulated rainfall. The chapter consists of data and methodology sections, followed by results, discussion, and conclusion sections. The methodology section includes the WRF model description as used in this thesis and its urban fraction configuration. Three model simulations were conducted and compared. For all three simulations, one single rainfall event occurring on 25th June 2012 is evaluated. The impact of updating urban fraction and urban parameters is conducted by comparing 24-h and 2-h accumulated rainfall amount and its spatial distribution against observed daily rainfall from gauging station and CHIRPS satellite data.

3.2. *Data*

In this section, the selected rainfall event and the data used for model verification are presented.

3.2.1. Selected event

For this study, the 25th June 2012 rainfall event that has caused a localized flood event in Kampala was selected. Of this event, two types of rainfall observations are present; rain gauge measurements and satellite. On 25th June

2012, two rain gauge stations were in operation in Kampala city: Automatic Weather Station (AWS) at the Makerere University campus recording at the 10-minute interval and Kampala Central station at a 24-hour interval. The 24-hour rainfall data of Kampala central station is collected from the Global Summary of the Day (GSOD) dataset provided by the National Climatic Data Center (NCDC). At Makerere University, a daily total of 66.2 mm was recorded, and Kampala Central station recorded 60 mm, which is a typical 2-year return period event.

Besides, satellite estimated rainfall from Climate Hazards Group InfraRed Precipitation with Station data (CHIRPS) (Funk et al., 2015) is retrieved for model evaluation. CHIRPS is considered as one of the best rainfall products for decision-making in East Africa (Cattani et al., 2018; Diem et al., 2019). The CHIRPS rainfall data has 0.05 degree (~5.5km) spatial and daily temporal resolutions. For the WRF model evaluation, the CHIRPS rainfall data is rescaled using linear interpolation to the innermost domain of WRF spacing, which is 1 km x 1 km.

3.3. *Mesoscale WRF modelling system*

The WRF model is a mesoscale atmospheric modelling system designed for both meteorological research and numerical weather prediction. The governing equations used are divided into six categories: (a) perfect gas law, (b) conservation of mass, (c) conservation of momentum, and (d) conservation of scalar (conservation of heat, water, and other trace gases). A detailed description of the governing equations is given in (Jacobson); Holton (1992). The equations set used in WRF are characterized by a fully compressible, non-hydrostatic. Its vertical coordinate is a terrain-following hydrostatic pressure coordinate; see for details (Holton, 1992); Pielke Sr (2002) and WRF user guide Wang et al. (2018b).

For atmospheric simulations (e.g., rainfall simulation), WRF has two components (see Figure 1.1), with the first WRF pre-processing system (WPS) and second the forecast model components. The WPS components start with a model domain configuration, prepare input data, and model initial conditions. With a series of WPS utilities, the model domain is set up using static geographic information datasets such as topography and land use, including updating urban fraction components and soil. Next, it ingests, reformats, and interpolates the requisite first-guess atmospheric data (e.g., a global analysis data of ERA-5) to the user-specified domains. Finally, input fields are put on model's vertical levels, and initial and lateral boundary conditions are generated. WRF is then ready to run.

The atmospheric modelling is done by using the model's forecast component, which handles Input/Output (I/O) and parallel-computing communications. The WRF modelling system is built in a hierarchical modelling system to handle the complex model simulation, which is written primarily in FORTRAN, can be built with a number of compilers, and runs predominately on platforms with UNIX operating systems. In addition to the dynamic solver, the forecast component of the model has a wide range of physics packages for atmospheric processes such as microphysics, cumulus parametrization, planetary boundary layer, and urban canopy parameterization. This chapter presents urban canopy parameterization and its use in the WRF model, while other parametrization schemes considered in this thesis will be discussed in Chapter 4.

3.3.1. The WRF model Configuration and setting

This thesis uses the WRF-ARW version 4 (Wang et al., 2012) with a two-way nested domain configuration. The WRF model setup consists of four domains centered on Kampala. The four domains are a 27 km outer fixed domain (D01) and three fixed nest domains of 9 km (D02), 3 km (D03), and 1 km (D04), with 31 × 31 grid points (Table 3.1), as shown in **Figure 3.1,** conform to the most recommended ratio of 1:3 by Liu et al. (2012).

Table 3.1 Weather Research and Forecasting (WRF) model settings used in the current study.

Model	**WRF v 4.1**			
Characteristics	Domain 1 (D01)	Domain 2 (D02)	Domain 3 (D03)	Domain 4 (D04)
Horizontal grid resolution	27 km	9 km	3 km	1 km
Horizontal Dimensions	31 x 31 x 31	31 x 31 x 31	31 x 31 x 31	31 x 31 x 31
Time step 60 seconds	adaptive time step	adaptive time step	adaptive time step	adaptive time step
Initial-boundary conditions	ERA-5 (30 km)	simulation of domain 1	simulation of domain 2	simulation of domain 3
Model run period	0000 UTC 24 June -1800 UTC 26 June 2012			

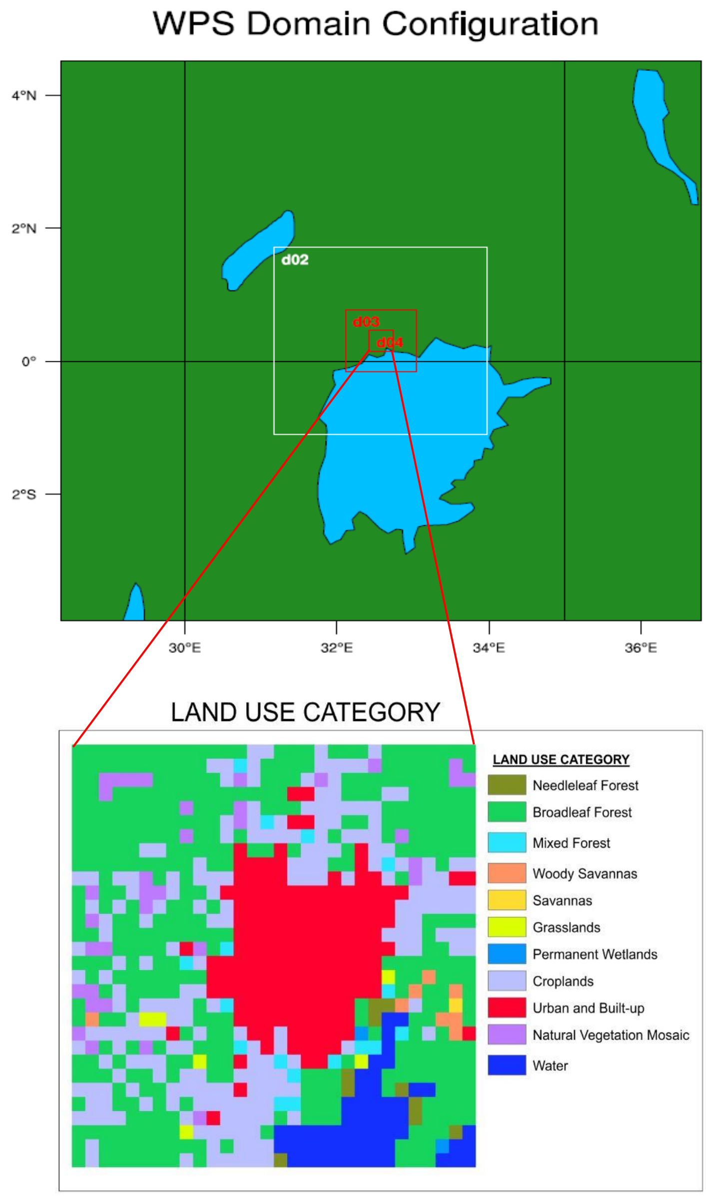

Figure 3.1 Study area: WRF model configuration and the land use category default used in the model.

Kampala is central in all four domains. For each domain, the Mercator projection system is used. For the 25th June 2012 event, the selected MP-CP-PBL parametrization combination was Marrison, Grell Freitas, and ACM2, based on the sensitivity assessment described in chapter 4. These MP, CP, and PBL schemes are used for all domains, while the urban canopy parameterization is only applied for the 1 km domain following the procedure suggested by the WRF model manual. Initial and boundary conditions are retrieved from the ERA5 global Reanalysis Model, with a resolution of 30 km (Hersbach et al., 2020). Following Sun et al. (2015), the static lake surface temperature of Lake Victoria was set to 24°C. The model simulation is carried out for three days from 24th June 00:00 UTC to 26th June 2012 24:00 UTC, which implies that the model starts 24-h prior to the beginning of the rainfall event and stops 24-h after the storm.

3.3.2. Urban canopy model

The urban canopy model is one of the optional parameterization schemes implemented in the WRF model to account for urbanization (Urban fraction) and associated parameters for the meteorological processes through the energy partitioning modelling system. The available WRF urban canopy schemes are the multi-layer urban canopy model (MUCM) (Martilli et al., 2002) and the Single-Layer Urban Canopy Model (SLUCM) (Chen et al., 2011). The MUCMs incorporate building effect parametrization (BEP) and a building energy model (BEM) (Salamanca et al., 2010), which are used to deal with sources and sinks of heat. The SLUCM neglects the variation in building height and density in the model grids and uses only a simplified street canyon (i.e., walls, roof, and roads) geometry to represent urban surfaces. A study by Paul et al. (2018) indicates MUCM better simulates the extreme rainfall amount and its spatial distribution compared to when using SLUCM. However, MUCM requires detailed building data and parameters, which are not easy to be acquired based on the literature reviews or remote sensed information, thus, it's challenging to apply in a data-scarce area like Kampala. Here, we used the Single Layer urban Canopy Model implemented in the WRF model.

The SLUCM parametrization scheme Kusaka et al. (2001); Chen et al. (2011) was used in this study to accommodate the effects of the urban surface on simulated rainfall within the WRF model. This scheme employs a common single-layer street canon representation of urban areas with its numerical framework well-elaborated under Song and Wang (2015). The scheme is simple mainly because it uninvolved the effect of building parameterization (e.g., variation in building height and building density) as in the case of the Multi-Layer urban canopy model (MUCM) Martilli et al. (2002). The single-layer urban canopy model in the WRF is coupled to the NoahMP land surface model through a parameter called "two-dimensional urban fraction (FRC_URB2D)". The NoahMP land surface model handles the grid's non-urban fraction (vegetation cover), while the SLUCM handles the urban fraction. The detailed physics options and parametrization used in the SLUCM are found in (Nunez and Oke, 1977); Skamarock et al. (2005); (Song and Wang, 2015).

The SLUCM requires urban fraction (urban map) and urban parameters linked to the urban fraction for model simulation. As the default urban fraction acquired from the MODIS with all urban extent assigned to a single urban value does not represent a city's true extent and position, we updated the urban fraction based on the satellite-derived urban fraction of Kampala. In this study, the urban land use fraction developed by Perez Molina (2019) that is used for integrated urban flood modelling in Kampala was used. At the same time, the urban parameters linked to the urban fraction were adjusted through a literature review (Brousse et al., 2016; Cai et al., 2018; Oliveros et al., 2019).

The updated urban land use fraction is derived based on the 30-m resolution Landsat image 2016 (Perez Molina, 2019) and is shown in **Figure 3.2**. This adjusted urban fraction is generated using a supervised classification by sorting the satellite image pixels into three major urban land cover categories: Built-up, including buildings and pavements, non-built, and bare soil. These three urban land cover classes are developed as an array of cells, each with an associated fraction of land cover (for built-up, vegetation, and bare soil) and finally, add up to 1, see Perez Molina (2019) for details. As seen in figure 3.2, the urban fraction value is close to 1 in the high-intensity urban areas (i.e., areas around the city center), while in the sub-urban areas, the urban fraction value is close to zero. In general, the higher the intensity of built-up areas (urban fraction 1), the lower the vegetation cover and vice versa. For the WRF modelling, we used the built-up fraction of the Landsat image (**Figure 3.2**) to replace the default urban fraction in the WRF model's preprocessing following a similar procedure Skamarock (2008). The new urban fraction exists at a higher spatial resolution (i.e., 30 m) than the WRF innermost domain cell size, 1 km. To match with the WRF cell size, the new urban fraction cell size is rescaled by using the program in the WRF Preprocessing System (WPS); see user guide Guide (2009).

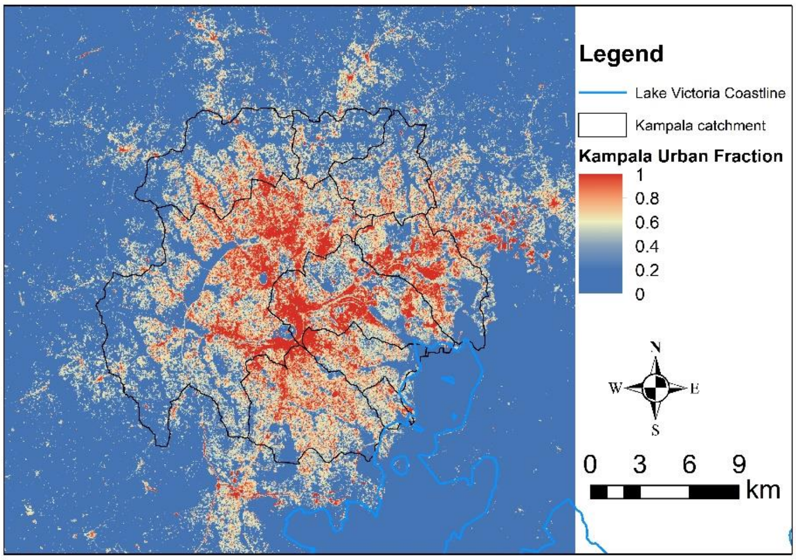

Figure 3.2 Kampala urban fraction as derived from the Landsat image (Pérez-Molina et al., 2017)

3.3.3. *Model simulation*

Three simulations are performed in order to distill the impact of changing urban fractions as well as adjusting urban parameters used in the SLUCM. By default, WPS's geogrid program in the WRF model uses the land use categories based on the Moderate-resolution Imaging Spectroradiometer (MODIS) observational data (Ran et al., 2015). With the WRF version 4 release, the MODIS land use data is updated and available at a resolution of 30 seconds with 20 land use categories (Wang et al., 2018b). This dataset contains the land-cover classification of the international Geosphere-Biosphere programme and is modified for the Noah land surface model (Gilliam and Pleim, 2010). Within this land-use classification, the default urban fraction (base map in the WPS) is represented by the homogeneous urban fraction with all cell values assigned to 0.9 (HIR) (**Figure 3.3**). The default urban parameters dataset that is linked with this default urban fraction is also provided as part of the WPS static data and listed in the URBPARM.TBL file, as shown in **Table 3.2** (second column).

Therefore, the first simulation (hereafter DUF_DUP) uses the default urban fraction with the default urban parameters (**Table 3.2** second column). The second simulation (hereafter DUF_AUP) uses the default urban fraction (**Figure**

3.3) with adjusted urban parameters (**Table 3.2** third column), where values were adjusted based on literature (Loridan and Grimmond, 2012; Wouters et al., 2016; Brousse et al., 2019), as shown in **Table 3.2** (third column).

Table 3.2 Default and adjusted urban parameter values assigned to the urban fraction

Parameter`s Name (unit)	Default urban parameter value	Adjusted urban parameter value
Roof height (m)	7.5	15
Road width (m)	9.8	10
Roof width (m)	9.4	20
Standard deviation of roof height (m)	3	1.5
Albedo (–)		
Roof	0.2	0.1
Wall	0.2	0.1
Road	0.2	0.15
Emissivity (–)		
Roof	0.9	0.85
Wall	0.9	0.9
Road	0.95	0.95
Conductivity of materials (Cal cm^{-1} s^{-1} C^{-1})		
Roof	0.67	0.4
Wall	0.67	1
Road	0.404	0.8
Heat capacity of materials (Cal cm^{-3} C^{-1})		
Roof	1.00E+06	1.20E+06
Wall	1.00E+06	1.20E+06
Road	1.40E+06	1.50E+06
Total thickness of material layers (m)		
Roof	0.05	0.50
Wall	0.05	0.30
Road	0.25	1.00

The third simulation (hereafter SUF_AUP) is with an updated land use fraction based on the Landsat 2016 image, with the adjusted urban parameters. For the SUF_AUP simulation, we have replaced the default homogeneous urban fraction with a heterogeneous urban fraction to define Kampala's more realistic urban representation.

The hypothesis is that adjusting the default urban fraction with the satellite-derived urban fraction would have improved the simulated rainfall's performance over the urbanized catchment than using the default urban fraction. The default urban fraction is homogeneous with an urban fraction value of 0.9 everywhere, which is not the real representation of Kampala city. In reality, Kampala's urban fraction representation is mainly located in the city center, while other locations have lower urban fraction values. The adjusted urban land use fraction is inserted into WRF following the steps of the input data format and processes through the WRF preprocessing system (WPS) (Wang et al., 2007; Guide, 2009). It is worth noting that according to Loridan and Grimmond (2012), the default urban parameter values in WRF, when no information is provided, do not represent urban surfaces of any city, and therefore, it is recommended not to use these values as its. Hence, the possible fourth simulation using the Updated urban fraction with the default urban parameter values is considered redundant in this case study.

3.3.4. Model verification

To evaluate the validity of the simulated rainfall in the innermost domain D04, we used the relative error (RE) index by Tian et al. (2017). Model performance in simulating the event is evaluated using observed rainfall data from two gauging stations and CHIRPS data. The comparison with the two gauging stations is carried out with respect to the gridcell rainfall amount at the station locations. In contrast, the comparison with the CHIRPS was carried out as 24-h accumulated rainfall distribution over the catchment and the area-averaged amount.

The RE index (eq. 3.1) in percentages computes the simulated accumulated 24-h rainfall, S, with respect to observed rainfall at the station location, O. In the case of comparing WRF with CHIRPS data, S and O are the average values of all grids inside the innermost domain of WRF, while in case of 2 stations, the WRF values, S, of gridcell is taken which is located at the rain gauge station, O.

$$RE = \frac{S - O}{O} x100 \text{ -------------------------- } 3.1$$

RE measures the three relative errors of WRF simulated accumulated rainfall at each gauging station and area-averaged with CHIRPS. To measure the overall magnitude of error for each simulation, the average relative error (ARE) of the three evaluation locations is calculated based on the three absolute Res (i.e., REs at two gauging stations and area-averaged).

Additional to RE for all simulations (i.e., DUF_DUP, DUF_AUP, and SUF_AUP), the impact of adjusted model settings on simulated rainfall is evaluated in the form of spatial distribution for objective analysis in two main aspects: maximum rainfall amount and its spatial distribution over the catchment, and time evolution. The event's time evolution over two hours from 11:00 to 12:50 UTC is presented, similar to when the 25th June 2012 observed rainfall event occurred.

3.4. Results

This section presents the impact of the updated urban fraction in the WRF model, including urban parameters on the simulated rainfall in terms of maximum accumulated 24-h rainfall amount and its spatial distribution, and the time evolution of peak rainfall amount distribution over two hours. Three simulations are intercompared as well as compared to the observed rainfall as represented in CHIRPS data and by two rain gauge stations. The evaluation focuses on the HIRE of the 25th June 2012 event that has triggered the flood hazard in the Kampala catchment.

The following section 3.4.1 describes the representation of the satellite-derived urban fraction in the WRF model and its comparison with the default urban fraction. The impact of adjusted urban parameters on the simulated rainfall and the comparisons are presented in sections 3.4.2. and 3.4.3, then followed by discussion and conclusion in sections 3.5 and 3.6.

3.4.1. Representation of the updated urban fraction

The new urban fraction for Kampala is different from the default urban fraction from WPS in two main aspects: (a) the fraction of urbanization and (b) the spatial extent of the city.

(a) Fraction of the urbanization

The urban fraction parameter in WRF defines the percentage of the grid cell covered by the impervious urban facets, while the remaining fraction is treated as a pervious, vegetated surface. Figure 3.3 shows that the default urban fraction of 0.9 is higher than the intensity of the new urban fraction. In the default urban fraction (**Figure 3.3**), the city is represented by a homogeneous high-intensity residential urban fraction (pixels value of 0.9 as represented by red color). This representation is overstretched for a city like Kampala because the urban fraction of 0.9 often represents a high-density residential pixel value, see, for example, Stewart and Oke (2012). Based on the Landsat image classification, the updated urban fraction cells have an average value of 0.64, which realistically represents the low-intensity urban residential category. In the right-sided map, the city center is partly represented by orange color because uninhabitable wetlands (blue areas in **Figure 3.2**) are located next to high-intensity pixels in the LandSat image. Compared to the default urban fraction, the updated urban fraction adds considerable details of the urban fraction. In particular, previously high-density residential areas were replaced by low fraction urban pixel value. Due to the resampling from 30 m Landsat resolution to 1 km WRF resolution, the resulting urban fraction for the city center is around 0.7. The highest urban fraction is (0.9) found on the city's eastern outskirts, where all-terrain is suitable for constructing buildings.

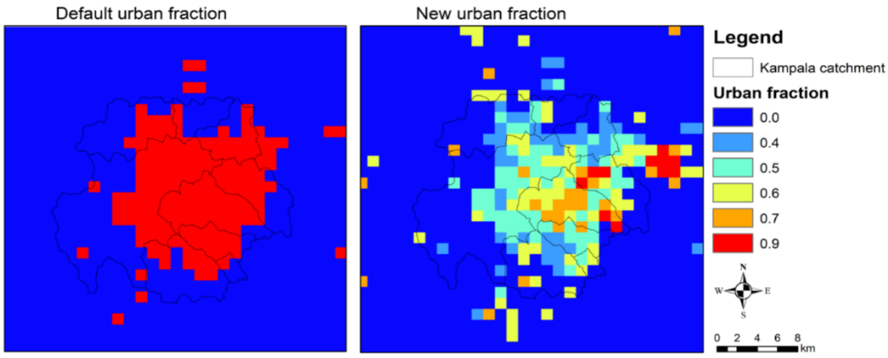

Figure 3.3 The default urban and updated urban fraction representation used for urban simulation. All pixels in the domain d04 of WRF represent 1 km. The default urban fraction (left) is from Noah LSM based on MODIS observation *(Ran et al., 2015),* whereas the updated urban fraction (right) is derived from a Landsat image developed using the cellular automata model (Perez Molina, 2019).

(b) Spatial extent of the city

Another important aspect of the new urban fraction map is its spatial extent, which adds considerable detail to the extent of urban areas in domain d04 compared to the default urban extent. As shown in **Figure 3.3**, the new urban fraction covers a wider area of about 50 pixels more than the default urban fraction. About 40 pixels initially represented by Croplands, and 7 pixels represented by Broadleaf Forest, and the rest with Natural Vegetation mosaics (see **Figure 3.1**) are now classified as an urban fraction. The changes in croplands into the urban fraction are particularly located in the city's eastern and southern parts. In contrast, the change of Broadleaf Forest to the urban fraction is located in the Northern part of the city.

3.4.2. 24-h Cumulative rainfall analysis

This section presents rainfall analysis from DUF_DUP, DUF_AUP, and SUF_AUP simulations and their comparison with the observations.

The spatial distribution of the total 24-h rainfall amount from CHIRPS (Funk et al., 2015) and 3 WRF simulations are shown in **Figure 3.4**. Based on the CHIRPS rainfall, the maximum rainfall accumulations are located to the south-east of the Kampala city catchment along Lake Victoria's coastline with a peak accumulation of 43 mm as indicated by ***X***. It is worth noting that the CHIRPS 24-h rainfall amount at the gauging stations is 30 mm, which is about a half less than the amount at gauging stations.

In the DUF_DUP simulation, the maximum rainfall accumulation (80 mm) is located in the southwest part of the Kampala catchment, as indicated by ***X*** in **Figure 3.4b**. Heavy rainfall above the observed (i.e., 60 mm) extends from Lake Victoria in the south/southeast to the northwest part of the Kampala catchment.

In the DUF_AUP simulation, the accumulated rainfall's spatial distribution follows a similar distribution pattern as the DUF_DUP, except that the peak accumulation is increased (89 mm) as indicated by X ***Figure 3.4c***. Moreover, the cluster of peak accumulation locations moves further to the city's northwest (i.e., peak accumulation is moved to the city's western outskirts, as indicated by ***Y*** in ***Figure 3.4c***).

The spatial rainfall pattern changed in the simulation with the updated urban fraction and its parameters (SUF_AUP). The heavy rainfall is concentrated at the city's center with a peak accumulation of 82 mm, as shown in spot X in ***Figure 3.4d***. The heavy rainfall distribution indicates the cluster of peak rainfall at three different locations (two along the coastline of Lake Victoria and one in the city center).

The results of three WRF simulations, both in terms of maximum accumulated rainfall and its spatial distribution, do not agree with that of CHIRPS rainfall. The insets in figures 4.*3b, c, and d* show the difference plots of the simulation compared to CHIRPS. The difference in accumulated rainfall between the CHIRPS and the DUF_DUP and DUF_AUP simulations is maximum, which is about 17 and 22 mm (*dark yellow color in the insets in the bottom-right corner in* ***Figure 3.4b&c***), respectively, while in the other locations, the difference is negative (*light yellow color*). In the updated urban simulation, the difference in accumulated rainfall between the CHIRPS and the SUF_AUP simulation is 40 mm at the spotted location (*red color in the insets in the bottom-right corner in* ***Figure 3.4d***). The maximum negative difference in the accumulated rainfall of above -60 mm is located in the city center (*dark Blue color*), which indicates that the peak simulated rainfall is off the location compared to that of CHIRPS in all cases.

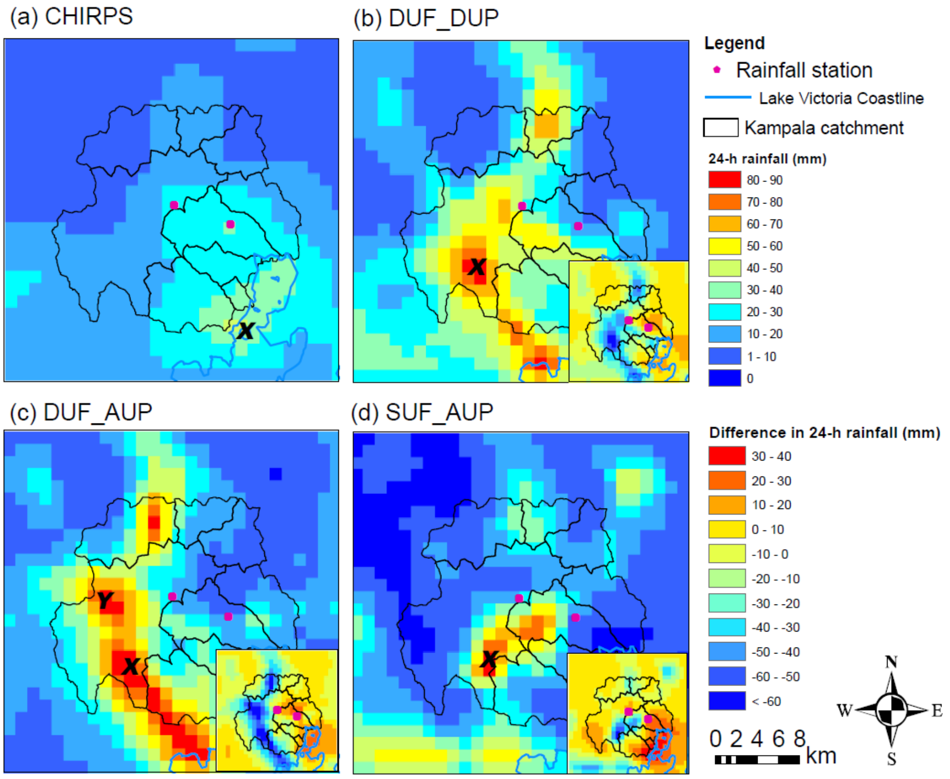

Figure 3.4 24-h accumulated rainfall for (a) CHIRPS, (b) DUF_DUP, (c) DUF_AUP, and (d) SUF_AUP simulations. The insets in the bottom-right corner in (b), (c), and (d) are the difference of the 24-h accumulated rainfall in the DUF_DUP, DUF_AUP, and SUF_AUP simulations from the CHIRPS observation, respectively.

Table 3.2 summarizes the comparison of three WRF simulated gridcell-total accumulated rainfall with the observation at the station locations AWS and GSOD and area-averaged rainfall with that of CHIRPS. As shown in the table, for all three WRF simulations, the simulations underestimate compared to the observed rainfall at rain gauging locations, which is also indicated by RE's large negative values. In contrast, compared to the CHIRPS area-averaged rainfall amount over the innermost WRF domain, all simulations are overestimating.

However, the SUF_AUP simulation performs better with a lower relative error (13 %) compared to the DUF_DUP and DUF_AUP with higher RE of 50 % and 44 %, respectively (**Table 3.2**). Comparing the three simulations using the ARE, the SUF_AUP simulation performs better with a relatively lower absolute error value of 53 %.

Table 3.3 Comparison of WRF rainfall with the station and regridded CHIRPS rainfall for DUF_DUP, DUF_AUP, and SUF_AUP simulations for 25th June 2012 rainfall events in Kampala, Uganda. The areal rainfall amount is the average of all grids in the innermost domain of WRF.

Simulations	Gridcell-rainfall_AWS (mm)			Gridcell-rainfall_GSOD (mm)			Area_averaged rainfall (mm)			ARE
	AWS	WRF	RE (%)	GSOD	WRF	RE (%)	CHIRPS	WRF	RE (%)	ARE (%)
DUF_DUP	66	25	-62	60	13	-78	16	24	+50	63
DUF_AUP	66	16	-75	60	13	-78	16	23	+44	66
SUF_AUP	66	21	-68	60	13	-47	16	18	+13	53

3.4.3. *2-h Cumulative Rainfall analysis*

The WRF model simulations are also examined to understand the event's time evolution over the catchment. **Figure 3.5** shows the cumulative rainfall curves for the observation and three WRF simulations at the AWS location. Based on the Automatic Weather Station data, we know that the 25th June 2012 rainfall event lasted for two hours from 1100 UTC to 1250 UTC (+3 GMT local time). As shown in the figure, compared to observation, storms start a half-hour earlier for SUF_AUP and a half-hour later for DUF_DUP and DUF_AUP simulations. The time to peak (the time at the steepest slope attain) is about an hour after the observation for both StandardWPS and UFD_Parameter simulations, but about three hours for the SUF_AUP simulation. In the SUF_AUP simulation, the station location has experienced the second storm's passage within three hours. The first peak coincides well with the observed event but with a lower rain rate per minute. The second rain rate, which has a higher rain rate per minute, attains its peak an hour after the first event at about 14:00 hour.

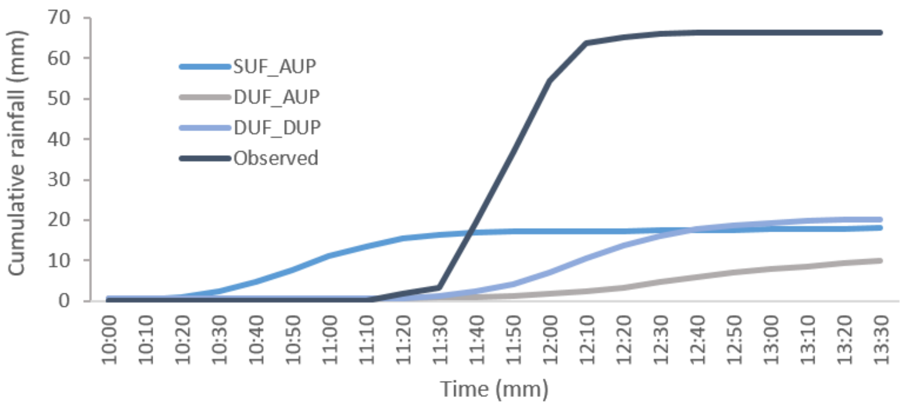

Figure 3.5 *Cumulative rainfall curves for observation and three WRF simulations at the AWS location. Gridcell-rainfall curves for the DUF_DUP, DUF_AUP, and SUF_AUP simulations are shown in two-hour time windows from 11:00 to 12:50, equivalent to the observation at the AWS location.*

The spatial distribution of the 2-hour rainfall over the catchment is also examined, as shown in **Figure 3.6**. In the DUF_DUP simulation in the same period of two hours, the cluster of maximum rainfall accumulation (61 mm) is located to the southeast of the Kampala catchment area (i.e., on the edge of the catchment boundary) and extended further to the north-west of the catchment boundary. In the DUF_AUP simulation, the pattern of rainfall distribution over the catchment is similar to that of the DUF_DUP, but the maximum rainfall accumulation (72 mm) is located in the northwest of the catchment area. In contrast to DUF_DUP, in the SUF_AUP simulation, the rainfall pattern is different, with a single maximum rainfall accumulation (75 mm) located in the city center.

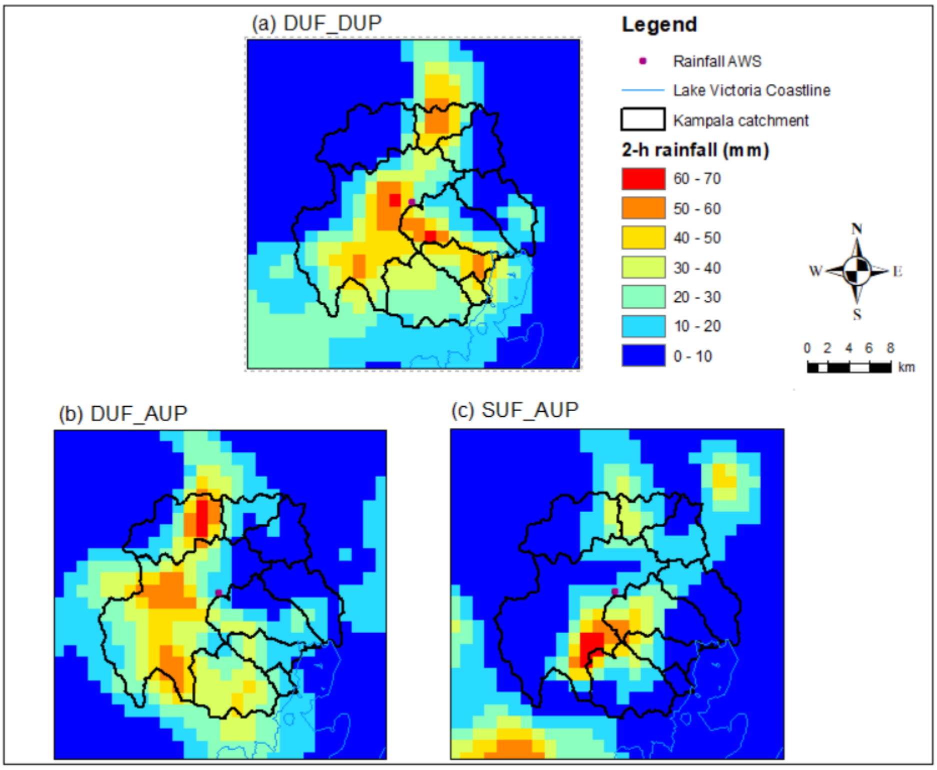

Figure 3.6 2-h accumulated rainfall distribution for model simulations for the period of 11:00 – 12:50 UTC on 25th June 2012 (the same period as the observed rainfall using AWS in Kampala): (a) DUF_DUP, (b) DUF_AUP and (c) SUF_AUP simulations.

Comparison of DUF_AUP and SUF_AUP simulations with the DUF_DUP simulation over the catchment is also presented to analyze the impact of urban setting changes. The difference in accumulated rainfall between the DUF_DUP and the DUF_AUP simulations is about 22 mm (***Figure 3.7a***). The negative difference of above -30 mm is located at the outskirt of the northwest of the Kampala catchment (*dark blue color*). In the case of SUF_AUP simulation, the accumulated rainfall difference with the DUF_DUP simulation is more than 40 mm at several locations, as shown in **Figure 3.7b**. The maximum negative difference of above -30 mm is located in the city center and in the northeast of the catchment (*dark Blue color*), indicating that the location of 2-h peak rainfall when using SUF_AUP simulation is different compared to that of the DUF_DUP simulation.

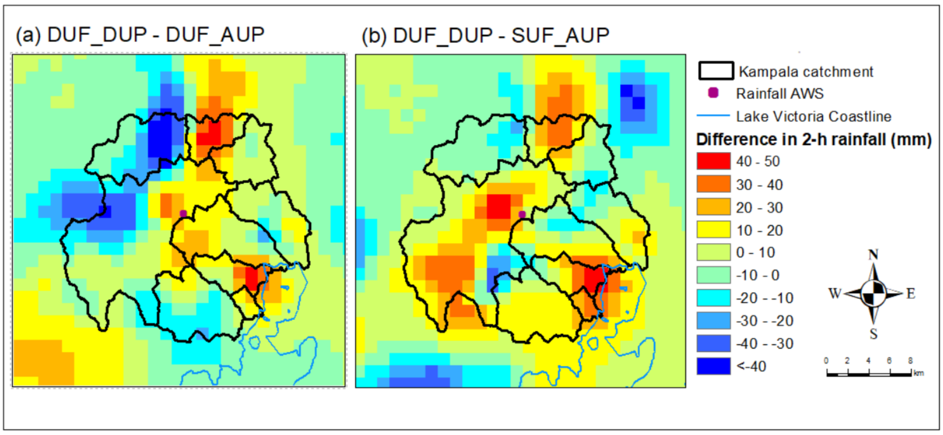

Figure 3.7 2-h accumulated rainfall difference for the period of 11:00 – 12:50 UTC on 25th June 2012 (the same period as the observed rainfall using AWS in Kampala): subtractions of DUF_AUP (a) and SUF_AUP (b) simulations from DUF_DUP simulation.

3.5. *Discussion*

To assess the impact of the updated urban fraction and adjusted urban parameter settings on a flooding triggering rainfall event, three WRF simulations are intercompared as well as compared with observations. It has been well documented that the representation of urban surface modifies temperature/wind profiles and the corresponding moisture transport, which might significantly affect the spatial distribution and amount of rainfall, see for example, (Lei et al., 2008; Ryu et al., 2016); Paul et al. (2018). Moreover, several studies, for example, (Loridan and Grimmond, 2012; Brousse et al., 2019; Dai et al., 2019) indicated that the default urban fraction and the corresponding parameter in the WRF model might incorrectly represent the true extent and values of the urban surfaces for individual cities. Hence, representing the correct urban fraction in the mesoscale atmospheric modelling system is essential for optimal rainfall simulation over the urbanized area. Therefore, this study's emphasis is mainly on the setup of the mesoscale atmospheric modelling system with a more realistic urban fraction and urban parameters for Kampala city. Three different simulations are carried out using the WRF model: DUF_DUP, DUF_AUP, and SUF_AUP simulations to evaluate the impact of WRF rainfall simulation over the city. The simulated rainfall analysis and evaluation focus on the high-intensity, convective rainfall event that has caused urban flood hazards on 25th June 2012, using rain gauge data and CHIRP observations for comparison.

The results of all three simulations indicate that the modelled rainfall is overestimated compared to CHIRPS and underestimated when comparing gridcell values with gauging station records. However, the SUF_AUP simulation shows relatively better results with a lower absolute relative error score compared to the other two simulations. Although the simulated gridcell maximum rainfall amount is overestimated compared to observation in the SUF_AUP simulation, the area-averaged rainfall over the catchment is rather in good agreement with that of CHIRPS. When comparing the overall magnitude of error for each simulation, the SUF_AUP simulation performs better with a lower ARE score of 31%.

The results show that the spatial distribution of the simulated rainfall over the Kampala catchment is influenced by the proper representation of the urban parameters in the WRF model. In the DUF_AUP simulation, the urban surface is represented by the homogeneous urban fraction map and adjusted urban parameters. The simulated rainfall is considerably similar to the DUF_DUP simulation in a pattern, with displacements of the precipitation towards the northwest. Notably, adjusting the urban parameters (see Table 3.2), where most values changed in favor of more heat absorption by buildings during the daytime, is the main factor causing the displacement in the city's simulated rainfall; this is in parity with the find of Patel et al. (2019). Hence, the proper representation of urban parameters becomes vital as they affect the distribution of rainfall accumulation (Li et al., 2013).

Furthermore, in addition to adjusting urban parameters, proper representation of urban fraction in the WRF model strongly influenced the spatial distribution and amount of the simulated event over the city. In the SUF_AUP simulation in which the more realistic map of an urban fraction was used, the peak rainfall amount's spatial location changed compared to DUF_DUP and is located in the city center. Compared to the default MODIS based Noah urban fraction (Ran et al., 2015), the new urban fraction represents the more realistic extent of the city and fraction, which is mainly due to the methodology applied to produce the urban fraction explicitly and also due to the source of the data (Perez Molina, 2019).

Changes in urban parameters and urban fraction alter moisture and energy fluxes as well as the thermodynamic characteristics, which affect the initiation and intensification of convective processes over a city (Paul et al., 2018). In this study, in the default urban fraction, the city is represented by the medium-high intensity urban category, which affects the spatial distribution of peak rainfall accumulation. Besides, adjusting urban parameters with the default urban fraction further enhances the distribution of peak rainfall accumulation. The changes in rainfall can be explained by the diurnal variation in temperature and wind profile; as suggested by Shastri et al. (2015), higher vertical wind velocity and lower surface wind speed promote circulation by converging low-level moisture to more moisture for precipitation. Moreover, urbanization enhances thermal contrast between the city and lake, leading to strong breeze circulation, as Seino et al. (2018) suggested. Consequently, the spatial distribution of the peak rainfall accumulation is further located inland in the DUF_DUP and DUF_AUP simulation cases. In contrast, lowering the urban intensity, as in SUF_AUP, creates less thermal contrast leading to the peak rainfall accumulation concentrated in the city center and close to the coastline. Moreover, a lower urban fraction, as in SUF_AUP, means a lower sensible heat, which affects the planetary boundary layer and atmospheric instability over the city, resulting in a lower rainfall amount than when using DUF_DUP and DUF_AUP simulations. Similar studies (Zhong et al., 2015; Ryu et al., 2016; Paul et al., 2018; Zhang et al., 2018b) support our findings that the presence of urbanization modifies rainfall occurrences, primarily due to changes in the meteorological variables (e.g., fluxes, mass, and momentum).

3.6. Conclusion

The mesoscale WRF model standard representation of the urban areas is often not representative of cities. For Kampala, the urban fraction is adjusted based on satellite information. This chapter analyses the new urban fraction's impact and adjusted urban parameters on the high-intensity rainfall event of 25th June 2012. Three simulations are compared: one with the default WPS settings for urban fraction and its parameters (DUF-DUP), one simulation adjusting only the urban parameters (DUF_AUP), and finally, one implementing the new urban fraction in combination with adjusted urban parameters (SUF_AUP). The peak rainfall and its spatial distribution over the Kampala catchment were evaluated using observed rainfall data from two gauging stations and satellite precipitation dataset CHIRPS.

When considering all three simulations, the WRF model overestimates rainfall compared to the CHIRPS and underestimates compared to gridcell values at gauging stations. The discrepancies between the model simulations and the CHIRPS observations are due to the known limitation of CHIRPS in capturing the maximum rainfall amount. Additionally, due to the absence of a dense urban gauging station network, there is no proper Spatio-temporal record of the rainfall event over the city. Based on the available observations, the SUF_AUP simulation with a more realistic urban fraction and adjusted urban parameters shows relatively better performance with the lowest ARE score compared to the other two simulations. Consequently, SUF_AUP results in a more realistic rainfall simulation compared to when using the default urban fraction.

Overall, this chapter demonstrated that adjusting urban fraction as well as the urban parameters used by the urban canopy model impacts the spatial-temporal distribution of high-intensity rainfall events. An extensive analysis of the wind profiles and heat and moisture fluxes is required to attribute the observed changes in local and regional rainfall patterns in more detail. The results from the SUF_AUP simulation reported in this chapter produced a more realistic rainfall amount and its distribution over the catchment. Therefore, the WRF model configuration with the new urban fraction and urban parameters is used in this thesis.

Chapter 4: Evaluation of the WRF model to simulate a high-intensity rainfall event over Kampala, Uganda

This chapter is published as a peer-reviewed paper:
Yakob Umer, Janneke Ettema, Victor Jetten, Gert-Jan Steeneveld, Reinder Ronda. Evaluation of the WRF model to simulate a high-intensity rainfall event over Kampala, Uganda.
Water **2021**, *13*(6), 873; **https://doi.org/10.3390/w13060873**

Abstract

Simulating high-intensity rainfall events that trigger local floods using a Numerical Weather Prediction model is challenging as rain-bearing systems are highly complex and localized. In this study, we analyze the performance of the Weather Research and Forecasting (WRF) model's capability in simulating a high-intensity rainfall event using a variety of parameterization combinations over the Kampala catchment, Uganda. The study uses the high-intensity rainfall event that caused the local flood hazard on 25 June 2012 as a case study. The model capability to simulate the high-intensity rainfall event is performed for 24 simulations with a different combination of eight microphysics (MP), four cumulus (CP), and three planetary boundary layer (PBL) schemes. The model results are evaluated in terms of the total 24-h rainfall amount and its temporal and spatial distributions over the Kampala catchment using the Technique for Order of Preference by Similarity to Ideal Solution (TOPSIS) analysis. Rainfall observations from two gauging stations and the CHIRPS satellite product served as a benchmark. Based on the TOPSIS analysis, we find that the most successful combination consists of complex microphysics such as the Morrison 2-moment scheme combined with Grell-Freitas (GF) and ACM2 PBL with a good TOPSIS score. However, the WRF performance to simulate a high-intensity rainfall event that has triggered the local flood in parts of the catchment seems weak (i.e., 0.5, where the ideal score is 1). Although there is high spatial variability of the event with the high-intensity rainfall event triggering the localized floods simulated only in a few pockets of the catchment, it is remarkable to see that WRF is capable of producing this kind of event in the neighborhood of Kampala. This study confirms that the capability of the WRF model in producing high-intensity tropical rain events depends on the proper choice of parametrization combinations.
Keywords: *deep convection; high-intensity rainfall event; Kampala; parametrization combinations; TOPSIS; Uganda; WRF model evaluation*

4.1. *Introduction*

Numerical weather prediction (NWP) models are powerful tools in simulating rainfall amount and its spatial and temporal distributions in a hydrological catchment (Li et al., 2017). However, modelling high-intensity rainfall events (henceforth HIRE) that trigger localized floods is challenging as the rain-bearing systems might be highly complex, dynamic, and localized. High-intensity rainfall events that may trigger a localized flood are characterized by high peak rainfall intensity in a short duration (approximately 1-5 hours) and occur in the catchment of 100 km^2 or less (Braud et al., 2016). The occurrence and distributions of the high-intensity rainfall in the catchment are highly convective that can be influenced by the meteorological systems from micro to macroscales. In Equatorial East Africa, these meteorological systems are primarily the Inter-Tropical convergence Zone (ITCZ) (Anyah, 2005) and the land-lake breeze circulation systems controlled by Lake Victoria (Sun et al., 2015). At a local scale, HIREs can be influenced by the local land-surface state, e.g., the position and extent of urban land use (Paul et al., 2018). Therefore, modelling HIREs using NWP models requires a proper consideration of the driving dataset determining the meteorological systems and the urban land use fraction in the model domain.

The Weather Research and Forecasting (WRF) numerical weather prediction model (Powers et al., 2017) has been recognized for simulating the amount and distribution of rainfall required for catchment hydrological applications (e.g., (Flesch and Reuter, 2012; Pennelly et al., 2014; Cassola et al., 2015)). The WRF model is widely praised, particularly for its capability to simulate local-scale rainfall-producing phenomena, e.g., convective systems driven by lake surface temperature, topography, and urbanization (e.g., (Ryu et al., 2016; Paul et al., 2018)). However, the high-intensity rainfall triggering the localized flood event is one of the most challenging variables to handle in NWP because the driving processes are complex and interact at various scales (Davolio et al., 2009). Consequently, the actual rainfall amount and its distribution in time and space required for localized flood modelling are incorrectly simulated in the catchment (Tian et al., 2017; Rodrigo et al., 2018). The WRF model's difficulties in simulating the localized events can be associated with the model sensitivity to initial and boundary conditions, domain size, and parameterization schemes (Liu et al., 2012).

The WRF model`s parameterization schemes and their associated meteorological processes often determine rainfall simulation. Testing all combinations of schemes is often unfeasible in terms of computational time and data storage (Tan, 2010). The sensitivity of certain parameterization combinations for rainfall simulation has been well-documented, for example, (Argüeso et al., 2011; Efstathiou et al., 2013; Sikder and Hossain, 2018). They concluded that the main parameterization schemes and their combination determining the simulated rainfall are microphysics (MP), Cumulus parametrization (CP), and planetary boundary layer (PBL). However, the optimal parameterization combination varies from location to location, depending on the underlying meteorological processes (Liu et al., 2012; Sikder and Hossain, 2016).

The flash floods in Kampala, Uganda's capital and political city, is mainly triggered by HIREs that occur in the two main rainy seasons: a long rainy season from March to May and a short rainy season from October to December and the transition months between the season (Douglas et al., 2008; Sliuzas et al., 2013). The rainfall event on 25th June 2012, which occurred at the cessation of the long rainy season, has caused a substantial flash hazard in the city. This rainfall event is an example of HIRE with a duration of two hours and a peak intensity of over 100 mm/hr, which caused a flood depth of above 1 meter in the flood-prone areas (Umer et al., 2019). However, the lack of sufficient rain gauge data hampers a proper flood hazard assessment, which is vital for city planning. Therefore, it is essential to know whether the WRF model can simulate such an event in the complex climate system of Equatorial East Africa.

Previous WRF studies in the Lake Victoria basin analyzed the model performance on the seasonal and monthly rainfall distribution over the entire basin. For example, (Argent et al., 2015; Otieno et al., 2018) suggested the Betts-Miller-Janjic scheme (BMJ) and Kain-Fritsch (KF) cumulus schemes in combination with WSM5 microphysics and Yonsei University (YSU) Planetary Boundary Layer (PBL) options as suitable schemes for monthly and seasonal rainfall distribution over the Lake Victoria basin. Opio et al. (2020) also suggested the Grell 3D cumulus scheme combined with the SBU-YLin microphysical scheme appropriate for numerical simulations of extreme rainfall in equatorial regions. However, it is difficult to objectively identify the best parameterization combination because each combination ranked differently depending on the validation metric, the observation used model verification, and the model resolution being considered. Nonetheless, no specific papers appear to use WRF over Kampala region to study extreme rainfall associate with deep convection. Our study focused on evaluating the performance of the WRF model in simulating high-intensity rainfall associated with a flood-triggering, convective system over the Kampala catchment. Since the spatial contrast between the city and Lake Victoria in the tropics requires a special configuration, we are one of the first to perform such a widespread model evaluation in terms of parameterization testing. This evaluation is considered essential as the first step towards the application of WRF events for constructing design storms of a given return period, for example, (Shiau, 2003; De Luca and Biondi, 2017), involving rain peak and total rainfall volume, for flood hazard modeling. Toward this, WRF design storms of a given geographical location can be constructed based on a defined threshold. The work here only focuses on simulating and evaluating high-intensity rainfall events as the driver for flood models instead of the flood modeling itself.

This study's main objective is to analyze the performance of parametrization combinations in WRF to simulate the 25 June 2012 HIRE to evaluate the applicability of WRF for urban flood modeling in Kampala. The paper is particularly focused on evaluating WRF performances on the rainfall characteristics (i.e., total rainfall amount, spatial and temporal distributions) that are essential for flood triggering mechanisms. The model's capability in simulating the event is assessed by considering the sensitivity of 24 different simulations as the combinations of eight MP, four CU, and three PBL parameterizations. Recognizing the impact of considering CP in the innermost domain, the result of rainfall amount for each simulation with and without CP is also evaluated. Two specific research questions are: (1) How does the WRF model perform in simulating the HIRE amount and its distributions over the Kampala catchment? (2) What are the optimum MP-CP-PBL parametrization combinations for simulating HIRE for 25 June 2012 over Kampala, Uganda? Finally, a framework for the applicability and usability of the simulated rainfall event for flood modeling in the Kampala urban catchment is presented. The following section describes the study area and data used, model configuration, and verification indices. The study results are reported in Section 3, then followed by discussion and conclusion in Sections 4 and 5, respectively.

4.2. *Materials and Method*

4.2.1. Study area

The study area is Kampala city, the capital and political city of Uganda. Geographically, the city is located on the northern shore of Lake Victoria, and it is characterized by flood-prone wetland areas separating the hills of over 1300 m elevations (**Figure 4.1**). The precipitation climatology of the Lake Victoria basin is characterized by two main rainy seasons: March-May (MAM), known as the long rainy season, and October–December (OND), known as the short rainy season (Kizza et al., 2009). In both seasons, rainfall is primarily controlled by the persistent seasonal migration of the ITCZ and its interactions with the surrounding topography and Lake Victoria (Anyah, 2005). At the mesoscale level, the rain-producing systems are mostly convection systems associated with Lake breeze circulation and the surrounding mountains (Anyah, 2005; Sun et al., 2015). The HIRE in the afternoon of 25th June 2012 caused a substantial flood problem in the city's flood-prone areas. The June event has occurred at the end of the prolonged rainy season, and it can be characterized as a convective system. The common synoptic systems producing June rainfall are (1) moisture-bearing southeasterlies wind coming from a high-pressure ridge in the Southern Indian Ocean; (2) moisture-bearing southwesterly wind generated by the shift of ITCZ that comes from both the Indian ocean and the Congo Basin (Osman and Hastenrath, 1969; Camberlin, 2018).

4.2.2. Observed rainfall data

On June 25, 2012, two rain gauge stations were in operation in Kampala city: Automatic Weather Station (AWS) in the Makerere University recorded at the 10-minute interval and Kampala Central station at a 24-hour interval (**Table 4.1**) with the 24-hour accumulated rainfall of 66.2 and 60 mm, respectively. The observed accumulated 24-hour rainfall event is a typical 1-in-2 year return period event. The 24-hour rainfall data of Kampala central station is collected from the Global Summary of the Day (GSOD) dataset provided by the National Climatic Data Center (NCDC) acquired through the World Meteorological Organization. Both gauge data are used for model performance assessment.

In addition, the satellite estimated rainfall from Climate Hazards Group InfraRed Precipitation with Station data (CHIRPS) (Funk et al., 2015) is retrieved for model evaluation. The CHIRPS observed rainfall data has a 0.05 degree (~5.5km) spatial and daily temporal resolutions. It is one of the best rainfall products for decision-making in East Africa (Cattani et al., 2018; Diem et al., 2019). For the WRF model evaluation, the CHIRPS rainfall data is first rescaled to the D04 grid spacing (see section 2.3), which is 1 km x 1 km, and then extracted for the Kampala catchment (see **Figure 4.1c**). The CHIRPS product shows a maximum rainfall (above 40 mm/day) along the coast of Lake Victoria, while the northern part of the city received lower rainfall of up to 5 mm/day.

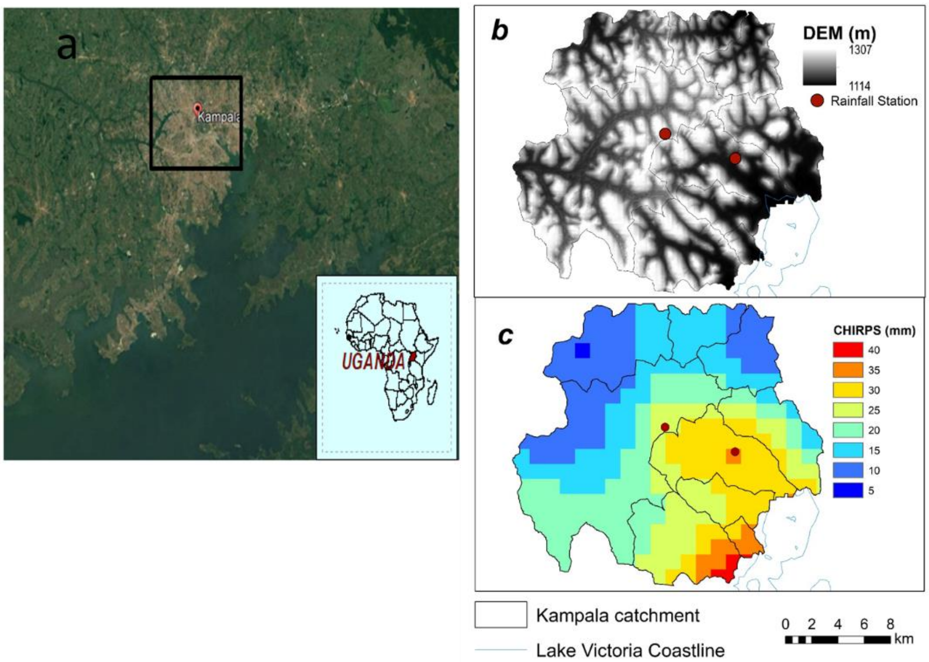

Figure 4.1 Study area and rainfall data used: (a) Location of the study area with google map, (b) Gauging station location and the Digital Elevation map of Kampala city; (c) satellite rainfall estimation based on CHIRPS.

4.3. *WRF model Setting and Configuration*

In this study, the WRF model, version 4 (Wang et al., 2012), was used to study the temporal and spatial distribution of high-intensity rainfall events in Kampala. The WRF model configuration consists of four domains with 27 km, 9 km, 3 km grid spacing as outer domains, and 1 km as the innermost domain (see **Figure 3.1**, section 3.3.1).

The parameterization schemes were designed to solve the sub-grid scale processes that are not explicitly resolved because they are spatially too small but affect the atmospheric state at the resolved scale. The formulation and computation of the currently available parametrizations are designed, tested, and evaluated in a particular region and tuned to work best in a specific atmospheric environment; hence, the model performance may differ from one instance to another. Therefore, it is important to evaluate and verify the applicability and performance of the currently available parametrizations and their combinations for our specific region and atmospheric environment. This study explicitly focused on microphysics, cumulus parametrization, and planetary boundary layer for high-intensity rainfall sensitivity analysis. For all simulations during sensitivity analysis, the effect of urban canopy parameterization on high-intensity rainfall is considered.

Table 4.1 WRF parametrization schemes used in the current study

Physics options	Naming	Description of parametrization schemes
	WSM 3	WRF Single Moment 3-class scheme (Hong et al., 2004)
Microphysics scheme (MP)	WSM 5*	WRF Single Moment 5-class scheme (Hong et al., 2004)
	WSM 6	WRF Single Moment 6-class scheme (Hong and Lim, 2006)
	EF*	The Eta Ferrier scheme (Ryan, 1996)
	T*	Thomson et al. double moment scheme (Thompson et al., 2008)
	M2	Morrison et al. 2-Moments scheme (Morrison et al., 2009)
	WDM 5*	WRF Double Moment 5-class scheme (Lim and Hong, 2010)
	WDM 6	WRF Double Moment 6-class scheme (Lim and Hong, 2010)
Cumulus parametrization (CP)	KF	Kain-Fritsch (new Eta) scheme (Kain, 2004)
	BMJ	Betts-Miller-Janjic scheme (Janjić, 2000)
	GF	Grell-Freitas ensemble scheme (Grell and Freitas, 2014)
	G3D*	Grell 3D ensemble scheme (Grell and Dévényi, 2002)
Planetary Boundary Layer (PBL)	YSU	Yonsei University PBL (Hong et al., 2006)
	ACM2	Asymmetrical Convective Model version 2 PBL (Pleim, 2007)
	BL	Bougeault-Lacarrere PBL (Bougeault and Lacarrere, 1989)
Radiation-Shortwave	Dudhia	Dudhia Shortwave scheme (Dudhia, 1989)
Radiation-Longwave	RRTM	Rapid Radiative Transfer Model Longwave (Mlawer et al., 1997)
Land Surface model	NoahMP	Unified Noah land-surface model (Niu et al., 2011)
Surface Layer	SF_SFCLAY	Revised MM5 Monin-Obukhov scheme (Jiménez et al., 2012)
Urban Physics	SLUCM	Single-layer urban Canopy Model (Kusaka et al., 2001)

not included in 24 MP-CP-PBL combinations

4.3.1. Microphysics

The cloud microphysics Scheme is the process by which the evolution of the hydrometeor particle size distribution is predicted. The WRF model used the bulk microphysics parametrization to predict the transport, physical change, and thermodynamic effects of the total hydrometeor population in clouds, either liquid or frozen or a mixture of both. Hydrometeors in a bulk microphysics parametrization are described by one or more physical characteristics of the particles (such as mass and number densities). Their processes depend on the definition of source-sink terms in their prognostic equation. This transport equation is derived from a spectral balance equation for the hydrometeor size distribution function using the method of moments (Beheng, 2010). The WRF bulk microphysics parametrization is either a single-moment if the scheme includes prognostic equations to predict the mass or a multi-moment scheme if the schemes include prognostic equations to predict both mass and number densities. The complexity of these schemes varies in formulations from the single moment (e.g., WSM families (Hong et al., 2004)) to two-moment schemes (e.g., Morrison (Morrison et al., 2005; Morrison et al., 2009; Morrison and Milbrandt, 2010)). The sensitivity experiments of these schemes have been evaluated to simulate high-intensity and extreme rainfall events (Argüeso et al., 2011; Sikder and Hossain, 2016). In this thesis, we used all available microphysics schemes (hereafter MP) in the WRF model and combined with cumulus schemes and PBL to evaluate the performance of the combinations in simulating (HIRE) triggering the localized flood in the urban catchment (see **Table 4.1**).

4.3.2. Cumulus parametrization

Cumulus parametrization (CP) in the WRF model is the process to represent the collective effect of the sub-grid scale clouds, which cannot be resolved explicitly. The consideration of cumulus parametrization in the WRF model resolves sub-grid scale vertical fluxes and rainfall due to convective clouds. It hence plays an important role in regulating the pattern and distribution of the simulated rainfall events (Jeworrek et al., 2019). Different cumulus parametrizations have different techniques to resolve subgrid-scale processes regarding condensation in the updraft, evaporation in the downdraft, cooling due to the evaporation of falling rain below the cloud base, turbulent mixing at the cloud edge with the environment, entrainment, detrainment, and subsidence compensation in the boundary layer. Some schemes use a simple cloud model with updrafts and downdrafts, including the effects of detrainment and entrainment with a cloud model based on a mass flux formulation and removal of CAPE (Convective available potential energy), for example, the Kain and Fritsch scheme (KF) (Kain, 2004). Other convective schemes are adjustment type schemes, for instance, the Betts–Miller scheme (BM) (Betts and Miller, 1993), where vertical profiles of temperature and humidity are adjusted until stability is achieved. The CP used in the thesis is listed in **Table 4.1**.

4.3.3. Planetary Boundary Layer

A planetary boundary layer (PBL) is a column of the atmosphere in which the exchanges of essential phenomenon for cloud development and precipitation such as moisture, heat, and momentum occur through mixing associated with turbulent eddies. The turbulent eddies, which are often happening in the lower-tropospheric layer of the atmosphere, determine the evolution of the thermodynamic elements. The scales at which the turbulent eddies operated are too small to be explicitly represented in the mesoscale NWP models. Thus, their effects are expressed in these models via the use of PBL parameterizations. The theoretical development and formulation of PBL have been focused on profiles of mean and parameterized flux (Pleim, 2007; Stensrud, 2009). In this thesis, all PBL types available in the WRF model catalog have been considered, as shown in **Table 4.1**.

4.3.4. Other model parameterization schemes

Other model parameterization schemes used in this research, which include the Radiation schemes, land surface schemes, and surface layer schemes, are also described in **Table 4.1**. For this study, the Dudhia and Rapid Radiative Transfer Model (RRTM) schemes are selected for shortwave and longwave radiation parameterization, respectively. The RRTM scheme incorporates the detailed absorption spectrum effects, considering water vapor, carbon dioxide, and ozone. It is combined with the cloud-radiation shortwave scheme and interacts with the model cloud and precipitation fields (Mlawer et al., 1997). Dudhia scheme (Dudhia, 1989) is sophisticated enough to account for long-wave and short-wave interactions with explicit cloud and clear-air. It also provides surface long and short wave fluxes without calling surface radiation fluxes.

In this study, the land surface scheme, which determines the hydrologic and atmospheric processes that take place at the interface between the earth surface and the atmosphere, such as infiltration and evaporation processes, are determined by using the Unified Noah land-surface model (Noah) MP (Niu et al., 2011). These land surface processes have scales much smaller than the horizontal resolution of mesoscale atmospheric models. The schemes that simulate the average areal behavior of land surface processes over a computational grid of the mesoscale atmospheric model are called land surface parameterization schemes. They mainly provide ground temperature as an output, which is calculated by sensible heat, latent heat, radiative fluxes, and surface layer atmospheric properties. Surface moisture availability, sub-soil temperature, and moisture profiles can also be provided. In the case of the surface layer scheme, the revised MM5 Monin-Obukhov similarity theory is used for calculating surface heat and moisture fluxes (Jiménez et al., 2012).

4.4. Model evaluation

To quantify the spatiotemporal performance of the simulated rainfall in the innermost domain, d04, the relative error (RE) index by (Tian et al., 2017) and 2D verification indices by (Liu et al., 2012) are used (**Table 4.1**). The evaluation is carried out for one day focusing only on June 25, 2012, using 10-minute time series of observed and accumulated 24-hour satellite-based rainfall data. The RE index was used to evaluate the performance of the 24-hour accumulated area-averaged rainfall over the Kampala catchment, as indicated in **Figure 4.1b**. The 2D verification indices were used to evaluate the simulated rainfall's spatial and temporal distribution on 10-minute and 24-hour periods. The temporal distribution was evaluated by using the continuous 2D verification indices against 10-minute data from the AWS, while for the spatial distribution, the categorical and continuous 2D verification indices were evaluated against 24-hour accumulated rainfall data from the two gauging stations and CHIRPS. We used the multi-criteria decision technique named TOPSIS by (Sikder and Hossain, 2016) to choose the likely optimum parametrization combinations. In this study, the TOPSIS analysis is based on the RE index's rescaled error scores and 2D verification indices. It is noteworthy that although 24-hour model results evaluation is not a suitable time scale to represent flash floods, since the observational dataset (i.e., CHIRPS and rainfall data Kampala central station) is available on a daily time scale, the model performance of the actual rainfall amount and its spatial distribution is evaluated at a daily time step.

The parametrization combinations selected based on TOPSIS criteria intended to represent the best WRF MP-CP-PBL combinations used to simulate the high-intensity rainfall event triggering the localized flood over the Kampala catchment. However, the usability of the selected combinations for the localized flood modelling can be different depending on whether we are aiming for the actual or potential flood modelling. Actual flood modelling requires spatially moving rainfall in the catchment as input to a hydrologic model. Potential flood modelling requires a representative homogeneous rainfall as a design for a chosen return period as input to a hydrologic model. At the end of this study, the applicability and usability of the best likely parametrization combinations for both flood modelling will be discussed.

4.4.1. Relative Error index (RE)

The relative error index in percentages (RE) computes the simulated accumulated 24-hour rainfall, S, with respect to the CHIRPS observed values, O (equation 1 in **Table 4.2**). In the equation, S and O are the average values of all the grids inside the Kampala catchment. For areal calculation, CHIRPS rainfall, which is originally at 5.5 km resolution, was first resampled to the D04-domain of WRF (1 km) spatial resolution and then extracted for the Kampala catchment.

4.4.2. 2D verification indices

The temporal performance of WRF was evaluated using three continuous 2D indices: the Root Mean Square Error (RMSE), the Mean Bias Error (MBE), and Standard Deviation (SD) (equations 2 - 4 in **Table 4.2**). These three indices are computed using the automatic weather station data, Oi, where n is the number of time steps 144 (10-minute time step for one-day simulation). The simulated time series data, Si, are the values of the 24 WRF simulations extracted at the automatic weather station location. For RMSE and SD, the calculated values range between 0 - ∞, while for MBE, the values can vary between -∞ - ∞.

Table 4.2 Types of indices and their equations used for WRF simulated rainfall evaluation

Indices type	Formula	Perfect score	Remark
(1) Percentage Relative Error (RE%)	$\frac{S-O}{O}x100$	0	RE%-calculated using catchment areal 24-hour rainfall of WRF simulated and CHIRPS estimation; measures the relative error of WRF simulated accumulated areal catchment rainfall compared to CHIRPS
2D continuous indices			***Used for spatial distribution verification when an accumulated rainfall is used and temporal distribution verification when time series rainfall data is used***
(2) Root Mean Square Error (RMSE)	$\sqrt{\frac{1}{n}\sum_{i=1}^{n}(Si-Oi)^2}$	0	RMSE-measures the average magnitude error of the WRF simulated rainfall corresponding to the observed rainfall; does not indicate the direction of the deviations.
(3) Mean Bias Error (MBE)	$\frac{1}{n}\sum_{i=1}^{n}(Si-Oi)$	0	MBE- measures the average cumulative error of the WRF simulated rainfall but does not show the correspondence between the simulation and observation. It also shows the direction of the error whether its negative or positive
(4) Standard Deviation (SD)	$\sqrt{\frac{1}{n-1}\sum_{i=1}^{n}(Si-Oi-MBE)^2}$	0	SD-measures the variation of the overall magnitude of the simulation error due to MBE
2D Categorical Indices			***Used for spatial verification of WRF simulated total rainfall amount with respect to CHIRPS estimates at grid level***
(5) Probability of detection (POD)	$\frac{RR}{RR+NR}$	1	POD-Indicate what grid rainfall correctly simulated compared the CHIRPS grid rainfall. Sensitivity to the frequency of rainfall occurrence during the event; ignores false alarms.
(6) Frequency bias index (FBI)	$\frac{RR+RN}{RR+NR}$	1	FBI-Indicates the tendency of overestimation (FBI > 1) or underestimation (FBI < 1) of WRF simulated rainfall occurrence
(7) False alarm ratio (FAR)	$\frac{RN}{RR+RN}$	0	FAR-Indicates the grids of the WRF simulated rainfall that have no rainfall compared to the CHIRPS grids. It ignores the misses and sensitive to the frequency of rainfall occurrence during the event
(8) Critical success index (CSI)	$\frac{RR}{RR+RN+NR}$	1	CSI-Indicates how the grids rainfall simulated by WRF corresponds to the CHIRPS estimates. It penalizes both misses and false alarms and sensitive to hits

The performance of WRF in the spatial dimension ware evaluated using the same three 2D continuous indices (equations 2 - 4, **Table 4.2**) and four 2D categorical indices (equations 5 - 8, **Table 4.2**). Note that 2D categorical indices will only use in space, not in time. In the spatial dimension, Si and Oi indicate the simulated and observed 24-hour accumulated rainfall amount. The observed 24-hour rainfall amount is based on two gauging stations (n = 2; AWS and Kampala Central), and the simulated values of the 24 WRF simulations were extracted at these two gauging locations. The four 2D categorical indices proposed by (Davis et al., 2009) were used in combination with the rescaled CHIRPS rainfall data. These verification indices are chosen as the probability of detection (POD), the frequency bias index (FBI), the false alarm ratio (FAR), and the critical success index (CSI). Their calculations check on the agreement between WRF and

CHIRPS per grid cell, using the contingency table shown in **Table 4.3**. Since our interest is in evaluating the simulated HIRE, these indices' threshold is considered 25% of the maximum rainfall amount. The calculated values for POD, FAR, and CSI range between zero and one, whereas FBI values range from 0 - ∞.

Table 4.3 Contingency table of WRF simulation against CHIRPS rainfall estimates

WRF/CHIRPS	$Rain_{CHIRPS}$	No rain
$Rain_{WRF}$	RR (hits)	RN (false alarm)
No rain	NR (miss)	NN (correct negative)

4.4.3. *Technique for Order of Preference by Similarity to Ideal Solution*

To select the likely optimum parametrization combinations that represent the overall best model performance for the rainfall event, we used a multi-criteria decision analysis technique using the relative closeness to the ideal solution proposed by (Sikder and Hossain, 2016; Stergiou et al., 2017; Sikder and Hossain, 2018). It is called the Technique for Order of Preference by Similarity to Ideal Solution (TOPSIS) Relative closeness Value (RCV). For the TOPSIS RCV calculation, we used the scores of RE, the 2D continuous, and 2D categorical indices. Based on these indices, we have a set of 11 criteria for each of the 24 MP-CP-PBL simulations (3 for the temporal dimension, i.e., MBE, RMSE, and SD; 7 for the spatial dimension, i.e., MBE, RMSE, SD, POD, FBI, FAR and CSI; and RE). To compute TOPSIS RCV, first, the calculated indices have to be rescaled (Sikder and Hossain, 2018) (**Table 4.4**). The rescaled values are related to the original error by defining the threshold values based on the original indices' minimum and maximum values. As some 2D verification indices are computed for both spatial and temporal dimensions, the subscript "r" represents generally rescaled, whereas 'rs' and 'rt' represent rescaled for spatial and temporal dimensions, respectively. All rescaled values range from 0 to 1, 0 represents the worst, and 1 represents the perfect score.

The overall model performance in the temporal dimension is calculated by using a single score, the so-called "Temporal Extent Score (TES), which is calculated as the weighted average of the values of three re-scaled 2D continuous indices (Equation (4.9)). The model performance in the spatial dimension is computed by using a single score, the so-called "Spatial Extent Score (SES)," which is calculated by taking the weighted average of the re-scaled spatial 2D categorical and 2D continuous indices; see equation (4.10).

$$TES = \frac{RMSErt+MBErt+SDrt}{3} \quad (4.9)$$

$$SES = \frac{PODrs+FBIrs+FARrs+CSIrs+RMSErs+MBErs+SDrs}{7} \quad (4.10)$$

The overall model performance in both dimensions is calculated with the so-called Unified Score (US), which is the weighted average of all 11 rescaled error indices, including the RE index, see equation (4.11). A higher unified score represents a better overall model performance in the catchment boundary.

$$US = \frac{REr + PODrs + FBIrs + FARrs + CSIrs + RMSErs + MBErs + SDrs + RMSErt + MBErt + SDrt}{11} \quad (4.11)$$

Table 4.4 Rescaled indices from the original error indices

Rescaled Error indices	Threshold
POD_{rs} = POD	
FBI_{rs} = (FBI_{max} - FBI); when FBI>1	
FBI_{rs} = FBI; when FBI<1	
FAR_{rs} = 1 - FAR	
CSI_{rs} = CSI	
REr = (1-RE/REmin); when RE<0	REmin=-0.89
$RMSE_{rt}$ = (1-RMSE/$RMSE_{max}$)	$RMSE_{max}$=4
MBE_{rt} = 1-MBE/MBE_{max}; when MBE>0	MBE_{max} = 0.5
MBE_{rt} = 1-MBE/MBE_{min}; when MBE<0	MBE_{min} = -0.5
SD_{rt} = (1-SD/Sd_{max})	Sd_{max}=4
$RMSE_{rs}$ = (1-RMSE/$RMSE_{max}$)	$RMSE_{max}$=61
MBE_{rs} = 1-MBE/MBE_{max}; when MBE>0	MBE_{max} = 61
MBE_{rs} = 1-MBE/MBE_{min}; when MBE<0	MBE_{min} = -61
SD_{rs} = (1-SD/Sd_{max})	Sd_{max}=52

The threshold values for RMSEmax, RMSEmin, MBEmax, MBEmin, SDmax, and SDmin are in mm

4.5. Results

For evaluating the WRF simulated rainfall event over the Kampala catchment, both the cumulative rainfall and its temporal and spatial distributions are equally important (**Table 4.2**). The three unified scores were computed based on the rescaled values of RE and 2D verification schemes (eq.9-11).

4.5.1. WRF performance of accumulated 24-hour rainfall

To evaluate the performance of WRF in simulating accumulated 24-hour rainfall, we compared the area-averaged 24-hour rain over the catchment from the 24 WRF simulations with the CHIRPS rainfall using the relative error (eq.1, **Table 4.5**). As the perfect score of RE is zero, lower RE values indicate a close simulation of rainfall to CHIRPS. The best performing combination for the event simulation in the catchment is M2-GF-ACM2, with an RE value of -2.4%. Next, the combinations WSM6-KF-BL and M2-KF-BL perform significantly better than the other combinations with RE scores of -39.9% and -47.0%, respectively. WSM3-KF-YSU is the least performing with a RE value of -89.3%. All 24 WRF simulations have a negative RE (%), which indicates an underestimation of the WRF simulated rainfall compared to CHIRPS estimates.

Table 4.5 WRF Performance evaluation of 11 indices and their scores for 24 MP-CP-PBL combinations; Underlined indicates the top 3 simulations for each index; bold indicates the least performing combination.

Combinations	Areal amount		Temporal Dimension			Spatial dimension indices						
						Contineous			Categorical			
	Areal (mm)	RE (%)	MBE (mm)	RMSE (mm)	SD(mm)	MBE (mm)	RMSE (mm)	SD (mm)	POD	FBI	FAR	CSI
CHIRPS	16.8											
M2-GF-ACM2	16.4	-2.4	0.44	**3.82**	2.56	3.39	12.37	16.99	0.35	0.41	0.14	0.33
WSM6-KF-BL	10.1	-39.9	0.20	2.86	**2.87**	-31.43	31.50	2.99	0.30	0.40	0.25	0.27
M2-KF-BL	8.9	-47.0	-0.34	2.68	2.67	-48.56	48.56	0.16	0.20	0.23	0.13	0.19
WSM3-GF-ACM2	6.7	-60.1	-0.33	2.54	2.53	-48.94	48.96	2.22	0.30	0.60	0.49	0.23
WSM3-KF-BL	6.3	-62.5	-0.19	2.89	2.65	-9.14	20.11	**25.34**	0.20	0.33	0.13	0.18
WSM6-GF-YSU	5.7	-66.1	-0.45	2.59	2.56	-50.24	52.28	20.44	0.24	0.32	0.23	0.23
M2-GF-BL	5.6	-66.7	-0.33	2.56	2.55	-49.55	49.58	2.35	0.35	0.38	0.08	0.34
M2-GF-YSU	5.2	-69.0	-0.42	2.57	2.54	-57.80	57.86	3.80	0.30	0.31	0.02	0.30
WSM6-GF-ACM2	4.3	-74.4	-0.32	2.30	2.28	-49.60	49.68	4.05	0.40	0.43	0.07	0.39
WDM6-KF-YSU	3.9	-76.8	-0.30	2.60	2.60	-49.88	50.33	9.45	0.20	0.20	0.00	0.20
WDM6-BMJ-ACM2	3.5	-79.2	-0.38	2.64	2.62	-54.40	54.40	1.17	0.18	0.18	0.00	0.18
WDM6-GF-BL	3.5	-79.2	-0.37	2.66	2.64	-45.89	46.50	10.63	0.13	0.16	0.15	0.13
WSM6-BMJ-BL	3.5	-79.2	-0.39	2.61	2.59	-54.40	54.41	1.53	0.25	0.29	0.12	0.25
WSM3-BMJ-YSU	3.4	-79.8	-0.36	2.66	2.64	-49.84	49.91	3.73	0.38	0.43	0.11	0.36
WSM3-BMJ-BL	3.3	-80.4	-0.43	2.58	2.55	-56.00	56.39	9.32	0.36	0.43	0.15	0.34
M2-KF-YSU	2.9	-82.7	-0.42	2.58	2.55	-59.70	59.71	1.40	0.12	0.14	0.16	0.11
WDM6-GF-YSU	2.9	-82.7	-0.21	2.30	2.30	-40.70	42.18	15.67	**0.05**	**0.12**	0.56	**0.05**
WDM6-GF-ACM2	2.6	-84.5	-0.38	2.38	2.36	-56.46	56.50	2.85	0.13	0.40	**0.68**	0.10
WSM3-GF-YSU	2.5	-85.1	**-0.44**	2.60	2.57	**-60.73**	**60.78**	3.44	0.15	0.30	0.52	0.14
WSM6-KF-YSU	2.4	-85.7	-0.37	2.67	2.66	-55.89	55.99	4.67	0.13	0.28	0.53	0.12
WDM6-BMJ-BL	2.3	-86.3	-0.42	2.61	2.59	-57.92	57.95	2.75	0.13	0.31	0.59	0.11
WDM6-KF-BL	2.2	-86.9	-0.43	2.53	2.51	-53.60	54.26	11.96	0.16	0.16	0.01	0.16
WSM6-BMJ-YSU	2.1	-87.5	-0.41	2.62	2.59	-53.84	54.03	6.37	0.31	0.44	0.29	0.28
WSM3-KF-YSU	1.8	**-89.3**	-0.35	2.73	2.72	-54.81	55.04	7.18	0.11	0.20	0.42	0.11

4.5.2. *WRF performance in the temporal dimension*

To evaluate the temporal performance of the WRF model, we used the three 2D continuous indices (eq.2-4, **Table 4.2**) and the TES score (eq. 9) to compare rainfall time-series from the WRF simulations with AWS at 10-minute resolution (**Table 4.5** and **Figure 4.3**). For all the three indices (i.e., RMSE, MBE, and SD), the lower the error scores, the better the WRF model performs. The MBE values vary between -0.19 mm (best) to -0.45 mm (worst) (see **Table 4.5** and the bar in blue color, **Figure 4.2**). The best combinations for temporal rainfall distribution simulation, according to MBE, are WSM3-KF-BL, WSM6-KF-BL, and WDM6-GF-YSU, with values between -0.19 mm and -0.21 mm, respectively. As shown in the figure, MBE values for all combinations are negative, except for the M2-GF-ACM2 combination (0.44 mm), which suggests that WRF is generally underestimating the simulated rainfall amount in time. As shown in the figure, the lowest values for SD and RMSE are found when using WDM6-GF-YSU and WSM6-GF-ACM2. The least performing combination for RMSE is M2-GF-ACM2 (3.82 mm) and WSM6-KF-BL (2.87 mm) for SD, which means the timing of the rain is different, corresponding to the observation. Unlike MBE, for both RMSE and SD, the error's magnitude is higher when the difference between the simulated and the observed rainfall is higher. Other combinations also perform reasonably, with the error scores varying between -0.2 mm to -0.44 mm for MBE, 2.5 to 3 mm for RMSE, and 2.4 to 2.9 mm for SD.

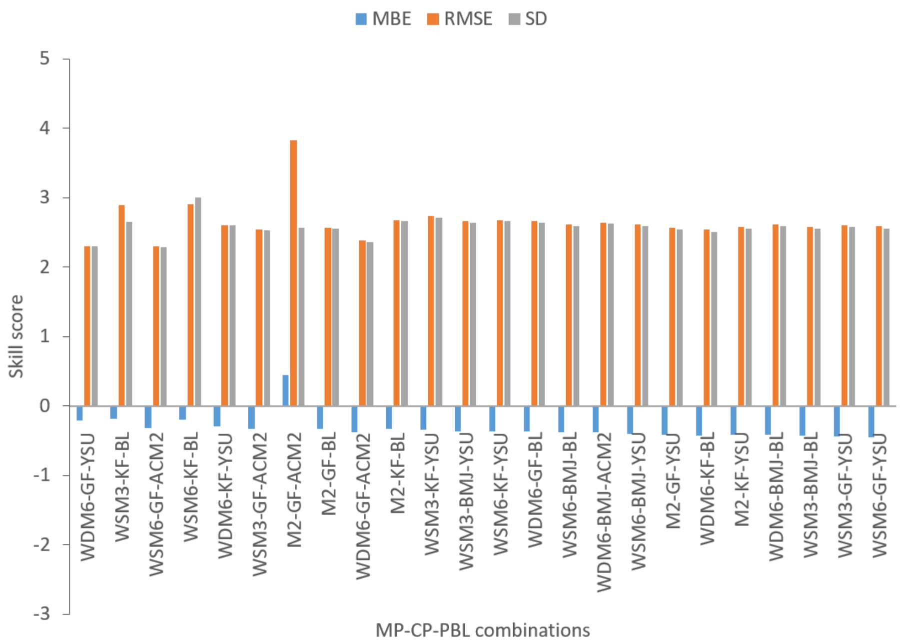

Figure 4.2 Performance of WRF simulated rainfall in the temporal dimension for 24 MP-CP-PBL combinations at AWS location (each bar represents one simulation per 2D evaluation results).

4.5.3. WRF performance in the spatial dimension

To evaluate the performance of WRF simulated rainfall in the spatial dimension, we used three 2D continuous (eq. 2-4, **Table 4.2**) and four categorical indices (eq.5-8, **Table 4.2**). The 2D continuous indices give the WRF performance with respect to the observed cumulative rainfall amount at the two gauging stations, while the 2D categorical indices provide information about the grid rainfall distribution compared to CHIRPS. **Figure 4.3a** and **Table 4.5** show the results for the 2D continuous indices. The MBE best-performing combinations are M2-GF-ACM2, WSM3-KF-BL, and WSM6-KF-BL with values of 3.4 mm, -9.1 mm, and -31.4 mm, respectively. The MBE score's negative sign indicates that the simulated 24-hour rainfall is underestimated compared to the observation, except for M2-GF-ACM2. Like MBE, the best performing combinations according to RMSE are M2-GF-ACM2, WSM3-KF-BL, and WSM6-KF-BL with values of 12.4 mm, 20.1 mm, and 31.5 mm, respectively. The least performing combination is WSM3-GF-YSU, with a higher RMSE score of 60.8 mm, which means the simulated rainfall amount is incorrectly placed compared to the two gauging stations. For the SD index, M2-KF-BL, WDM6-BMJ-ACM2, and M2-KF-YSU combinations perform best with an error score of 0.16 mm, 1.2 mm, and 1.4 mm, respectively. The lower values of RMSE and SD mean that the spatial distribution of the simulated rainfall amount is correctly simulated corresponding to the two gauging stations, while high RMSE and SD indicate displacement in the space of the simulated rainfall.

The error scores for MBE, which is more representative of the total rainfall amount error, are much lower than that of RMSE and SD. The lower MBE score but larger RMSE and SD mean that the rain bringing systems are both scattered and displaced. For instance, when using M2-GF-BL, three clusters of events with a maximum rainfall amount and its intensity in the range of the observation are placed at the distance of 12 km, 6 km, and 15 toward South-East, West, and North-West of the catchment boundary, respectively. Similarly, when using WSM6-GF-ACM2, HIRE with a rainfall intensity equivalent to the observation is simulated outside the catchment boundary along the coast of Lake Victoria (see **Figure 4.6**).

Figure 4.3b and **Table 4.5** show the results of four 2D categorical indices. A higher score for POD, FBI, and CSI, together with a lower FAR score, indicates a better WRF model spatial performance than the CHIRPS rainfall. The FBI index for all combinations is below 1, meaning that the WRF model underestimates the spatial dimension compared with the CHIRPS rainfall. The combination WSM3-GF-ACM2 outperforms the others with an FBI value of 0.60. POD and CSI produce the same top 3 combinations as for MBE and RMSE, i.e., WSM3-BMJ-YSU, WSM6-GF-ACM2, and WSM3-BMJ-BL, which are also scoring high on the FBI index. The least performing combination for these three indices is WDM6-GF-YSU. The fourth categorical index, the FAR index, shows a different top 3 with a perfect score of 0.00 for the combinations of WDM6-KF-YSU and WDM6-BMJ-ACM2 and a near-perfect score of 0.01 for WDM6-KF-BL.

All combinations show a relatively low POD score together with a high FAR score, which indicates that WRF spatial rainfall distribution was only to a limited degree in accordance with CHIRPS rainfall. Also, CSI's skill scores are low; for instance, the skill scores for WDM6-GF-ACM2 and M2-KF-YSU are 0.10 and 0.11, where the perfect score is 1, indicating that the simulated rainfall falls in the wrong locations compared to CHIRPS.

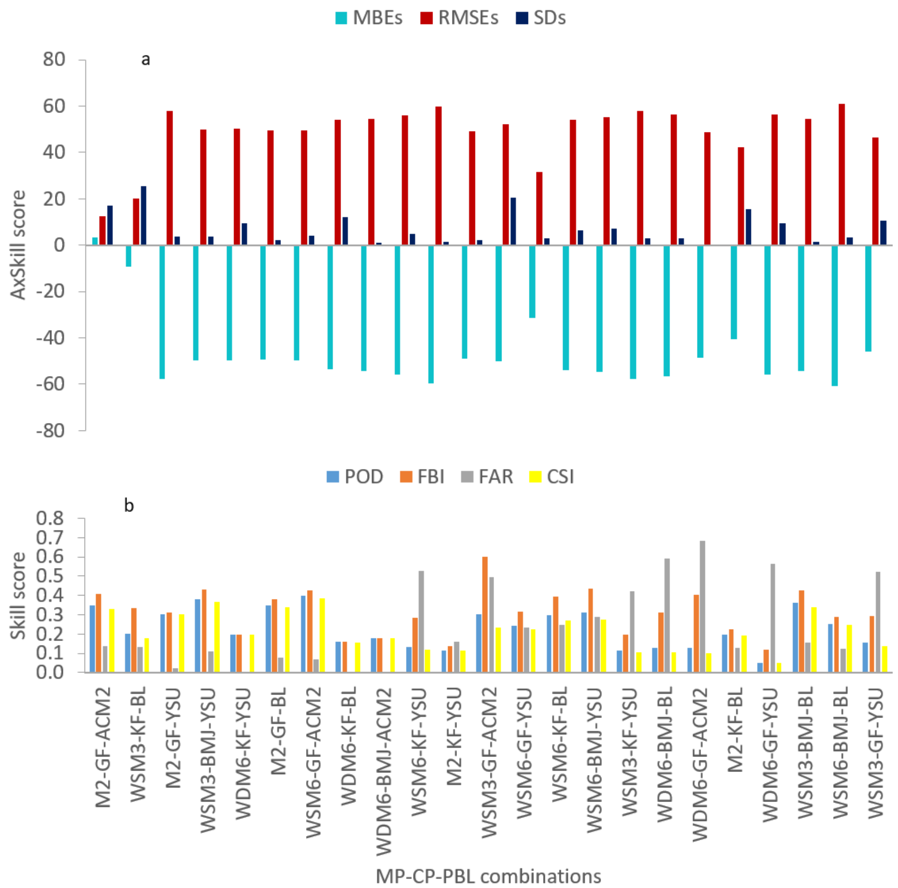

Figure 4.3 Performance of WRF simulated rainfall in the spatial dimension for 24 MP-CP-PBL combinations (each bar represents one simulation): (a) the evaluation results of the continuous indices at an automatic weather station and GSOD-NCDC station; (b) the evaluation results of categorical indices for CHIRPS rainfall distribution. Both (a) and (b) share the same X label.

4.5.4. TOPSIS analysis

To identify the optimum MP-CP-PBL combinations for simulating HIRE triggering the localized flood over the Kampala catchment, we computed the unified scores for TES, SES, and US-based on the rescaled indices of the RE and 2D verification indices. For the temporal dimension, we calculated a single score, Temporal Extent Score (TES, eq.4.9), based on the re-scaled 2D index. The results in **Figure 4.4** and **Table 4.6** indicate that the event's timing is reasonably simulated when using the combinations of WDM6-GF-YSU, WSM3-KF-BL, and WSM6-GF-ACM2 with TES scores of 0.48, 0.41, and 0.40, respectively. WSM6-GF-YSU is the least performing combination with a TES score of 0.27. Although the overall TES skill score is low compared to the ideal score of 1, all combinations are able to capture the convective characteristics of the event, which occurs in the afternoon time of the day

In the spatial dimension, the overall performance of the WRF model is calculated using the Spatial Extent Score (SES, eq. 4.10). **Figure 4.4** reveals that the simulated rainfall's spatial distribution is fairly captured when using M2-GF-ACM2, WSM6-KF-BL, and WSM3-KF-BL combinations with the SES score of 0.62, 0.52, and 0.52, respectively. The least performing combinations for the spatial rainfall distribution simulation in the catchment are WDM6-GF-YSU and WDM6-BMJ-BL, with the SES score of 0.28 and 0.29, respectively, which means the simulated rainfall is displaced compared to the observation.

The TOPSIS unified score, US (eq. 4.11), combines all verifications indices, which are based on comparison with the CHIRPS and two rain gauge data. **Figure 4.4** shows the overall unified score results, US, in a bar plot, with the best scores at the top. The combinations M2-GF-ACM2, WSM6-KF-BL, and WSM3-KF-BL are the best performing, with US scores of 0.53, 0.53, and 0.47. The lower US scores are for WSM3-GF-YSU and WDM6-BMJ-BL combinations, with both cores 0.26. For all combinations, the unified score is generally lower compared to the ideal score of 1.

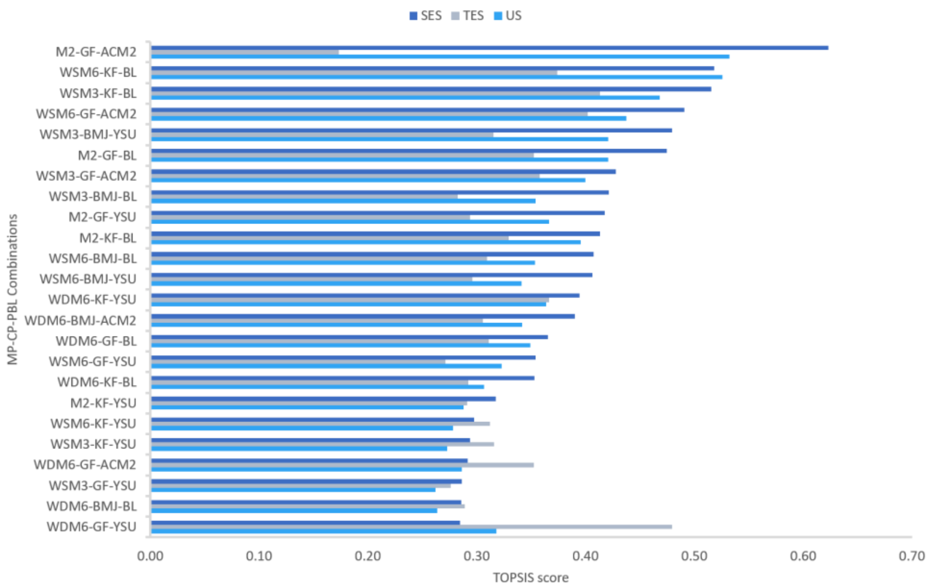

Figure 4.4 The results of the TOPSIS score (TES, SES, and the US) for 24 MP-CP-PBL combinations. SES and US ranked from top to down as best to worst. The higher value represents the best combination

The best-ranked combinations to simulate HIRE based on uS have an excellent SES score but a low TES score. In the hydrological application of localized flood modelling using an event-based hydrologic model, the most determining factor is the rainfall amount and its intensity. Therefore, the low TES score is less problematic.

The ranking in **Table 4.6** indicates that the combinations suitable for temporal distribution may not necessarily be ideal for simulating the event's amount and spatial distribution, and vice-versa. Striking is the performance of the WDM6-GF-YSU combination being ranked at 1st for TES and last, 24th, for SES, resulting in 17th rank for the US, which indicates that the combination performs well for the timing of the event does not perform well for areal accumulated 24-hour rainfall and spatial rainfall distribution. In contrast, the WSM3-KF-BL and M2-GF-ACM2 combinations, which are ranked in the 2nd and 3rd for temporal distribution, are ranked in 3rd and 4th for SES, resulting in a 3rd and 4th place for US score. A good performance for all three TOPSIS scores means that these two combinations perform well in time and space over the catchment. Note that most of the weak performing combinations for TES also have poor performances for SES and, thus, for uS, except for the WDM6-GF-combination, as mentioned above. According to the overall US score, the best performing MP-CP-PBL combination is M2-GF-ACM2, which is ranked 1st for SES, 1st for RE, and 7th for TES.

Table 4.6 Comparison of the combinations` evaluation index values and their ranks, ranked according to RE score; Underlined indicates the top 3 simulations for each index; bold indicates the least performing combination

Combinations	RE(%)		TES		SES		US	
	Score	Rank	Score	Rank	Score	Rank	Score	Rank
M2-GF-ACM2	-2.4	1	0.36	7	0.62	1	0.53	1
WSM6-KF-BL	-39.9	2	0.37	4	0.52	2	0.53	2
M2-KF-BL	-47.0	3	0.33	10	0.41	10	0.30	8
WSM3-GF-ACM2	-60.1	4	0.36	6	0.43	7	0.40	7
WSM3-KF-BL	-62.5	5	0.41	2	0.52	3	0.47	3
WSM6-GF-YSU	-66.1	6	0.31	13	0.35	16	0.32	16
M2-GF-BL	-66.7	7	0.35	8	0.47	6	0.42	6
M2-GF-YSU	-69.0	8	0.29	18	0.42	9	0.37	9
WSM6-GF-ACM2	-74.4	9	0.40	3	0.49	4	0.44	4
WDM6-KF-YSU	-76.8	10	0.37	5	0.39	13	0.36	10
WDM6-BMJ-ACM2	-79.2	11	0.31	16	0.39	14	0.34	14
WDM6-GF-BL	-79.2	12	0.31	14	0.37	15	0.35	13
WSM6-BMJ-BL	-79.2	13	0.31	15	0.41	11	0.35	12
WSM3-BMJ-YSU	-79.8	14	0.32	12	0.48	5	0.42	5
WSM3-BMJ-BL	-80.4	15	0.28	22	0.42	8	0.35	11
M2-KF-YSU	-82.7	16	0.29	20	0.32	18	0.29	19
WDM6-GF-YSU	-82.7	17	0.48	1	0.28	24	0.32	17
WDM6-GF-ACM2	-84.5	18	0.35	9	0.29	21	0.29	20
WSM3-GF-YSU	-85.1	19	0.28	23	0.29	22	0.26	24
WSM6-KF-YSU	-85.7	20	0.27	24	0.30	19	0.28	21
WDM6-BMJ-BL	-86.3	21	0.29	21	0.29	23	0.26	23
WDM6-KF-BL	-86.9	22	0.29	19	0.35	17	0.31	18
WSM6-BMJ-YSU	-87.5	23	0.30	17	0.41	12	0.34	15
WSM3-KF-YSU	-89.3	24	0.32	11	0.20	20	0.27	22

4.5.5. *The Impact of Cumulus Parameterization Schemes on the Simulated Rainfall*

As indicated in the previous section, some of the MP-CP-PBL combinations, particularly those with the more sophisticated microphysics (e.g., WDM6), underperform in simulating this HIRE, which could be due to the CP effect. Therefore, this section evaluates the impact of CP on the simulated rainfall in the innermost domains. Here, each simulation is re-run with CP-off. The result is presented in terms of area-averaged amount and the spatial distribution of 2-

h rainfall for the selected combinations over the catchment. The 2-h event (i.e., 1100 UTC to 1250 UTC (Kampala +3 GMT)) is equivalent to the observation using the Automatic Weather Station (AWS). We know that the 25 June 2012 rainfall lasted for two hours from 14:00 to 15:50 local time as observed using the AWS. Hence, we used the simulated event during this time to examine its distribution over the catchment.

Table 4.7 summarizes the area-averaged rainfall amount for CP-on and CP-off for all 24 combinations and their comparison with respect to the CHIRPS amount. The change in amount is given as a difference between CP-on and CP-off (6th column, **Table 4.7**); positive/negative difference indicates a decrease/increase in amount, respectively. The impact of CP-off is not uniform: for M2-GF-ACM2, WSM3-KF-BL, and WDM6-GF-YSU, the rainfall amount is reduced with the differences between CP-on and CP-off of 0.4, 2.8, and 2.9 mm, respectively, while for WSM3-BMJ-YSU, WDM6-GF-ACM2, and WDM6-BMJ-BL, the amount is substantially increased with differences between CP-on and CP-off −5.0, −10.6, and −8.4 mm, respectively. As shown in the table, the M2-GF-ACM2 combination is ranked 1st with CP-on as well as with CP-off. However, the combinations that rank 2nd (WSM6-KF-BL) and 3rd (M2-KF-BL) with CP-on are ranked 7th and 18th with CP-off. The bottom-ranked combination with CP-off is WDM6-GF-YSU with zero rainfall amount, which eventually ranks 17th with CP-on.

Table 4.7 Comparison of 24-h area-averaged rainfall amount (mm) with and without CP in the inner domain and RE calculated with respect to CHIRPS rainfall amount. The number in the bracket represents the rank.

	CP-on		CP-off		(CP-on) - (CP-off)
MP-CP-PBL Combinations	Area_Averaged Rainfall	RE(%)	Area_Averaged Rainfall	RE(%)	Difference
CHIRPS	16.8				
M2-GF-ACM2	16.4	-2.4 (1)	16	-4.8 (1)	0.4
WSM6-KF-BL	10.1	-39.9 (2)	9.8	-41.7 (7)	0.3
M2-KF-BL	8.9	-47.0 (3)	1.8	-89.3 (18)	7.1
WSM3-GF-ACM2	6.7	-60.1 (4)	6.1	-63.7 (13)	0.6
WSM3-KF-BL	6.3	-62.5 (5)	3.5	-79.2 (15)	2.8
WSM6-GF-YSU	5.7	-66.1 (6)	0.3	-98.2 (22)	5.4
M2-GF-BL	5.6	-66.7 (7)	7.7	-54.2 (9)	-2.1
M2-GF-YSU	5.2	-69.0 (8)	6.7	-60.1 (11)	-1.5
WSM6-GF-ACM2	4.3	-74.4 (9)	10.3	-38.7 (6)	-6
WDM6-KF-YSU	3.9	-76.8 (10)	2.4	-85.7 (16)	1.5
WDM6-BMJ-ACM2	3.5	-79.2 (11)	1.7	-89.9 (19)	1.8
WDM6-GF-BL	3.5	-79.2 (12)	1.5	-91.1 (20)	2
WSM6-BMJ-BL	3.5	-79.2 (13)	10.4	-38.1 (5)	-6.9
WSM3-BMJ-YSU	3.4	-79.8 (14)	8.4	-50.0 (8)	-5
WSM3-BMJ-BL	3.3	-80.4 (15)	4.8	-71.4 (14)	-1.5
M2-KF-YSU	2.9	-82.7 (16)	6.6	-60.7 (12)	-3.7
WDM6-GF-YSU	2.9	-82.7 (17)	0	-100.0 (24)	2.9
WDM6-GF-ACM2	2.6	-84.5 (18)	13.2	-21.4 (3)	-10.6
WSM3-GF-YSU	2.5	-85.1 (19)	7.1	-57.7 (10)	-4.6
WSM6-KF-YSU	2.4	-85.7 (20)	1.9	-88.7 (17)	0.5
WDM6-BMJ-BL	2.3	-86.3 (21)	10.9	-35.1 (4)	-8.6
WDM6-KF-BL	2.2	-86.9 (22)	1	-94.0 (21)	1.2
WSM6-BMJ-YSU	2.1	-87.5 (23)	15.1	-10.1 (2)	-13
WSM3-KF-YSU	1.8	-89.3 (24)	0.1	-99.4 (23)	1.7

Furthermore, there are also differences found in the peak rainfall amount and the event's spatial orientation over the catchment with and without CP. **Figure 4.5** displays the spatial distribution of the combinations with double-moment MP for CP-on with their counterparts CP-off. In best-ranked combinations, M2-GF-ACM2 (first row, **Figure 4.5**), the 2-h maximum rainfall (73 mm) is placed in the city center, where the CP-off simulation has a slightly reduced peak amount (71 mm) and moved to the southwest of the catchment. In contrast, in WDM6-GF-ACM2 CP-on (4th row, **Figure 4.5**), the 2-h maximum rainfall amount (46 mm) is simulated at the north-east outskirt of the catchment, and with CP-off, the maximum rainfall amount of 52 mm is located in the southern and southwest outskirts of the catchment. In the CP-on simulation, for instance, in M2-GF-ACM2 (first row, **Figure 4.5**), the spatial pattern of a peak rainfall event is oriented southeast over the catchment. In contrast, in the CP-off simulation, the theWDM6-GF-ACM2 (4th row, Figure 4.5) shows the peak intensity oriented southwest-northeast, while for WDM6-BMJ-BL (6th row, **Figure 4.5**), the peak rainfall is concentrated at a specific location in the catchment.

As shown in **Figure 4.5** and **Table 4.7,** CP-off's performance in producing area-averaged rainfall amount and its grid cell peak amount that can trigger the localized flood in the catchment is weak compared to CP-on simulation. Particularly, the grid cell peak rainfall amount for M2-GF-ACM2, which is the optimum combination for flash flood modeling, has performed better for CP-on than when using CP-off. Therefore, in the remainder of this paper, we tested the top three combinations with CP-on in the innermost domain to evaluate the impact of spatial and temporal rainfall variability on urbanized flash flood modeling.

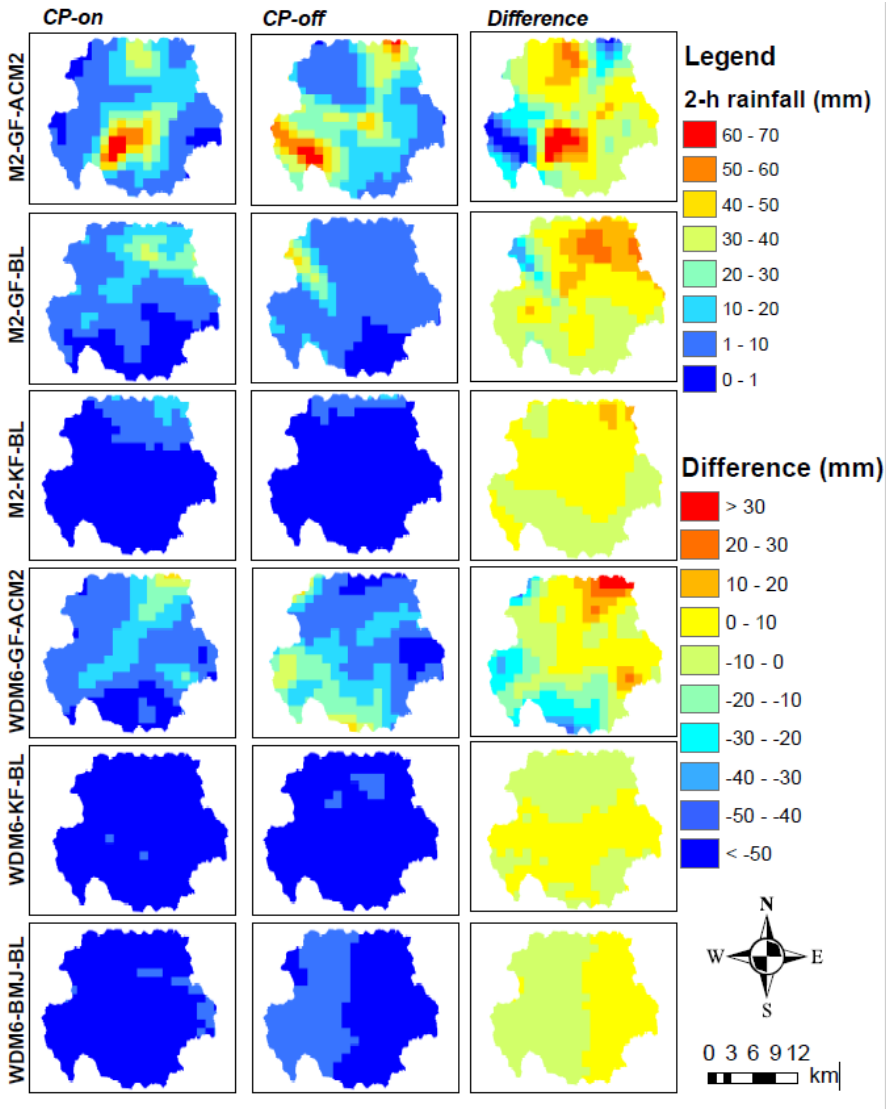

Figure 4.5 Spatial distribution of 2-h accumulated rainfall amount (mm) from 1100 UTC to 1250 UTC during 25 June 2012 for the 1-km domain with CP-on and CP-off. The difference represents the subtraction of CP-off from CP-on (i.e., CP-on-CP-off).

4.5.6. *Best performing combinations for localized flood modelling*

The best performing WRF combinations could serve for localized flood modelling in the catchment in two ways: (1) *Actual flood modelling*, where the spatially moving rainfall event in the catchment can be used as input to a hydrologic model, or (2) *Potential flood modelling*, where a representative homogeneous rainfall for a chosen return period is used as input to a hydrologic model. For the first application, WRF rainfall data could serve as the actual flood event to study the characteristics of the flooding in the catchment. For the second application, the use of the representative homogeneous event as a design storm for a given return period is required as a standard for flood hazard assessment.

(1) *Actual flood modelling:* The WRF simulated rainfall output is directly used as input to a hydrologic model, where for Early Warning System (EWS) purposes, for instance, the total rainfall amount and its variation in time and space is essential. **Figure 4.6** shows the accumulation of 10-minute interval WRF rainfall for the three best performing combinations according to the US score. As seen in the figure, the city of Kampala is much bigger than the simulated convective events. The M2-GF-ACM2 (**Figure 4.6a**) and WSM3-KF-BL (**Figure 4.6c**) put the hotspot of rainfall just south of the center, whereas WSM6-KF-BL (Figure 4.6b) simulates moderate-intensity rainfall in the southeast part of the city. These maps confirm the results from 2D categorical indices (session 3.3). **Figure 4.6d** shows the rainfall time series observed by the AWS (blue) and the simulated rainfall hotspots in the city. Although the total 24-hour rainfall amount is moderate for all combinations, it is enough to trigger the localized flood event in the catchment, depending on the location where it fell.

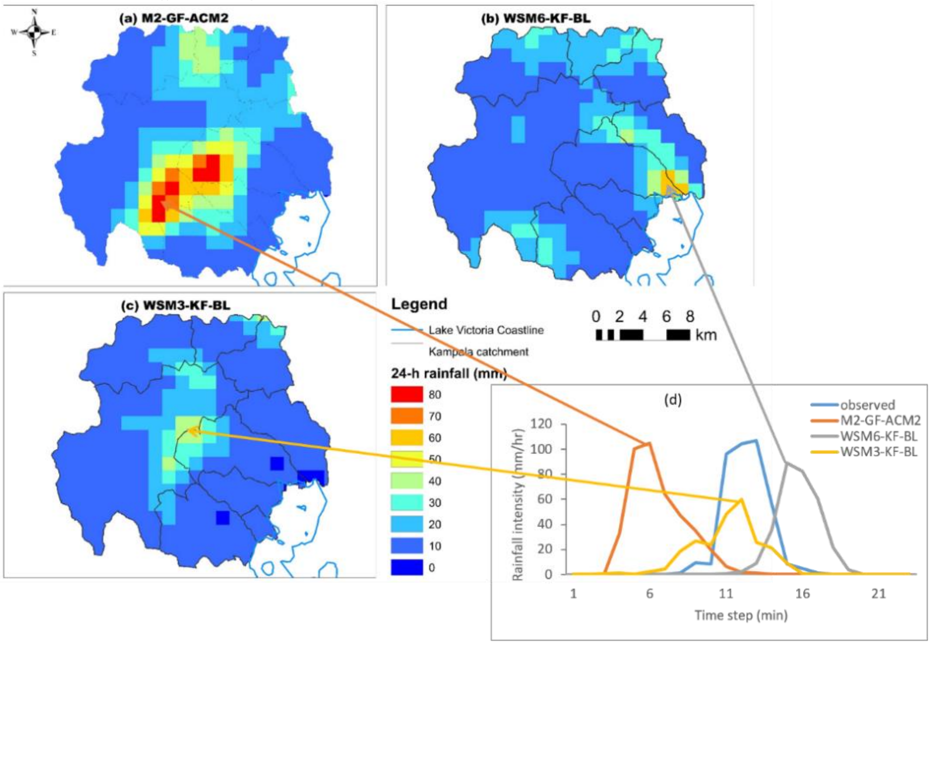

Figure 4.6 Spatially distributed high-intensity rainfall triggering the localized flood in the Kampala catchment for the three best WRF simulations using (a) M2-GF-ACM2, (b) WSM6-KF-BL, and (c) WSM3-KF-BL combinations; (d) rainfall intensity for the three best combinations extracted at AWS. Timestep in every 10-minute.

(2) *Potential flood modelling:* Instead of directly using WRF rainfall output for the hydrologic model, we can use a representative event and apply it homogeneously in the catchment, considering the fact of randomness in the simulations of the rainfall hotspots (**Figure 4.6**). For potential flood modelling, the accuracy of rainfall intensity, event duration, and total amount matter, as the combination determines whether the soil's infiltration rate and water capacity are exceeded with flooding as a result. In line with actual flood modelling, the US score leads to the selection of best-performing combinations. The temporal behavior of these combinations differs. As seen in **Figure 4.6d**, the maximum peak intensity from M2-GF-ACM2 is 112 mm/hr, which is similar to the observation (108 mm/hr), whereas the duration is 2 hours longer than observed. In contrast, the WRF rainfall intensity for WSM3-KF-BL shows a much lower peak intensity 60 mm/hr and a 3-hour longer event duration than observed, but the timing of the peak intensity is the same as observed. In WSM6-KF-BL, the peak intensity at the shown location (**Figure 4.6b**) is 96 mm/hr, which is moderately lower than observed where the event duration of the peak event for WSM6-KF-BL is about 2-hours longer than observed. The fact that the timing of the peak event by most WRF combinations is off compared to observations is irrelevant for potential flood modelling.

4.6. Discussion

To evaluate the ability of the WRF model in simulating HIRE that has the potential to cause the localized urban flood, we evaluated MP-CP-PBL parametrization combinations in Kampala city, Uganda. In the absence of a dense rain gauge network, two rain gauge stations and the satellite rainfall estimation derived from CHIRPS (Funk et al., 2015) were used for model evaluation. The HIRE that occurred on 25 June 2012 is considered a case study, which caused a devastating flash flood in Kampala's built-up areas. In total, 24 rainfall-producing parametrization combinations as microphysics (MP), cumulus scheme (CP), and PBL are evaluated in this paper. We have carried out 48 different simulations (24-with CP-on and 24-with CP-off) in the innermost domain of the WRF model at 1 km resolution. The combinations with CP-off are used to evaluate the impact of the cumulus scheme in the innermost domain of WRF by comparing rainfall amount and spatial distribution. The CP-off runs were not further used as the simulated rainfall amount, and peak distribution are weak compared to the CP-on run. We used the simulations with CP-on for detailed the parameterization combination's performance analysis by applying the relative error and 2D verification indices. The TOPSIS method was used to select the optimum parametrization combinations to simulate the extreme rainfall event triggering floods in the Kampala catchment.

With CP-on, the rainfall amount and its spatial distribution are best simulated when using M2-GF-ACM2, while the temporal distribution is best captured using WDM6-GF-YSU. The results show that some combinations behave very well in TES but low in SES, while others score low in both SES and TES (a misplaced system will arrive too late or early at its AWS destination). So, to select the best combination with minimum differences in TES and SES, we computed the US score, which is the average of the area-averaged rainfall (RE), temporal (TES), and spatial (SES) rainfall distribution scores. Based on the US score, the HIRE that triggered the localized flood in the Kampala catchment is best simulated when using M2-GF-ACM2, followed by WSM6-KF-BL and WSM3-KF-BL. The US score of 0.53 for this combination means that the WRF model relatively well captures the rain-producing processes. Looking at top scores, it is clear that there is not one MP, CP, or PBL scheme outperforming the others: the interaction between the CP-MP-PBL schemes determines its performance skill.

From the results, it stands out that the WRF model's ability to simulate the HIRE is mainly determined by a proper selection of the parametrization combinations. However, some individual schemes and their combination outperform others to simulate the HIRE over the study area. For instance, complex schemes such as M2 and WSM6 in combination with GF cumulus parameterization and ACM2 PBL simulate better the amount and intensity of the event. The sophisticated microphysics incorporates the crucial hydrometeors needed for deep convection where we have a mixture of vapor, liquid water, ice, graupel to resolve cloud condensation; see also (Hong and Lim, 2006; Lim and Hong, 2010). Hence, the statistical outcome kind of confirms the reality behind physics. Previous studies, for example, (Sikder and Hossain, 2018; Opio et al., 2020), also indicated similar outcomes when using these types of microphysics schemes for simulating extreme rainfall events. Furthermore, the results of this study indicated that the combination with WSM3, which misses physics for multi-species of hydrometeors, performs better in capturing the event's intensity and location. In contrast, the combination with the most sophisticated physics, WDM6, with a very suitable combination for deep convection for the tropics, underperforms the event's amount and intensity. However, WDM6 still ranks top in simulating the temporal characteristics of the HIRE. With regard to cumulus parametrization, the scheme that was designed for the tropics, as indicated by Grell and Freitas (2014), for instance, Grell Freitas (GF), outperforms the other schemes. GF is a scale-aware scheme, which means that its activity will depend on the model's spatial resolution; hence at 1 km, GF is highly sensitive, which is one reason the HIRE is well simulated with this scheme. A similar study by Mugume et al. (2017) also indicates GF performance is better in simulating rainfall over Western Uganda. As their study considers a longer period, it is difficult to make a proper comparison; however, it is still interesting to see that GF is one of the best CP applicable in simulating HIRE in the equatorial East African region. When we consider the outperforming PBL, the scheme that was designed for unstable conditions in the PBL, such as ACM2, outperforms in this study. A similar study in the tropical region by Ngailo et al. (2018) also indicated that the KF cumulus parametrization scheme and ACM2 PBL, in combination with Lin microphysics, perform better in simulating heavy rainfall events in Tanzania. In their study, however, the use of GF and ACM2 in combination with WSM6 shows poor results with high error scores.

To test the CP-off impact on the simulated rainfall, we carried out each simulation without CP in the innermost domains of WRF. Accordingly, with CP-off, the area-averaged rainfall amount is best simulated when using M2-GF-ACM2, followed by WSM6-BMJ-YSU and WDM6-GF-ACM2. The CP-off affects the spatial distribution and patterns of the simulated rainfall over the catchment. The CP-off combinations with WDM6 microphysics and Betts-Miller cumulus schemes show an increase in amount compared to the CP-on simulations. The combinations with M2 and GF indicate a mixed result with sometimes a decrease in amount other time an increase in amount, which might be due to the instability effect during the simulation time. The striking point is that among the best and least performing combinations are the combination with the WDM6 scheme. For instance, WDM6-GF-YSU produces zero rainfall amount (ranked 24th), while WDM6-GF-ACM2 produces high rainfall amount (ranked 3rd), which indicates that PBL is the main controlling factor for this specific combination. Furthermore, the CP-on simulation shows that the BMJ CP scheme produces light rainfall with good performance in simulating the event's spatial distribution (higher POD) but is very weak in detecting the event's intensity and amount over the catchment. In contrast, with the CP-off simulation, a high rainfall amount over the catchment is enhanced when using BMJ, which resembles the findings by (Argent et al., 2015) that suggest BMJ's superiority in simulating rainfall distribution over the Lake Victoria basin.

In general, this study shows that there are no systematic trends in simulated rainfall with specific MP-CP-PBL schemes, nor when using CP-on or CP-off. For instance, in the CP-on simulation, based on TOPSIS criteria, the combination with a simple MP (e.g., WSM3) sometimes outperforms the complex MP (e.g., WDM6), and vice-versa in other times. Similarly, in the simulation with CP-off, based on rainfall amount, the combinations with WDM6 rank both 3rd and least depending on the considered CP and PBL schemes, which depend on the local processes. Our findings are in line with various studies that indicated different CP's effects on the simulated rainfall depending on the analyzing domain, location, and spatiotemporal resolutions (Sikder and Hossain, 2016; Han and Hong, 2018; Paul et al., 2018).

The best performing parameterization schemes and their combinations for the 25 June 2012 event are not necessarily suitable for simulating other HIRE or the seasonal and monthly rainfall simulation in the Lake Victoria basin. Previous studies found different MP and CP schemes favorable for simulating the amount and spatial distribution of rainfall in the Lake Victoria basin. The discrepancies between our results and the previous studies in the region arise from several factors. Firstly, the combinations applicable for monthly or seasonal rainfall simulation are not necessarily applicable to the event-based simulation. For instance, (Otieno et al., 2018) found WSM6 in combination with KF and YSU to simulate the mean rainfall pattern in the core rainy season (MAM and OND) across the Lake Victoria basin. Their study points out that the applicability of the WRF model in simulating rainfall over the lake domain is weak, probably due to the different rainfall-producing systems active in the Lake Victoria region. Argent et al. (2015) suggested the combination of WSM5 with BMJ and YSU schemes to simulate best the pattern of the monthly rainfall distribution across the Lake basin where, in our case, these combinations instead perform weakly. Secondly, the parameterization combinations that are applicable for simulating rainfall patterns in a large domain, for instance, as in the case of (Opio et al., 2020), might not necessarily be applicable for the localized, high-resolution event simulation. Lastly, the difference in observed data that was used for verifying the model result. Due to the data-limitation issues, most of the studies in the region have used satellite rainfall observations (e.g., TRMM and CHIRPS) as a benchmark for WRF model verification. Since satellite rainfall estimation has a limitation in detecting the extreme rainfall event, for example, (AghaKouchak et al., 2011; Stampoulis et al., 2013), a decision that can be made based only on these observations might also be contributed to the discrepancies in the model results. Therefore, this study highlights that for the event-based WRF model simulation, the MP-CP-PB procedure at high spatial and temporal resolutions, as opposed to the previous studies, produces promising results appropriate for local hydrological applications.

Looking at the absolute scores, the maximum unified score (US) is 0.5 (M2-GF-ACM2 and WSM6-KF-BL), which indicates that the WRF skill to simulate the localized rainfall event over the city is far from the optimal score of 1. Nonetheless, given the event's convective characteristics, which occurred in the non-main rainy season, the score's result is reasonably good. Similar studies on simulating different storm types using the WRF model also indicate that unevenly distributed event is weakly simulated compared to simulating evenly distributed events. Studies by Liu et al. (2012); Tian et al. (2017) confirm that the processes driving an unevenly distributed localized rain event are highly complex and challenging for the WRF model to capture correctly. Moreover, the weak performance of WRF for this event over the Kampala catchment might also be due to the limited observed rainfall data to verify this single event over the city. The absence of a dense urban and regional rain gauge network will also impact the quality of satellite-based rainfall estimate CHIRPS as a verification dataset and of the ERA-5 re-analysis dataset, which provides lateral and initial boundary conditions for WRF as it is less constrained over the Lake Victoria region. Combined with the data limitation issues for detailed model evaluation, there are also some issues (e.g., rainfall thresholds applied for contingency calculation) when using the contingency metrics for evaluating the spatial distribution of an event for a hit or a miss with respect to a CHIRPS. As this observed data will be spatially not independent, e.g., if the weather system travels too far north compared to the observations, this will happen in all grid cells in the neighborhood, which is one of the weak sides to apply these metrics.

Although WRF seems to perform locally rather poorly, its results are promising for hydrological flood modeling purposes because several WRF parametrization combinations are capable of producing the current HIRE that is essential for triggering localized floods in Kampala city. For flood hazard modeling, e.g., using an event-based hydrological model, the volume of rainwater is as important as the peak intensity for triggering localized floods. Our WRF results show a high temporal and spatial variability between the simulated events over the city. Using these WRF simulated moving events in time and space with different magnitudes of rainfall at different locations in the catchment could primarily lead to a better understanding of the local flood characteristics. Similarly, the HIRE time series extracted from the representative grid cell location could be applied as homogeneous input for a flood model to get information on the flood-prone areas in Kampala. In the absence of observed hydrological data (e.g., discharge or water level) and accurate information on the sewer system, it is challenging to calibrate and evaluate the output of such a hydrological model (Umer et al., 2019). The limitation for both applications seems that simulated temporal and spatial variation in rain intensity and volume for this single event is too large to support flood decision-making.

Furthermore, it is important to outline that the current study is an illustrative example, not a full climatology, nor justification for utilizing this model set-up for other HIREs over this region. We mainly focused on evaluating WRF performances on the rainfall characteristics (i.e., total rainfall amount, spatial and temporal distributions) that are essential for triggering the localized flood in the catchment. Therefore, the selected optimum combination is only applicable to the 25 June 2012 event, not for simulation of other HIREs in different seasons, or not used for long time series simulation over the region. As each HIRE in the flood season has a likely unique WRF parametrization combination setup at 1 km spatial resolutions, it is advisable to explore the best choices for each flood season to validate the WRF model through sensitivity analysis and then use it for a practical purpose.

4.7. Conclusion

This study shows that the WRF mesoscale NWP model successfully simulates the rainfall amount and its distribution for a single HIRE that triggered the localized flood in Kampala city. Modeling HIREs proves to be challenging as the rain-bearing systems are highly variable, localized, and complex. We evaluated the 24 MP-CP-PBL parameterization combinations' ability to simulate the HIRE in the complex climate system of urbanized and data-scarce Kampala city, Uganda. We considered the 25 June 2012 HIRE that has caused the localized flood hazard in the city's flood-prone areas. The model results are evaluated against rainfall data from two gauging stations and the CHIRPS satellite rainfall estimates.

In total, the performance of 24 parameterization combinations using four microphysics (MP) (Morrison, WSM6, WSM3, and WDM6), three cumulus parametrization (CP) (GF, KF, and BMJ), and three PBL schemes (ACM2, BL, and YSU) was verified by using the relative error, continuous and categorical indices, and the TOPSIS decision analysis criteria. The performance is evaluated in terms of 24-h areal catchment rainfall amount and its temporal and spatial distributions over the Kampala catchment. The results of this study showed that only a few parameterization combinations correctly reproduced the observed HIRE in the catchment boundary, which suggests that the performance of the WRF model depends strongly on a proper choice of the parametrization combinations. Besides recognizing the effect of cumulus parameterization on the simulated rainfall, each simulation is re-run with CP-off and compared the results in terms of rainfall amount and spatial distribution over the innermost domain. The result indicated that with CP-off simulation, there is a variation in the simulated rainfall amount, peak intensity, and pattern orientation compared to simulations using CP-on. However, in terms of the best performance for localized flood modeling, still, the same combination performed best with CP-off as CP-on. Compared with the CP-on simulations, the total rainfall amount is enhanced with some schemes while reduced in other cases, indicating no systematic trends in the simulated rainfall with specific schemes or combinations.

Based on the TOPSIS criteria, the M2-GF-ACM2, WSM6-KF-BL, and WSM3-KF-BL are the optimum top three MP-CP-PBL combinations to simulate the current HIRE over the Kampala catchment. It is noteworthy that as WRF parametrization schemes' performance is highly dependent on the meteorological processes associated with convective events studied, the top-ranked MP-CP-PBL combinations are only applicable for this 25 June 2012 event. Due to the event's convective characteristics, the HIRE triggering the localized floods simulated only in a few pockets of the catchment while the rest of the catchment areas have no rainfall. The optimum parametrization combinations are capable of simulating the event's rainfall intensity similar to the observed rainfall intensity at the AWS location but displaced.

As simulated rainfall intensity is the primary input for the event-based hydrologic model for the localized flood modeling in the catchment, there is enough potential for exploring further use of the WRF model for potential flood hazard modeling. More events need to be simulated and evaluated to conclude on the optimal parameterizations combinations per season or synoptic system. At the same time, the construction of a design storm from actual events is not straightforward as it requires statistical model development as well as consideration of the different approaches to defining a design storm with assigned return periods. This study showed that WRF rainfall could be a very valuable asset for flash flood modeling in a city where high-quality direct and remotely sensed observations of rainfall are limited.

Acknowledgments: We would like to express our thanks to the University of Twente for funding this research. We also acknowledge the NWO Physical Science Division project number SH-312-15.

Conflict of interest: The authors declare no conflict of interest.

Evaluation of the WRF model to simulate a high-intensity rainfall event

Chapter 5: Application of the WRF model rainfall product for the localized flood hazard modelling in a data-scarce environment

This chapter is published as a peer-reviewed paper, removing minor modifications and duplications.

Y. M. Umer, V.G. Jetten, J. Ettema, Lombardo, L. Application of the WRF model rainfall product for the localized flood hazard modelling in a data-scarce environment. Journal of Natural hazards DOI: 10.1007/s11069-021-05117-6
https://doi.org/10.1007/s11069-021-05117-6

Abstract: Urban flood hazard model needs rainfall with high spatial and temporal resolutions for flood hazard analysis to accurately simulate flood dynamics in complex urban environments. However, in many developing countries, such high-quality data is scarce. Data that exist are also spatially biased towards airports and urban areas in general, where these locations may not represent flood-prone areas. One way to gain insight into the rainfall data and its spatial patterns is through numerical weather prediction models. As their performance improves, these might serve as alternative rainfall data sources for producing optimal design storms required for flood hazard modelling in data-scarce areas. To gain such insight, we developed WRF design storms based on the spatial distribution of high-intensity rainfall events simulated at high spatial and temporal resolutions. Firstly, three known events (i.e., 25 June 2012, 13 April 2016, and 16 April 2016) that caused the flood hazard in the study area are simulated using the WRF model. Secondly, the potential gridcell-events that are able to trigger the localized flood hazard in the catchment are selected and translated to the WRF design storm form using a quantile expression. Finally, three different WRF design storms per event are constructed: Lower, median, and upper quantiles. The results are compared with the design storms of 2 and 10-year return periods constructed based on the alternating-block method to evaluate differences from a flood hazard assessment point of view. The method is tested in the case of Kampala city, Uganda. The comparison of the design storms indicates that WRF design storms properties are in good agreement with the alternating block design storms. Mainly, the differences between the produced flood characteristics (e.g., hydrographs and the number of flood gird cells) when using WRFLs versus 2-year and WRFUs versus 10-year alternating block storms are very minimal. The calculated aggregated performance statistics

(F scores) for the simulated flood extent of WRF design storms benchmarked with the alternating block storms also produced a higher score of 0.9 for both WRF lower quantiles versus 2-year and WRF upper quantile versus 10-year alternating block storm. The result suggested that the WRF design storms can be considered an added value for flood hazard assessment as they are closer to real systems causing rainfall. However, more research is needed on which area can be considered as a representative area in the catchment.

Keywords: Alternative design storm, High-intensity rainfall event, IDF curve, flood hazard modelling, potential gridcell-event, representative gridcell-events, WRF model, Quantile expression of cumulative rainfall

5.1. Introduction

With the increasing effect of urbanization and climate change in recent times, urban floods are becoming more frequent and devastating (Hirabayashi et al., 2013; Duan et al., 2016). Especially Africa is the most affected region by floods next to Asia (CRED and UNISDR, 2015). Notably, poor communities in Sub-Saharan African cities are disproportionately affected by urban floods, the latter being exacerbated by climate change (Douglas et al., 2008; Sliuzas et al., 2013; Perez Molina, 2019). Therefore, there is a growing effort at national, regional, and local levels focusing on urban flood hazard modelling as part of integrated flood management (IFM) to cope with urban floods (Sy et al., 2016; Pérez-Molina et al., 2017; Sy et al., 2020). Strategies to cope with urban floods, such as adaptation and mitigation, require an urban flood hazard assessment, where a high-quality input dataset is essential for effective flood hazard modelling. Flood hazard is an analysis that combines hazard intensity with a return period or probability of occurrence. The intensity of floods is usually characterized as a combination of the extent and maximum water level. Unfortunately, it is rare that flood observations are good enough to derive a probability from observed floods. Therefore, the probability of floods is replaced by the probability of the driver, the rainfall, for which good records exist with global coverage. There are two steps concerning rainfall in a flood hazard analysis. The return period of extreme rainfall is calculated from daily rainfall records, based on maximum daily rainfall per year over a period of 20-30 years, on which extreme value statistics is applied (fitting, for instance, a Gumbel distribution). It is important to note that the stakeholders often choose the return periods based on their capacity for disaster prevention and mitigation measures. The return periods and associated rainfall values are based on annual maximum 24-h rainfall. It is important to take these established maximum rainfall values as a starting point so that the results of any alternative method can be clearly related to flood mitigation activities.

However, the 24-h maximum rainfall is not enough for flood hazard assessment. A flood model needs rainfall with a high temporal resolution to accurately simulate flood dynamics in complex urban environments. Therefore, the second step is that design storms are used with a shape derived from probability density functions based on high-resolution rainfall data as close as possible to the area (see, e.g., (Chen and Hill, 2007; Balbastre-Soldevila et al., 2019)). Design storms are developed initially to dimension drainage channels for peak discharge (Keifer and Chu, 1957); but for flood hazard modelling, which depends on rainfall-infiltration dynamics (e.g., (Chen and Hill, 2007; Balbastre-Soldevila et al., 2019; Umer et al., 2019)), it requires more accurate design storms on the aspects of peak intensity and its temporal characteristics. Conventionally, in the areas where long records of observed rainfall with a high temporal resolution are available, design storms of a shorter duration are developed from the intensity-duration frequency (IDF) curves, using various methods such as the alternating-block method giving a slightly asymmetrical event (Guo and Hargadin, 2009; Sun et al., 2019).

Both steps have inherent problems. The frequency-magnitude analysis is by necessity tied to a location where long observation records exist. These are scarce and often spatially biased towards airports and urban areas in general, where long records are commonly established. These locations may not be representative of flood-prone areas, and the spatial density of observations may not capture the spatial variability of the rainfall patterns. Similarly, not enough detailed data exists to establish IDF curves, essential for reliable estimation of design storms with higher return periods (e.g., T = 10, 25, 50, and 100 years) (Mugume and Butler, 2017). In such areas, the common practice is to use simplified procedures developed based on limited rainfall observations to provide a representative design storm of that region. For instance, Fiddes et al. (1974) developed a simplified method for predicting design storms of a given return period in East Africa, based on observed rainfall records ranging between 8-30 years. This results in a local flood hazard prediction based on a design storm that forms a generalized regional IDF curve, which is problematic. At the same time, weather phenomena that cause floods have spatial extents varying form relatively small convective storms to continental size phenomena such as monsoons.

One of the ways to gain insight into the spatial patterns of rainfall is numerical weather prediction models. As their performance improves, these might serve as alternative rainfall data sources for producing optimal design storms required for flood hazard modelling in such a data-scarce area. A second source is high-resolution global; satellite data such as GPM and GSMAP that provides 0.1 degrees 30-minute rainfall estimates (Yang et al., 2020). In this study, we use the Weather Research and Forecasting (WRF) model (Powers et al., 2017) to gain insight into the amount and distribution of rainfall events required for flash flood food modelling (e.g., (Hong and Lee, 2009; Leung and Qian, 2009; Pennelly et al., 2014; Liu et al., 2015; Li et al., 2017; Chawla et al., 2018a)). With the usability of the recently released high-resolution ERA5 reanalysis climate data as boundary conditions, the model can consider the large-scale atmospheric processes linked to the high-intensity rainfall triggering flood events in the catchment (Giannaros et al., 2020; Greco et al., 2020). Moreover, the WRF model is able to consider the local-scale processes affecting the rainfall, such as the effect of the urban extent and position on extreme rainfall distribution (Paul et al., 2018; Zhang et al., 2018b; Oliveros et al., 2019). In the same way, the WRF model is robust in considering the variability of the storms across wide areas and its flexibility to reproduce rainfall data at the spatial and temporal resolution that can be needed for the flood hydrology model (Liu et al., 2012; Chawla et al., 2018b; Tian et al., 2020). Thus, when appropriately configured and validated, the WRF model is a suitable tool for simulating the high-intensity rainfall events and spatial variability for flood modelling (Zittis et al., 2017; Sikder and Hossain, 2018).

A recent study by Sikder et al. (2019) indicated the usability of the WRF rainfall simulations of moderate-intensity and high-intensity rainfall events for actual urban flood modelling in Houston, USA. However, the WRF simulated actual rainfall events are not directly used for the flood hazard modeling. With the actual use of the WRF rainfall product, the magnitude of the gridcell events is spatially different and creates discrimination in the simulated flooding over the catchment, which is challenging for flood hazard analysis. Design gridcell rainfall events have to be created. As there is no common way to create the WRF simulated events into the design storms, we need a new method to convert the WRF simulated rainfall events into the design storm form for flood hazard modelling. This study presents a new methodology to translate WRF simulated high-resolution convective rainfall events into design storms for flood hazard modelling. The performance of the WRF based design storms performance is evaluated against the existing alternating-block method design storms obtained from the pre-established IDF curves in order to evaluate differences from the point of view of flood hazard assessment. The strengths and weaknesses of our proposed method are discussed with the potential need for further steps. As a study area, the rapidly growing city of Kampala is used, specifically, the northern Lubigi catchment where floods frequently happen in the former wetlands, where dense informal settlements (slums) exist (Sliuzas et al., 2013; Perez Molina, 2019; Umer et al., 2019). The Kampala City council has adopted a 10-year return period as the basis for the improvement of the surface drainage system to cope with a certain level of flooding.

5.2. *Method*

Figure 5.1 presents the framework we implemented to translate four WRF simulated High-Intensity Rainfall Events (HIREs) into a given return period's WRF design storm. The four storms are chosen because flooding was reported in the study area on those dates, and they are different in duration, magnitude, and peak intensity. The framework illustrates the WRF design storm's (right-side) comparison with the IDF-based alternating-block method (IDF-AB) design storms. The IDF-AB design storms of 2 and 10-year return periods (hereafter 'AB2yr' and 'AB10yr') are compared with the WRF design storms that are expressed as the quantiles (explained below). The IDF-AB and the WRF design storms are compared and used as input for flood hazard modelling with the model openLISEM (Baartman et al., 2012; Jetten, 2014; Umer et al., 2019).

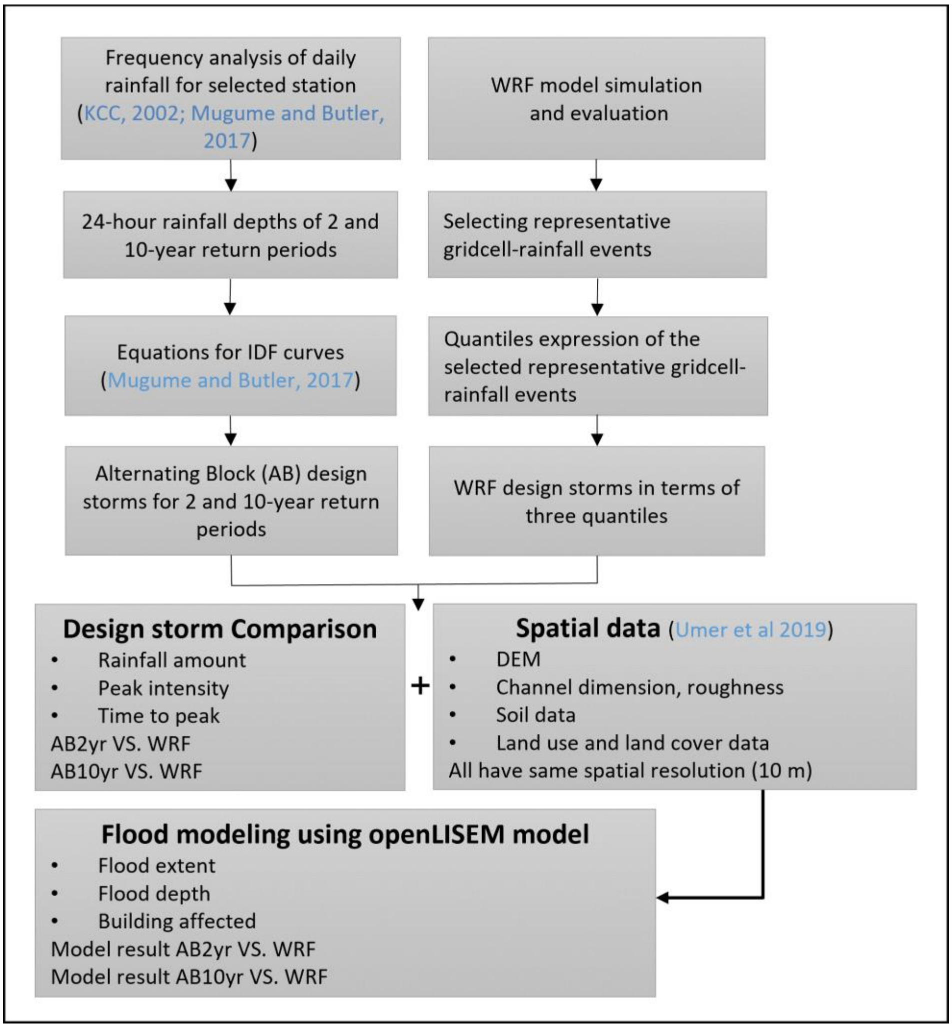

Figure 5.1 The workflow of this study to construct design storms from WRF simulated gridcell-rainfall events, and its comparison with design storms derived based on the Alternative-block method, including their application for flood hazard modelling in the case study

5.2.1. WRF model settings

The WRF design storms are constructed based on the WRF simulated high-intensity rainfall events (HIRE) produced at the spatial resolution of 1 km (rectangle represented by the grey color in **Figure 1.2**, section 1.5). The WRF model (version 4.1, (Powers et al., 2017)) was configured to simulate four known HIRE (i.e., 25 June 2012, 03 September 2013, 13 April 2016, and 16 April 2016) that have caused flooding in Kampala, Uganda. For initial and boundary conditions, the ERA5 (Hersbach and Dee, 2016) dataset was utilized. The model simulation and evaluation follow the MP-CP-PBL procedure introduced and discussed in (Umer et al., 2021), where MP refers to microphysics, CP-cumulus parametrization, and PBL is the planetary boundary layer. Accordingly, for 25 June 2012, the best combination is the double moment Marrison (M2) scheme combined with Grell-Freitas (GF) and ACM2. For 03 September 2013, it is WSM3 scheme with GF and ACM2, while for both 13 and 16 April 2016, the best combination is the WSM6 scheme with Kaint-Fritsch (KF) and ACM2. For each HIRE analysis, we considered only the model output in the innermost domain of WRF with spatial and temporal resolutions of 1 km and 10 minutes. The convective and independent model output event at 1 km and 10 minutes resolutions (hereafter gridcell-event) are converted into design storms to serve as input for urban flood modelling.

5.2.2. WRF design storms

Following the WRF simulation of the selected HIREs, the method follows a two-step procedure. The assumption here is that all the gridcell-events in the inner domain of WRF are considered separate and spatially independent rain events as these events are highly localized due to their convective nature. In fact, we considered each gridcell as a virtual rainfall station.

i. Step 1: selection of potential gridcell-events

The grid cell rainfall events that have the potential to cause flooding are selected based on existing local rainfall information to serve as an area-dependent threshold. For this case study, the threshold is based on the depth and peak intensity of a 2-year return period storm for Kampala, estimated from the frequency analysis of daily rainfall in Kampala (Mugume and Butler, 2017). This is considered the minimum event that triggers local floods in the former wetlands and flood plains. As such, the city's flood lines and drainage system are designed for events of 2-year or more (KCCA, 2010). Therefore, the gridcell-events in the innermost domain of WRF are identified and selected if they fulfill both criteria:

I. For moving storms, select grid cells with a total rainfall amount equal to or exceeding 2- year return period, and

II. Select grid cells with the peak intensity equal to or exceeding the peak intensity of 2-year return period

ii. Step 2: selection of representative gridcell-events

To select the representative gridcell-events to define the WRF design storms, we summarized their distribution into quantiles following a two-stepped procedure. Initially, we examined the cumulative distribution functions (CDF) for each of the considered rainfall events for each of the potential grid cells selected under section 2.2.1. In the second step, we extracted the maximum value from each CDF and calculated its probability density function (PDF). As a result, we focused on the total rainfall amount for each HIRE and examined its distribution over space for each potential grid cell. We computed three quantiles from the calculated PDFs, with probabilities p = 0.025, 0.5, and 0.975. In this way, we aimed at extracting a sample from the bulk of the distribution (median) and the expected variability associated with it (95% confidence interval or the range between the left and right tails of the distribution). For each of the three quantiles (hereafter the WRF design storms), the storm events are expressed in terms of their properties such as rainfall amount, peak intensity, and the time dynamics, which mainly include the time to peak intensity and the elapsed time for the derived cumulative rainfall.

5.2.3. IDF design storms

To investigate the performance of the constructed WRF design storms, we compared them with the classically derived IDF design storms known as alternating block design storms. The steps to obtain design storms from the IDF curves are divided into two: frequency analysis of the daily (24-h) point rainfall depths for various return periods. In this case, we used the estimated rainfall depth of Kampala from the literature, as indicated by (Fiddes et al., 1974) (Mugume and Butler, 2017) (KCCA, 2010). The second step is to convert the 24-h rainfall depth of different return periods into the shorter duration design storms, using the so-called Alternating Block method. We follow (Mugume and Butler, 2017) using equations 1 and 2 for constructing the IDF design storms.

$$I_R = \frac{a}{(t+b)^c} \text{-----------------------------} 5.1$$

Where I_R (mm/hr) is the maximum intensity corresponding to a rainfall duration t and a, b and c are constants. By eliminating `a', **Equation 1** can be simplified into **Equation 2**.

$$R_T = \frac{t}{24}\left(\frac{24+b}{b+t}\right)^c * R_d \text{--------------------------} 5.2$$

Where R_T is the rainfall depth for any duration, t, R_d is the 24-h rainfall depth for different return periods. The extracted design storms representing T = 2 and T = 10 years return period were used as a reference to compare with the design storms constructed based on the WRF simulated HIRE. The WRF and standard IDF-based design storms are independent in terms of data used, and the method followed, but both produce rainfall properties of a given storm that can be used for flood hazard modelling. For comparison purposes, the two design storms are constructed for the same duration (2 hours) and time aggregation (10-minute), which is essential to make a fair comparison. The purpose of this comparison is mainly to see how the WRF design storms' rainfall properties determine the flood hazard characteristics evolve compared to that of the standard IDF design storms. The detailed statistical characteristics and derivation of the parameters in Equation 2 are less important and beyond the scope of this study.

In this study, the IDF design storms of T = 2 and 10 = years are compared with the WRF design storms expressed as the three quantiles visually in terms of their total rainfall amount (mm), peak intensity (mm/h), and the time dynamics. All design storms are defined with the time aggregation of a 10-minute interval, and also, to make a fair comparison, all design storms are considered the total duration of 2 hours. In equation 2, we used the 24-rainfall depth reported by KCCA (2010). As the design storm duration is considerably reduced (i.e., from 24-h to 2-h duration), the resulting rainfall depth is also reduced, resulting in lower rainfall depths for both return periods than the actual rainfall depth of 24-hour duration. The constants in equations 1 and 2 are taken from Fiddes et al. (1974), who at that time had only a few years of data regarding the whole of east Africa. In addition, (Fiddes et al., 1974) used a wider area to get the constants 'b' and 'c', and so they may be area representative but not for Kampala specific. Moreover, the constants are to be derived from sub-daily observations to extrapolate 24-hour rainfall to the part of the curve that is highly non-linear.

However, in the absence of detailed long-term sub-hourly observed data, the same procedure can be followed and used the existing constants to construct the IDF-AB design storms of 2 and 10 years.

5.2.4. Flood model openLISEM

To analyze the applicability of the constructed WRF design storms for flood hazard simulation, we used an event-based-integrated flood model called openLISEM (Baartman et al., 2012; Jetten, 2014; Umer et al., 2019). The model is an integrated spatial hydrological model that simulates infiltration excess runoff for extreme rainfall events and shallow floods in urban and rural catchments (Habonimana, 2014; Nurritasari et al., 2015; Pérez-Molina et al., 2017). A detailed description of the model is given in chapter 2 (section 2.2.4).

For this case study, the openLISEM model is set up at the upper Lubigi catchment, Kampala, with the constructed design storms to simulate the flood hazard. Other model input data, such as land use fraction, soil properties, and channel dimensions, were kept the same for all simulations.

The WRF design storms' appropriateness for flood hazard modeling is evaluated by using each design storm as input to the hydrologic model. In general, the flood model is simulated using WRF design storms and 2 for the design storms constructed using the alternating-block method). Finally, the constructed design storms as a tabular form are used as an input to the flood model to evaluate the WRF design storms' appropriateness for flood hazard modeling. The result of the flood model will be analyzed in terms of flood hydrographs, flood extent maps, flooded area, and structural damage using the model results from the alternating block method as a reference. The simulated flood hydrograph analysis at the main outlet is essential to understand whether the channel size is sufficient to drain a peak flood of each design storm compared to the existing channel capacity. The analysis of the results in terms of flood extent and flood area is also useful to understand better the urban footprint exposure to the flooding triggered by different design storms. To emphasize the applicability of the WRF design storms in terms of flood exposure, the comparison in terms of structural damage will also be carried out by considering Kampala's average building size of 90 m² (Sliuzas et al., 2013).

The WRF design storms' appropriateness in simulating the flood extent will be compared with the results from the IDF-based flood model results through pixel-by-pixel comparison using F statistical measures, which has been used in many flood extent studies (Schubert and Sanders, 2012; Yan et al., 2014; Amarnath et al., 2015). Specifically, the simulated flood extent maps using the WRF design storms are compared with AB2yr/AB10yr using a simple aggregate performance measure, F, following a similar procedure presented in several flood extent studies (Aronica et al., 2002; Horritt and Bates, 2002; Amarnath et al., 2015). The F is calculated as:

$$F = \frac{A}{A+B+C} \quad \text{-----------------------------} \quad 5.3$$

Where 'A' is the number of cells correctly predicted by both WRF design storms and the AB2yr/AB10yr; 'B' is the number of cells predicted as flooded with WRF design storms that are simulated non-flooded by the AB2yr/AB10yr (over-estimation); 'C' is the number of cells simulated as non-flooded with WRF design storms that are simulated as flooded with AB2yr/AB10yr (under-estimation). The F performance measure is applied here to investigate the WRF design storms' appropriateness for flood extent modelling compared to AB2yr/AB10yr based on the aggregated score, which varies between 0 and 1; a higher value is better.

5.3. *Case study*

We choose Kampala, the capital city of Uganda, as a case study to test the method. The city is an ideal location to test the method because it is one of the exemplary sub-Saharan African city's frequently affected by flooding. At the same time, the lack of high-quality rainfall data hinders the proper flood hazard modelling for managing this recurrent flooding. Advances in the methodology, such as the one introduced in this study, to utilize the low-cost model output data for flood hazard modelling, are essential to make the city more resilient.

The city is located near Lake Victoria at the central latitude of 0^0 '19' N and longitude 32^0 '35' E and has about 350 km^2 total area (see **Figure 1.2,** section 1.5). The high-intensity rainfall events that are mainly influenced by the inter-tropical zone (ITCZ) and the topography of the Lake Victoria basin, combined with soil information properties and urban expansion, are already triggering the localized flooding in the city (Pérez-Molina et al., 2017; Umer et al., 2019). The threat of urban flooding in the city is also aggravated by the unplanned urban expansion in former wetlands and poor drainage management of the surrounding hills (Douglas et al., 2008; Sliuzas et al., 2013). Consequently causing estimated annual damage between $1.3 million and $7.3 million and is expected to increase under changing climate conditions (Taylor et al., 2015).

The study area considers the upper Lubigi catchment (polygon represented by the yellow color in **Figure 1.2, section 1.5**) within Kampala city as a case study to investigate the applicability of the constructed designs storms for flood hazard modelling. The catchment's currently functioning drainage system was designed and implemented based on the 2002 and 2010 masterplan (KCC, 2002; KCCA, 2010). According to the master plan, the 'primary drains' (*i.e.*, the widest channels draining the main valleys) and the former wetlands are canalized and widened. At the same time, narrow culverts are replaced by a series of large box culverts to drain a peak discharge of about 67 m^3/s, which represents the 24-hour duration design storms of the 1-in-10-year return period (Sliuzas et al., 2013). In the master plan, it is also reported that the secondary and tertiary drainage systems were designed to accommodate the flood peak of a 1-in-2 year event. The Upper Lubigi catchment is chosen for this case study because it represents an urban catchment where ground data essential for flood hazard modelling is available through the regular project and MSc fieldwork in collaboration with Makerere University (Sliuzas et al., 2013; Habonimana, 2014; Rossiter, 2014; Pérez-Molina et al., 2017).

5.3.1. Selected events

Four storm events that have caused flood hazards in the city were used to test the developed methodology. The first convective storm event occurred on 25 June 2012 with an observed daily total rainfall amount of 66 mm (a typical 2-year return period event). An automatic weather station (AWS) in the city indicated that the event lasted for only 1 hour and 30 minutes. The second storm occurred on 03 September 2013, with total daily rainfall of 52 mm. The third and fourth events occurred in the main rainy season on 13 and 16 April 2016 with 46 and 44 mm total rainfall. For the second, third, and fourth events, information on sub-hourly temporal distribution is not available as the automatic gauging station was not operational.

This study used two rainfall data sources. These are observed daily rain gauge data (see F**igure 1.2**) and satellite rainfall estimation from Climate Hazards Group InfraRed Precipitation with Station data (CHIRPS) (Funk et al., 2015). Sub-daily rainfall data from AWS is available only for the 25 June 2012 storm, and thus, for consistency, the WRF model verification is only conducted by using daily rain gauge data collected from the WMO global daily summary of the day. Both CHIRPS and rain gauge observations are available for the four individual events considered. CHIRPS data is available at a daily time step and spatial resolution of 5 km, and it is used as the areal average of the grid value extracted to the WRF innermost domain. In contrast, a comparison of WRF simulation with the gauging station is carried out with respect to the grid value at the gauging location.

5.3.2. *Existing IDF curves*

In this study, the existing design storms of T = 2 and T = 10-year return periods are obtained from the pre-established IDF curves of Kampala. The pre-established IDF curves of Kampala are derived from rainfall depths of different return periods following the procedure illustrated by (Mugume and Butler, 2017), and it presents the graphical illustration of the relationship between rainfall intensity (mm/h) and duration *(h)* (**Figure 5.2**).

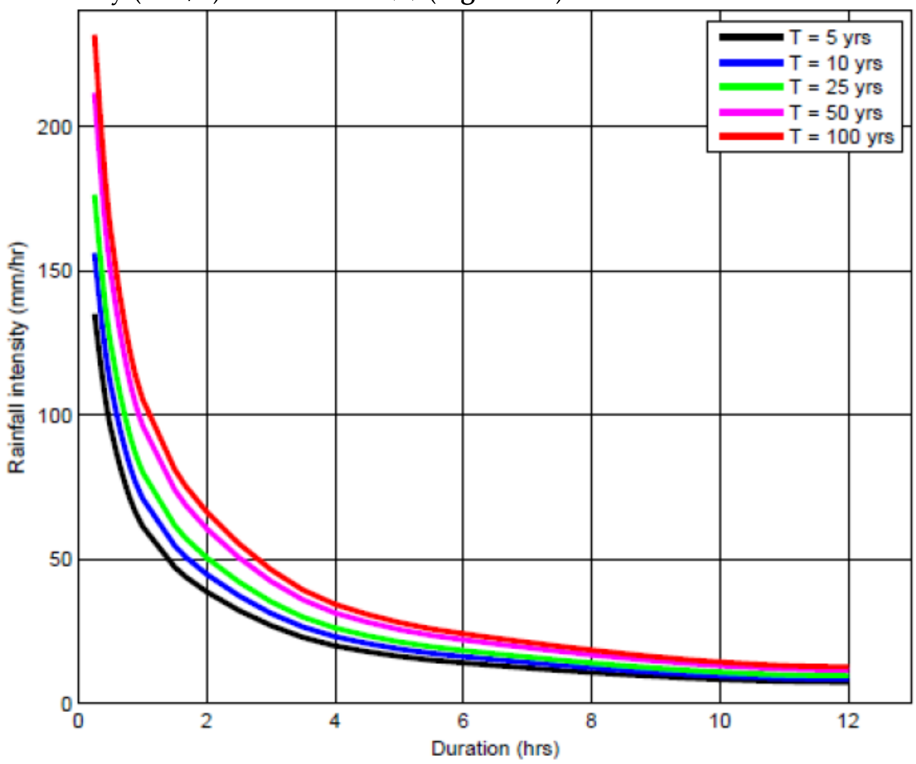

Figure 5.2 Pre-established intensity-duration-frequency curves for Kampala (Source: (Mugume and Butler, 2017)). The curves show that for all T, large variations in rainfall intensities occur at rainfall durations less than 4 hours. In our current study, we will derive design storms with a rainfall intensity duration of 2 hours to comply with the rainfall intensity duration of the WRF simulated events.

Table 5.1 shows frequency analysis of the daily (24-hour) point rainfall depths for various return periods as collected from the literature. As shown in the table, the derived rainfall depths for the respective return periods are different, mainly because of the observed rainfall's short records and the applied methods. For the WRF design storms criteria, the minimum rainfall depth of 60 mm is used as a cutoff threshold, where 100 mm/h is the maximum peak intensity belonging to a rainfall depth of 60 mm. The KCC study (KCC, 2002) is adopted for deriving the IDF-based design storms of a given return period (i.e., T = 2 and 10-year events) because the city's flood plain maps and drainage systems are built based on these design storms.

Table 5.1 The derived 24-hour point rainfall depth of Kampala for different return periods (source, (KCCA, 2010), considered observed years 36; (Mugume and Butler, 2017), considered observed years 51; and (Fiddes et al., 1974), considered observed years 14).

Return period, T	24-h rainfall depth [mm] (Mugume et al.2017)	24-h rainfall depth [mm] (KCC study 2002)
2	59.9	66
5	80.3	87
10	92.8	103
25	104.8	123.8
50	125.8	143
100	137.8	162

5.4. Results

This section presents the results on the developed design storms from two main aspects: (1) the results of WRF design storms derived through the representative gridcell-events, and (2) the comparison of WRF design storms with that of the alternating-block method in terms of their rainfall properties.

5.4.1. WRF design storms

i. Simulated high-intensity rainfall events

Four HIREs used for design storm construction are simulated using the optimum WRF parametrization combinations (Umer et al., 2021). The simulated daily precipitation for the inner domain of WRF at 1 km spatial resolution is shown in **Figure 5.3**. During events in the non-main rainy season (i.e., 25 June 2012 and 03 September 2013), patchy rainfall occurs over the catchment, where events in the main rainy season (i.e., 13 and 16 April 2016) show a relatively evenly distributed rainfall over the catchment.

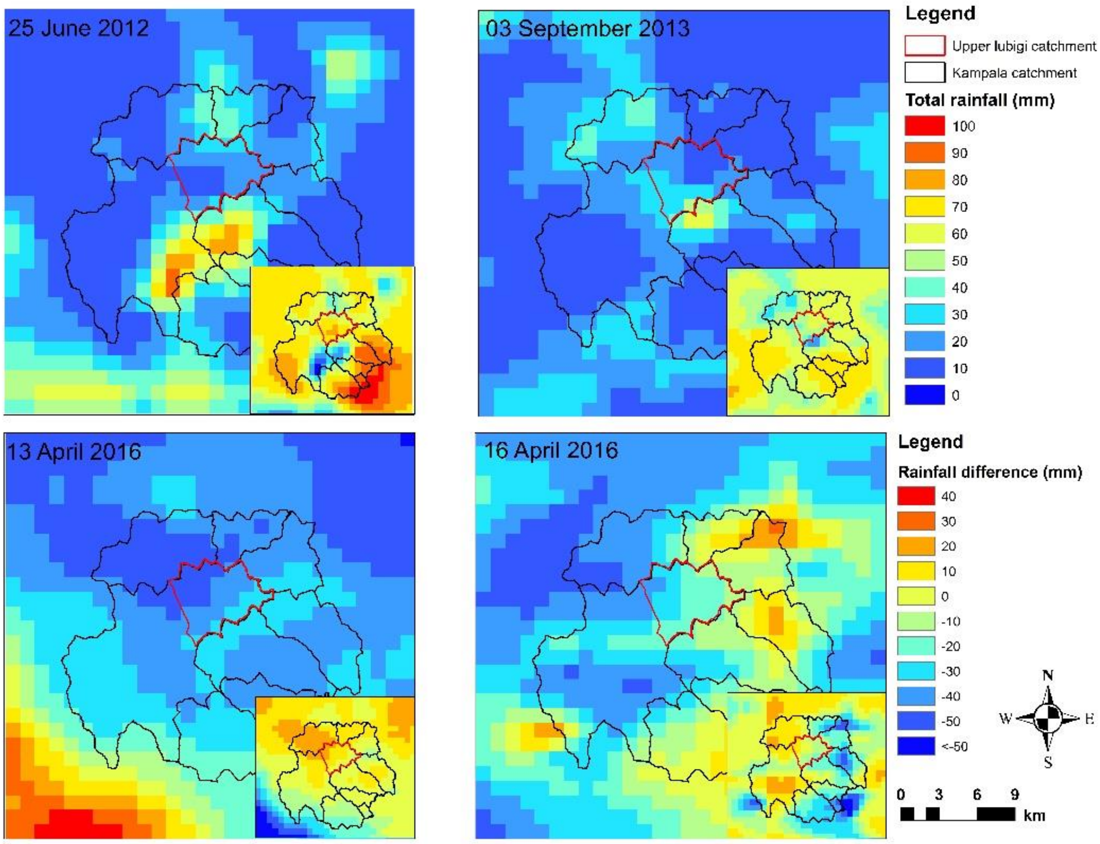

Figure 5.3 Simulated 24-h rainfall amount for four different events in the innermost domain of the WRF model. The insets in the bottom-right corner are the subtractions of the 24-h accumulated rainfall simulations from that in the CHIRPS observation.

Table 5.2 compares the simulated 24-hour rainfall amount with the gauging station and CHIRPS in the inner domain of WRF. For 25 June 2012 and 03 September 2013, the simulated grid cells 24-hour rainfall amount at the gauging location is very low, with the differences between the observation and simulation of about +43 and +33 mm, respectively. The big difference between the observation and simulation rainfall amount at the gauging location is attributed to the sparse distribution of the simulated events. The heterogeneity in the simulated events in this season is also indicated by the lower area-averaged rainfall differences between simulation and CHIRPS. The rainfall events in the non-main rainy season are mainly influenced by the mesoscale convective system (e.g., Lake Victoria topography), which results in patchy rainfall over the catchment.

In contrast, in the case of 13 April, 2016 and 16 April 2016, the simulated grid cell's 24-rainfall amount at the gauging location is close to the observation with the differences of 2.6 and 6.5 mm, respectively. The areal-averaged rainfall amount for 13th and 16th April 2016 is 46.5 and 27.2 mm, which is much higher than the CHIRPS amount. Compared to the CHIRPS, the higher areal-averaged rainfall amount indicates the relatively uniform gridcell-rainfall amount simulated over the catchment and suggests that the prevailing weather is more of a synoptic-scale system. Hence, the distribution of the simulated rainfall amount is relatively homogeneous, covering more areas than the events that occurred in June and September (**Figure 5.3**).

Table 5.2 Comparing WRF rainfall with the stations and CHIRPS rainfall for the best physics combinations simulated for four different rainfall events caused floods hazard in Kampala, Uganda. The areal rainfall amount is the average of all grids in the innermost domain of WRF. CHIRPS is first re-grid to the inner domain of WRF, and then the average of all grids similar to the WRF domain is used. The difference is the substruction of simulation from observed.

Simulated events	Observed Rainfall (mm)	Simulated rainfall at gauging location (mm)	The difference at gauging location (mm)	CHIRPS rainfall Area average (mm)	Simulated rainfall Area average (mm)	Difference Areal (mm)
25 June 2012	60.1	16.9	+43.2	16.0	18.0	-2.1
03 September 2013	52.1	19.0	+33.1	4.7	11.2	-10.5
13 April 2016	46.0	43.4	+2.6	13.4	46.5	-33.1
16 April 2016	43.9	37.4	+6.5	19.1	27.2	-8.1

ii. Potential grid cell selection

Step 1 in constructing a WRF design storm is to identify the potential gridcell-events that can cause the flood hazard. We considered only WRF grid cells in the inner domain with the storm's total rainfall amount above 60 mm and a peak intensity equal to or above100 mm/h, following the criteria introduced in section 5.2.2 (I). Figure 5.4 shows the relationship between the simulated storm's total rainfall amount and peak intensity for the four events in the inner domain of WRF. As shown in the figure, we have four locations considering 60 mm of rainfall amount and 100 mm/hr of peak intensity as the standard point: Upper and Lower left, and Upper and Lower right.

The upper right of each graph in (Figure 5.4) represents grid cells during the storm with total rainfall amount and peak intensity equal to 60 mm or 100 mm/hr. The grid cells in the upper right are the potential grid cells selected for WRF design storm construction and are described in the next section. The upper left's grid cells have a high rainfall volume but a peak intensity of less than 100 mm/h. The rainfall events in this area can cause the flood, but possibly with a slower response and with a lower flood peak. The lower left represents grid cells during these four events with the lower rainfall amount and intensity. Therefore, this area represents too little rainfall to trigger the urban flood for the desired return period. The lower right location represents grid cells of these four events with rainfall amounts lower than 60 mm, but higher rainfall intensity above 100 mm/h. The rainfall in this location represents short-duration, high-intensity events and can be very important for flood control elements such as culverts. The numbers of potential gridcell-events that fulfill the criteria and are then selected for design storm construction are 6, 43, and 45, for 25 June 2012, 13 April 2016, and 16 April 2016, respectively, while the 03 September 2013 event is excluded as zero grid-cells fulfilled both criteria.

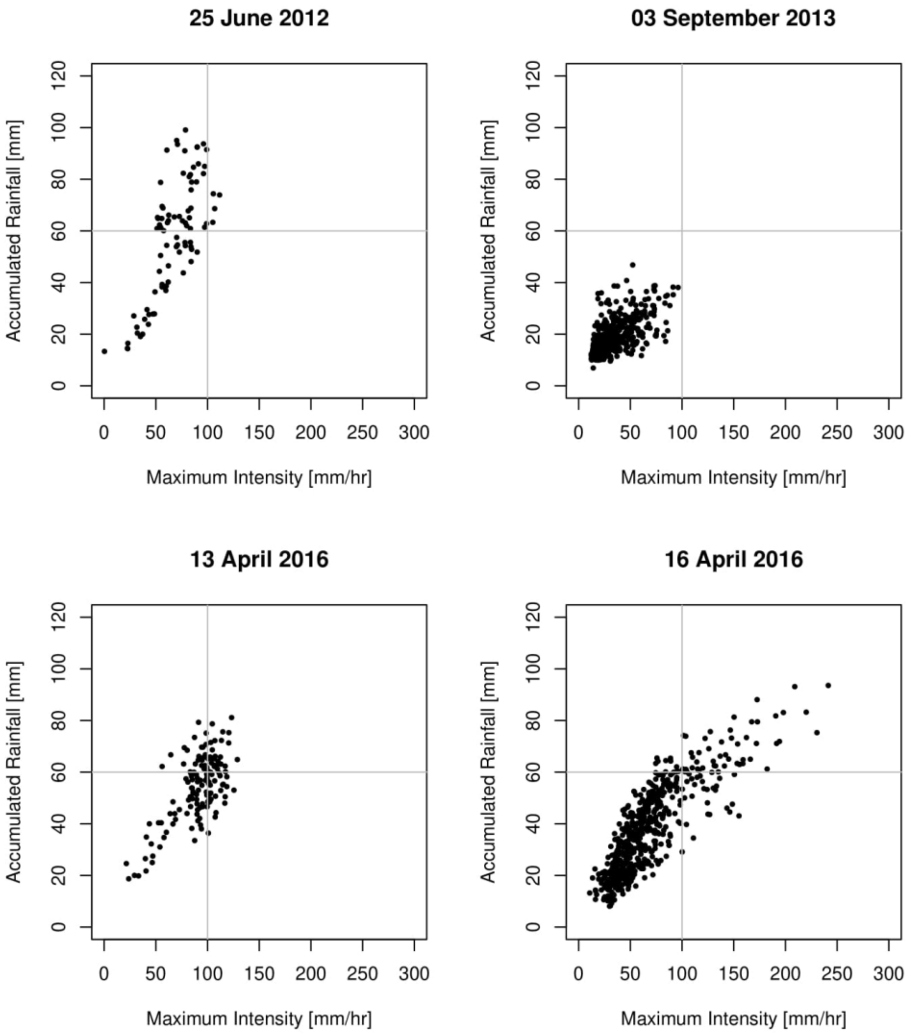

Figure 5.4 Relationship between storm's rainfall amount and peak intensity for four events considered in this study; the 03 September 2013 event is not used for this study as the simulated event does not fulfill the criteria. Each dot is a gridcell within the inner domain of WRF.

iii. Representative grid cell selection

In the second step, to select the representative gridcell-events in the 1st quadrant that are used to define the WRF design storm, we used a quantile expression of the cumulative rainfall event (see section 5.2.2 (II)). **Figure 5.5** summarizes the corresponding results for the three HIREs. As shown in the top row figures, the PDFs show a near-gaussian distribution only for the 13 April 2016, whereas for the events on 25 June 2012 and 16 April 2016, the distributions appear bimodal and positively skewed, respectively. The bottom row in Figure 6 shows the cumulative distribution functions (CDF) for the three considered rainfall events are. The quantiles Q = 0.025, Q = 0.50, and Q = 0.975 are highlighted in grey and are considered as the representative rainfall events defined as the WRF design storms.

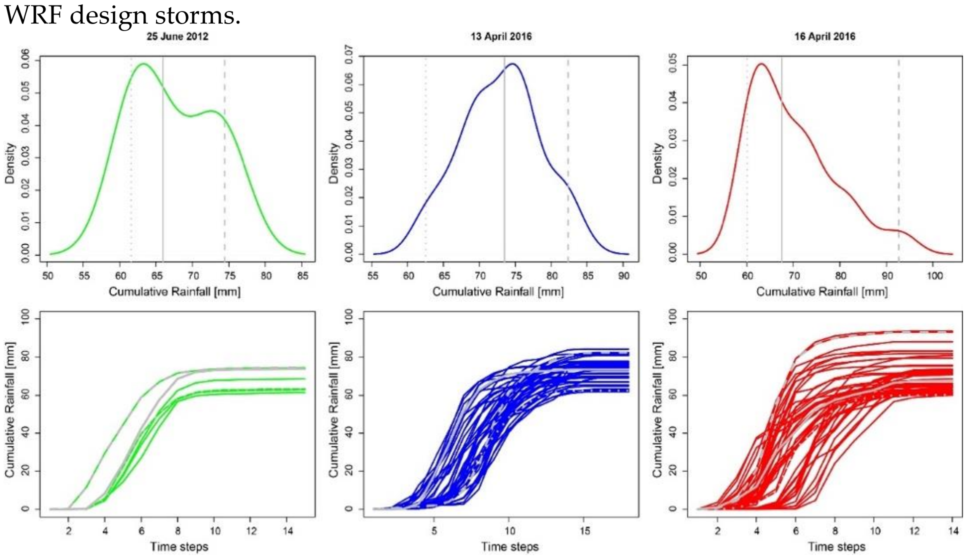

Figure 5.5 The results of quantile function: (Top) Density distribution; (bottom) Cumulative curves of the gridcell-events with the storms' rainfall amount equal or exceeding 1-in-2 year return period event. Each line in the bottom graphs represents the time series of the dots in Figure 5.4. The grey lines represent percentiles of the total rainfall amount: the smoothed grey line represents the median, the dotted grey line represents the lower quantiles, and the dashed grey line represents the upper quantiles.

Following this quantile expression, we have defined nine WRF design storms (i.e., the three grey lines that are shown in **Figure 5.5** for each event). For simplicity, the acronyms for the WRF design storms are as follows: lower quantiles (hereafter 'WRFL'), median (hereafter 'WRFM'), and upper quantiles (hereafter 'WRFU'). Hence, each event's WRF design storms are an acronym as WRF1L, WRF1M, and WRF1U for 25 June 2012, WRF2L, WRF2M, and WRF2U for 13 April 2016, and WRF3L, WRF3M, and WRF3U for 16 April 2016.

5.4.2. *Comparing design storms*

To compare the WRF design storm with the IDF-AB design storms, we considered three properties of the developed design storms as relevant: the total rainfall amount (mm), peak intensity (mm/h), and time dynamics. Time dynamics are the peak intensity's temporal characteristics, which include the time to peak intensity and the elapsed time for the derived cumulative rainfall. These rainfall properties are summarized in **Table 5.3** and **Figure 7**, including the IDF-based design storms' properties.

Table 5.3 Basic properties of the design storms constructed using WRF and the alternating-block method.

	Lower Quantile (WRFL)			Median Quantile (WRFM)			Upper Quantile (WRFU)		
Design storm	Peak Intensity (mm/h)	Cumulative rainfall (mm)	Time to peak (minute)	Peak Intensity, (mm/h)	Cumulative rainfall (mm)	Time to peak (minute)	Peak Intensity, (mm/h)	Cumulative rainfall (mm)	Time to peak (minute)
WRF1	104.8	63.2	50	111.5	73.7	50	105.8	74.7	30
WRF2	103.2	62.3	60	107.0	73.5	60	135.0	82.1	60
WRF3	135.1	60.1	60	116.3	67.6	50	209.0	93.3	50
AB2yr	110.9	58.2	70						
AB10yr	174.7	91.7	70						

i. Cumulative rainfall

Cumulative rainfall amount is the leading property that characterizes the constructed design storms. As shown in **Table 5.3**, the derived total rainfall depth for T = 2 and 10 years events (i.e., 'AB2yr' and 'AB10yr') is 58.2 and 91.7 mm. The result shows that compared to AB2yr, the total rainfall amount is overestimated for all cases that is by +10 % for WRF1L, +7 % for WRF2L, and +3 % for WRF3L. For all three WRF simulated HIREs, the total rainfall amount for WRFM is also higher than that of AB2yr but slightly lower than that of AB10yr. In the case of WRFU, the total rainfall amount is within a range of 16-35 mm compared to that of the AB2yr storm, which indicates that the WRFU result is about half higher than that of the AB2yr event. Compared to AB10yr, the total rainfall amount for WRFL and WRFM is considerably lower. The result shows that, compared to AB10yr, the total rainfall amount is underestimated by -23 % for WRF1U and -12 % for WRF2U, but overestimated by +0.2 % for WRF3U.

ii. Peak intensity

As **Figure 5.6** shows, the derived peak intensity for AB2yr and AB10yr is 111 and 175 mm/hr. The WRF design storms' peak intensities vary between 103 mm/h for WRF2L to 209 mm/h for WRF3U mm/h, which are relatively close to that of AB2yr and AB10yr, respectively. Compared to AB2yr, WRF3L overestimated by peak intensity by +18%, but underestimates the peak intensity for WRF1L and WRF2L, with the differences of -6 % and -8 %, respectively. The result also shows that, compared to AB10yr, the WRF1U and WRF2U underestimates the peak intensity by -65 % and -29 %, but overestimated for WRF3U by +18 %.

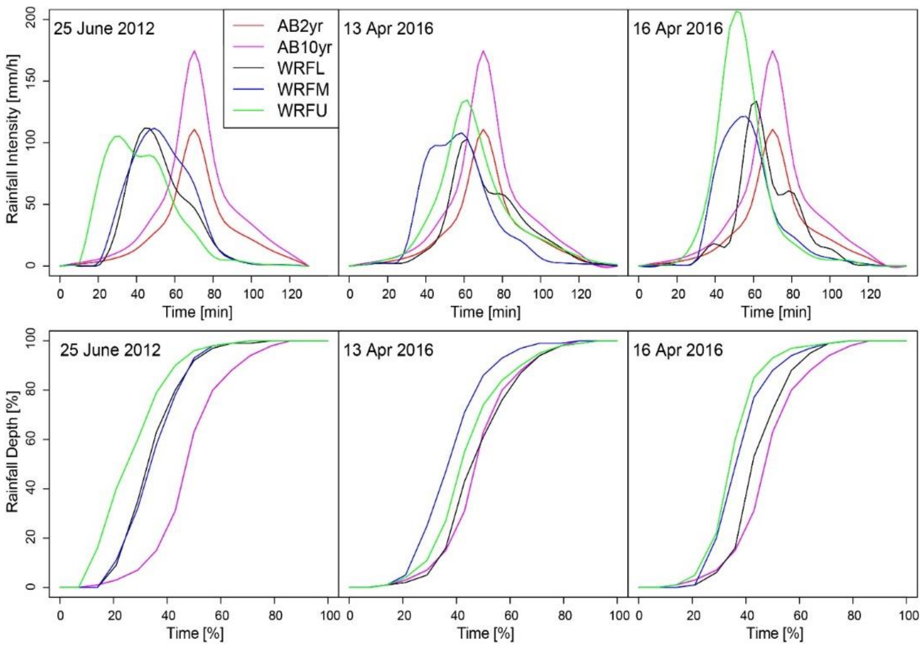

Figure 5.6 Constructed design storms: peak intensities and cumulative curves for WRF and alternating-block design storms. Cumulative curves for AB2yr and AB10yr events are overlapped.

iii. Time dynamics

The third relevant property of the constructed design storm is the derived peak intensity's temporal characteristics, including the time to peak intensity and the elapsed time for the derived cumulative rainfall (**Figure 5.6**, bottom row). As shown in the figure, the peak intensity for IDF-AB design storms is attained at the center of the total duration. One of the IDF-AB design storm characteristics is that the derived peak intensity is attained at the center of the storm duration, which does not resemble the simulated events, particularly considering the convective storm with peak intensity reach immediately after the events. Notably, for all WRF1 design storms, the maximum intensity is reached 20-40 minutes earlier than the alternating-block design storms. Similarly, for WRF2 and WRF3, the peak intensity attains its maximum about 10-20 minutes before the alternating-block design storms. While this may not be important for flood hazard analysis, it may be relevant for early warning studies, where time to peak rainfall and peak discharge is essential.

The design storm temporal pattern can also be analyzed by comparing the cumulative rainfall depth and elapsed time expressed as the percentages (**Figure 5.6**, bottom row). As shown in the figure, the pattern of all design storms is similar. The nearly leveled slope represents the beginning and ending section of the storm, connected with a sharp rise in the center, representing a higher rainfall intensity and a significant portion of the total rainfall amount. For most WRF design storms, the total rainfall amount of more than 60 % occurs between 30 % to 50 % of their duration, which is higher than the IDF-AB, in which over 50 % of rainfall amount occurs between 50 % to 70 % of its duration.

5.5. Results of flood hazard modelling

To investigate the WRF design storms' appropriateness for flood hazard modelling, we used the nine design storms illustrated in (**Figure 5.6**, top row) as input to the openLISEM model (section 5.3.3). The model results produced by using AB2yr and AB10yr are used as a benchmark. The flood model outputs are discussed in terms of flood hazard characteristics, including flood hydrographs, flood extent maps, flood areas, and flood impact on the number of buildings.

5.5.1. Flood hydrograph

Figure 5.7 shows the resulting hydrographs at the catchment outlet for 11 design storms (i.e., 9 for WRF design storms and 2 for the alternating-block method). As shown in the figure, a similar low peak discharge is obtained when using AB2yr as well as the WRF design storm with the lower total rainfall amount and peak intensity (i.e., WRFL). In contrast, the highest peak discharge is obtained when using the AB10yr and WRFU design storms, which have a higher total rainfall amount and peak intensity. In particular, a flood peak obtained at the catchment outlet when using WRF3U is about 70 m^3/s, which is above the reference flood control structure's capacity (i.e., 67m3/s).

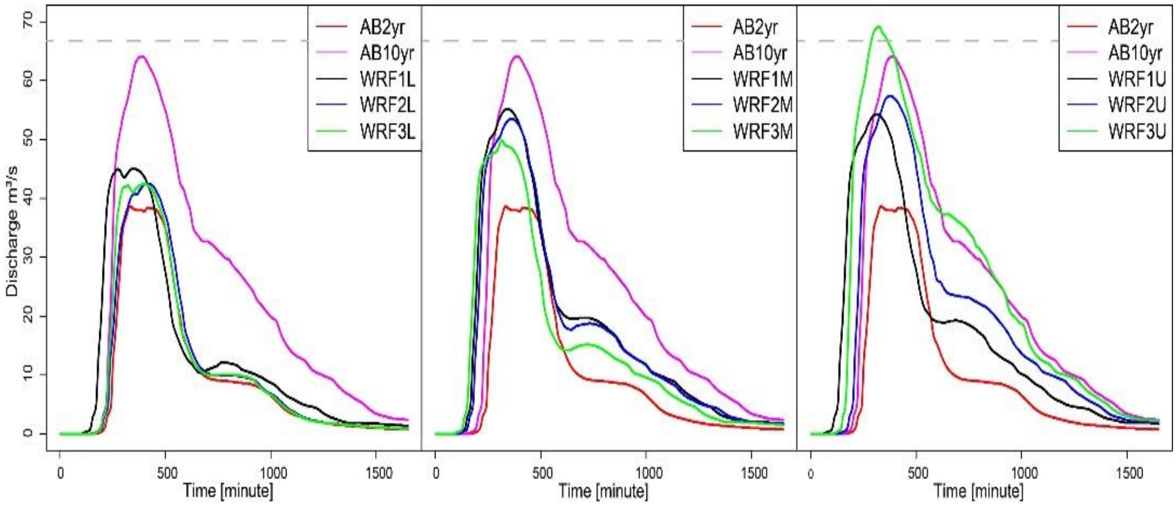

Figure 5.7 Hydrographs at the catchment outlet: From left to right: WRFL versus AB2yr and AB10yr; WRFM versus AB2 and AB10yr; and WRFU versus AB2yr and AB10yr. The dashed horizontal line represents the reference discharge of 67 m3/s.

5.5.2. Simulated flood extent

Table 5.4 shows the calculated F scores for 9 WRF design storms benchmarked with AB2yr and AB10yr. Compared to the AB2yr event, WRF1L, WRF2L, and WRF3L produce a better flood extent with higher F scores of 0.87, 0.94, and 0.94, respectively. Compared to AB2yr, WRFUs overestimate the flood extent, which results in a lower F score (**Table 5.**4, first row). On the contrary, considering the AB10yr event as a benchmark, WRF1M, WRF2U, and WRF3U produce a better flood extent with higher F scores of 0.85, 0.89, and 0.91, respectively. Compared to AB10yr, WRFLs underestimate the flood extent, which results in lower F scores (**Table 5.4**, second row). As shown in the table, the aggregate score decreases as we go from left to right in the table (i.e., from WRFL to WRFU) when comparing with AB2yr) and vice-versa when comparing with AB10yr. The results indicate that for WRFL, the comparison with AB2yr is more appropriate, while for WRFU, the comparison with AB10yr is more appropriate.

Table 5.4 Model results of flood hazard characteristics in the Upper Lubigi catchment in Kampala: (1) & (2) Performance measures, F score, of WRF flood extent benchmarked with alternating-block design storms; (3) calculated total flooded area based on water deeper than 10 cm; (4) number of structures (buildings) affected by flood calculated based on an average structure size of 90m²

Flood hazard characteristics	Design storms										
	AB2yr	AB10yr	WRF1L	WRF2L	WRF3L	WRF1M	WRF2M	WRF3M	WRF1U	WRF2U	WRF3U
(1) Flood extent (F score, benchmarked by AB2yr)			0.87	0.94	0.91	0.76	0.78	0.79	0.78	0.73	0.59
(2) Flood extent (F score, benchmarked by AB10yr)			0.74	0.67	0.71	0.85	0.83	0.82	0.82	0.89	0.91
(3) Flood area (sq.km)	3.3	5.9	3.8	3.2	3.7	4.3	4.2	4.1	4.1	4.7	7.3
(4) Affected building (Number)	4258	7258	5058	4425	4777	5977	5850	5711	5761	6299	8223

5.5.3. Flood depth

In order to verify the applicability of the WRF design storms in producing flood depth maps used for flood hazard analysis, we compare flood depth maps produced when using the 9 WRF design storms with the results when using the IDF-AB storms based on a visual comparison of the maps. Figure 9 shows the depths of food water in the catchment area produced when using the WRF and IDF-AB design storms. As shown in the figure, following the topography of the catchment area, the low-lying areas and wetlands are flooded when using all design storms with flood depths varying between 0.5 to 2.6 m. However, as we go from WRFL to WRFU or as the return period increases, so too do the flood depths, as would be expected. Thus, maximum water depths of 2 m and above are simulated when using WRFU and AB10yr. The results are compatible with previous studies in the catchment (Sliuzas et al., 2013; Umer et al., 2019), whose results indicated that the wetlands of the catchment are fully flooded with design storms of typical 2-year events or more.

In Fig. 9, red circle *a*, we showed the relevant location used for comparison of WRFL versus AB2yr. When using all WRFL, the simulated flood depths are between 1.5 to 2 m, but with AB2yr, the flood depth is between 1.0 to 1.5 m at the same place, which is due to the lower cumulative rainfall amount of AB2yr compared to that of WRFLs. In comparing WRFU with AB10yr (at circle *b*), the simulated flood depths are above 2.0 m in all cases. However, the number of grid-cells flooded with flood depths of greater than 2.0 m is more in the case of WRF3U compared to AB10yr.

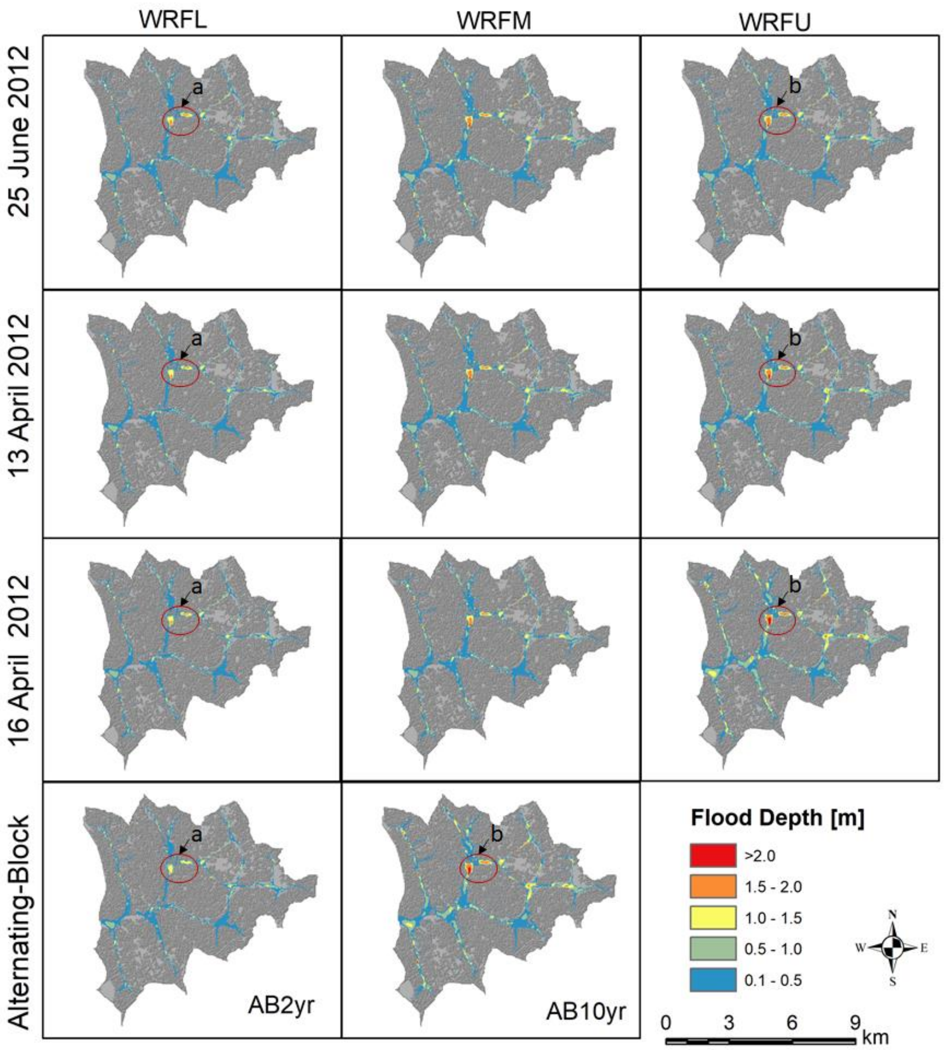

Figure 5.8 Comparison of flood extent map simulated using AB2yr/AB10yr and for WRF3 design storm at three arbitrary locations overlaid with the building of Kampala: (a) represents flood extent of WRF3L combined with AB2yr and AB10yr events; (b) represents flood extent of WRF3M combined with AB2yr and AB10yr events; (c) represents flood extent of WRF3U combined with AB2yr and AB10yr events. The underlying black/white image is a built-up/non-built-up area of Kampala.

As the intensity for the flooding is often expressed as the maximum depth at any grid-cell, a frequency distribution of that would be directly interesting for flood hazard analysis. Toward this, we produced the histogram of the water depths versus its frequency and compared the flood depths differences at any grid-cell when using the WRF and IDF-AB storms. As a showcase, flood depth differences per grid-cell between the WRF3 design storms and the IDF-AB storms are given in Fig. 10. As shown in the figure, for WRF versus AB2yr (Fig. 10, top row), the results with WRF flood depths are slightly higher; hence, the histogram differences are skewed in the positive x-direction. However, when comparing WRF versus AB10yr, except for WRF3U, the histogram differences in water depths are negative. For instance, in the case of 'WRF3L - AB2yr', the flood depths differences per grid-cell are concentrated around zero with the frequency of 90 %, while for 'WRF3U - AB2yr', the flood depths difference is greater than zero and the frequency around the zero value is 40 % with its distribution spreads toward the positive x-axis. The figure also shows that the WRF results have little bias/slight overestimation of flood depths when using the lower and median quantiles and large differences of flood depths when using the upper quantile design storm with respect to AB2yr. The figure also shows that the flood depths when using WRF are underestimated at WRF3L and WRF3M and slightly overestimated water depths at WRF3U with respect to the AB10yr. It is important to note that the maximum flood depths differences per grid-cell for 'WRF3L – AB2yr' and 'WRF3U – AB10yr' is less than 0.2 with frequency distribution concentrated near-zero value, which indicates that the WRFL and WRFU design storm can be relevant for 2-year and 10-year return period flood hazard assessment, respectively.

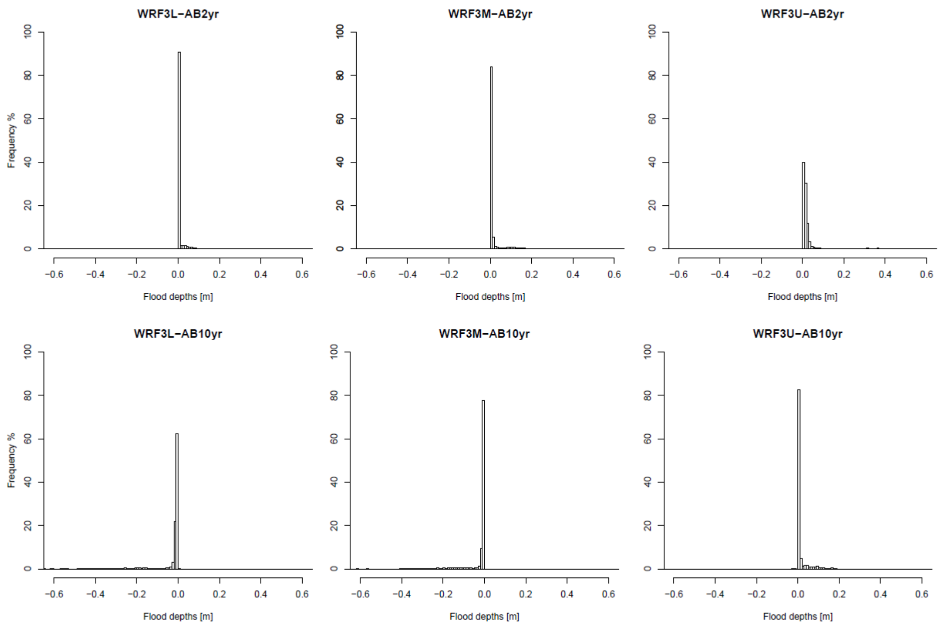

Figure 5.9 Frequency distribution (%) of the differences between the flood depths (meter) per grid-cell from the flood depth maps produced using WRF minus the IDF-AB design storms for the case of 16 April 2016 (WRF3).

5.5.4. Effects of flooding on buildings

To analyze the applicability of the constructed design storms for flood hazard modelling, we also compared the results in terms of flood effect on the building. The effect of the flood extent on the building is calculated considering the building's areal density of 90 m^2. **Table 5.4**, row 4, shows the number of building affected by the flood extent (water depth <10 cm) when using 11 design storms. Notably, the number of buildings affected by the flood extent when using WRF1L, WRF2L, and WRF3L are 5058, 4425, and 4777, respectively, slightly higher than when using AB2yr (i.e., 4258). In contrast, more buildings are affected by flood extent when using AB10yr (7258) and WRFU (i.e., 5761, 6299, and 8223 for WRF1U, WRF2U, and WRF3U, respectively), which is characterized by higher total rainfall amount and peak intensity. In all cases, the number of buildings affected by flood extent is well correlated with the inundated areas (see **Table 5.4**, 3rd Row).

Moreover, model results (not shown here) also indicated that for all 11 design storms, the number of buildings affected by the flood is more at lower water depth (i.e., 10 - 50 cm) and less at higher water depth (i.e., depths > 50 cm). For instance, due to the flood depth ranges 10 - 50 cm, the number of affected buildings is 3-9 times higher than at flood depths > 50 cm. The results show that the maximum flood depth is more confined in the non-built-up areas represented by wetlands, consequently less effect on built-up.

5.6. Discussion

The study presents a new method to get a location-specific design storm based on WRF simulated high-intensity rainfall events, which proved to be suitable for flood hazard modelling in the data-scarce area. The method presented is flexible as it can be based on any desired combination of event magnitude and peak intensity. The magnitudes can be based on disaster mitigation plans of the stakeholders in the areas. However, while the magnitude is relatively straightforward to derive from a Gumbel analysis, the peak intensity may not be well known. A peak intensity could come from high-resolution rainfall measurement, or in the absence of that, from satellite imagery (30-minute intensity) or even an IDF curve analysis. All of these have associated uncertainty. Rainfall measurements and IDF curves may not have long time records, so selecting a characteristic peak intensity is less evident when time series are not very long. Besides, the construction of valid IDF curves relies on storm data. Peak intensity can also be derived from satellite imagery, and for instance, GPM-IMERG has a 30-minute time interval with global coverage dating back to the year 2000. Therefore, the time series derived from these images is already 20+ years, but while aggregated values (3-day and weekly totals) show good agreement with ground measurements, the 30-minute intensities do not show a high correlation in general (Fang et al., 2019; Chen et al., 2020).

In this study, the data are based on WRF, but operating WRF is not an easy task. The parameterization needs to be properly done and is area-dependent. Purely as a method to derive design storms, this is a large task. However, many meteorological services in countries use the WRF model or other weather models for weather forecasting, so good knowledge on the local parametrization of a weather model may be locally available.

Weather models do not produce pixel-precise results, i.e., the spatial patterns of rainfall do not coincide with ground-based measurements. The patterns are a result of complex atmospheric physics of the entire lower atmosphere, and the interaction with the earth's surface can still be improved (Ryu et al., 2016; Paul et al., 2018). This is not immediately a problem for flood hazard analysis, as a hazard is not based on a real event but is a simulation of a potential situation: for a given storm of a known size and probability of occurrence, the potential maximum effect (i.e., water level and extent) is simulated. Therefore, that event can be derived from anywhere as long as it is representative of the weather patterns of Kampala (in our case). Practically this was done by selecting the grid cells in the inner domain area as being representative, but this is only a practical choice. More research would be needed to determine which area can be considered representative for an area.

5.7. Conclusion

The main aim of this study was to present a new methodology to translate WRF simulated high-resolution convective rainfall events into a design storm form and evaluate its performance against the existing alternating-block method design storms obtained from the pre-established IDF curves. The differences between the WRF and IDF-AB design storms are evaluated from the point of view of flood hazard modelling and then discussed the strengths and weaknesses of our proposed method. In order to do this, we developed WRF design storms based on the spatial distribution of high-intensity rainfall events simulated at high spatial and temporal resolutions. The potential gridcell-events were selected and translated to the WRF design storm form using a quantile expression of the cumulative rainfall distribution. Consequently, three different WRF design storms per event were constructed: Lower (WRFL), median (WRFM), and upper quantiles (WRFU). The results are compared with IDF-AB design storms of 2 and 10-year return periods (i.e., AB2yr and AB10yr) to evaluate differences from a flood hazard assessment point of view. We found that the developed WRF design storms performed well compared to the alternating block design storms, particularly the results between WRFL vs. AB2yr and WRFU vs.AB10yr. WRFLs produce hydrographs similar to that of AB2yr, with their peaks quakily attenuated by the existing structure and the wetlands. The WRFUs also produce similar hydrograph similar to AB10yr, except for WRF3U, which has a slightly higher peak hydrograph (+4 %) than the existing channel capacity. In order to evaluate the appropriateness of the WRF design storms for flood hazard assessment, we compared the maximum flood depth at every grid-cells in terms of frequency distribution. We found that for both WRFLs vs. AB2yr and WRFUs vs. AB10yr, the number of the grid-cells and intensity of the flood depths are higher when using WRF design storms. Moreover, The use of WRF3U for flood hazard modelling leads to more maximum flood depths of over 2 m per grid-cells compared to AB10yr.

Nevertheless, the overall definition of the WRF design storms is greatly affected by the selection criteria, which would subsequently affect the flood dynamics in the catchment. Notably, the chosen threshold can affect the lower and median quantiles even though the interest tends to focus on the extreme event represented by the upper quantile from the flood hazard point of view. In our case study, the flood in Kampala is considered hazardous with the design storm of a 2-year return period; as such, we decided on our threshold based on the existing local information to showcase the method. Besides, by using the quantile descriptions, the results would not be overly sensitive to the criteria. Eventually, the threshold could come from the regional information, not necessarily the accurate local information is needed.

The result suggests that the WRF design storm can be obtained from the grid-cell rainfall events, which are defined as the representative rainfall pattern over the catchment. This design storm can be considered as an added value for flood hazard assessment as they are closer to real systems that are causing rainfall. However, more research is needed on which area can be considered as a representative area in the catchment. The main weakness in using the NWP model output for flood hazard modelling in the data scarce-area is having a validated WRF rainfall product, as limited observed data can lead to modelling and model result uncertainties. Even with these uncertainties, the construction of design storms is considered solid and robust, as the three events gave rather similar design storms. More importantly, this quantile description allows for more diverse design storms, doing justice to the atmospheric systems causing large-scale or convective rainfall over the area. However, as many areas have validated numerical weather prediction models or have sufficient observed data to validate the model, this approach has the potential to be applied in many more regions to support Integrated Flood Management.

Chapter 6: Synthesis

Floods are one of the common natural disasters with the largest impacts on society. Urban floods are fluvial, coastal, pluvial, and flash floods that occur in cities (Vojinovic, 2015). With the rising trends in urbanization and climate change, urban flood risk is rapidly increasing because economic growth often does not result in effective prevention measures and flood-sensitive land-use planning (ten Veldhuis, 2011; Jha, 2012; Hammond et al., 2015). Integrated Flood Management (IFM) approaches are essential in reducing urban flood risk through proactive measures (Vojinovic, 2015; Debele et al., 2019; Sahani et al., 2019), which requires proper flood hazard and risk assessment as a basis.

Flood hazard mapping is one of the components of IFM, which often relies on flood modelling. These models are used to simulate flood characteristics, including flood extent, duration, depth, and velocities, which are used to define the flood hazard (Vojinovic et al., 2016; Baky et al., 2020). The flood simulation requires high-quality datasets, including precipitation with high resolution in space and time, soil information, urban land use information, topography, channel dimensions, surface roughness, and information of control structures. However, flood hazard assessment in many cities in developing countries is challenging due to the lack of high-quality data, especially related to topography and historical precipitation and discharge records. The lack of a high-quality dataset has resulted in flood hazard maps with high uncertainty, which hamper proper flood management (Tingsanchali, 2012; Juarez Lucas and Kibler, 2016). Nevertheless, the continuous improvements in high-resolution remote-sensing, geospatial data availability, and modelling capacities offer new opportunities to study flood hazards in data-scarce areas.

Therefore, the present study aimed to explore publicly available geospatial datasets and their integration with hydro-meteorological modelling systems to overcome the data-scarcity challenges, specifically, to explore the data of extreme rainfall, soil, and land-cover information for urban flood modelling. This thesis proposes that the existing problem with lack of soil information can be reduced by using the SoilGrids from the ISRIC soil database and its coupling with satellite-derived land cover data. At the same time, in the absence of high resolution observed rainfall data, Numerical Weather Prediction (NWP) can be used in the estimation of high-intensity rainfall events (HIRE) used for flood hazard assessment, although the uncertainty of the location of the convective storms is still difficult to address. However, given the fact that there is a lack of ground truth for bias correction of the open-source dataset, there might be uncertainty propagation from the open data sources to the flood modelling system, which is outside the scope of the current study.

6.1. Main contributions

The work contributes to localized flood modelling in the urbanized and data-scarce area by i) exploring different soil data sources providing the soil information applicable for flash flood modelling, and evaluating the effect of urbanization interferences on the soil information by incorporating the satellite driven urban land use fraction, ii) Evaluating the performance of the mesoscale numerical weather forecasting model WRF in simulating the HIRE in the data-scarce area, iii) explore the design storms of a given return period based on the WRF simulated HIREs for flood hazard assessment in the data-scarce area. The innovative aspect of this research is that, besides exploring open-source global datasets for flood modelling in the data-scarce area, the derived dataset is numerically integrated to advance urban flood hazard modelling. The research's practical application is mainly to support an integrated flood management system by producing flood hazards in an urbanized catchment with data limitations. A detailed explanation of the finding under each component is discussed in the next sections.

6.1.1. Exploring soil data sources for localized flood hazard modelling

This study (Chapter 2) explores different soil data sources to derive urban soil information for localized flood modelling. Three different soil databases have been evaluated for their applicability to drive the required soil information: (1) the FAO soil database (SMFAO), (2) SoilGrids from ISRIC soil database (SMSG), and (3) soil information from *in situ* measurement and then extrapolated to the whole catchment through soil-landscape relationships (SMLS). The soil information derived from the three soil databases would directly be used as input to the flood model for localized flood modelling. However, in urban areas, the soil information derived from global soil databases has its limitations because most of the urban area is built-up, and soils have often been modified, which is difficult to incorporate in the soil databases. In Kampala's case, wetlands (i.e., areas covered by clay soil) are highly degraded as wetlands largely changed into a settlement, and agricultural cultivation (KCCA, 2010), thus, highly compacted.

Moreover, there is also increasing in impervious surface area (e.g., Perez Molina (2019) shows that in 2004 the number of buildings was 15522 but in 2010 increases to 35253), which dominantly modifies the topsoil. Therefore, how the presence of sealing, compacted soil, and fragmented vegetation areas related to the infiltration processes is less known. For this reason, a combination of the global soil databases with the satellite-derived urban land cover information was made to derive the effective soil information needed for the flood model, which is a novel and useful strategy.

The derived soil information is then used as the input to openLISEM integrated flood modelling system to assess their impact on flood dynamics in the urbanized catchment. The impact analysis is evaluated as the compacted and uncompacted soil condition. The results indicated that the flood dynamics are highly sensitive to different soil databases, and the incorporation of soil compaction into the soil information has the largest impact on the flood dynamics in the catchment. The model simulation result indicates that SMSG is the best soil data source for localized flood modelling in urbanized areas in the absence of in situ measurements. The study's outcome showed that open-source data choice strongly influences both the quantity and spatial variability of infiltration, which directly affects runoff and flooding. On top of that, the effect of sealing and compaction is equally essential and nearly outweighs the differences caused by the use of different soil databases. Moreover, the flood model results obtained when using the compacted soil information show flood extent maps close to the actual flood boundaries, which can be considered as a feasible model setup for further flood modelling in the Kampala catchment.

The freely available global soil database is a vital source for advancing urban flood modelling in data-scarce areas. However, as the soil database alone cannot provide detailed urban soil structure information, for example, compacted soil versus uncompacted soil, the LULC, and soil database integration would be essential to prove the optimal soil information required for flood modelling. Thus, as we have made in the Kampala case, one has to take into consideration that soil data pre-processing should be done with respect to urban soil compaction and vegetation cover. Thus, interferences of urbanization on soil structure information can be overcome by incorporating satellite-derived LULC into soil information extracted from global soil databases. Moreover, reliable flood characteristics are better simulated when incorporating the satellite-driven urban land use fraction into the soil database. Hence, it is highly recommendable for future application of the soil databases in the urbanized catchment to consider the impact of urban compaction on the soil databases. The urban soil information derived from the global soil databases that consider the effect of urban features through explicit consideration of land cover data, as presented here, forms a practical solution to solve soil data limitations for proper flash flood modelling.

The soil water information produced here is essential for proper flood simulation (i.e., for rainfall-infiltration dynamics) in the urbanized areas. Thus, good soil moisture data for further flood hazard modelling is used in this thesis. The results produced here are essential information for proper flood simulation in the urbanized area, and thus, acceptable soil data for further flood modelling used in this thesis.

However, besides soil physical structure, urbanization can also affect the soil texture, and detailed information on this important issue is missing from the soil databases. For instance, the idea that soil is always removed and building materials are used and cannot be mapped is only partly true. For example, in rapidly expanding cities like Kampala, people just build on natural soil because they have no money for a foundation. The soil texture is not altered. Only in the case of high-rise buildings and large construction do we have building materials, and this issue needs to be addressed in the future. As a procedure, the soil properties maps from soil databases need to be transformed to hydrological parameters for which pedotransfer functions are used. However, there is a range of possibilities here. We show only one set (Saxton and Rawls, 2006), but other pedotransfer functions may give different results. So there remains a high uncertainty. Moreover, this study shows how to incorporate soil structural changes such as compaction and the effect of vegetation cover, but these need to be verified on the ground. We recommend here that there is **urgent action needed to collect data on urban soils for disaster risk management, whether it is for flood management, sustainable urban drainage systems, urban food production, or any other predictions in which soil characteristics play a large role.**

6.1.2. Performance evaluation of the simulated rainfall events

Besides urban soil information, spatial precipitation data is often lacking in many developing countries. A numerical weather prediction (NWP) model, such as the Weather Research and Forecasting (WRF) Model, is an important tool to produce rainfall products for localized flood modelling in data-scarce environments. Although the WRF model has been widely used for modelling extreme rainfall events (Jeworrek et al., 2019; Sikder et al., 2019), its applicability in data-scarce areas for flood modelling at catchment scale with high spatial-temporal resolutions is not fully explored. Moreover, besides the complexity of the rain-producing systems in Equatorial East Africa with highly varying extreme rainfall events (Anyah, 2005; Chang'a et al., 2020), the set-up of the WRF model for an urbanized catchment is also another challenging issue. For instance, data for model initialization and boundary conditions are still poor. All parameterization schemes in the NWP model are designed for the mid-latitude weather system, and it may not fit properly the tropical weather system. Besides, due to a lack of observations (both ground and upper air observations), model verification and calibration is challeginging. The work presented in this thesis focused on the application of the WRF model simulation of HIRE for proper flood modelling (Chapter 3 and 4). This work's novelty is the use of the parametrization combination procedure and the configuration of the WRF model with the reliable urban fraction map that represents the correct position and extent of the city. Furthermore, in this thesis, we used the latest ERA5 global reanalysis dataset as boundary conditions, while the soil hydraulic properties used in the WRF model was adjusted according the appropriate soil information derived from the SMSG database. Finally, the rainfall data required for flood modelling was dynamically downscaled to the Kampala catchment at high spatial-temporal resolutions of 1 km and 10-minute.

Chapter 3 evaluated the satellite-derived urban fraction's appropriateness in the WRF model for simulating high-intensity rainfall events in the urbanized area. Three different simulations are performed in order to distill the impact of changing urban fractions and adjusted urban parameters on the simulated rainfall. All model simulations are configured at high spatial (1 km) and temporal (10-minute) resolutions forced with the latest ERA5 global reanalysis dataset. The model result was validated using the rainfall observation from the gauging station and CHIRPS data. The results showed that the simulated rainfall using the updated urban fraction performs better with a relatively lower error. The satellite-derived urban map represents a more realistic extent and intensity of the urban fraction with a heterogeneous urban fraction, which results in more realistic rainfall simulations. The conclusion in Chapter 3 was that although the comparison of the simulated rainfall with observed rainfall is weak, the use of a satellite-derived urban fraction in the WRF model, which represents the correct position and extent of the city, is essential for rainfall simulation in the area.

In chapter 4, the procedure to select proper parameterization combinations of the WRF for proper HIRE simulation was evaluated through sensitivity analysis. Here, the WRF model set-up with the updated urban fraction is used for the WRF model simulation as the combination of microphysics (MP), cumulus parameterization (CP), and planetary boundary layer (PBL) (i.e., MP-CP-PBL). The analysis showed that the performance of the WRF model in simulating HIRE that triggers the localized flood depends on a proper selection of parametrization combinations. The validation results based on both area-averaged CHIRPS rainfall and locally measured rainfall showed that the event has a unique MP-CP-PBL combination. As CHIRPS rainfall does not provide the extreme rainfall event, we used it to indicate the rainfall's spatial distribution over the catchment, whereas the simulated rainfall amount and its temporal distribution were evaluated using data from the gauging station. The performed sensitivity analysis also supports this conclusion. The result indicates that the current parameterization combinations are only applicable to the chosen events, not for simulation of other events or not used for long time series simulation. As each flood season has a likely unique WRF parametrization combination setup at 1 km spatial resolutions, it is advisable to explore the best choices for each flood season to validate the WRF model through sensitivity analysis. For instance, when using it for early warning systems and actual flood modelling purposes.

The procedures presented in chapters 3 and 4 that aimed to improve the WRF model's performance in simulating HIRE have indicated considerable improvements in the simulated events. The result showed that the urban fraction's effect on the simulated event is as significant as the effect that occurred by the MP-CP-PBL combinations. Hence, the proper representation of the extent and position of the urban land use map would have a similar impact on the simulated rainfall as the lake Victoria surface temperature (e.g., Sun et al. (2015)) and the WRF parametrization schemes (e.g., Argent et al. (2015)). Moreover, contrary to previous studies by Argent et al. (2015); Otieno et al. (2018) that indicate that the WRF model is poorly applicable for rainfall simulation over the Lake Victoria basin, the sensitivity analysis procedure followed in this thesis can be used in practice. We have shown that the model has some performance skills in simulating rainfall at a sub-daily scale with accurate parameterization schemes. Therefore, future research efforts that use the WRF model for HIRE simulation must consider all factors that affect the local-scale climate system, which influences the amount and the spatial variability of the simulated event. These factors are the effect of the LULC and soil information (i.e., static dataset), which should be optimally adjusted using publicly available geospatial datasets.

6.1.3. Application of WRF simulated HIRE for localized flood hazard modelling

Knowing that WRF is quite capable of simulating real events as supported by sensitivity analysis, with some deviations in the exact location and timing of HIREs, we are exploring its value as a potential replacement of rain gauge measurements for flood hazard assessment. Therefore, chapter 5 aimed to fulfill these needs.

Here (in chapter 5), we constructed design storms of a given return period based on grid-cell WRF simulated events by selecting the representative gridcell-events. Three representative WRF design storms were constructed using the quantile expression of the total rainfall amount as WRFL, WRFM, and WRFU, representing the lower, median, and upper quantiles of gridcell-rainfall events, respectively. For illustrative purposes, the constructed WRF design storms were compared with the classical alternating-block storms (T = 2 & 10 = year return periods), which were obtained from the equations representing the pre-established IDF curves of the area. The results are compared in terms of three rainfall properties: total rainfall depth, peak intensity, and time to peak intensity. The rainfall properties for WRFL are equivalent to that of the T = 2-year event, while WRFU`s properties are equivalent to that of the T = 10-year event. The representative gridcell-rainfall events also better characterize the event's convective properties, which shows an early peaking of the storm with a steep rise until the maximum intensity, compared to the alternating-block storms where the peak intensity attains at the middle of the storm duration. Another significant strength of the procedure followed in this research is recognizing each grid cell as a virtual station, which plays a crucial role in capturing the event's spatial distribution over the catchment.

The constructed design storms are then used as an input to the flood model for simulating flood dynamics in the upper Lubigi catchment in Kampala. The results indicate a wide range of peak discharge, flood extent, and the affected number of built-up areas due to different total rainfall amounts and peak intensity used among the constructed design storms. The flood model results further indicate that the use of three WRF design storms per event can thoroughly indicate the level of uncertainty in the simulated flood hazard in the catchment. Overall, the WRF design storms can give an insight into the applicability and usability of the numerical weather prediction model outputs for flash flood modelling in the urbanized and data-scarce area. Thus, the proposed approach that translated the WRF simulated high-intensity rainfall events into a design storm proved suitable for urban flood hazard modelling in Kampala.

The main objective of the thesis was to assess the suitability of open-source geospatial datasets and their integration with hydro-meteorological modelling systems to overcome the data-scarcity challenges and advance the localized flood hazard modelling in the urbanized environment. The approach presented in this thesis allows us to overcome the data scarcity and advances our flood hazard modelling in the urbanized and data-scarce catchment. The application of an event-based integrated flood modelling system is a novel approach to assess urban flood hazards, with high-intensity rainfall and soil characteristics as the main mechanisms causing the spatial dynamics of the flood in the catchment. High-intensity rainfall creates a rapid runoff within a relatively small catchment, which can result in localized flooding. At the same time, urban soil information determines runoff production by influencing the infiltration processes in the catchment. However, we should be aware that urban flood modelling in a developing country is driven by complex urban characteristics and hydrometeorological factors. Hence, proper urban flood hazard assessment cannot be solved by optimizing only soil information and extreme rainfall data scarcity. For effective flood hazard management in the city, other factors of urban flood modelling, including but not restricted to the Digital elevation model (DEM), sustainable urban drainage system management (DSM), consideration of scenario development, and the effect of different risk reduction measures should be assessed and evaluated, as discussed in the next section.

6.2. Future perspectives

The flood modelling framework and approaches presented in this thesis provide ample scope for further improvements. This section is designed as a way forward to *advance the approaches, frameworks, and concepts followed in this thesis for proper urban flood modelling and drawing a path forward* for urban flood management in the data-scarce area.

6.2.1. Improving approaches followed in the thesis

i) Further exploration of the geospatial databases

With the increase in the availability of satellite observation and global databases, there is a massive opportunity for improving flood hazard assessment in data-scarce regions. These datasets can be used to improve both the flood model using openLISEM and the meso-scale atmospheric modelling using WRF. As a proxy to *in situ* measurements, satellite data for variables of the surface water, atmosphere, soil, and land use land cover have been demonstrated to be useful information for flood hydrology applications (Revilla Romero, 2016; Dhib et al., 2017; Kabenge et al., 2017; Platnick et al., 2017; Zhang et al., 2018a; Perez Molina, 2019). Although in this thesis, we considered only a few of them, there are many more to improve the flood modelling, particularly in areas of the atmospheric river and surface hydrology. We considered soil and rainfall information here because accurate soil data and precipitation information directly impact the flooding processes through the soil capacity to store infiltration water and the total volume of water entering the catchment.

In the area of the atmospheric data, the satellite rainfall estimation such as the Global Precipitation Measurement (GPM) (Zhang et al., 2018a) and the Meteosat Second Generation (MSG) (Dhib et al., 2017), which have high temporal resolution need to be explored as they have the ability to detect the rainfall intensity, which can be used for verifying the HIRE simulated by WRF model. Also, the use of the MODIS atmospheric product (MODATM) from Platnick et al. (2017) contains a combination of key atmospheric parameters, including cloud fraction at 10 km spatial resolution, which can be used to verify the WRF simulated cloud product.

In the case of surface hydrology, satellite-derived flood extents (e.g., Satellite Aperture Radar (SAR)) have successfully been used as a proxy for calibration/validation of hydrodynamic models (Mason et al., 2014; Amarnath et al., 2015; Shen et al., 2019). Therefore, the verification of the hydrodynamic model result, particularly for flood plain mapping in the large wetlands, should be explored.

Other applications based on the satellite-derived data that need to be considered for flood modelling in the data-scarce area are related to soil moisture. Particularly, in the absence of streamflow measurement for flood hydrology calibration, the spatial extent of the soil moisture estimates from the advanced microwave scanning radiometer 2 (AMSR2) mission (Wehbe et al., 2019) could be used as a benchmark. Therefore, the application of AMSR2 data and its coupling with flood hydrology should be explored, particularly for the large-scale hydrological application of flood early warning systems.

ii) Further improvements in HIREs simulation

The main requirements for urban flood modelling are high-quality rainfall data, which can be obtained through the mesoscale NWP modelling system. Based on the current study, we have identified three major issues (weaknesses) in simulating HIRE using the WRF model and its flood application. These issues are the rainfall differences simulated when using different parametrization combinations, the effect of modelling system and local processes (i.e., urbanization) on the simulated rainfall, and the procedure to use the simulated events for the localized flood modelling in the catchment. If improvements and further research in some of these areas are carried out in the near future, this will present a step forward in using the WRF rainfall product for urban flood application in the catchment.

The procedure presented in this thesis showed the possibility of using certain WRF parametrization combinations (i.e., MP-CP-PBL) to simulate the events that represent the main rainy season (e.g., 13 April 2013 and 16 April 2016) and the non-main rainy season (e.g., 25 June 2012 and 03 September 2013). We found enormous simulated rainfall differences among the different combinations, which indicates a need for more sensitivity analysis to select the best combinations for the specific event. For this purpose, high-quality rainfall data is seriously required for detailed model verification. Therefore, it is highly recommendable to deploy more gauging stations in the catchment. Another way forward with the WRF model could be evaluating/extending the current combinations with more flood-triggered events and see whether there is a certain preference for combinations, for instance, a season or time in a season. For example, it is extending the selected 13 April 2016 combination for the MAM season. The decision of whether to continue with the selected combinations or not for the respective seasons can be made by using a decision tree, as shown in **Figure 6.1**. Suppose the selected combination is not preferable for the time in a season, which is most likely the case. In that case, it means the floods in each season have a unique WRF parametrization combination at a 1 km spatial resolution. Hence, further research could be required to extend the procedure for more events from different seasons to improve these results' confidence.

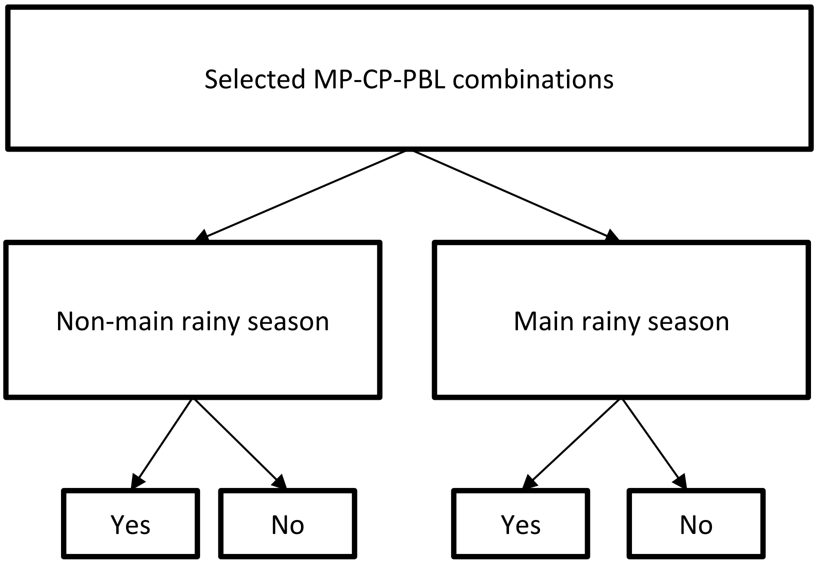

Figure 6.1 Decision tree to evaluate the preferences of the selected MP-CP-PBL combinations for HIRE simulation using the WRF model setup at 1 km spatial resolution

Another way to make optimum WRF model simulation is by incorporating the satellite-derived urban fraction into the WRF model to represent the city's correct position and extent; hence, assess its effect on the processes leading to the localized extreme rainfall events. During this thesis's work, the satellite-derived urban fraction of the city of Kampala is correctly incorporated into the WRF modelling system. However, the detailed impact of the inserted urban fraction on meteorological variables leading to rainfall changes, similar to the studies by Brousse et al. (2019); Oliveros et al. (2019), needs to be analyzed.

Moreover, although the detailed diagnoses of the parametrization schemes are least focused in this thesis, it is also worth mentioning that the overall representation of the parametrization schemes in the study area is weak. Therefore, detailed research should be carried out to address this issue with data from the region. A focus area could be toward understanding cloud and precipitation processes that lead to improved model parameterizations. Above all, the WRF model-based HIRE simulation will benefit more from the use of enhanced observations, advanced data assimilation methods, and rapid updates, as indicated by Fritsch and Carbone (2004); Clark et al. (2016).

6.2.2. *A path forward for integrated flood management*

The urban flood hazard assessment aims to build a resilient city by minimizing human and economic losses, which implies that the more urban residents adapt to the hazard, the more conducive the environment is for the society towards sustainable urban development (Jha, 2012; Liao, 2012). To achieve this aim, integrated flood management (IFM) measures, as proposed by the World Meteorological Organization (WMO), which comprise all actors who are responsible for flood management, are being recommended (Vojinovic and Abbott, 2012). Under the IFM framework, the linkage of technical, social, and decision-maker approaches towards addressing the impacts and providing solutions for flooding would generally be proposed, as shown in **Figure 6.2**. A technical aspect will be responsible for addressing the natural and technical root causes of the flood and assessing flood hazards from a holistic point of view. The decision-makers are responsible for producing a strategic framework of coherent policy development, while a social aspect is responsible for enhancing stakeholder engagement and promoting community linkages to technical aspects and other policy domains. The work in this thesis contributes to the technical aspect of the framework. The result showed that it is possible to produce a proper flood hazard map required for IFM in the data-scarce areas of the developing countries. I believe that by following the suggested framework, the goal of IFM can be achieved. The following sub-sections explicitly looked at some of the issues related to the elements of the technical aspect of IFM in the developing country.

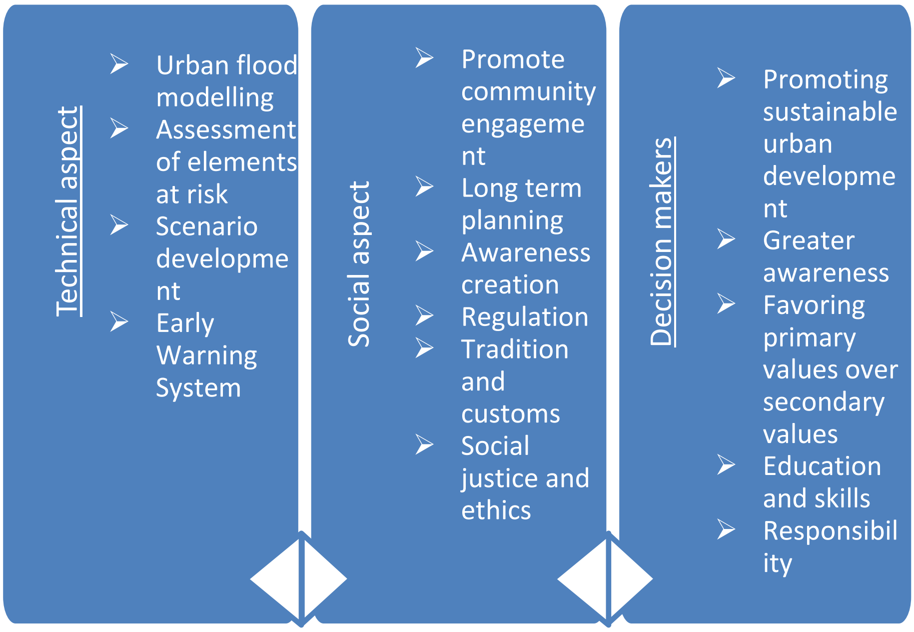

Figure 6.2 Integrated flood management (IFM) framework that can be implemented in the developing country (adapted from (Vojinovic, 2015))

a. *Improving urban flood hazard modelling*

Under the technical aspect of IFM, the primary element that requires further improvement is the basic dataset used for developing the flood model. This study showed that the use of open sources geospatial databases had been recognized as a great prospect towards addressing the key issue with data limitation for proper urban flood modelling in developing countries. Besides, the use of integrated flood modelling with openLISEM, which is adjusted to represent the correct urban soil characteristics for proper flood modelling is arguably a key strength of the current study. There are still limitations and critical issues to be addressed in view of urban flood modelling in developing countries. The limited data availability and limited access to data are still the prevailing issues, which require a great innovation for spatial data infrastructure in developing countries. This innovative data infrastructure and data collection require political will and enterprise investment. The spatial data infrastructure lies at the foundation for proper flood hazard assessment. This is mainly because urban flood simulation requires a systematic representation of the complex urban geomorphology and detailed topographic data such as LiDAR (Light Detection and Ranging) and UAV-based models for properly formulating and solving the shallow water equations (SWEs). Yet this urban morphology information is still not fully accessible for many urban catchments in developing countries. Furthermore, the representation of the flood driving factors such as anthropogenic factors (e.g., litter) in the flood model is complex due to a lack of information. Thus, a weak representation of flood modelling systems and flood driving factors can lead to numerical errors and uncertainties. Therefore, urban flood analysis and research can advance these issues by combining knowledge potential and computer powers in moving forward the urban flood modelling system.

b. *Assessment of Elements at risk*

A good strategy for integrated flood management requires flood risk maps, which are produced as the integration of flood hazard, exposure, and vulnerability. The last two components of flood risk modelling are challenging to quantify, particularly in developing countries, due to the lack of data (Nur and Shrestha, 2017; Hamidi et al., 2020). However, the IFM practices are targeted to understand urban flood hazard, vulnerability, and exposure through community participation, develop robust but low-cost methodologies and enhance the availability of good quality flood information. The element at risk is often characterized by the number of structures, population, objects, and likes exposed to flood. The analysis of the elements at risk can be assessed through the framework developed by Birkmann (2006); Birkmann (2007), and the required information can be collected through questionnaires-interview and satellite remote sensing. Furthermore, an up-to-date database of elements at risk can also be obtained from OpenStreetMap and is found to be a suitable and cost-effective alternative for supporting local governments and communities in risk assessment and emergency planning (Schelhorn et al., 2014). In this thesis, it was shown that the land cover data extracted from the satellite image proved to be essential to assess the number of buildings affected by the floods. However, the explicit information on the number of people, the number of insured buildings for the flood event, the number of economic sectors, and institutions exposed to flooding is not explicitly considered. Therefore, I believe that by collecting detailed information on the affected objects, the full exposure of objects and the vulnerability to flooding can be assessed.

c. Scenario development: Landuse-Landcover and climate change impact assessment

Future climate change and urbanization enhance warming in the city, as reported by Jia et al. (2019), which further enhances extreme rainfall; hence, expected to increase flood hazards in the urbanized environment. Considering such impact requires combined LULC and climate change assessment on processes preceding floods, which are essential for effective urban flood management. In such cases, future urban growth scenarios can be developed for a city, for example, by using the cellular automata (CA) model. For instance, Perez Molina (2019) projected the urban growth of Kampala, representing the year the 2030s using the cellular automata model as an array of cells, each with an associated fraction of land cover (for built-up, vegetation, and bare soil). Combined with the climate change scenarios from the climate model output as the model boundary conditions, the projected HIRE used for design storm estimation could be built following a similar procedure by Pappenberger et al. (2012); Liew et al. (2014). Therefore, the combined integration of climate change scenarios and urban growth into flood management is possible by considering the frequent flooding triggered by extreme rainfall events due to the combined effect of climate change and urbanization.

Land use-land cover (LULC) change is a complex process that links both natural and human systems. As such, it has both a direct and indirect impact on flooding and flood-related problems. The direct impact of land cover is well studied; for example, in the case of Kampala, Perez Molina (2019) has shown how the city's physical expansion determined the city's flood dynamics. The least known but very important aspect of flood-related problems is the impact of LULC change on storms' behaviour over the area through the modifications of local and regional atmospheric circulations (Alexander et al., 2006; Ashley et al., 2012). Based on this thesis's findings, it is evident that the urban land cover data derived from the satellite can be used in the NWP model for assessing the impact of urbanization on rainfall characteristics. Therefore, using the satellite-derived LULC change data can help to create a LULC map of the different periods at different scales and used in the NWP model to carry out LULC change impact assessment on storm behavior and then link to flood hazard assessment.

Sustainable urban flood management also requires the mainstreaming of climate change information into the decision-making system. It is evident that as a result of climate change, there is a clear tendency of increasing extreme precipitation events and frequent flooding affecting urban drainage systems

(Grum et al., 2006; Arnbjerg-Nielsen et al., 2013). Moreover, the recent Intergovernmental Panel on Climate Change (IPCC) 6th report Masson-Delmotte et al. (2021) further indicated a likely increase in precipitation extremes over the Central-East African region leading to pluvial flooding. The report further indicated that for 1.5 and 2^0 C global warming levels, precipitation extremes would increase for future climate scenarios that lead to widespread flooding in these regions. The report is very alarming for cities like Kampala, where many poor communities live in flood plains and reclaimed wetlands and are exposed to localized and frequent flooding during the rainy season, resulting in loss of lives and property. It is further indicated that by Perez Molina (2019) that the impacts of the floods are exacerbated by poor city planning as these neighborhoods have no drainage systems. The frequency and intensity of floods are expected to increase with climate change. Therefore, impact assessment of future climate change and mainstreaming it into the city development plan is vital for better urban flood management.

The currently available approach for assessing climate change scenarios for urban flood management is mainly through design event uplifts ratios and applying climate model output driven by emission scenarios (Gersonius et al., 2012; Berggren et al., 2014). Typically, for less detailed analysis, simple uplift ratios (percentage change of the available rainfall data) are used to make a future assessment of the potential impact of climate change on an area. However, for more detailed analysis, a time series rainfall data can be used, which allows the construction of design storms for a range of return periods as has been used in a number of studies despite the difficulties associated with convective rainfall representation (Lu and Qin, 2019; Zhou et al., 2019).

d. *Early Warning System*

With the use of the WRF model modelling system, the result can also be used for the early warning system (EWS) as actual flood modelling. As opposed to the flood hazard modelling, actual flood modelling requires operational rainfall prediction as now cast or forecast; it requires real-time forecast products that are used as initial and boundary conditions for the WRF model. These include the European Center for Medium-range Weather Forecast (ECMWF) (Kidd et al., 2013) and the Global Forecasting System (GFS) developed by the National Oceanic and Atmospheric Administration (NOAA) that available: https://www.ncdc.noaa.gov/data-access/model-data/model-datasets/global-forcast-system-gfs). By selecting appropriate parametrization combinations for a given event, following the same procedure indicated in this study, the WRF model can be set up with the operation dataset and used for operational flood modelling similar to the study by Sikder et al. (2019); Ming et al. (2020). The quality of the forecast product for the EWS can also be improved by incorporating through the ensemble forecast of the parameterization. Moreover, incorporating the data assimilation systems into the WRF modelling system can also improve the forecast product. Once the rainfall product is produced, the next step is to set up the flood modelling system to produce flooding (either inundation or peak hydrograph) based on the simulated WRF rainfall forecast (nowcast). The WRF-openLISEM coupling system would produce the forecasted discharge data, following a similar procedure by Givati et al. (2016); Ryu et al. (2017). For pluvial flooding/flash flooding like in Kampala, the offline coupling of the WRF model with an integrated hydrology model, such as openLISEM, currently set up and used in this thesis, is potentially useful and recommendable.

6.3. Conclusion

Strategies to cope with floods, such as flood hazard mapping, rely on the effective modelling of the flood characteristics using the flood models. One of the main challenges for flood modelling in the data-scarce area is obtaining the model required data such as high-intensity rainfall events and soil information used for an integrated flood modelling system. The current work on using open-source geospatial databases and the NWP modelling system can potentially overcome the data availability problem on a broader scale. Moreover, exploring more about geospatial databases and their integration with the hydrometeorological modelling system may not only overcome the data-scarcity problem. Still, it can also be used for future impact assessment. However, the limited data quality and limited access to data are still the prevailing issues, which require a great innovation for spatial data infrastructure in developing countries. This requires political will and enterprise investment for innovative data infrastructure and data collection. For sustainable urban flood management at the local scale, the IFM framework, which comprises all actors responsible for flood management, needs to be implemented. To ward this, the tailored data required for effective flood modelling should come from cooperation between technical experts, social, and decision-makers.

Appendix A Structure and Functionality of openLISEM model

A simplified scheme of the openLISEM model's routine order is given in figure A1. The processes within LISEM can be classified into two categories: Hydrology and Sediment. These are respectively colorized blue and red. General processes such as reading input data are colorized green. The flow processes can be categorized as Overland Flow, Channel Flow, and Flooding. Examples of required maps are also given for each process. In this thesis, we considered the hydrological part of the model, and information on the model can be found on https://lisemmodel.com.

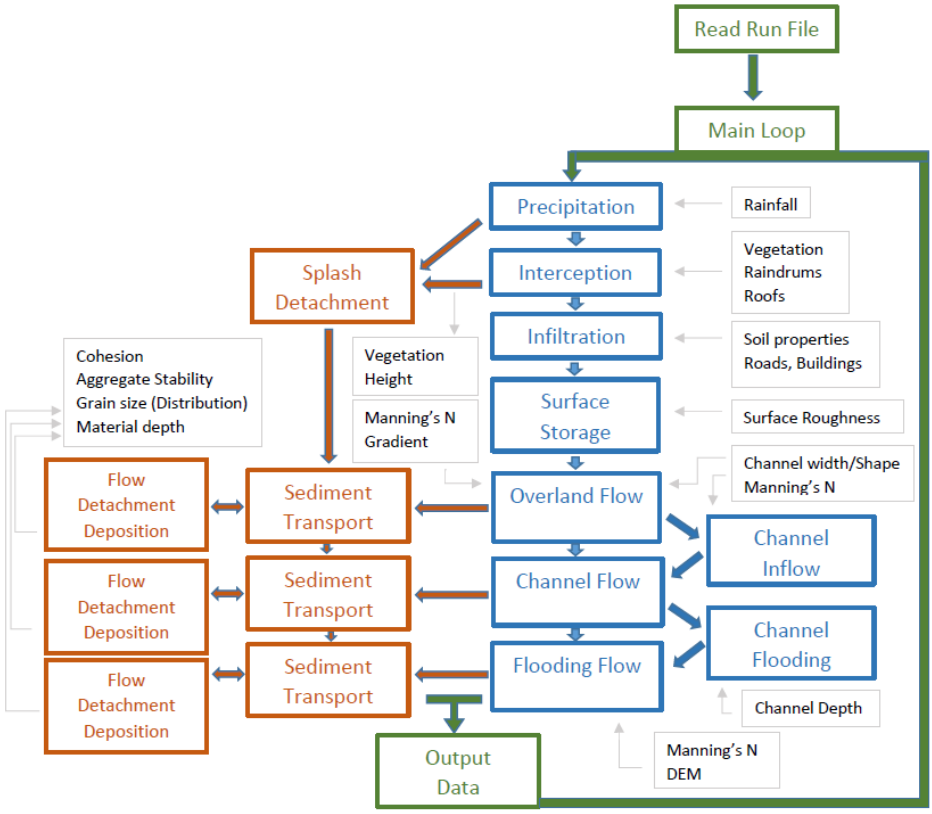

Figure A1. Flow chart of openLISEM model (see https://lisemmodel.com). From right to left: blue represents hydrological and flow processes, red represent surface erosion processes.

In this thesis, openLISEM is further developed to couple it with compaction scenario (soil physical structure) and WRF predicted rainfall product, enabling input of rainfall for single event rainfall product as design storm form.

Within LISEM, compacted soil can be modeled. For each cell, a compacted fraction can be provided, with accompanying saturated conductivity values. The final saturated conductivity is calculated using the equation:

$Ks,eff = Ks*(1-fcomp) + Ks,comp\ fcomp$

With

Ks,eff the effective saturated conductivity ($m\ s-1$)

$fcomp$ the compacted soil fraction (−)

$Ks,comp$ the saturated conductivity for compacted soil ($m\ s-1$)

Where the actual infiltration equation calculated based on the Green & Ampt (1911) infiltration method assumes that a wetting front moves downwards into the soil layers parallel to the soil surface:

$$f = f_{pot} = -K_s\left(\psi\,\frac{\theta_s-\theta_i}{F}+1\right)$$

With

$fpot$ the potential infiltration rate ($m\ s-1$)

F the cumulative infiltrated water (m)

θs the porosity ($m3\ m-3$)

θi the initial soil moisture content ($m3\ m-3$)

Ks the saturated conductivity ($m\ s-1$)

Zf the depth of the wetting front (m)

ψ the matric pressure at the wetting front ($h=\psi+Z$) (m)

And

$$Z_f = \frac{F}{\theta_s - \theta_i}$$

This method can be applied for both a 1 layer or 2 layer system. Beneath these layers, an open or closed boundary can be chosen.

In the case of compaction, the model is designed to handle sub-gridcell surface properties (Figure A2). A gridcell can contain bare soil, compacted soil, vegetated surface, a road, a house, and a channel. These surface characteristics are supplied in separate layers as fractions of the total cell area. The base layer is formed by the soil surface with its hydrological characteristics, and the user supplies additional maps that trigger additional hydrological processes in the model. The presence of vegetation will, for example, result in an interception on the part of the gridcell. The presence of a house will result in roof storage and a partly impermeable surface, and a road will have sedimentation but no infiltration or erosion, see, for example, the following schemation:

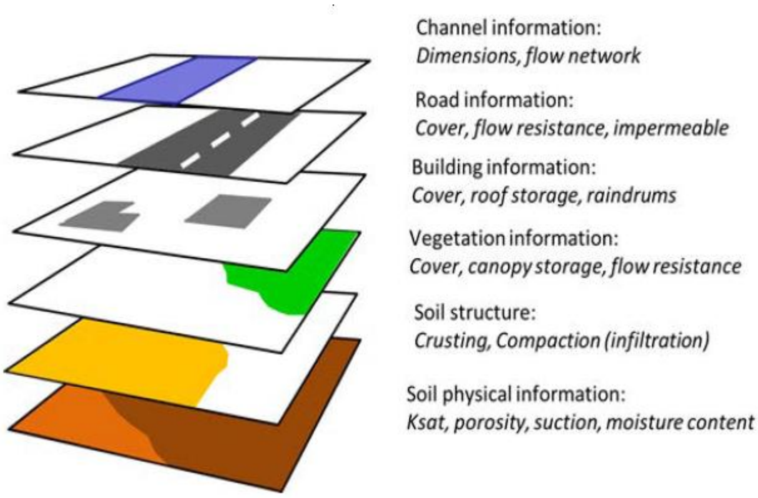

Figure A2: Input data which is modelled on a sub-gridcell

Appendix B Input/output database structure

This section will describe the preparation for all input data categories.

Input data category

Input data category	**Needed base maps**
Topography	Digital Elevation model
Rainfall	Rainfall
Land use/cover	Land use unit map and use property table
Soil type	Soil use unit map and soil property table
Infrastructure	Land use unit map

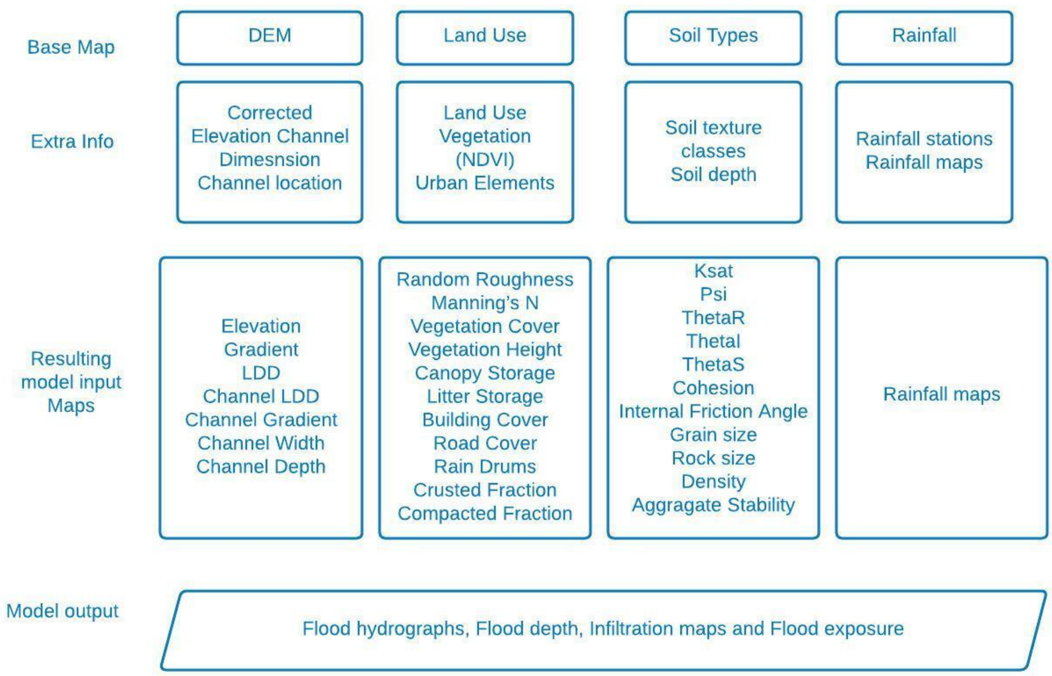

Figure B1: Input database category and its preparation

All databases are prepared by using the PCRaster script and created all input data automatically from base maps, and all datasets are in PCRaster format.

Bibliography

Abdelbaki, A.M., Youssef, M.A., Naguib, E.M., Kiwan, M.E., El-giddawy, E.I., 2009. Evaluation of pedotransfer functions for predicting saturated hydraulic conductivity for US soils, 2009 Reno, Nevada, June 21-June 24, 2009. American Society of Agricultural and Biological Engineers, pp. 1.

Abebe, G.A., 2013. Quantifying urban growth pattern in developing countries using remote sensing and spatial metrics: A case study in Kampala, Uganda. University of Twente Faculty of Geo-Information and Earth Observation (ITC).

AghaKouchak, A., Behrangi, A., Sorooshian, S., Hsu, K., Amitai, E., 2011. Evaluation of satellite-retrieved extreme precipitation rates across the central United States. Journal of Geophysical Research: Atmospheres, 116(D2).

Alexander, L.V. et al., 2006. Global observed changes in daily climate extremes of temperature and precipitation. Journal of Geophysical Research: Atmospheres, 111(D5). DOI:10.1029/2005jd006290

Alexander, P.J., Bechtel, B., Chow, W.T.L., Fealy, R., Mills, G., 2016. Linking urban climate classification with an urban energy and water budget model: Multi-site and multi-seasonal evaluation. Urban Climate, 17: 196-215. DOI:https://doi.org/10.1016/j.uclim.2016.08.003

Amarnath, G., Umer, Y.M., Alahacoon, N., Inada, Y., 2015. Modelling the flood-risk extent using LISFLOOD-FP in a complex watershed: case study of Mundeni Aru River Basin, Sri Lanka. Proc. IAHS, 370: 131-138.

Amoako, C., 2012. Emerging issues in urban flooding in African cities-The Case of Accra, Ghana, 35th AFSAAP annual conference proceedings.

Anyah, R.O., 2005. Modeling the variability of the climate system over Lake Victoria Basin.

Argent, R., Sun, X., Semazzi, F., Xie, L., Liu, B., 2015. The development of a customization framework for the WRF Model over the Lake Victoria basin, Eastern Africa on seasonal timescales. Advances in Meteorology, 2015.

Argüeso, D. et al., 2011. Evaluation of WRF parameterizations for climate studies over southern Spain using a multistep regionalization. Journal of Climate, 24(21): 5633-5651.

Arnbjerg-Nielsen, K. et al., 2013. Impacts of climate change on rainfall extremes and urban drainage systems: a review. Water Science and Technology, 68(1): 16-28. DOI:10.2166/wst.2013.251

Bibliography

Aronica, G., Bates, P., Horritt, M., 2002. Assessing the uncertainty in distributed model predictions using observed binary pattern information within GLUE. Hydrological processes, 16(10): 2001-2016.

Ashley, W.S., Bentley, M.L., Stallins, J.A., 2012. Urban-induced thunderstorm modification in the Southeast United States. Climatic Change, 113(2): 481-498. DOI:10.1007/s10584-011-0324-1

Baartman, J.E., Jetten, V.G., Ritsema, C.J., de Vente, J., 2012. Exploring effects of rainfall intensity and duration on soil erosion at the catchment scale using openLISEM: Prado catchment, SE Spain. Hydrological processes, 26(7): 1034-1049.

Baky, M.A.A., Islam, M., Paul, S., 2020. Flood Hazard, Vulnerability and Risk Assessment for Different Land Use Classes Using a Flow Model. Earth Systems and Environment, 4(1): 225-244. DOI:10.1007/s41748-019-00141-w

Balbastre-Soldevila, R., García-Bartual, R., Andrés-Doménech, I., 2019. A Comparison of Design Storms for Urban Drainage System Applications. Water, 11(4): 757.

Beheng, K.D., 2010. The evolution of raindrop spectra: A review of microphysical essentials. Rainfall: State of the science, 191: 29-48.

Berggren, K., Packman, J., Ashley, R., Viklander, M., 2014. Climate changed rainfalls for urban drainage capacity assessment. Urban Water Journal, 11(7): 543-556. DOI:10.1080/1573062X.2013.851709

Berthier, E., Andrieu, H., Creutin, J., 2004. The role of soil in the generation of urban runoff: development and evaluation of a 2D model. Journal of hydrology, 299(3): 252-266.

Betts, A.K., Miller, M.J., 1993. The Betts-Miller scheme, The representation of cumulus convection in numerical models. Springer, pp. 107-121.

Bhattacharya-Mis, N., Lamond, J., 2011. A review of the flood risk situation in African growing economies.

Bhattacharya, N., Lamond, J., 2011. A review of urban flood risk situation in African growing economies. na.

Birkmann, J., 2006. Indicators and criteria for measuring vulnerability: Theoretical bases and requirements. Measuring vulnerability to natural hazards: Towards disaster resilient societies: 55-77.

Birkmann, J., 2007. Risk and vulnerability indicators at different scales: Applicability, usefulness and policy implications. Environmental Hazards, 7(1): 20-31. DOI:10.1016/j.envhaz.2007.04.002

Bougeault, P., Lacarrere, P., 1989. Parameterization of orography-induced turbulence in a mesobeta--scale model. Monthly Weather Review, 117(8): 1872-1890.

Bout, B., Jetten, V., 2018. The validity of flow approximations when simulating catchment-integrated flash floods. Journal of Hydrology, 556: 674-688.

Bout, B., Lombardo, L., van Westen, C.J., Jetten, V.G., 2018. Integration of two-phase solid fluid equations in a catchment model for flashfloods, debris flows and shallow slope failures. Environmental modelling & software, 105: 1-16.

Braud, I. et al., 2016. Advances in flash floods understanding and modelling derived from the FloodScale project in South-East France.

Brooks, R., Corey, T., 1964. HYDRAU uc properties of porous media. Hydrology Papers, Colorado State University, 24: 37.

Brousse, O. et al., 2019. using local climate zones in Sub-Saharan Africa to tackle urban health issues. Urban climate, 27: 227-242.

Brousse, O., Martilli, A., Foley, M., Mills, G., Bechtel, B., 2016. WUDAPT, an efficient land use producing data tool for mesoscale models? Integration of urban LCZ in WRF over Madrid. Urban Climate, 17: 116-134. DOI:https://doi.org/10.1016/j.uclim.2016.04.001

Brunner, G.W., 1995a. HEC-RAS River Analysis System. Hydraulic Reference Manual. Version 1.0, Hydrologic Engineering Center Davis CA.

Brunner, G.W., 1995b. HEC-RAS River Analysis System. Hydraulic User's Manual. Version 1.0, HYDROLOGIC ENGINEERING CENTER DAVIS CA.

Cai, M., Ren, C., Xu, Y., Lau, K.K.-L., Wang, R., 2018. Investigating the relationship between local climate zone and land surface temperature using an improved WUDAPT methodology – A case study of Yangtze River Delta, China. Urban Climate, 24: 485-502. DOI:https://doi.org/10.1016/j.uclim.2017.05.010

Camberlin, P., 2018. Oxford Research Encyclopedia of Climate Science Climate of Eastern Africa Geographical Features Influencing the Region’s Climate. Oxford University Press: Oxford, UK.

Cassola, F., Ferrari, F., Mazzino, A., 2015. Numerical simulations of Mediterranean heavy precipitation events with the WRF model: A verification exercise using different approaches. Atmospheric Research, 164: 210-225.

Cattani, E., Merino, A., Guijarro, J., Levizzani, V., 2018. East Africa rainfall trends and variability 1983–2015 using three long-term satellite products. Remote Sensing, 10(6): 931.

Chang’a, L.B. et al., 2020. Assessment of the Evolution and Socio-Economic Impacts of Extreme Rainfall Events in October 2019 over the East Africa. Atmospheric and Climate Sciences, 10(3): 319-338.

Bibliography

Chawla, I., Osuri, K.K., Mujumdar, P.P., Niyogi, D., 2018a. Assessment of the Weather Research and Forecasting (WRF) model for simulation of extreme rainfall events in the upper Ganga Basin. Hydrol. Earth Syst. Sci., 22(2): 1095-1117. DOI:10.5194/hess-22-1095-2018

Chawla, I., Osuri, K.K., Mujumdar, P.P., Niyogi, D., 2018b. Assessment of the Weather Research and Forecasting (WRF) model for simulation of extreme rainfall events in the upper Ganga Basin. Hydrology & Earth System Sciences, 22(2).

Chen, F. et al., 2011. The integrated WRF/urban modelling system: development, evaluation, and applications to urban environmental problems. International Journal of Climatology, 31(2): 273-288.

Chen, H. et al., 2020. Comparison analysis of six purely satellite-derived global precipitation estimates. Journal of Hydrology, 581: 124376. DOI:https://doi.org/10.1016/j.jhydrol.2019.124376

Chen, J., Hill, A., 2007. Modeling urban flood hazard: just how much does dem resolution matter?, papers and proceedings of applied geography conferences. [np]; 1998, pp. 372.

Chen, Y., Day, S.D., Wick, A.F., McGuire, K.J., 2014. Influence of urban land development and subsequent soil rehabilitation on soil aggregates, carbon, and hydraulic conductivity. Science of the Total Environment, 494: 329-336.

Chogyal, J., 2013. The Current and Future Flood Situation, Bwaise III, Kampala, Uganda, Africa. University of Twente Faculty of Geo-Information and Earth Observation (ITC).

Clark, P., Roberts, N., Lean, H., Ballard, S.P., Charlton-Perez, C., 2016. Convection-permitting models: a step-change in rainfall forecasting. Meteorological Applications, 23(2): 165-181. DOI:10.1002/met.1538

Cosby, B., Hornberger, G., Clapp, R., Ginn, T., 1984. A statistical exploration of the relationships of soil moisture characteristics to the physical properties of soils. Water resources research, 20(6): 682-690.

CRED, UNISDR, 2015. The Human Cost of Weather-related Disasters 1995–2015. Center for Research on the Epidemiology of Disasters and UN Office for ….

Dai, J., Wang, X., Dai, W., Chang, M., 2019. The impact of inhomogeneous urban canopy parameters on meteorological conditions and implication for air quality in the Pearl River Delta region. Urban Climate, 29: 100494. DOI:https://doi.org/10.1016/j.uclim.2019.100494

Davis, C.A., Brown, B.G., Bullock, R., Halley-Gotway, J., 2009. The method for object-based diagnostic evaluation (MODE) applied to numerical forecasts from the 2005 NSSL/SPC Spring Program. Weather and Forecasting, 24(5): 1252-1267.

Davolio, S. et al., 2009. High resolution simulations of a flash flood near Venice. Natural Hazards and Earth System Sciences, 9(5): 1671-1678.

De Luca, D.L., Biondi, D., 2017. Bivariate return period for design hyetograph and relationship with t-year design flood peak. Water, 9(9): 673.

De Roo, A., Wesseling, C., Ritsema, C., 1996. LISEM: a single-event physically based hydrological and soil erosion model for drainage basins. I: theory, input and output. Hydrological processes, 10(8): 1107-1117.

Debele, S.E. et al., 2019. Nature-based solutions for hydro-meteorological hazards: Revised concepts, classification schemes and databases. Environmental research, 179: 108799.

Delestre, O. et al., 2014a. FullSWOF: A software for overland flow simulation, Advances in hydroinformatics. Springer, pp. 221-231.

Delestre, O. et al., 2014b. FullSWOF: A free software package for the simulation of shallow water flows. arXiv preprint arXiv:1401.4125.

Dhib, S., Mannaerts, C.M., Bargaoui, Z., Retsios, V., Maathuis, B.H.P., 2017. Evaluating the MSG satellite Multi-Sensor Precipitation Estimate for extreme rainfall monitoring over northern Tunisia. Weather and Climate Extremes, 16: 14-22. DOI:https://doi.org/10.1016/j.wace.2017.03.002

Di Baldassarre, G., Brath, A., Montanari, A., 2006. Reliability of different depth-duration-frequency equations for estimating short-duration design storms. Water resources research, 42(12).

Diem, J.E., Konecky, B.L., Salerno, J., Hartter, J., 2019. Is equatorial Africa getting wetter or drier? Insights from an evaluation of long-term, satellite-based rainfall estimates for western Uganda. International Journal of Climatology.

Dixon, P.G., Mote, T.L., 2003. Patterns and causes of Atlanta's urban heat island–initiated precipitation. Journal of Applied Meteorology, 42(9): 1273-1284.

Dottori, F., Todini, E., 2013. Testing a simple 2D hydraulic model in an urban flood experiment. Hydrological Processes, 27(9): 1301-1320.

Douglas, I., 2017. Flooding in African cities, scales of causes, teleconnections, risks, vulnerability and impacts. International journal of disaster risk reduction, 26: 34-42.

Douglas, I. et al., 2008. Unjust waters: climate change, flooding and the urban poor in Africa. Environment and urbanization, 20(1): 187-205.

Bibliography

Duan, W. et al., 2016. Floods and associated socioeconomic damages in China over the last century. Natural Hazards, 82(1): 401-413.

Dudhia, J., 1989. Numerical study of convection observed during the winter monsoon experiment using a mesoscale two-dimensional model. Journal of the atmospheric sciences, 46(20): 3077-3107.

Dudhia, J., 2014. A history of mesoscale model development. Asia-Pacific Journal of Atmospheric Sciences, 50(1): 121-131.

Efstathiou, G., Zoumakis, N., Melas, D., Lolis, C., Kassomenos, P., 2013. Sensitivity of WRF to boundary layer parameterizations in simulating a heavy rainfall event using different microphysical schemes. Effect on large-scale processes. Atmospheric research, 132: 125-143.

Fang, J. et al., 2019. Evaluation of the TRMM 3B42 and GPM IMERG products for extreme precipitation analysis over China. Atmospheric Research, 223: 24-38. DOI:https://doi.org/10.1016/j.atmosres.2019.03.001

FAO, 1991. The Digitized Soil Map of the World. Food and Agriculture Organization Rome, Italy.

FAO, U., 1974. Soil Map of the World 1: 5000000, Vol. I, Legend.

Fiddes, D., Forsgate, J., Grigg, A., 1974. The prediction of storm rainfall in East Africa.

Flesch, T.K., Reuter, G.W., 2012. WRF model simulation of two Alberta flooding events and the impact of topography. Journal of Hydrometeorology, 13(2): 695-708.

Frank, C.W. et al., 2020. The added value of high resolution regional reanalyses for wind power applications. Renewable Energy, 148: 1094-1109. DOI:https://doi.org/10.1016/j.renene.2019.09.138

Fratini, C.F., Geldof, G.D., Kluck, J., Mikkelsen, P.S., 2012. Three Points Approach (3PA) for urban flood risk management: A tool to support climate change adaptation through transdisciplinarity and multifunctionality. Urban Water Journal, 9(5): 317-331. DOI:10.1080/1573062X.2012.668913

Fritsch, J.M., Carbone, R., 2004. Improving quantitative precipitation forecasts in the warm season: A USWRP research and development strategy. Bulletin of the American Meteorological Society, 85(7): 955-966.

Funk, C. et al., 2015. The climate hazards infrared precipitation with stations—a new environmental record for monitoring extremes. Scientific data, 2: 150066.

Fura, G.D., 2013. Analysing and Modelling Urban Land Cover Change for Run-off Modelling in Kampala, Uganda. University of Twente Faculty of Geo-Information and Earth Observation (ITC).
Gersonius, B. et al., 2012. Developing the evidence base for mainstreaming adaptation of stormwater systems to climate change. Water Research, 46(20): 6824-6835. DOI:https://doi.org/10.1016/j.watres.2012.03.060
Giannaros, C. et al., 2020. Hydrometeorological and Socio-Economic Impact Assessment of Stream Flooding in Southeast Mediterranean: The Case of Rafina Catchment (Attica, Greece). Water, 12(9): 2426.
Gijsman, A., Jagtap, S., Jones, J., 2002. Wading through a swamp of complete confusion: how to choose a method for estimating soil water retention parameters for crop models. European Journal of Agronomy, 18(1-2): 77-106.
Gilliam, R.C., Pleim, J.E., 2010. Performance assessment of new land surface and planetary boundary layer physics in the WRF-ARW. Journal of Applied Meteorology and Climatology, 49(4): 760-774.
Givati, A., Gochis, D., Rummler, T., Kunstmann, H., 2016. Comparing one-way and two-way coupled hydrometeorological forecasting systems for flood forecasting in the Mediterranean region. Hydrology, 3(2): 19.
Greco, A., De Luca, D.L., Avolio, E., 2020. Heavy Precipitation Systems in Calabria Region (Southern Italy): High-Resolution Observed Rainfall and Large-Scale Atmospheric Pattern Analysis. Water, 12(5): 1468.
Green, W.H., Ampt, G.A., 1911. Studies on soil phyics, 1. The flow of air and water through soils. The Journal of Agricultural Science, 4(1): 1-24.
Gregory, J.H., Dukes, M.D., Jones, P.H., Miller, G.L., 2006. Effect of urban soil compaction on infiltration rate. Journal of soil and water conservation, 61(3): 117-124.
Grell, G.A., Dévényi, D., 2002. A generalized approach to parameterizing convection combining ensemble and data assimilation techniques. Geophysical Research Letters, 29(14): 38-1-38-4.
Grell, G.A., Freitas, S.R., 2014. A scale and aerosol aware stochastic convective parameterization for weather and air quality modeling. Atmos. Chem. Phys, 14(10): 5233-5250.
Grillakis, M. et al., 2016. Initial soil moisture effects on flash flood generation–A comparison between basins of contrasting hydro-climatic conditions. Journal of hydrology, 541: 206-217.
Grum, M., Jørgensen, A.T., Johansen, R.M., Linde, J.J., 2006. The effect of climate change on urban drainage: an evaluation based on regional climate model simulations. Water Science and Technology, 54(6-7): 9-15. DOI:10.2166/wst.2006.592

Bibliography

Guide, W.U., 2009. Chapter 3: WRF Preprocessing System (WPS). Land Use and Soil Categories in the Static Data. Available online: http://www2. mmm. ucar. edu/wrf/users/docs/user_guide_V3/users_guide_chap3. htm (accessed on 1 March 2014).

Güneralp, B., Lwasa, S., Masundire, H., Parnell, S., Seto, K.C., 2017. Urbanization in Africa: challenges and opportunities for conservation. Environmental Research Letters, 13(1): 015002.

Guo, J.C., Hargadin, K., 2009. Conservative design rainfall distribution. Journal of Hydrologic Engineering, 14(5): 528-530.

Habonimana, H.V., 2014. Integrated Flood Modeling in Lubigi Catchment Kampala. University of Twente Faculty of Geo-Information and Earth Observation (ITC).

Hamidi, A.R., Wang, J., Guo, S., Zeng, Z., 2020. Flood vulnerability assessment using MOVE framework: a case study of the northern part of district Peshawar, Pakistan. Natural Hazards, 101(2): 385-408. DOI:10.1007/s11069-020-03878-0

Hammond, M.J., Chen, A.S., Djordjević, S., Butler, D., Mark, O., 2015. Urban flood impact assessment: A state-of-the-art review. Urban Water Journal, 12(1): 14-29. DOI:10.1080/1573062X.2013.857421

Han, J.-Y., Hong, S.-Y., 2018. Precipitation forecast experiments using the Weather Research and Forecasting (WRF) Model at gray-zone resolutions. Weather and Forecasting, 33(6): 1605-1616.

Hapuarachchi, H., Wang, Q., Pagano, T., 2011. A review of advances in flash flood forecasting. Hydrological processes, 25(18): 2771-2784.

Harrison, K.W., Kumar, S.V., Peters-Lidard, C.D., Santanello, J.A., 2012. Quantifying the change in soil moisture modeling uncertainty from remote sensing observations using Bayesian inference techniques. Water Resources Research, 48(11).

Hengl, T. et al., 2017. SoilGrids250m: Global gridded soil information based on machine learning. PLoS one, 12(2): e0169748.

Hersbach, H. et al., 2020. The ERA5 global reanalysis. Quarterly Journal of the Royal Meteorological Society.

Hersbach, H., Dee, D., 2016. ERA5 reanalysis is in production. ECMWF newsletter, 147(7): 5-6.

Hirabayashi, Y. et al., 2013. Global flood risk under climate change. Nature Climate Change, 3(9): 816-821.

Holanda, M.A.C.R.d., Soares, W.d.A., 2019. Analysis of the effect of impermeability of urban soils on the infiltration of rainwater in the city of Recife, PE. Revista Ambiente & Água, 14(4).

Holton, J., 1992. An introduction to dynamic meteorology Academic Press New York 511.

Hong, S.-Y., Dudhia, J., Chen, S.-H., 2004. A revised approach to ice microphysical processes for the bulk parameterization of clouds and precipitation. Monthly Weather Review, 132(1): 103-120.

Hong, S.-Y., Lee, J.-W., 2009. Assessment of the WRF model in reproducing a flash-flood heavy rainfall event over Korea. Atmospheric Research, 93(4): 818-831.

Hong, S.-Y., Lim, J.-O.J., 2006. The WRF single-moment 6-class microphysics scheme (WSM6). Asia-Pacific Journal of Atmospheric Sciences, 42(2): 129-151.

Hong, S.-Y., Noh, Y., Dudhia, J., 2006. A new vertical diffusion package with an explicit treatment of entrainment processes. Monthly weather review, 134(9): 2318-2341.

Hopson, T.M., Webster, P.J., 2010. A 1–10-day ensemble forecasting scheme for the major river basins of Bangladesh: Forecasting severe floods of 2003–07. Journal of Hydrometeorology, 11(3): 618-641.

Horritt, M., Bates, P., 2002. Evaluation of 1D and 2D numerical models for predicting river flood inundation. Journal of hydrology, 268(1-4): 87-99.

Hunter, N.M., Bates, P.D., Horritt, M.S., Wilson, M.D., 2007. Simple spatially-distributed models for predicting flood inundation: a review. Geomorphology, 90(3-4): 208-225.

Huong, H.T.L., Pathirana, A., 2013. Urbanization and climate change impacts on future urban flooding in Can Tho city, Vietnam. Hydrology and Earth System Sciences, 17(1): 379.

Isunju, J.B., Kemp, J., 2016. Spatiotemporal analysis of encroachment on wetlands: a case of Nakivubo wetland in Kampala, Uganda. Environmental monitoring and assessment, 188(4): 203.

Isunju, J.B., Orach, C.G., Kemp, J., 2016. Hazards and vulnerabilities among informal wetland communities in Kampala, Uganda. Environment and Urbanization, 28(1): 275-293.

Jacobson, M.Z., Fundamentals of Atmospheric Modeling, 1998. Cambridge University Press.

Janjić, Z.I., 2000. Comments on “Development and evaluation of a convection scheme for use in climate models”. Journal of the Atmospheric Sciences, 57(21): 3686-3686.

Jetten, V., 2014. A brief guide to openLISEM. Electronic document.

Bibliography

Jeworrek, J., West, G., Stull, R., 2019. Evaluation of Cumulus and Microphysics Parameterizations in WRF across the Convective Gray Zone. Weather and Forecasting, 34(4): 1097-1115.

Jha, A.K.B., Robin Lamond, Jessica, 2012. Cities and Flooding: A guide to integrated urban flood risk management for 21st century. Cities and Flooding. DOI:10.1596/978-0-8213-8866-2

Jia, G. et al., 2019. Land–Climate Interactions. Climate Change and Land: An IPCC Special Report on Climate Change, Desertification, Land Degradation, Sustainable Land Management, Food Security, and Greenhouse Gas Fluxes in Terrestrial Ecosystems. food security, and greenhouse gas fluxes in terrestrial ecosystems: 1-186.

Jiménez, P.A. et al., 2012. A revised scheme for the WRF surface layer formulation. Monthly Weather Review, 140(3): 898-918.

Juarez Lucas, A.M., Kibler, K.M., 2016. Integrated Flood Management in developing countries: balancing flood risk, sustainable livelihoods, and ecosystem services. International Journal of River Basin Management, 14(1): 19-31.

Kabenge, M., Elaru, J., Wang, H., Li, F., 2017. Characterizing flood hazard risk in data-scarce areas, using a remote sensing and GIS-based flood hazard index. Natural hazards, 89(3): 1369-1387.

Kain, J.S., 2004. The Kain–Fritsch convective parameterization: an update. Journal of Applied Meteorology, 43(1): 170-181.

KCC, 2002. Inventories: Nakivubo channel rehabilitation project, Kampala Drainage Master Plan. Kampala.

KCCA, 2010. KAMPALA DRAINAGE MASTER PLAN.

KCCA, 2012. Kampala Physical Development Plan Draft Report: Updating Kampala Structure Plan

and Upgrading the Kampala GIS Unit.

Keifer, C.J., Chu, H.H., 1957. Synthetic storm pattern for drainage design. Journal of the hydraulics division, 83(4): 1-25.

Kidd, C., Dawkins, E., Huffman, G., 2013. Comparison of precipitation derived from the ECMWF operational forecast model and satellite precipitation datasets. Journal of Hydrometeorology, 14(5): 1463-1482.

Kizza, M., Rodhe, A., Xu, C.-Y., Ntale, H.K., Halldin, S., 2009. Temporal rainfall variability in the Lake Victoria Basin in East Africa during the twentieth century. Theoretical and applied climatology, 98(1-2): 119-135.

Knievel, J., 2006. Numerical weather prediction (nwp) and the wrf model. no. August.
Konrad, C.P., 2003. Effects of urban development on floods. US Department of the Interior, US Geological Survey.
Kusaka, H., Kondo, H., Kikegawa, Y., Kimura, F., 2001. A simple single-layer urban canopy model for atmospheric models: Comparison with multi-layer and slab models. Boundary-layer meteorology, 101(3): 329-358.
Kutílek, M., Nielsen, D.R., 1994. Soil hydrology: texbook for students of soil science, agriculture, forestry, geoecology, hydrology, geomorphology and other related disciplines. Catena Verlag.
Lei, M. et al., 2008. Effect of explicit urban land surface representation on the simulation of the 26 July 2005 heavy rain event over Mumbai, India.
Leung, L.R., Qian, Y., 2009. Atmospheric rivers induced heavy precipitation and flooding in the western US simulated by the WRF regional climate model. Geophysical Research Letters, 36(3).
Li, D., Bou-Zeid, E., Baeck, M.L., Jessup, S., Smith, J.A., 2013. Modeling Land Surface Processes and Heavy Rainfall in Urban Environments: Sensitivity to Urban Surface Representations. Journal of Hydrometeorology, 14(4): 1098-1118. DOI:10.1175/jhm-d-12-0154.1
Li, J. et al., 2017. Extending flood forecasting lead time in a large watershed by coupling WRF QPF with a distributed hydrological model. Hydrology and Earth System Sciences, 21(2): 1279-1294.
Liao, K.-H., 2012. A Theory on Urban Resilience to Floods—A Basis for Alternative Planning Practices. Ecology and Society, 17(4). DOI:10.5751/ES-05231-170448
Liew, S.C., Raghavan, S.V., Liong, S.Y., 2014. How to construct future IDF curves, under changing climate, for sites with scarce rainfall records? Hydrological processes, 28(8): 3276-3287.
Lim, K.-S.S., Hong, S.-Y., 2010. Development of an effective double-moment cloud microphysics scheme with prognostic cloud condensation nuclei (CCN) for weather and climate models. Monthly weather review, 138(5): 1587-1612.
Lin, T.-S., Cheng, F.-Y., 2016. Impact of soil moisture initialization and soil texture on simulated land–atmosphere interaction in Taiwan. Journal of Hydrometeorology, 17(5): 1337-1355.
Liu, J., Bray, M., Han, D., 2012. Sensitivity of the Weather Research and Forecasting (WRF) model to downscaling ratios and storm types in rainfall simulation. Hydrological Processes, 26(20): 3012-3031.
Liu, J. et al., 2015. A real-time flood forecasting system with dual updating of the NWP rainfall and the river flow. Natural Hazards, 77(2): 1161-1182.

Bibliography

Liu, Z., Zhang, H., Liang, Q., 2019. A coupled hydrological and hydrodynamic model for flood simulation. Hydrology Research, 50(2): 589-606.

Loridan, T., Grimmond, C., 2012. Multi-site evaluation of an urban land-surface model: intra-urban heterogeneity, seasonality and parameter complexity requirements. Quarterly Journal of the Royal Meteorological Society, 138(665): 1094-1113.

Lu, W., Qin, X., 2019. Integrated framework for assessing climate change impact on extreme rainfall and the urban drainage system. Hydrology Research, 51(1): 77-89. DOI:10.2166/nh.2019.233

Mahmood, R., Pielke Sr, R.A., McAlpine, C.A., 2016. Climate-Relevant Land Use and Land Cover Change Policies. Bulletin of the American Meteorological Society, 97(2): 195-202.

Management, A.P.o.F., 2009. Integrated flood management: Concept paper. World Meteorological Organization.

Markandya, A., Cabot-Venton, C., Beucher, O., 2015. Economic assessment of the impacts of climate change in Uganda.

Martilli, A., Clappier, A., Rotach, M.W., 2002. An urban surface exchange parameterisation for mesoscale models. Boundary-layer meteorology, 104(2): 261-304.

Mason, D.C., Giustarini, L., Garcia-Pintado, J., Cloke, H.L., 2014. Detection of flooded urban areas in high resolution Synthetic Aperture Radar images using double scattering. International Journal of Applied Earth Observation and Geoinformation, 28: 150-159. DOI:https://doi.org/10.1016/j.jag.2013.12.002

Masson-Delmotte, V. et al., 2021. IPCC, 2021: Climate Change 2021: The Physical Science Basis. Contribution of Working Group I to the Sixth Assessment Report of the Intergovernmental Panel on Climate Change. Cambridge University Press Cambridge, UK.

Mhonda, A., 2013a. Evaluating flash flood risk reduction strategies in built-up environment in Kampala, University of Twente.

Mhonda, A., 2013b. Evaluating flash flood risk reduction strategies in built-up environment in Kampala. University of Twente Faculty of Geo-Information and Earth Observation (ITC).

Miller, J.D., Hess, T., 2017. Urbanisation impacts on storm runoff along a rural-urban gradient. Journal of Hydrology, 552: 474-489.

Ming, X., Liang, Q., Xia, X., Li, D., Fowler, H.J., 2020. Real-Time Flood Forecasting Based on a High-Performance 2-D Hydrodynamic Model

and Numerical Weather Predictions. Water Resources Research, 56(7): e2019WR025583. DOI:10.1029/2019wr025583
Mlawer, E.J., Taubman, S.J., Brown, P.D., Iacono, M.J., Clough, S.A., 1997. Radiative transfer for inhomogeneous atmospheres: RRTM, a validated correlated-k model for the longwave. Journal of Geophysical Research: Atmospheres, 102(D14): 16663-16682.
Morrison, H., Curry, J., Khvorostyanov, V., 2005. A new double-moment microphysics parameterization for application in cloud and climate models. Part I: Description. Journal of the atmospheric sciences, 62(6): 1665-1677.
Morrison, H., Milbrandt, J., 2010. Comparison of two-moment bulk microphysics schemes in idealized supercell thunderstorm simulations. Monthly Weather Review.
Morrison, H., Thompson, G., Tatarskii, V., 2009. Impact of cloud microphysics on the development of trailing stratiform precipitation in a simulated squall line: Comparison of one-and two-moment schemes. Monthly weather review, 137(3): 991-1007.
Mugume, I. et al., 2017. Assessing the performance of WRF model in simulating rainfall over western Uganda. J. Climatol. Weather Forecast, 5(1): 1-9.
Mugume, S.N., Butler, D., 2017. Evaluation of functional resilience in urban drainage and flood management systems using a global analysis approach. Urban Water Journal, 14(7): 727-736.
Neal, J. et al., 2011. Evaluating a new LISFLOOD-FP formulation with data from the summer 2007 floods in Tewkesbury, UK. Journal of Flood Risk Management, 4(2): 88-95.
Ngailo, T.J. et al., 2018. Assessing Weather Research and Forecasting (WRF) Model parameterization schemes skill to simulate extreme rainfall events over Dar es Salaam on 21 December 2011. Journal of Geoscience and Environment Protection, 6(01): 36.
Niu, G.Y. et al., 2011. The community Noah land surface model with multiparameterization options (Noah-MP): 1. Model description and evaluation with local-scale measurements. Journal of Geophysical Research: Atmospheres, 116(D12).
Nkwunonwo, U., Whitworth, M., Baily, B., 2020. A review of the current status of flood modelling for urban flood risk management in the developing countries. Scientific African: e00269.
NRCS, U., 1993. Soil Survey Division Staff (1993) Soil Survey Manual. Soil Conservation Service. US Department of Agriculture Handbook, 18: 315.

Bibliography

Nunez, M., Oke, T.R., 1977. The energy balance of an urban canyon. Journal of Applied Meteorology, 16(1): 11-19.

Nur, I., Shrestha, K.K., 2017. An Integrative Perspective on Community Vulnerability to Flooding in Cities of Developing Countries. Procedia Engineering, 198: 958-967. DOI:https://doi.org/10.1016/j.proeng.2017.07.141

Nurritasari, F.A., Sudibyakto, S., Jetten, V.G., 2015. OpenLISEM Flash Flood Modelling Application in Logung Sub-Catchment, Central Java. Indonesian Journal of Geography, 47(2): 132-141.

O'brien, J., 2007. FLO-2D users manual. Nutrioso, Arizona, June.

Oliveros, J.M., Vallar, E.A., Galvez, M.C.D., 2019. Investigating the Effect of Urbanization on Weather Using the Weather Research and Forecasting (WRF) Model: A Case of Metro Manila, Philippines. Environments, 6(2): 10.

Ongoma, V., Chen, H., Omony, G.W., 2018. Variability of extreme weather events over the equatorial East Africa, a case study of rainfall in Kenya and Uganda. Theoretical and applied climatology, 131(1-2): 295-308.

Onyutha, C., Willems, P., 2015. Spatial and temporal variability of rainfall in the Nile Basin. Hydrology and Earth System Sciences, 19(5): 2227.

Opio, R., Sabiiti, G., Nimusiima, A., Mugume, I., Sansa-Otim, J., 2020. WRF Simulations of Extreme Rainfall over Uganda's Lake Victoria Basin: Sensitivity to Parameterization, Model Resolution and Domain Size. Journal of Geoscience and Environment Protection, 8(04): 18.

Osman, O.E., Hastenrath, S., 1969. On the synoptic climatology of summer rainfall over central Sudan. Archiv für Meteorologie, Geophysik und Bioklimatologie, Serie B, 17(4): 297-324.

Ossola, A., Hahs, A.K., Livesley, S.J., 2015. Habitat complexity influences fine scale hydrological processes and the incidence of stormwater runoff in managed urban ecosystems. Journal of environmental management, 159: 1-10.

Otieno, G., Mutemi, J., Opijah, F., Ogallo, L., Omondi, H., 2018. The Impact of Cumulus Parameterization on Rainfall Simulations over East Africa. Atmospheric and Climate Sciences, 8(03): 355.

Pappenberger, F., Dutra, E., Wetterhall, F., Cloke, H.L., 2012. Deriving global flood hazard maps of fluvial floods through a physical model cascade. Hydrology and Earth System Sciences, 16(11): 4143-4156.

Pappenberger, F., Thielen, J., Del Medico, M., 2011. The impact of weather forecast improvements on large scale hydrology: analysing a decade of

forecasts of the European Flood Alert System. Hydrological Processes, 25(7): 1091-1113.
Patel, P., Ghosh, S., Kaginalkar, A., Islam, S., Karmakar, S., 2019. Performance evaluation of WRF for extreme flood forecasts in a coastal urban environment. Atmospheric Research, 223: 39-48. DOI:https://doi.org/10.1016/j.atmosres.2019.03.005
Paul, S. et al., 2018. Increased spatial variability and intensification of extreme monsoon rainfall due to urbanization. Scientific reports, 8(1): 3918.
Pennelly, C., Reuter, G., Flesch, T., 2014. Verification of the WRF model for simulating heavy precipitation in Alberta. Atmospheric Research, 135: 172-192.
Pérez-Molina, E., Sliuzas, R., Flacke, J., 2018. Simulating Spatial Patterns of Urban Growth in Kampala, Uganda, and Its Impact on Flood Risk, GIS in Sustainable Urban Planning and Management. CRC Press, pp. 295-306.
Pérez-Molina, E., Sliuzas, R., Flacke, J., Jetten, V., 2017. Developing a cellular automata model of urban growth to inform spatial policy for flood mitigation: A case study in Kampala, Uganda. Computers, Environment and Urban Systems, 65: 53-65.
Perez Molina, E., 2019. Spatial planning, growth, and flooding: Contrasting urban processes in Kigali and Kampala.
Pielke Sr, R., 2002. 2002: Mesoscale Meteorological Modeling. Academic Press, 676pp.
Platnick, S. et al., 2017. The MODIS cloud optical and microphysical products: Collection 6 updates and examples from Terra and Aqua. IEEE Trans Geosci Remote Sens, 55(1): 502-525. DOI:10.1109/TGRS.2016.2610522
Pleim, J.E., 2007. A combined local and nonlocal closure model for the atmospheric boundary layer. Part I: Model description and testing. Journal of Applied Meteorology and Climatology, 46(9): 1383-1395.
Powers, J.G. et al., 2017. The weather research and forecasting model: Overview, system efforts, and future directions. Bulletin of the American Meteorological Society, 98(8): 1717-1737.
Rahmati, O. et al., 2020. Development of novel hybridized models for urban flood susceptibility mapping. Scientific Reports, 10(1): 1-19.
Ran, L. et al., 2015. Sensitivity of the Weather Research and Forecast/Community Multiscale Air Quality modeling system to MODIS LAI, FPAR, and albedo. Journal of Geophysical Research: Atmospheres, 120(16): 8491-8511. DOI:10.1002/2015jd023424
Rawls, W., Brakensiek, D., 1989. Estimation of soil water retention and hydraulic properties, Unsaturated flow in hydrologic modeling. Springer, pp. 275-300.

Bibliography

Raynaud, D. et al., 2015. A dynamic runoff co-efficient to improve flash flood early warning in Europe: evaluation on the 2013 central European floods in Germany. Meteorological Applications, 22(3): 410-418.

Redfern, T.W., Macdonald, N., Kjeldsen, T.R., Miller, J.D., Reynard, N., 2016. Current understanding of hydrological processes on common urban surfaces. Progress in Physical Geography, 40(5): 699-713.

Revilla Romero, B., 2016. Improving Global Flood Forecasting using Satellite Detected Flood Extent. Utrecht University.

Richard, G., Cousin, I., Sillon, J., Bruand, A., Guérif, J., 2001. Effect of compaction on the porosity of a silty soil: influence on unsaturated hydraulic properties. European Journal of Soil Science, 52(1): 49-58.

Rodrigo, C., Kim, S., Jung, I., 2018. Sensitivity Study of WRF Numerical Modeling for Forecasting Heavy Rainfall in Sri Lanka. Atmosphere, 9(10): 378.

Rossiter, D.G., 2014. KampalaSoilsHydraulicPropertiesReport.pdf.

Ryan, B., 1996. On the global variation of precipitating layer clouds. Bulletin of the American Meteorological Society, 77(1): 53-70.

Ryu, Y.-H., Smith, J.A., Bou-Zeid, E., Baeck, M.L., 2016. The influence of land surface heterogeneities on heavy convective rainfall in the Baltimore–Washington metropolitan area. Monthly Weather Review, 144(2): 553-573.

Ryu, Y. et al., 2017. Applying a coupled hydrometeorological simulation system to flash flood forecasting over the Korean Peninsula. Asia-Pacific Journal of Atmospheric Sciences, 53(4): 421-430.

Sahani, J. et al., 2019. Hydro-meteorological risk assessment methods and management by nature-based solutions. Science of the Total Environment, 696: 133936.

Salamanca, F., Krpo, A., Martilli, A., Clappier, A., 2010. A new building energy model coupled with an urban canopy parameterization for urban climate simulations—part I. formulation, verification, and sensitivity analysis of the model. Theoretical and applied climatology, 99(3-4): 331.

Salvadore, E., Bronders, J., Batelaan, O., 2015. Hydrological modelling of urbanized catchments: A review and future directions. Journal of hydrology, 529: 62-81.

Santanello Jr, J.A., Peters-Lidard, C.D., Kumar, S.V., 2011. Diagnosing the sensitivity of local land–atmosphere coupling via the soil moisture–

boundary layer interaction. Journal of Hydrometeorology, 12(5): 766-786.
Saxton, K.E., Rawls, W.J., 2006. Soil water characteristic estimates by texture and organic matter for hydrologic solutions. Soil science society of America Journal, 70(5): 1569-1578.
Schelhorn, S.-J., Herfort, B., Leiner, R., Zipf, A., De Albuquerque, J.P., 2014. Identifying elements at risk from OpenStreetMap: The case of flooding, ISCRAM.
Schipper, L., Pelling, M., 2006. Disaster risk, climate change and international development: scope for, and challenges to, integration. Disasters, 30(1): 19-38.
Schubert, J.E., Sanders, B.F., 2012. Building treatments for urban flood inundation models and implications for predictive skill and modeling efficiency. Advances in Water Resources, 41: 49-64.
Seino, N., Aoyagi, T., Tsuguti, H., 2018. Numerical simulation of urban impact on precipitation in Tokyo: How does urban temperature rise affect precipitation? Urban Climate, 23: 8-35. DOI:https://doi.org/10.1016/j.uclim.2016.11.007
Shastri, H., Paul, S., Ghosh, S., Karmakar, S., 2015. Impacts of urbanization on Indian summer monsoon rainfall extremes. Journal of Geophysical Research: Atmospheres, 120(2): 496-516. DOI:https://doi.org/10.1002/2014JD022061
Shen, X., Wang, D., Mao, K., Anagnostou, E., Hong, Y., 2019. Inundation extent mapping by synthetic aperture radar: A review. Remote Sensing, 11(7): 879.
Shiau, J., 2003. Return period of bivariate distributed extreme hydrological events. Stochastic environmental research and risk assessment, 17(1): 42-57.
Sikder, M.S., Ahmad, S., Hossain, F., Gebregiorgis, A.S., Lee, H., 2019. Case Study: Rapid Urban Inundation Forecasting Technique Based on Quantitative Precipitation Forecast for Houston and Harris County Flood Control District. Journal of Hydrologic Engineering, 24(8): 05019017.
Sikder, M.S., Hossain, F., 2018. Sensitivity of initial-condition and cloud microphysics to the forecasting of monsoon rainfall in South Asia. Meteorological Applications, 25(4): 493-509.
Sikder, S., Hossain, F., 2016. Assessment of the weather research and forecasting model generalized parameterization schemes for advancement of precipitation forecasting in monsoon-driven river basins. Journal of Advances in Modeling Earth Systems, 8(3): 1210-1228.

Bibliography

Skamarock, W.C., 2004. Evaluating mesoscale NWP models using kinetic energy spectra. Monthly weather review, 132(12): 3019-3032.

Skamarock, W.C., 2008. A description of theadvanced research WRF version 3. Tech. Note: 1-96.

Skamarock, W.C. et al., 2005. A description of the advanced research WRF version 2, National Center For Atmospheric Research Boulder Co Mesoscale and Microscale ….

Sliuzas, R., Flacke, J., Jetten, V., 2013. Modelling urbanization and flooding in Kampala, Uganda. Network-Association of European Researchers on Urbanisation in the South (N-AERUS) XIV, Enschede: 12-14.

Song, J., Wang, Z.-H., 2015. Interfacing the urban land–atmosphere system through coupled urban canopy and atmospheric models. Boundary-layer meteorology, 154(3): 427-448.

Stampoulis, D., Anagnostou, E.N., Nikolopoulos, E.I., 2013. Assessment of high-resolution satellite-based rainfall estimates over the Mediterranean during heavy precipitation events. Journal of Hydrometeorology, 14(5): 1500-1514.

Stensrud, D.J., 2009. Parameterization schemes: keys to understanding numerical weather prediction models. Cambridge University Press.

Stergiou, I., Tagaris, E., Sotiropoulou, R.-E.P., 2017. Sensitivity assessment of WRF parameterizations over Europe, Multidisciplinary digital publishing institute proceedings, pp. 119.

Stewart, I.D., Oke, T.R., 2012. Local climate zones for urban temperature studies. Bulletin of the American Meteorological Society, 93(12): 1879-1900.

Sun, X., Xie, L., Semazzi, F., Liu, B., 2015. Effect of lake surface temperature on the spatial distribution and intensity of the precipitation over the Lake Victoria basin. Monthly Weather Review, 143(4): 1179-1192.

Sun, Y., Wendi, D., Kim, D.E., Liong, S.-Y., 2019. Deriving intensity–duration–frequency (IDF) curves using downscaled in situ rainfall assimilated with remote sensing data. Geoscience Letters, 6(1): 17.

Sy, B. et al., 2016. Participatory approach for flood risk assessment: the case of Yeumbeul Nord (YN), Dakar, Senegal. WIT Trans. Built Env, 165: 331-342.

Sy, B., Frischknecht, C., Dao, Q.-H., Consuegra Zammit, D., Giuliani, G., 2020. Reconstituting past flood events: the contribution of citizen science. Hydrology and Earth System Sciences, 24(1): 61-74.

Tan, E., 2010. Development of a methodology for probable maximum precipitation estimation over the American River watershed using the WRF model, 71.

Tayefi, V., Lane, S., Hardy, R., Yu, D., 2007. A comparison of one-and two-dimensional approaches to modelling flood inundation over complex upland floodplains. Hydrological Processes: An International Journal, 21(23): 3190-3202.

Taylor, T., Markandya, A., Mwebaze, T., Sebbit, A., Rautenbach, H., 2015. Economic Assessment of the Impacts of Climate Change in Uganda. Case Study on Water and Energy Sector Impacts in the Mpanga River Catchment.

ten Veldhuis, J.A.E., 2011. How the choice of flood damage metrics influences urban flood risk assessment. Journal of Flood Risk Management, 4(4): 281-287. DOI:10.1111/j.1753-318X.2011.01112.x

Teng, J. et al., 2017. Flood inundation modelling: A review of methods, recent advances and uncertainty analysis. Environmental Modelling & Software, 90: 201-216.

Thompson, G., Field, P.R., Rasmussen, R.M., Hall, W.D., 2008. Explicit forecasts of winter precipitation using an improved bulk microphysics scheme. Part II: Implementation of a new snow parameterization. Monthly Weather Review, 136(12): 5095-5115.

Tian, J. et al., 2020. A coupled atmospheric-hydrologic modeling system with variable grid sizes for rainfall-runoff simulation in semi-humid and semi-arid watersheds: How does the coupling scale affects the results? Hydrology and Earth System Sciences Discussions: 1-36.

Tian, J., Liu, J., Yan, D., Li, C., Yu, F., 2017. Numerical rainfall simulation with different spatial and temporal evenness by using a WRF multiphysics ensemble. Natural Hazards & Earth System Sciences, 17(4).

Tingsanchali, T., 2012. Urban flood disaster management. Procedia engineering, 32: 25-37.

Trinh, T. et al., 2018. Integrating global land-cover and soil datasets to update saturated hydraulic conductivity parameterization in hydrologic modeling. Science of the Total Environment, 631: 279-288.

Umer, Y., Ettema, J., Jetten, V., Steeneveld, G.-J., Ronda, R., 2021. Evaluation of the WRF Model to Simulate a High-Intensity Rainfall Event over Kampala, Uganda. Water, 13(6): 873.

Umer, Y.M., Jetten, V.G., Ettema, J., 2019. Sensitivity of flood dynamics to different soil information sources in urbanized areas. Journal of Hydrology, 577: 123945. DOI:https://doi.org/10.1016/j.jhydrol.2019.123945

Bibliography

UN, D., 2015. World urbanization prospects: The 2014 revision. United Nations Department of Economics and Social Affairs, Population Division: New York, NY, USA, 41.

Van Steenbergen, N., Willems, P., 2013. Increasing river flood preparedness by real-time warning based on wetness state conditions. Journal of hydrology, 489: 227-237.

Van Westen, C., Jetten, V., Trigg, M., Alkema, D., 2015. Report on methodologies for hazard mapping in the Caribbean.

Vermeiren, K., Van Rompaey, A., Loopmans, M., Serwajja, E., Mukwaya, P., 2012. Urban growth of Kampala, Uganda: Pattern analysis and scenario development. Landscape and urban planning, 106(2): 199-206.

Vojinovic, Z., 2015. Flood Risk: The Holistic Perspective. IWA Publishing.

Vojinovic, Z., Abbott, M.B., 2012. Flood risk and social justice. IWA Publishing.

Vojinovic, Z. et al., 2016. Holistic approach to flood risk assessment in areas with cultural heritage: a practical application in Ayutthaya, Thailand. Natural Hazards, 81(1): 589-616.

Wang, P. et al., 2018a. Effects of urbanization, soil property and vegetation configuration on soil infiltration of urban forest in Changchun, Northeast China. Chinese geographical science, 28(3): 482-494.

Wang, W. et al., 2007. User's guide for advanced research WRF (ARW) modeling system version 3. Mesoscale and Microscale Meteorology Division–National Center for Atmospheric Research (MMM-NCAR).

Wang, W., Beezley, C., Duda, M., 2012. WRF ARW V3: user's guide. Wang, C. Beezley, M. Duda, et al. URL: http://www. mmm. ucar. edu/wrf/users (accessed: 11.01. 2013).

Wang, W. et al., 2018b. User's Guides for the Advanced Research WRF (ARW) Modeling System, version 3.

watershed St Lucia, B.d.O., 2016. Flood modelling for Integrated Watershed Management.

Wehbe, Y. et al., 2019. Analysis of an extreme weather event in a hyper-arid region using WRF-Hydro coupling, station, and satellite data. Nat. Hazards Earth Syst. Sci., 19(6): 1129-1149. DOI:10.5194/nhess-19-1129-2019

Westerberg, I., McMillan, H., 2015. Uncertainty in hydrological signatures. Hydrology and Earth System Sciences, 19(9): 3951.

Wikle, C.K., 2005. Atmospheric modeling, data assimilation, and predictability. Taylor & Francis.

Wösten, J., Lilly, A., Nemes, A., Le Bas, C., 1999. Development and use of a database of hydraulic properties of European soils. Geoderma, 90(3-4): 169-185.

Wouters, H. et al., 2016. The efficient urban canopy dependency parametrization (SURY) v1. 0 for atmospheric modelling: description and application with the COSMO-CLM model for a Belgian summer. Geoscientific Model Development, 9(9): 3027-3054.

Yan, K., Pappenberger, F., Umer, Y.M., Solomatine, D.P., Di Baldassarre, G., 2014. Regional Versus Physically-Based Methods For Flood Inundation Modelling In Data Scarce Areas: An Application To The Blue Nile.

Yang, J.-L., Zhang, G.-L., 2011. Water infiltration in urban soils and its effects on the quantity and quality of runoff. Journal of soils and sediments, 11(5): 751-761.

Yang, M., Liu, G., Chen, T., Chen, Y., Xia, C., 2020. Evaluation of GPM IMERG precipitation products with the point rain gauge records over Sichuan, China. Atmospheric Research, 246: 105101. DOI:https://doi.org/10.1016/j.atmosres.2020.105101

Zehe, E., Blöschl, G., 2004. Predictability of hydrologic response at the plot and catchment scales: Role of initial conditions. Water Resources Research, 40(10).

Zhang, J., Lin, L.-F., Bras, R.L., 2018a. Evaluation of the Quality of Precipitation Products: A Case Study Using WRF and IMERG Data over the Central United States. Journal of Hydrometeorology, 19(12): 2007-2020. DOI:10.1175/jhm-d-18-0153.1

Zhang, W., Villarini, G., Vecchi, G.A., Smith, J.A., 2018b. Urbanization exacerbated the rainfall and flooding caused by hurricane Harvey in Houston. Nature, 563(7731): 384-388.

Zhang, Y. et al., 2019. Regional patterns of extreme precipitation and urban signatures in metropolitan areas. Journal of Geophysical Research: Atmospheres, 124(2): 641-663.

Zhong, S., Qian, Y., Zhao, C., Leung, R., Yang, X.Q., 2015. A case study of urbanization impact on summer precipitation in the Greater Beijing Metropolitan Area: Urban heat island versus aerosol effects. Journal of Geophysical Research: Atmospheres, 120(20): 10,903-10,914.

Zhou, Q., Leng, G., Su, J., Ren, Y., 2019. Comparison of urbanization and climate change impacts on urban flood volumes: Importance of urban planning and drainage adaptation. Science of The Total Environment, 658: 24-33. DOI:https://doi.org/10.1016/j.scitotenv.2018.12.184

Zischg, A.P., Felder, G., Mosimann, M., Röthlisberger, V., Weingartner, R., 2018. Extending coupled hydrological-hydraulic model chains with a

Bibliography

surrogate model for the estimation of flood losses. Environmental modelling & software, 108: 174-185.

Zittis, G., Bruggeman, A., Camera, C., Hadjinicolaou, P., Lelieveld, J., 2017. The added value of convection permitting simulations of extreme precipitation events over the eastern Mediterranean. Atmospheric research, 191: 20-33.

Summary

Strategies to cope with floods, for instance, integrated flood management, require proper flood hazard assessment. Such flood hazard assessment relies on the flood modelling approaches, which require high-quality and quantity data to produce realistic flood hazard maps. In many cities in the developing countries, also known as data scarce-areas, flood modelling is challenging as there is sparse or no observation on rainfall data and soil information used for proper model development, model calibration, and validation. However, open-source geospatial data and the NWP model rainfall product can overcome the data scarcity problem. Therefore, this Ph.D. thesis aimed to explore publicly available geospatial datasets and their integration with hydro-meteorological modelling systems to overcome the data-scarcity challenges, specifically, to explore the data of extreme rainfall, soil, and land-cover information for flash flood modelling in the urbanized catchment. The findings are summarized into three phases, as discussed in the following.

The first phase of this Ph.D. study focuses on exploring soil information used for flash flood modelling in the urbanized catchment. Accordingly, the soil information that is determining the infiltration processes (i.e., Ksat, porosity, initial condition, soil matric suction, and soil depth) is derived following three different soil databases: (1) FAO soil map (SMFAO); (2) soil map derived based on the soil-landscape relationships (SMLS), and (3) soil map derived from the SoilGrids database (SMSG)). The soil information derived from these data sources is believed to be overcome the data limitation problem. However, the open-source soil databases cannot correctly consider the local features (e.g., wetlands, fragmented vegetation cover, and soil compaction), which would lead to the data quality problem. Therefore, in this study, the local features' influence on the derived soil information is numerically adjusted by incorporating the land cover data derived from the satellite image. The derived soil information is then used as the input to openLISEM integrated flood modelling system to assess their impact on flood dynamics in the urbanized catchment. The impact analysis is evaluated as the compacted and uncompacted soil condition. The results indicated that the flood dynamics are highly sensitive to different soil databases. The incorporation of soil compaction into the soil information has the largest impact on the flood dynamics in the catchment. This study showed that open-source data choice strongly influences both the simulated quantity and spatial variability of the infiltration, which directly affects runoff and flooding. On top

Summary

of that, the effect of sealing and compaction is equally essential and nearly outweighs the differences caused by the use of different soil databases.

The second part of the Ph.D. thesis is to model and analyze the high-intensity rainfall product using the WRF model, which combined two main research objectives (chap.3 & 4 in the document). The first objective is to evaluate the satellite-driven urban fraction appropriateness in the WRF model for simulating high-intensity rainfall events in urbanized areas. Three different simulations are performed in order to distill the impact of changing urban fractions and adjusted urban parameters on the simulated rainfall: The first simulation (1) StandardWPS, which is carried out using the default urban fraction with the default urban parameters; (2) UFD_Parameter, which is using the default urban fraction, but with adjusted urban parameters; and (3) Updated, which is with the updated urban fraction based on the Landsat 2016 image and the adjusted urban parameters. All model simulations are configured at high spatial (1 km) and temporal (10-minute) resolutions forced with the latest ERA5 global reanalysis dataset. The model result was validated using the rainfall observation from the gauging station and CHIRPS data. The results showed that the simulated rainfall performs better with a relatively lower error when using the updated urban fraction. The satellite-derived urban map represents a more realistic extent and intensity of the urban fraction with a heterogeneous urban fraction, which results in more realistic rainfall simulations. The second objective of the second part of the Ph.D. is to evaluate the suitability of the WRF model in simulating high-intensity rainfall events. Here, we evaluated the procedure to select the appropriate WRF parameterization combination for proper high-intensity rainfall simulation through the sensitivity analysis. The WRF model set up with the updated urban fraction is used for the WRF model simulation as the combination of microphysics, cumulus, and planetary boundary layer (i.e., MP-CP-PBL procedure). The result showed that the WRF model's ability to simulate the HIRE that can be used for flash flood modelling is highly determined by the appropriate selection of the parametrization combinations.

The last phase of this Ph.D. study focuses on examining the WRF rainfall product's applicability for urban flood hazard assessment by proposing a new methodology to select the representative gridcell-rainfall events from three known WRF simulated rainfall events (HIREs). The two-step procedure is followed. Firstly, the potential gridcell-rainfall events from the WRF simulated HIREs are selected based on the given criteria. Secondly, the representative gridcell-rainfall events as a design storm of a given return period are defined

using the quantile function where the quantile function is applied to the cumulative rainfall amount of each of the selected potential gridcell-rainfall events. Finally, three different gridcell-rainfall events representing the design storms varying between T = 2 and 10-year return periods are extracted for each three HIRE. The developed design storms are then compared with the design storms from the pre-established Intensity-Duration-Frequency (IDF) curves in terms of their 24-hour total rainfall amount (mm), peak intensity (mm/hr), and the time to peak intensity (minute). The constructed design storms are then applied to the openLISEM model for flood hazard modelling in Kampala's upper Lubigi catchment. The derived design storm can give an insight into the applicability and usability of the numerical weather prediction model outputs for flood modelling in the data-scarce areas.

In general, the results of this study indicates that open-source database such as SoilGrids and their combination with satellite-driven land-cover data can provide soil information needed for flood modelling in the data-scarce area. Moreover, the high-intensity rainfall that has the potential to trigger the localized flood can be produced using the mesoscale WRF model. However, the procedure to improve the performance of the NWP model in simulating high-intensity rainfall must be taken into consideration. The MP-CP-PBl procedure followed in this study and updating the urban fraction certainly improved the performance of the WRF model to simulate high-intensity rainfall. The WRF data-assimilation and model coupling system can further improve the model's performance in simulating the events.

Samenvatting

Strategieën om met overstromingen om te gaan, zoals geïntegreerde overstromingsmanagement, vereisen een weloverwogen inschatting van overstromingsgevaar. Zo'n inschatting is afhankelijk van overstromingsmodellen, die hoge kwaliteit data nodig hebben om het overstromingsgevaar realistisch in kaart te brengen. In veel steden in ontwikkelingslanden, ook wel gebieden met data schaarste genoemd, is het modelleren van overstromingen een uitdaging omdat er weinig metingen zijn van de regenval of de bodeminformatie. Deze metingen zijn nodig voor het ontwikkelen van een model en de kalibratie en validatie. Door middel van open-source geografische data en het regenvalproduct van het NWP model kan het probleem van data schaarste overkomen worden. Daarom is het doel van het onderzoek in dit proefschrift gericht om het onderzoeken van vrij toegankelijke geografische datasets en de toepassing voor hydro-meteorologische modellen om de uitdagingen met data schaarste aan te pakken. Het onderzoek richt zich vooral op de data over extreme regenval, informatie over de bodem en landgebruik voor overstromingsmodellering in stedelijke gebieden. Het onderzoek kan worden samengevat in drie onderdelen, die hieronder verder zijn toegelicht.

De eerste fase van het promotieonderzoek is gericht op het onderzoeken van bodeminformatie die te gebruiken is voor stedelijke overstromingsmodellen. Met name de bodeminformatie die het infiltratieproces beïnvloeden (Ksat, porositeit, zuigspanning, bodemdiepte en de aanvankelijke begin omstandigheden)is verkregen door middel van drie verschillende bodemdatasets: (1) FAO bodemkaart (SMFAO); (2) bodemkaart gebaseerd om bodem-landschap interactie (SMLS) en (3) de SoilGrids database (SMSG). Door middel van bodeminformatie afkomstig van deze bronnen is het geprobeerd de data schaarste op te vullen. Er zijn een aantal lokale eigenschappen die niet goed door de open-source data beschreven worden (bijv. drasland, gefragmenteerde vegetatiebedekking, bodemcompactheid) wat invloed heeft op de kwaliteit van de data. Daarom is in dit onderzoek de invloed van lokale eigenschappen op de bodeminformatie numeriek aangepast aan de hand van landgebruik informatie gebaseerd op satellietbeelden. De verkregen bodeminformatie is gebruikt als invoer voor het openLISEM overstromingsmodel, om zo het effect van de bodemeigenschappen op de overstromingsdynamiek in stedelijke gebieden te beoordelen. Deze analyse is uitgevoerd met zowel verdichte als onverdichte grond. De resultaten tonen aan dat de overstromingsdynamiek erg afhankelijk is van welke bodemdata er gebruikt is, waar vooral de compactheid van de bodem het meeste invloed heeft op de overstroming. Uit dit onderzoek is gebleken dat de keuze van datasets sterke invloed heeft op zowel de hoeveelheid en ruimtelijke variatie van de gesimuleerde infiltratie, wat van directe invloed is op de stroming en overstroming. Daarnaast is het effect van afdichting en compactheid van de bodem van even groot belang en weegt bijna zwaarder dan het verschil van bodemdatasets.

Het tweede deel van deze PhD bestaat uit het modelleren en analyseren van hoge intensiteit regenval aan de hand van het WRF model, waardoor de twee voornaamste onderzoeksdoelen worden gecombineerd (hoofdstuk 3 en 4). Het eerste doel bestaat uit het evalueren van de op satellietbeelden gebaseerde stedenfractie in het WRF model voor het simuleren van hoge intensiteit regenval in stedelijke gebieden. Drie verschillende simulaties zijn uitgevoerd om het effect te beoordelen van veranderende stedenfracties en aangepaste stedelijke parameters op de gesimuleerde regenval: (1) StandardWPS dat is uitgevoerd met de initiële stedenfractie met de initiële stedelijke parameters (2) UFD_Parameter met de initiële stedenfractie maar met aangepaste stedelijke parameters, en (3) de bijgewerkte versie, met de bijgewerkte stedenfractie gebaseerd om Landsat 2016 beelden en aangepaste stedelijke parameters. Alle simulaties zijn uitgevoerd op een hoge ruimtelijke resolutie (1km) en tijdsresolutie (10 minuten) geforceerd door middel van de laatste ERA5 globale dataset. De resultaten zijn gevalideerd door middel van regenvalobservaties van het het ijkingsstation en CHIRPS data. De resultaten laten zien dat de gesimuleerde regenval beter presteert met een relatieve lagere foutmarge wanneer de aangepaste stedenfractie is gebruikt. The op satellietbeelden gebaseerde stedenkaart laat een realistischere verspreiding en intensiteit van de stedenfractie zien met een heterogene stedenfractie, als gevolg van realistischere regenvalsimulaties. Het tweede onderzoeksdoel van het tweede deel van dit proefschrift is het evalueren van de bruikbaarheid van het WRF model in simulaties van hoge intensiteit regenval. Hierbij evalueren we de procedure voor het selecteren van geschikte WRF parameters combinaties voor nauwkeurige hoge intensiteit regenval simulaties door middel van gevoeligheidsanalyse. De instellingen van het WRF model met de aangepaste stedenfractie is gebruikt voor de WRF simulatie als de combinatie van microfysica, cumulus, en planeet grenslagen (MP-CP-PBL procedure). De resultaten laten zien dat de toepasbaarheid van het WRF model om HIRE te simuleren, wat gebruikt kan worden voor het beoordelen van overstromingsgevaar, erg afhankelijk is van het gebruikt van de juiste parametercombinaties.

Het laatste deel van de PHD focust op het onderzoeken van de toepasbaarheid van het WRF regenvalproduct voor het beoordelen van overstromingsgevaar door een nieuwe methode voor te stellen om representatieve regenval momenten te selecteren van drie bekende WRF gesimuleerde regenval momenten (HIREs). De tweetraps procedure is hiervoor gevolgd. Ten eerste, de mogelijke gridcell regenvalmomenten van de WRF gesimuleerde HIREs zijn geselecteerd gebaseerd op de gegeven criteria. Ten tweede zijn de representatieve gridcell regenvalmomenten gebruikt als een 'design storm' van een gegeven tijdsperiode, gedefinieerd door middel van kwartielfunctie waarvan de kwartielfunctie is toegepast op de cumulatieve hoeveelheid regen voor elk geselecteerde gridcell regenvalmoment. Als laatst zijn drie verschillende gridcell regenmomenten, die representatief zijn voor de 'design storms' variërend van 1-in 2 tot 1 in 10 jaar terugkeer periodes, afgeleid voor elk van de drie HIRE. De ontwikkelde 'design storm' is daarna vergeleken met de 'design storms' van eerder gedefinieerde Intensity-Duriation-Frequency (IDF) curves met betrekking tot de 24uur totale hoeveelheid regen (mm), maximale intensiteit (mm/uur) en tijd tot de maximale intensiteit (minuten). De ontwikkelde 'design storms' zijn daarna toegepast in het openLISEM model voor het modelleren van overstromingen in het hoge Lubigi stroomgebied van Kamapala. De verkregen 'design storms' kunnen een inzicht verschaffen in de toepasbaarheid en gebruik van numerieke weervoorspellingsmodellen voor overstromingsmodellen in een data schaars gebied.

In het algemeen zijn de resultaten van dit onderzoek dat vrij toegankelijke datasets zoals SoilGrids en de combinatie met op satellietbeelden gebaseerde landgebruik data bodeminformatie kan verschaffen die nodig is voor overstromingsmodelering in gebieden met data schaarste. Ook kan de hoge intensiteit van regenval die lokaal overstromingen kan veroorzaken worden gesimuleerd door middel van het mesoscale WRF model. Echter moet de procedure voor het verbeteren van het NWP model in het simuleren van hoge intensiteit regenval in overweging worden genomen. De MP-CP-PBJ procedure die gebruikt is in dit onderzoek, en ook de aangepaste stedenfractie heeft wel degelijk invloed gehad op de prestatie van het WRF model om hoge intensiteit regenval te simuleren. Het gebruik van WRF data assimilatie en model koppelingssystemen, bijvoorbeeld, het WRF-Hydro koppelingssysteem, kan de modelprestaties verder verbeteren.

About the Author

Yakob Umer was born on 10 January 1985 in Bale, Ethiopia. In 2004 he started with his Bachelor of Science (BSc) in Meteorology Science in Arba Minch University, Ethiopia. Right after completion of his BSc, he was recruited as a graduate assistant in the Department of Meteorology. In parallel with his job, he continued with a Master of Science (MSc) study in Meteorology Science at the same university. He completed his study in 2010 with the thesis "Climate Change Impact assessment on soil water availability and crop production in the Anjeni Watershed, Upper Blue Nile, Ethiopia." His MSc thesis work was part of the project called "Re-thinking adaptation options for Climate change" as a collaborative project between the International Water Management Institute (IWMI) in Addis Ababa office and Arba Minch University.

In 2011 Yakob won the Intergovernmental Panel on Climate Change (IPCC) award as a young researcher to work on climate change impact assessment on Blue Nile River. In the same year, he continued with his second MSc in Water Science and Engineering, with a specialization in Hydroinformatics at UNESCO-IHE Institute for Water Education, Delft, The Netherlands. He completed his study in 2013 with the research title "Flood Hazard Mapping: Comparison of Different Methods to estimate design floods in the Main Blue Nile Reach in Sudan." Afterward, he worked as a flood modeller at the IWMI headquarter office in Colombo, Sri Lanka, for almost one year. In that position, he had the opportunity to work on different projects that focused on West Africa and Southeast Asia, which led to a research product, "Modelling the Flood-risk extent using LISFLOOD-FP in a complex watershed: A case study of Mundeni Aru River Basin, Sri Lanka." Afterward, he joined Addis Ababa University, Institute of Geophysics, Space Science and Astronomy (IGSSA) as a research associate to work on a project that focused on climate change and water management in the Blue Nile Basin, Ethiopia.

In 2016 Yakob started as a Ph.D. researcher (AIO) at the Department of Earth System Analysis (ESA), Faculty of Geo-Information Science and Earth Observation (ITC) at the University of Twente, The Netherlands. He worked on exploring open source geospatial datasets and advances in hydrometeorological modelling systems to improve urban flood hazard assessment in scarce data areas. During his Ph.D., he collaborated with Wageningen University, meteorology, and air quality section to work on the mesoscale Numerical Weather Prediction (NWP) model to improve the simulation of high-intensity rainfall over the urbanized catchment in Kampala, Uganda. Thereafter, Yakob was employed as a postdoc in the ESA department at ITC, University of Twente, working on research related to the application of the NWP modelling system for landslide early warning system in Indonesia.

Author’s publications

Peer-reviewed Journal articles

Y.M Umer, V.G. Jetten, J. Ettema, Lombardo, L. 2022**.** Application of the WRF model rainfall product for the localized flood hazard modelling in a data-scarce environment **DOI: 10.1007/s11069-021-05117-6**

Y.M Umer, Janneke Ettema, Victor Jetten, Gert-Jan Steeneveld, Reinder Ronda. Evaluation of the WRF model to simulate a high-intensity rainfall event over Kampala, Uganda. 2021. **WATER 13(6)DOI 10.3390/w13060873**

Y. M. Umer, V.G. Jetten, J. Ettema. (2019)**.** Sensitivity of flood dynamics to different soil information sources in urbanized areas**,** Journal of Hydrology j.jhydrol.2019.123945

G Amarnath, **Y.M Umer**, N Alahacoon, Y Inada. (2015). Modelling the flood-risk extent using LISFLOOD-FP in a complex watershed: case study of Mundeni Aru River Basin, Sri Lanka, journal of PIAH, 370: 131-138

Kun Yan, Florian Pappenberger, **Y.M Umer**, Dimitri P Solomatine, Giuliano Di Baldassarre. (2014). Regional Versus Physically-Based Methods For Flood Inundation Modelling In Data Scarce Areas: An Application To The Blue Nile. Proceedings in Hydroinformatics,

Conference proceedings and presentation

Y.M Umer, J Ettema, V Jetten. (2019). Evaluation of WRF simulated Rainfall for Flash flood modelling in an Urbanized Catchment: Case study Kampala, Uganda Conference presentation: AGU Fall Meeting 2019, San Francisco, California, USA

J Ettema, B van den Bout, **Y.M Umer**, V Kokorev, V Jetten. (2019). Meteorological Data to improve Hydrological Design Storm Approach: **AGU Fall Meeting 2019, San Francisco, California, USA**

Y.M Umer, J Ettema, V Jetten. (2019). Applying WRF-openLISEM model coupling system to simulate flash flood hazard in Kampala, Uganda Poster presentation: EGU General Assembly 2019, Vienna, Austria

G Amarnath, Y Inada, S Ghosh, **Y.M Umer**, N Alahacoon, H Kota, R. (2015). Earth observation technologies for flood-risk mapping, modelling and management. Training manual prepared for Capacity Building Workshop on Earth Observation Technologies for decision making system. Training and conference with stakeholders 2014 and, University of Peradeniya. Postgraduate Institute of Science, Sri Lanka